THEORETICAL AND EXPERIMENTAL STUDIES OF GAS AND PARTICLE MOTION AROUND BUBBLES IN A TWO-DIMENSIONAL FLUIDISED BED

by

Alain L. F. Martin-Gautier

(Ing. I.G.C., University of Toulouse, France)

July 1974

A thesis submitted for the degree of

Doctor of Philosophy

of the University of London and for the

Diploma of Imperial College

Department of Chemical Engineering

and Chemical Technology.

Imperial College

London, S.W.7.

To Stéphanie

ABSTRACT

A theoretical model describing the motion of a Newtonian fluid around a circular cylinder has been derived. A boundary condition of zero-tangential shear stress was assumed at the surface of the cylinder. The equation was solved using finite-difference technique.

This model was applied to the motion of a two-dimensional gas bubble rising in a fluidised bed and the complete solution for the particulate and the gas phase was obtained.

Experiments were carried out by measuring the displacement of particles and the variations of the gas velocity induced by the rising bubble. The experiments were performed in a two-dimensional apparatus.

It is found that a Newtonian model for the fluidised bed does not describe the behaviour of all the variables and that the behaviour of the particulate phase is often better described by theories assuming an inviscid motion.

ACKNOWLEDGMENTS

I would like to express my sincere gratitude to Dr. D. L. Pyle for his constant help and interest throughout this research project. My gratitude goes also to Mr. W. Meneer and to my friend John for their assistance in the experimental part of this project.

The scholarship awarded by the Centre National de la Recherche Scientifique and the Royal Society has been greatly appreciated.

My many thanks to my wife, Claude, for her everyday help and encouragement and to my parents for their support during the course of my studies.

Alain Martin-Gautier,

July 1974.

LIST OF CONTENTS

	Pages
Abstract	3
Acknowledgements	4
List of Contents	5
List of Symbols	9
Chapter 1 Introduction and literature survey	12
1.1. Introduction	12
1.2. Literature survey	15
1.2.1. Interparticle forces and dense phase viscosity measurements.	15
1.2.2. Particle motion	25
1.2.3. Gas motion	31
1.3. Summary	34
Chapter 2 Equations of motion	38
2.1. General form of the equations	38
2.2. Assumptions	40
2.3. Equation of motion for the particulate phase	42
2.3.1. Simplification of the stress tensor	42
2.3.2. Partial differential equation in terms of the stream function	44
2.3.3. Dimensionless form of the equations	46
2.3.4. Boundary conditions	48
2.4. Equation of motion for the fluid phase	50
2.4.1. Expression for the interaction force $\underline{nf}$	50
2.4.2. Calculation of the gas pressure	53

Pages

2.4.3. Calculation of the Froude number 57

2.4.4. Voidage variations around the bubble 60

2.4.5. Solution for the gas flow 62

2.5. Conclusion 63

Chapter 3 Numerical Solution of the equations of motion 66

3.1. The transformed equations for the particulate flow 66

3.2. Finite difference form of the equations for the particulate flow 68

3.2.1. Vorticity equation 68

3.2.2. Equation for the stream function 76

3.3. Solution for the vorticity equation 78

3.4. Initial conditions for the particulate flow 83

3.4.1. Initial values for the stream function 83

3.4.2. Approximation of surface vorticity 84

3.5. Calculation Procedure 88

3.6. Pressure variations 90

3.6.1. Pressure variations along the axis of the bubble 90

3.6.2. Pressure variations on the bubble surface 94

3.7. Drag coefficient 97

3.8. Particle drift 99

3.9. Gas flow stream function 103

3.10. Conclusion 105

Chapter 4 Experimental 110

4.1. Experimental set-up 110

4.2. Method of measurements 111

Pages

Chapter 5 Theoretical and experimental results for the particulate flow 123

5.1. Theoretical results 123

5.1.1. Solution for the stream function and vorticity 132

5.1.2. Drift of particles 127

5.1.3. Drag coefficient 130

5.1.4. Variations of the bubble Froude number 133

5.1.5. Voidage variations 135

5.2. Experimental results 136

5.2.1. Results with respect to stationary axes. 136

5.2.2. Results with respect to axes moving with the bubble 140

5.3. Conclusion 143

Chapter 6 Theoretical and experimental results for the gas flow 184

6.1. Theoretical results 184

6.1.1. Solution for the pressure field 185

6.1.2. Streamlines of gas flow 190

6.2. Experimental results 192

6.2.1. Measurements on the bubble axis 192

6.2.2. Measurements on the bubble sides 198

6.3. Conclusion 200

Chapter 7 Indirect measurement of the bubble through-flow velocity 226

7.1. Theory 226

7.1.1. Laminar region: $Re_p < 0.5$ 229

7.1.2. Turbulent region: $Re_p > 1000$ 230

7.1.3. Intermediate region: $0.5 < Re_p < 1000$ 230

Pages

7.2. Application to a bubble rising in a fluidised bed 232

7.2.1. Through-flow velocity 232

7.2.2. Experimental 233

7.3. Theoretical values of the through flow determined from the viscous theory for a two dimensional bubble 235

7.4. Conclusion 237

Chapter 8 Conclusions 245

8.1. Theoretical results 245

8.2. Experimental results and comparison with theories. 247

8.3. General conclusion 248

References 250

Appendices 257

Appendix 1 Important relations in two dimensional flow - Cylindrical coordinates 258

Appendix 2 Application of hot wire anemometry to gas velocity measurements in a fluidised bed 260

A.2.1. Basic principle 260

A.2.2. Signal processing and sensor calibration 262

Appendix 3 270

A.3.1. Particle motion 270

A.3.2. Gas motion 272

Appendix 4 Computer programmes 276

A.4.1. Introduction 276

A.4.2. Flow diagrams 278

A.4.3 List of FORTRAN symbols 285

A.4.4. Listings of programmes 294

Appendix 5 Calculation of the Froude number in the case of Stokes's flow for the three- 342

LIST OF MAIN SYMBOLS

a	bubble radius
$c(\varepsilon)$	coefficient of added mass
C_D	drag coefficient on the bubble
C_{Dp}	drag coefficient on an isolated particle
d_p	diameter of particle
E	output voltage from the anemometer
$\underline{f}$	particle. fluid interaction force
$\underline{g}$	gravity
k	coefficient in throughflow velocity (Chapter 7)
k	increment in ξ direction
l	increment in η direction
n	concentration of particles per unit volume
P	pressure
r	radial coordinate
r_c	cloud radius
r_p	radius of particle
t	time
U	throughflow velocity (Chapter 7) $U = U_b + kU_o$
U_b	bubble velocity
U_o	superficial velocity at minimum fluidisation
$\underline{u}$	gas velocity
u_o	interstitial velocity at minimum fluidisation
V_p	falling velocity of an isolated particle
V_t	terminal velocity of an isolated particle
$\underline{v}$	particle velocity
x	vertical axis
X	drift of particle in x direction

y	horizontal axis
Y	drift of particle in y direction
Fr	Froude number $Fr = \frac{U_b^2}{ga}$
Re	bubble Reynolds number $Re = \frac{2a U_b \rho_p (1 - \varepsilon_o)}{\mu_p}$
Re_i	interstitial Reynolds number
Re_p	Reynolds number for an isolated particle
α_b	dimensionless ratio $\alpha_b = \frac{U_b}{u_o}$
β	fluid-particle drag coefficient
γ	dimensionless ratio $\gamma = \frac{\beta_o}{\beta}$
ε	voidage fraction
ζ	component of vorticity
η	coordinate in transformed plane θ direction
θ	angle
θ_i	included angle of spherical cap bubble
λ_p	bulk viscosity of particulate phase
μ_f, μ_p	viscosity
ν_f, ν_p	kinematic viscosity
ξ	coordinate in transformed plane r-direction
ρ	dimensionless radial component
ρ_a	acceleration factor
ρ_f, ρ_p	density
τ	dimensionless time on path line
τ'	dimensionless time on drift profile w. r. t. an undisturbed layer of particles above the bubble
$\underline{\tau}_f$, $\underline{\tau}_p$	stress tensor
τ_o	limiting shear stress

χ	gas stream function
Ψ	particle stream function
ω	overrelaxation factor
$\underline{\omega}$	vorticity vector
ω_v	underrelaxation factor

Subscripts

i	θ . direction
j	r . direction
f	fluid phase
p	particle phase
s	conditions at the bubble surface
o	minimum fluidisation conditions
r, ρ , ξ	radial component
θ , η	tangential component
x	vertical component
y	horizontal component
∞	conditions at the outer boundary

Superscripts

*	dimensionless quantity
(n), (p)	iteration number

CHAPTER I

INTRODUCTION AND LITERATURE SURVEY

1.1 Introduction

Fluidisation can be regarded as an unit operation in which a solid phase of particles is maintained in suspension by a fluid phase, i. e. in which the interaction force between the fluid and the particles counterbalances the weight of the dense phase.

The fluidising fluid can either be a gas or a liquid. The properties of gas and liquid fluidised beds are somewhat different, particularly in what concerns the formation of bubbles (or regions free of particles) within the dense phase. In this work we shall only be concerned with gas fluidised beds.

It is a common feature of gas fluidised beds that above a certain flow rate of fluid (bubbling point), bubbles of gas appear within the dense phase. Rowe and Partridge (1) and also Sutherland (2) were the first investigators to show that these bubbles were responsible for the rapid particle mixing which is observed. Furthermore bubbles of gas constitute a by-pass to the solid phase and can lead to an inefficient conversion in a fluidised bed operated as a catalytic chemical reactor.

From the two typical features of a fluidised bed which have just been mentioned, it is obvious that an understanding of the contact between the gas and the particles is essential. It is not surprising therefore that gas and solid mixing have received a considerable attention as is seen from the high number of references to be found

in the literature.

Our aim here is not to give a complete survey of all these works but to mention those which are of major importance and which directly relate to the theoretical and experimental work carried out in this thesis. A complete survey can be found for example in Fluidisation (3) edited by Davidson and Harrison or in Fluidisation Engineering (4) by Kunii and Levenspiel.

Another important feature of a fluidised system is that many of its properties are analogous to those of a viscous liquid albeit all theories of bubble motion developed so far assume that the particulate phase behaves like an inviscid fluid (Appendix 3). Many authors have suggested that this approach is too simplified and that interparticle forces should be introduced in the theory.

Furthermore in order to test directly theoretical predictions of bubble motion a certain number of experiments can be performed:

(i) measurements of the velocity of an isolated bubble.

(ii) measurements of gas penetration and its circulation within a cloud around the bubble for a fast moving bubble.

(iii) measurements of pressure variations in the vicinity of a bubble.

(iv) measurements of the voidage variations around a bubble.

(v) determination of the particle displacement caused by a bubble.

(vi) determination of the gas flow patterns and velocity in the vicinity of a bubble.

Experimental studies (i) and (ii) have received a lot of attention and many data are available in the literature (e.g. Rowe in Fluidisation

(5)). The pressure distribution (iii) and voidage variations (iv) have been studied to some extent in recent years (e.g. Littman and Homolka (6), Lockett and Harrison (7)).

Particle displacement, especially the displacement of layers of coloured particles has been measured (e.g. Potter in Fluidisation (8)) but few attempts are reported on determining the paths of individual particles as they move around the bubble.

Gas tracer injection has been used to evaluate the streamline motion of the gas phase (e.g. Rowe in Fluidisation (5)) but no experiments are reported on gas velocity measurements.

The aims of this work follow from what has been written previously:

(i) a new theory has been derived which includes inter-particle forces in form of a particulate phase viscosity μ_p

(ii) experiments to test this new theory and existing ones have been performed:

- by following the displacement of tracer particles as they move around a bubble
- by measuring the gas velocity variations in the vicinity of a bubble.

In the next section previous works to be found in the literature on these three points (interparticle forces, solid motion, gas motion) are reported. Finally in the last section a summary of the structure of this work is given.

1.2 Literature survey

1.2.1 Interparticle forces and dense phase viscosity measurements

The first coherent theory of bubble motion in a fluidised bed was introduced by Davidson in 1961 (9) and further developed by Davidson and Harrison (10). In this simple theory, particles are assumed to flow around the bubble in potential flow and the percolation of gas through the particulate phase is assumed to obey Darcy's law.

Modifications to Davidson's theory were given later by Jackson (11) and Murray (12) who used a more complete set of equations which introduced a momentum equation for the dense phase and, in the case of Jackson's theory, allowed variations of porosity in the neighbourhood of the bubble. However all these theories neglect the stress tensor for the particulate phase.

Theoretical studies have also been made with regard to the initiation and growth of small disturbances within the bed near incipient fluidisation. The first works of Jackson (13) and Pigford and Baron (14) have been criticized because they always predict an unstable behaviour of the fluidised bed. According to these authors, small disturbances like internal waves will always grow, while it has been proved experimentally that homogeneous fluidisation can exist under certain conditions (e.g. Geldart (15), de Jong et al (16), Agbim et al (17), Rowe (18)).

Murray (19), Anderson and Jackson (20) have noted the importance of the stress tensor in the analysis of stability but, although their theories predict a stable behaviour for surface waves, they still allow small disturbances to grow into instabilities.

Different approaches to this problem have therefore been made by Molerus (21), Ruckenstein and Tzeculescu (22). These authors included interparticle forces of the suspension in their analysis. Rietema (23) applied mechanical stress theory to fluidisation and also showed (24) that in order to satisfy the constancy of the pressure inside the bubble there must be a viscous dissipation at its surface due to the solid shear stress.

Evidence of interparticle forces has been shown experimentally by several sets of workers (e.g. Buysman and Peersman (25), Rietema (26), Verloop et al (27), Agbim et al (17), Rowe (18)) by studying the stability of ceilings of particles or by studying the delay in bubble appearance for fluid velocities greater than minimum of fluidisation conditions.

From the few indications given previously, the two following conclusions arise:

(i) analysis of the stability of a fluidised bed near incipient fluidisation shows the importance of the shear stress in the particulate phase.

(ii) This term is neglected in the present theories describing the motion of the particulate and fluid phases around a bubble.

As we have already noted in the previous section, a new theory is developed in this work which includes a viscosity μ_p for the dense phase. We shall therefore be concerned now with attempts to measure such a viscosity.

There is a very limited amount of data available in the literature. However, works on the viscosity of a fluidised bed can be classified in two classes: direct and indirect measurements.

(i) Direct measurements

In this case experiments were made using different types of viscometers:

Falling spheres

This method used by early workers has the great disadvantage of presenting a defluidised region on the surface of the sphere. The few data (Peters et al (28), Trawinski (29), Daniels (30)) are therefore questionable and often expressed in uncommon viscosity units.

Rotating viscometers

The most used methods are the Couette and torsional pendulum viscometers. A number of workers have been using paddle-type viscometers or rotating spheres (e.g. Stormer viscometer) and their data are expressed in units particular to the type of apparatus used. (Matheson et al (31), Furukawa et al (32), Kramers (33)). None of these values are useful quantitatively. Other workers have used a Couette viscometer but their rotating cylinder was moving too rapidly so that conditions near its surface were very different from those in the bulk of the bed (Shuster et al (34), Diekman et al (35), Fa. Key. Liu (36)).

The only reliable data seem to be those of Schügerl et al (37) and Hagyard and Sacerdote (38). The former workers used a Couette viscometer at low velocity and measured the torque exerted on the inner cylinder to maintain its rotation speed. They also noted the importance of the angular velocity of the cylinder by carrying out experiments at higher speeds. Furthermore, in order to prevent particles from slipping on the surface of the rotating cylinder,

Schügerl et al found it necessary to roughen the cylinder surface.

Hagyard and Sacerdote used a torsion pendulum viscometer to which an initial impulse was given. They, then, measured the rate of decay of the oscillations. For the same reason as Schügerl, they also roughened the cylinder surface. In addition the rotating body was only partially immersed in the bed so that no defluidisation could occur on its upper surface.

The importance of the quality of fluidisation is noted by these two sets of workers. Schügerl distinguishes between a semi-fluidised bed (a) and a fully fluidised bed (b) (ref. (39)).

(a) The transition between a packed bed and a fluidised bed is not instantaneous; there exists a region of semi-fluidisation which includes the point of minimum fluidisation as defined by a pressure drop vs. flow rate curve. In this region it is not possible to determine a viscosity which is independent of the shearing rate (Newtonian behaviour). On the contrary Schügerl found there is a limiting shear stress τ_o below which no movement of the particles can be observed (Figure 1.1). The particulate phase thus presents the properties of a Bingham-plastic fluid.

The motion of a single bubble injected into an incipiently fluidised bed has been widely studied. Schügerl (39) emphasizes that extrapolation of those results to bubbles in fully fluidised beds should be taken with care since the rheological properties are widely different. Hagyard and Sacerdote (38) also noted the importance of the fluidisation regime. In all their results there is a sharp increase in viscosity values near the inception of fluidisation. This increase can eventually appear for values of the fluidising gas velocity higher

than the minimum velocity of fluidisation. (Hagyard's Figure 3 (38)).

(b) For a fully fluidised bed both sets of workers agree on a Newtonian behaviour of the particulate phase in most cases; as can be seen on Figure 1.1, the value of τ_o sharply decreases when the fluidising gas velocity increases.

In addition Schügerl and Hagyard noted the importance of factors like the particle size, the size distribution and the nature of the particle surface (i. e. smooth or coarse). The proportion of fine particles seems to be particularly important and an increase in the viscosity is noted by Hagyard and Sacerdote for a certain percentage of fines in the mixture.

Schügerl also noted a departure from Newtonian behaviour for small particles but there is some disagreement between Schügerl and Hagyard on the influence of particle size. The former worker found that big and heavy particles have a higher viscosity than small and lighter ones, while Hagyard measured a constant kinematic viscosity of 130 centistokes for different sizes of spheres ranging from 125 μm to 305 μm. However the range of sizes measured by Schügerl was very much wider. Experiments by Furukawa and Ohmae (in Gelperin and Einstein (40)) tend to confirm Schügerl's conclusions on the influence of particle size on viscosity.

As will be seen in Chapter 4, viscosity data used in the exploitation of the experimental results (Chapters 5 and 6) are those of Schügerl (except for bigger particles for which no data are available). However one must bear in mind that many more rheological data are necessary and that the value of the bubble Reynolds number $\left(Re=\frac{2aU_b(1-\varepsilon_o)}{\nu_p}\right)$ calculated in Chapters 5 and 6 are only approximate.

(ii) Indirect measurements

Besides direct measurements of the viscosity of fluidised system, attempts have been made to deduce values from certain properties of an isolated bubble rising in the particulate phase at incipient fluidisation. We shall examine three methods.

(a) Murray (41) deduces an order of magnitude for the viscosity μ_p from the bubble motion. His analysis is for a Newtonian fluid and a value of the order of 10 poises is given, which is in fair agreement with direct measurements. However his method is subject to some criticism.

Murray calculates μ_p by equating the viscous drag coefficient calculated by Levich's dissipation method to the buoyancy force.

Thus $C_{Dv} = \frac{48}{Re}$ and $Re = \frac{2a U_b (1 - \epsilon_o)}{\nu_p}$

The buoyancy drag coefficient is given by :

$$C_D = \frac{8}{3} \frac{ag}{U_b^2}$$

Thus, at steady state

$$\frac{48}{Re} = \frac{8}{3} \frac{ag}{U_b^2}$$

whence $$\mu_p = \frac{1}{9} \frac{a^2 g \rho_p (1 - \epsilon_o)}{U_b}$$

and if we use Murray's expression for the bubble velocity:

$$U_b = \sqrt{\frac{ag}{3c}}$$

it follows:

$$\mu_p = \frac{1}{3\sqrt{3}} a^{\frac{3}{2}} g^{\frac{1}{2}} c^{\frac{1}{2}} \rho_p (1 - \varepsilon_o) \qquad (1.1)$$

a and c are measured experimentally and thus μ_p is known.

The ambiguity and limitation of this treatment appear immediately:

- strictly speaking, this analysis is only valid for a small bubble (say $a < 2cm$) which can be considered as spherical.
- Levich's method applies when $Re \gg 1$ which, if one assumes Schügerl's data on viscosity as valid, is true for a large gas bubble and therefore in contradiction with the previous statement.
- Furthermore equation (1.1) shows that the viscosity will depend on the bubble radius a, and a Newtonian behaviour of the fluidised bed no longer holds.

(b) Stewart (42) uses Reuter's experiments (43) on pressure variations along the center line of the bubble to deduce viscosity values. One of Reuter's conclusions is that the pressure difference between the top and the bottom stagnation points is equal to the pressure drop over the bubble height. Following Stewart, if h_b is the bubble height, the pressure change from the point of zero pressure difference to the front stagnation point is:

$$\frac{\rho_p h_b g}{2}$$

Furthermore Jackson's analysis gives the pressure rise to the bubble nose inside the particulate phase as $\frac{\rho_p U_b^2}{2}$

If one introduces a viscosity μ_p, an additional pressure term arises from:

$$\tau_{rr} = -2 \mu_p \frac{\partial v_r}{\partial r} \qquad \text{(Appendix 1)}$$

For a three-dimensional bed this can be written as:

$$\tau_{rr} = \frac{6 \mu_p U_b}{a}$$

A pressure balance at the front stagnation point gives:

$$\frac{6 \mu_p U_b}{a} + \frac{\rho_p U_b^2}{2} = \frac{\rho_p g h_b}{2}$$

The value of μ_p is therefore:

$$\mu_p = \frac{\rho_p a}{12} (U_b^2 - g h_b)$$

The value of the viscosity is therefore known when h_b and U_b have been measured experimentally. Values calculated by Stewart using the above method agree fairly well with Schügerl's experimental values for medium-sized particles ($100 \mu m < d_p < 300 \mu m$). The disagreement is important for small particles whilst for bigger particles ($d_p > 500 \mu m$) there are no experimental data to compare with, but the values calculated seem quite high.

(c) The most satisfactory method with regard to experimental data is that developed by Grace (44) by analogy with spherical-cap bubbles rising in viscous liquids. It must be noted that Grace's

calculations are limitedto three-dimensional bubbles since too few data on two-dimensional bubbles in liquid are available.

A certain number of workers (references given by Grace) have measured the included angle Θ_i of the spherical-cap bubble as a function of its Reynolds number. A general correlation is thus given by Grace as:

$$Re = 23e^{-0.004\Theta_i} \quad \text{with} \quad 200^\circ < \Theta_i < 260^\circ \qquad (1.2)$$

The included angle Θ_i has also been measured for bubbles rising in a three dimensional fluidised bed (Rowe and Partridge (45)). By analogy with a bubble in a liquid, it is therefore possible to deduce a Reynolds number (and hence a viscosity) for a bubble in a fluidised bed using equation (1.2).

The values given by Grace agree quite well for all sizes of particles with experimental data although there is no clear tendency on the effect of particle size on viscosity values.

As will be seen in Chapter 4 (Table 4.1), the viscosity value for Ballotini grade 7 has been taken from Grace's article. This value of 9.5 poises seems in better agreement with experimental evidence ($\sim$10 poises) than the one calculated by Stewart (26 poises).

(d) Besides the three methods quoted previously, some attempts are reported which use the analogy between a fluidised bed and a liquid flowing in an open channel.

Neuzil and Turcajova (46) note the same dependence of superficial velocity on fluidised bed viscosity than of temperature on the viscosity of a flowing liquid. From the known dependence of the latter

it is possible to calculate the dependence of the former. However this method does not give absolute values of the viscosity but only the ratio $\frac{\mu_p}{\mu_{po}}$ where μ_{po} has to be known from direct experimentation. Furthermore these authors neglect the presence of bubbles in the particulate phase which may affect the assumed analogy.

Siemes and Heller (47) used the same kind of analogy, but their fluidised bed was constituted of an open inclined channel, the bottom of which was made of a porous material through which air was flowing. Their viscosity values are in fair agreement with other published data.

Finally we shall mention the work of Rice et al (48) who measured the damping of oscillations artificially produced at the surface of a fluidised bed. Unfortunately their theoretical model does not give any clear conclusion on viscosity values and their comparison with data obtained using a Brookfield viscometer seems doubtful since they obtain values ranging from 300 poises to about 10 poises for a same flow rate depending on the viscometer rotation speed and on the type of spindle used.

From the works on rheological properties of the dense phase quoted in this section it is possible to mention the following general conclusions:

(i) Distinction must be made between a fluidised bed near incipient fluidisation and a fully fluidised bed. In the latter case a Newtonian behaviour can describe the rheological properties of the dense phase.

(ii) Direct and indirect methods confirm a value of the order of 10 poises for medium-sized particles. ($200\,\mu m < d_p < 500\,\mu m$).

(iii) Indirect measurements based on properties of bubbles should be preferred since no foreign body is introduced in the bed which modifies the properties of the dense phase at the body surface (e.g. regions of defluidisation).

(iv) Many more data are necessary to conclude on the influence of factors such as the particle size, the particle size distribution.

1.2.2 Particle motion

The mixing of two differently coloured solids was among the first observations made on fluidised beds (Brötz (49)). The rapid mixing of particles has led early workers to assume it is analogous to a diffusional process. Coefficients analogous to eddy or molecular diffusion coefficients have been measured (e.g. May (50), Leva and Grummer (51), van Deemter (52)). May and van Deemter also derived a theoretical model based on a two-phase representation of a fluidised bed. In the dense phase they assume random motion of the fluid and particles, the other phase being constituted by gas bubbles.

However experimental evidence (e.g. the early work of Gilliland and Mason (53)) tends to show that particles are carried up with bubbles and therefore that there is a downflow of particles in bubble-free regions. On this basis a countercurrent flow model has been developed (e.g. van Deemter (54), Bailie (55), Kunii and Levenspiel (4)).

The two models cited previously attempt to describe the mixing process in a vigorously fluidised bed but no description of the motion of individual particles is predicted. In order to have a clearer picture of the movement of individual particles in the mixing process, experiments of high-speed cinematography of tracer particles have been carried out.

Such experiments were first done by Toomey and Johnstone (56) and by Massimilla and Westwater (57). The aim of the former workers was to predict the heat transfer coefficient at the fluidised bed wall and they did not attempt to record the particle movement past a rising bubble. Massimilla and Westwater only studied the velocity of particles at the wall of a three-dimensional bed. They showed a predominance of vertical motion.

The direct influence of particle movement caused by a rising bubble was studied by Sutherland (2). He was the first worker to show that particle movement is a consequence of bubble formation. When bubbles are suppressed (e. g. near the inception of fluidisation) there is no movement and therefore no mixing.

It is possible to distinguish between two sorts of experiments (Figure 1.2)

(a) The displacement of a layer (or of an interface) of coloured particles caused by a rising bubble. The final profile of the layer is referred to as the drift profile.

(b) The displacement of individual tracer particles. Some experimental results and theoretical curves obtained from potential flow theory are shown on Figure 1.2.

(a) Rowe and Partridge (1) photographed the displacement of an interface of coloured particles. The bottom of their two-dimensional fluidised bed was filled with black particles, the top part with white ones. An injected bubble caused the displacement of black particles.

Numerous studies have been made in two and three dimensions by Rowe and co-authors (58,59). Experiments carried out in a two dimensional apparatus are easy to perform since the drift is directly visible. In a three-dimensional fluidised bed, X-ray photography or sectioning of the bed at different heights were performed.

Similar experiments were also made by Raso et al (60), Woollard and Potter (61), Singh et al (62) and Toei et al (63). Singh et al interpreted their results in terms of the bubble wake which was not considered by former workers. They showed that measuring the drift of a layer of coloured particles leads to a precise estimation of the wake fraction (i.e. the amount of particles carried upwards with the bubble).

From the experiments quoted previously, various authors suggested that the movement of a particle past a bubble is similar to that of an element of ideal fluid displaced by a sphere (or cylinder) in an infinite medium. This was pointed out by Rowe (58), Reuter (64) and Davidson (65). The theoretical drift has been first calculated by Darwin (66) and is represented on Figure 1.2.

However the experimentally measured drift was found to be much smaller in many cases (e.g. Toei et al (63)). In addition the

theory only predicts an upwards movement of the particles while it has been shown experimentally (e.g. Rowe and co-authors (58, 59)) that there is an upwards movement for the particles situated near the bubble axis and a downwards movement for particles situated on the sides of the bubble (Figure 1.2).

Toei et al (63), in addition to the perfect fluid assumption, assume that there is an imaginary wall moving upwards with the bubble, at the same velocity, and situated two radii below the bubble center. The final particle drift they obtain theoretically is similar (although not coincident) to the experimental profile, i.e. it shows a downwards displacement of some particles.

(b) Besides investigations of the final drift caused by the passage of a bubble, movement of individual particles flowing around a single bubble has been studied.

Theoretically, equations describing the motion of particles were first established by Maxwell (68) for two-dimensional flow. In his article Maxwell obtains a graphical solution which is remarkable. These equations were solved analytically by Darwin (66) and Lighthill (67) and extended to a three-dimensional flow. Some of the curves obtained are shown on Figure 1.2 and equations are given in Appendix 3.

The first experimental work on movement of individual particles is due to Gabor (69) who investigated the effect of finite boundaries in a two-dimensional bed. His experimental results are compared with the drift calculated from an extension of Davidson's theory by Collins (70) to account for wall effects. There is some disagreement between theory and experiments particularly for

particles situated near the axis of the bubble. Gabor attributed this discrepancy to the fact that particles near the axis of the bubble tend to fall through the bubble roof rather than to loop around it as predicted.

Subsequently Gabor (71) derived a theory which took account of wall effects and the height of the bed. The overall resulting movement is analogous to a countercurrent model with particles moving upwards in the centre and downwards near the wall. However "looping" of particles near the axis of rise of the bubble is still predicted. Gabor concludes that disagreement is not due primarily to boundaries effect but rather to the omission of interparticle forces.

Therefore in a third article (72), Gabor examined the influence of viscosity of the particulate phase in a large two-dimensional bed. Three models were tested: Newtonian fluid, power-law fluid, Bingham plastic fluid. His conclusion is that the latter model is the most appropriate. Schügerl's data (39) confirm this analysis, but only for a fluidised bed operated near the minimum of fluidisation, where it is possible to define a limiting shear stress τ_o. However in his model of Newtonian fluid, Gabor only considers the creeping flow limit where it is a well-known result that the theoretical drift is infinite. Furthermore, although not many details are given with regard to his experimental results, they seem to have concerned only relatively small bubbles.

Studies in three-dimensions are much more difficult. Movements of particles at the wall of a three-dimensional column have been investigated by Donsi et al (73). In their experimental method the initial and final positions of the bubble are well determined but its behaviour within the bed is unknown (e.g. splitting and recoalescing

as in Rowe's Figure 4.21(a) (5)). The drift profile obtained for bubbles rising in the centre of the column is in good qualitative agreement with those obtained by Rowe et al (59) and Woollard and Potter (61). However Donsi et al note the importance of wall effects which reduce the final drift.

Various attempts have also been made to measure particle velocities. In addition to the works of Toomey and Johnstone (56) and of Massimilla and Westwater (57), we may mention the study by Meissner (74) who derived a kinetic theory analogous to the kinetic theory of gases and by measuring the pressure exerted by the impact of the particles, he deduced a value for the average particle velocity.

Baeyens and Geldart (75) also measured the average particle velocity in a series of two-dimensional tests. Their theoretical model accounts for the bubble wake and drift. They found that particles in the bubble wake rise at the same velocity as the bubble itself.

Patureaux et al (76) measured the impact on a piezoelectric probe of particles displaced by single bubbles. Their results show particle velocities much lower than the results predicted from Davidson's theory. They attribute this discrepancy to high viscous forces on the surface of their probe. In addition, we suggest that the presence of a probe of appreciable dimension disturbs the flow of particles by inducing, for example, small gas bubbles on its surface.

From what has been said the following conclusions can be drawn:

(i) Darwin's theory for potential flow does not describe the actual displacement of particles induced by a rising bubble.

However there is still some incomplete evidence on the effect of a particulate phase viscosity.

(ii) Experiments show the importance of finite boundaries if the ratio $\frac{\text{bubble diameter}}{\text{characteristic dimension of apparatus}}$ is not small.

(iii) Experiments also show the importance of the particles falling from the bubble roof on the observed patterns of particle motion.

1.2.3 Gas motion

Numerous studies are reported in the literature in the field of gas mixing in a fluidised bed. An extensive survey has recently been made by Potter (8). The models quoted previously (countercurrent and diffusion) apply in the case of gas motion since they have been derived for both solid and gas phases (i. e. equations can be interchanged). However they assume that the bed is fluidised vigorously. Most of the experiments reported by Potter concern gas tracer studies made to test the above models and gas motion around a single bubble is not predicted.

Theoretical patterns of gas motion around a single bubble were first derived by Davidson (9) and by Davidson and Harrison (10) who predicted the existence of a gas cloud, i. e. a closed region around the bubble where the gas circulates, when the ratio $\frac{U_b}{u_o}$ is greater than 1. The existence of a gas cloud has been shown experimentally by Rowe et al (77) using injection of NO_2 bubbles and in the past ten years gas cloud measurements have been widely studied.

On the contrary there are very few studies reported on measurement of local properties of the gas flow. By injection of a continuous stream of NO_2 tracer gas injected from the bottom of a fluidised bed, Wace and Burnett (78) made conspicuous the stream line nature of the gas flow. However the trace given by an injection of NO_2 at a fixed point is not a stream line with respect to the moving bubble. It has been referred to by Rowe as a streak line. In order to compare with Davidson's predictions for the flow with respect to axis moving with the bubble, Rowe and Partridge (79) have calculated path lines and streak lines from Davidson's equations.

If χ is the gas stream-function with respect to the bubble moving steadily at U_b (axis O x y), then the velocity components are given by:

$$u_x = -\frac{\partial \chi}{\partial y}$$

$$u_y = \frac{\partial \chi}{\partial x}$$

and with respect to stationary axis (O' X Y):

$$u_X = u_x + U_b$$

$$u_Y = u_y$$

Now $\chi = F(x, y, \alpha_b, u_o)$ (Appendix 3)

Therefore at a given point (x, y) u_x, u_y and u_X can be calculated. After a time Δt, the bubble has moved by a distance $U_b \Delta t$. The new position (x, y) of an element of fluid after Δt is therefore determined by $u_X \Delta t$ and $u_Y \Delta t$. A new resultant velocity can, then,

be calculated and the second point on the line is obtained by averaging between the two last values of velocity. By this method Rowe and Partridge (79) constructed path lines of gas for different starting points.

It is important to note that a path line refers to the same element of fluid while a streak line is a continuous stream, i.e. a succession of different elements of fluid. Streak lines can be drawn by joining points of equal dimensionless time on different path lines issued from the same point.

If one suddenly stops the supply of NO_2, the end of the trace (i.e. an element of fluid) follows a path line. By measuring its displacement with time, Rowe and Partridge could determine the instantaneous velocity of interstitial gas. However they note that this method is very imprecise since the trace is usually thick and the end is not sharp.

Displacement of NO_2 tracer was also followed by Anwer and Pyle (80). They injected air bubbles into a layer of NO_2 tracer gas introduced by the bed distributor. The rising bubble caused the drift of the upper part of the NO_2 tracer, exactly as it does for a layer of coloured particles.

The velocity of the NO_2 - air interface on the axis of rise of the bubble is the velocity of interstitial gas. However this method is only applicable on the bubble axis which is known to be a gas flow stream line and therefore refers to the same element of fluid. Furthermore the above remark still applies since the interface is not sharp.

Rowe and Partridge find a good agreement between experimental

streak lines and those determined from Davidson's theory (the only theory available at that time) while Anwer and Pyle find better agreement with Murray's theory.

As far as we are aware, no other works report measurements of the variations in interstitial gas velocity around a rising bubble. From what has been written previously, two conclusions arise:

(i) gas tracer methods are not appropriate for velocity measurements since results are very inaccurate, due to the diffusion of the gas.

(ii) many more data are required using different methods. A part of this work deals with this problem.

1.3 Summary

The aims of this work have already been emphasized in the introduction to this chapter. However in view of the literature survey presented in the preceding section we can define more precisely the work which has been undertaken.

(i) A viscosity term μ_p has been introduced in the equations of motion for an isolated bubble rising in a large two-dimensional fluidised bed. Particles were supposed to be fully fluidised and only a Newtonian behaviour of the particulate phase was considered. Formulation of the theory and its numerical solution are given in Chapters 2 and 3.

(ii) Experiments were performed in a two-dimensional fluidised bed where the ratio $\frac{\text{bubble diameter}}{\text{dimension of apparatus}}$ was sufficiently large (i.e. $\geqslant 5$) so that wall effects could be neglected. Description of the experimental set-up is given in Chapter 4.

The following experiments were carried out:

1. Motion of tracer particles was photographed. Experimental results and their comparison with theories are given in Chapter 5.

2. Measurements of the gas interstitial velocity have been carried out using a new technique based on hot-wire anemometry (described in Chapter 4). Results and discussion are presented in Chapter 6.

3. The motion of individual particles falling inside a bubble from its roof has enabled us to estimate a value for the throughflow velocity. This is done in Chapter 7.

(iii) Finally, in Chapter 8, general conclusions are drawn from the work presented in this thesis.

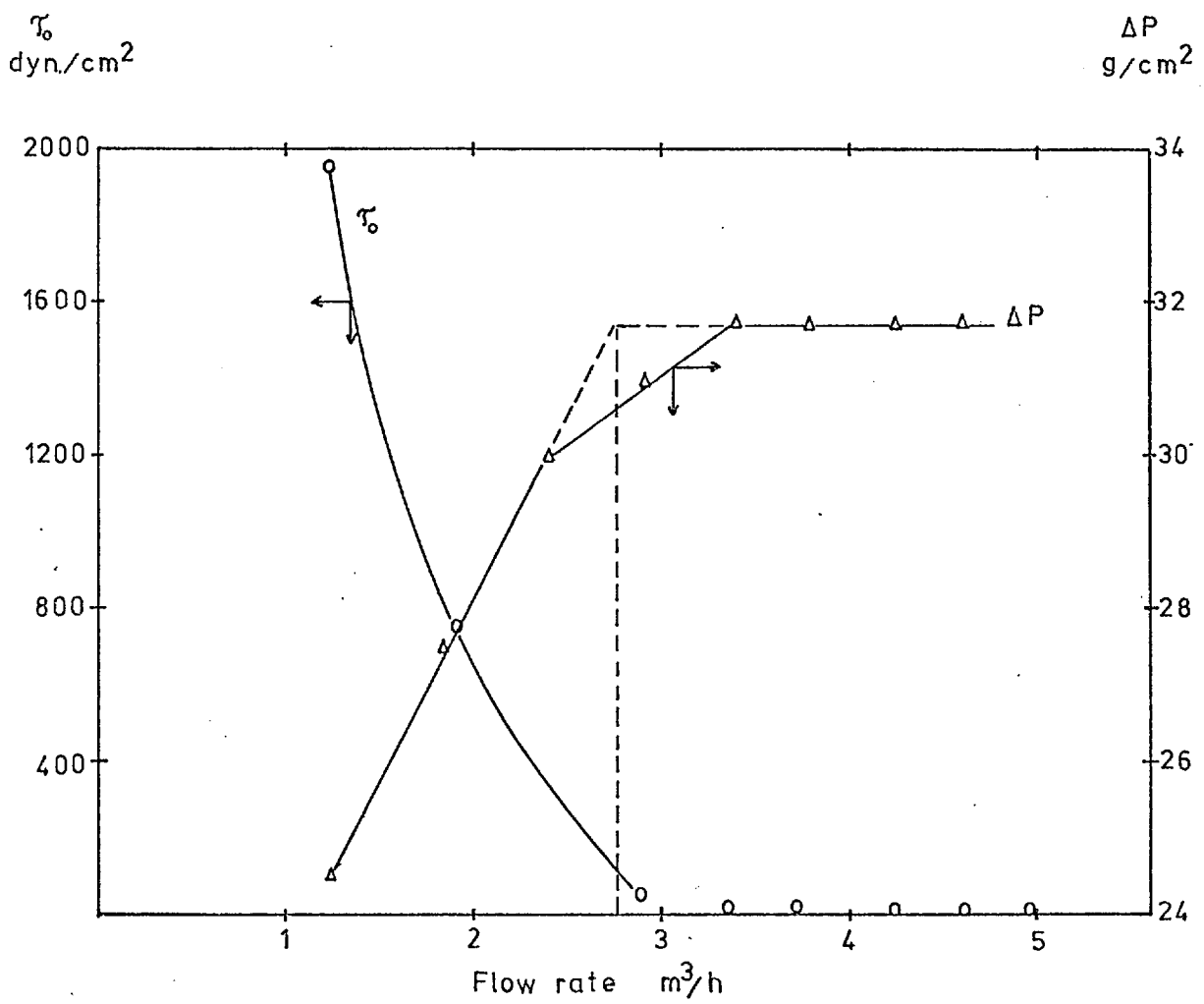


Figure 1.1

Limiting shear stress τ_0 and pressure drop as function of the gas flow rate.

Silicon-carbide particles $d_p = 190\,\mu m$.

(from Schügerl (39).)

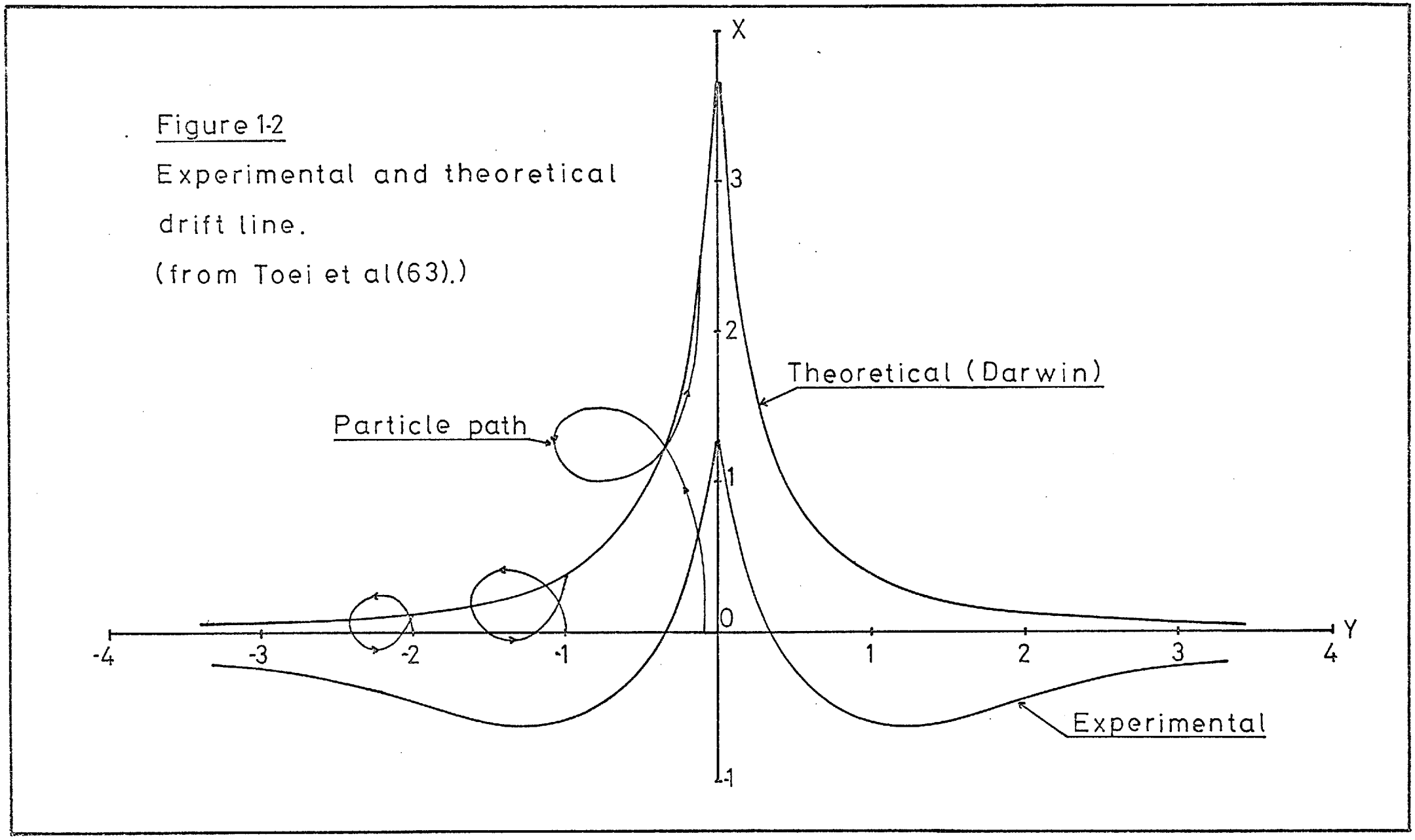


Figure 1-2

Experimental and theoretical drift line.

(from Toei et al(63).)

CHAPTER 2

EQUATIONS OF MOTION

In this chapter the equations of motion for the particles and for the gas phase are derived. Some assumptions are discussed which allow for the simplification of these equations so that they can be solved numerically.

2.1. General form of the equations.

The general form of the equations of continuity and motion can be written as:

continuity:

$$\frac{\partial \varepsilon}{\partial t} + \underline{\nabla} \cdot \varepsilon \underline{u} = 0 \qquad (2.1) \text{ fluid phase}$$

$$\frac{\partial (1-\varepsilon)}{\partial t} + \underline{\nabla} \cdot (1-\varepsilon)\underline{v} = 0 \qquad (2.2) \text{ particulate phase}$$

momentum:

$$\rho_f \varepsilon [\frac{\partial \underline{u}}{\partial t} + (\underline{u}.\underline{\nabla})\underline{u}] = -\underline{\nabla} P_f - \underline{\nabla}.\underline{\tau}_f + \varepsilon \rho_f \underline{g} - n\underline{f} \qquad (2.3) \text{ fluid phase}$$

$$\rho_p (1-\varepsilon)[\frac{\partial \underline{v}}{\partial t} + (\underline{v}.\underline{\nabla})\underline{v}] = -\underline{\nabla} P_p - \underline{\nabla}.\underline{\tau}_p + (1-\varepsilon)\rho_p \underline{g} + n\underline{f} \qquad (2.4)$$

particulate phase

The treatment which leads to these equations is discussed in detail by Anderson and Jackson (82) and also summarized by Jackson (81). The physical idea is to assume that the gas phase and the particulate phase may be treated as two interpenetrating continua by "averaging point variables over regions large enough to contain many particles, but small compared with the whole system" (Jackson (81)).

It is beyond the scope of this work to discuss the validity of such an assumption and for the moment we shall admit equations (2.1) to (2.4) as a good interpretation of the behaviour of the solid and fluid phases.

In a later section, when the experimental results are presented, the validity and form of these equations will be discussed in more detail.

In equations (2.3) and (2.4) $n\underline{f}$ is the force per unit volume of bed due to the fluid particle interaction, i.e. the interpenetration of the two continua. The other terms are identical to those of the Navier-Stokes equations for a single phase.

In the preceding set, the four equations (2.1) to (2.4) are independent and therefore we need four state variables which can be taken as:

$$\underline{u},\ \underline{v},\ P_f \text{ and } \varepsilon$$

The choice of $\underline{u}$ and $\underline{v}$ as variables in equations (2.3) and (2.4) is obvious and we shall discuss that of P_f and ε in section 2.4.2. All the other terms are dependent and related to one or several of the above variables.

2.2. Assumptions

Equations (2.1) to (2.4) enable one to find the general solution for any perturbation occuring in the fluidised bed. As stated in the introduction the object of this work is to study the flow of both phases around a single two dimensional gas bubble rising in the fluidised bed.

The main assumption is to suppose that the problem may be treated as one of steady flow with respect to axes moving with the bubble. This can be done if one assumes the velocity of rise of the bubble is nearly constant. Experiments show that it is reasonable to make such an assumption after the bubble has been travelling some distance in the fluidised bed. There is a fair amount of evidence to suggest that one can use the analogy between a bubble in a fluidised bed and a large gas bubble rising in a liquid of low viscosity, where it has been shown by Davies and Taylor (83) that:

$$U_b = k(ga)^{\frac{1}{2}}$$

Furthermore, although experiments show it is not strictly true, we shall assume that the bubble remains circular in shape. This simplifies greatly the treatment of the equations. Collins (70) has proposed, for the two dimensional case, a transformation from a circular shape to a kidney-shaped bubble. Nevertheless it seems, at this stage, unrealistic to complicate the solution. The thing one has to bear in mind is that the numerical solution we shall obtain for the rear of the bubble will be somewhat doubtful because of the assumed shape. We shall discuss this assumption in more detail when obtaining the solution for the pressure variations around the

bubble (see section 2.4.3).

In what follows we assume that the significant viscous contributions arise from the particulate phase; the form of these viscous terms is discussed in the next section.

We also neglect:

(i) - the rate of change of the fluid momentum : $\rho_f \varepsilon (\underline{u}.\underline{\nabla})\underline{u}$

(ii) - the viscous effect for the fluid : $\underline{\nabla}.\underline{\tau}_f$

(iii) - the gravity force for the fluid : $\rho_f \varepsilon \underline{g}$

In a gas-fluidised bed assumptions (i) and (iii) are justified since the density ratio $\frac{\rho_p}{\rho_f}$ is large and of $0(10^3)$ in most situations. As mentioned in a later section (section 2.3.4) the viscosity ratio $\frac{\mu_p}{\mu_f}$ is $0(10^5)$ and therefore $\frac{\nu_p}{\nu_f}$ is $0(10^2)$, which justifies assumption (ii). With the preceding remarks the set of equations therefore becomes:

$$\underline{\nabla}.\ \varepsilon\ \underline{u} = 0 \qquad (2.5)$$

$$\underline{\nabla}.\ (1-\varepsilon)\underline{v} = 0 \qquad (2.6)$$

$$\underline{\nabla} P_f + n\underline{f} = 0 \qquad (2.7)$$

$$\rho_p(1-\varepsilon)(\underline{v}.\underline{\nabla})\underline{v} = -\underline{\nabla}P_p - \underline{\nabla}.\underline{\tau}_p + \rho_p(1-\varepsilon)\underline{g} + n\underline{f} \qquad (2.8)$$

The difference between this set and Jackson's equations as applied to the motion of a bubble in a fluidised bed (81) lies in the two first

terms on the right hand side of (2.8) i.e. : $-\underline{\nabla} P_p - \underline{\nabla}.\ \underline{\underline{\tau}}_p$,

which take into account the particulate pressure and the viscous stress tensor.

2.3. Equation of motion for the particulate phase.

2.3.1. Simplification of the stress tensor

As indicated in the introduction, experiments made on the viscosity of a fluidised bed show a strong dependence upon the state of fluidisation. For a fully fluidised bed the viscosity is almost independent of the shearing rate and Newtonian behaviour is not an unrealistic description of the system's rheology (Schügerl (39)).

Thus, we shall assume that the stress tensor is given by:

$$\tau_{pij} = \mu_p(\epsilon)\left[\frac{\partial v_i}{\partial x_j} + \frac{\partial v_j}{\partial x_i}\right] + \left[\lambda_p(\epsilon) - \frac{2}{3}\mu_p(\epsilon)\right]\delta_{ij}\frac{\partial v_k}{\partial x_k}$$

This is given in tensor notation where the summation convention is implied and δ_{ij} is the Kronecker's symbol.

(i) The probable form of the shear and bulk viscosities is discussed in detail by Murray (19) where he gives the following expressions:

$$\mu_p = c_1\ \mu_f\ \frac{1-\epsilon}{\epsilon-\epsilon_s} \quad \text{and} \quad \lambda_p = c_2\ \mu_f\ \left(\frac{1-\epsilon}{\epsilon-\epsilon_s}\right)^3$$

where c_1 and c_2 are two constants and ϵ_s is the voidage for the corresponding packed bed at saturation.

At minimum fluidisation conditions ε is close to ε_s and therefore $\frac{1-\varepsilon}{\varepsilon-\varepsilon_s} > 1$, which suggests that in most cases (depending upon the values of c_1 and c_2) we have $\lambda_p > \mu_p$

At the present time nothing is known about the value of the bulk viscosity and therefore despite Murray's suggestion, we shall neglect λ_p even if we consider the particulate phase as a "dense liquid".

(ii) According to Murray's theory μ_p is going to depend on the local voidage. Experiments show that, except in the vicinity of a bubble, the voidage is nearly constant throughout the bed. However measurements of the voidage variations around a bubble are not very precise and therefore we shall assume that μ_p is constant everywhere.

(iii) As stated previously ε is one of the independent variables and cannot be taken as constant as in Davidson's (10) or Murray's (19) treatment. If one does so the set of equations (2.5) to (2.8) becomes overconstrained and one of the equations cannot be satisfied.

However, as will be shown later (see section 2.4.2), the set of equations is difficult to solve. We shall therefore use the iterative procedure proposed by Jackson (11).

As a first guess, we take $\varepsilon = \varepsilon_o$ except where it enters the drag coefficient β . The independent variable then becomes β . A solution is found for β which determines the new values of ε . Taking these values as starting point the procedure can be continued until convergence is satisfied for the values of ε .

In this work we shall limit ourselves to the first iteration, and with the above assumptions:

(2.6) reduces to $\nabla . \underline{v} = 0$

and (2.9) to $\tau_{pij} = \mu_p \left[\frac{\partial v_i}{\partial x_j} + \frac{\partial v_j}{\partial x_i} \right]$ (2.10)

or $-\underline{\nabla}.\ \underline{\tau}_p$ reduces to $\mu_p \nabla^2 \underline{v}$

Eliminating $\underline{nf}$ between (2.7) and (2.8) it follows that:

$$\rho_p(1-\varepsilon_o)(\underline{v}.\underline{\nabla})\underline{v} = -\underline{\nabla} P_p - \underline{\nabla} P_f + \rho_p(1-\varepsilon_o)\underline{g} + \mu_p \nabla^2 \underline{v}$$

as $\underline{g} = -\underline{\nabla}\,\Phi$ let us put $-\underline{\nabla} P = -\underline{\nabla} P_p - \underline{\nabla} P_f + \rho_p(1-\varepsilon_o)\underline{g}$ (2.11)

Then P will measure the difference in pressure between two points on the same horizontal line.

Thus the simplified equation to be solved:

$$\rho_p(1-\varepsilon_o)(\underline{v}.\underline{\nabla})\underline{v} = -\underline{\nabla} P + \mu_p \nabla^2 \underline{v} \qquad (2.12)$$

2.3.2. Partial differential equation in terms of the stream function

It is easy to show the following vector identity:

$$(\underline{v}.\underline{\nabla})\underline{v} = \frac{1}{2}\underline{\nabla} v^2 - \underline{v} \times (\underline{\nabla} \times \underline{v})$$

We also have: $\underline{\nabla} \times \underline{v} = \underline{\omega}$ where $\underline{\omega}$ is the vorticity vector.

Using the vector identity above and the continuity equation $\underline{\nabla}.\ \underline{v} = 0$, equation (2.12) becomes:

$$\rho_p(1-\varepsilon_o)\left[\frac{1}{2}\underline{\nabla}v^2 - \underline{v}\times\underline{\omega}\right] = -\underline{\nabla}P - \mu_p\underline{\nabla}\times\underline{\omega} \qquad (2.13)$$

rearranging (2.13) and taking the curl leads to:

$$\underline{\nabla}\times(\underline{v}\times\underline{\omega}) = \frac{\mu_p}{\rho_p(1-\varepsilon_o)}\underline{\nabla}\times(\underline{\nabla}\times\underline{\omega}) \qquad (2.14)$$

for $\underline{\nabla}\times(\underline{\nabla}P) = 0$ and $\underline{\nabla}\times(\underline{\nabla}v^2) = 0$

Equation (2.14) will be referred to as the vorticity equation.

Now let us consider a stream function Ψ which is defined (in cylindrical coordinates) by:

$$v_r = -\frac{1}{r}\frac{\partial\Psi}{\partial\theta}$$

$$v_\theta = \frac{\partial\Psi}{\partial r}$$

The components of the vorticity are: (see Appendix 1)

$$\sigma = 0$$

$$\varphi = 0$$

$$\zeta = \frac{1}{r}\frac{\partial}{\partial r}(rv_\theta) - \frac{1}{r}\frac{\partial v_r}{\partial\theta}$$

Using the expressions for v_r and v_θ in terms of the stream function, the last component of the vorticity becomes:

$$\zeta = \frac{1}{r}\frac{\partial \Psi}{\partial r} + \frac{\partial^2 \Psi}{\partial r^2} + \frac{1}{r^2}\frac{\partial^2 \Psi}{\partial \theta^2}$$

which may be written as:

$$\zeta = \nabla^2 \Psi \quad (2.15) \qquad \text{with } \nabla^2 = \frac{1}{r}\frac{\partial}{\partial r} + \frac{\partial^2}{\partial r^2} + \frac{1}{r^2}\frac{\partial^2}{\partial \theta^2}$$

The vorticity equation (2.14) then becomes:

$$\frac{\partial}{\partial r}(\zeta r v_r) + \frac{1}{r}\frac{\partial}{\partial \theta}(\zeta v_\theta) = \frac{\mu_p}{\rho_p(1-\varepsilon_o)} \nabla^2 \zeta$$

or

$$\frac{1}{r}\left[\frac{\partial \Psi}{\partial r}\frac{\partial \zeta}{\partial \theta} - \frac{\partial \Psi}{\partial \theta}\frac{\partial \zeta}{\partial r}\right] = \frac{\mu_p}{\rho_p(1-\varepsilon_o)} \nabla^2 \zeta \qquad (2.16)$$

Equations (2.15) and (2.16) are two partial differential equations describing the motion of the particulate phase around the bubble. They have to be solved simultaneously with the proper boundary conditions.

2.3.3. Dimensionless form of the equations

Let us put $\rho = \frac{r}{a}$, $\zeta^* = \frac{\zeta}{\zeta_o}$, $\Psi^* = \frac{\Psi}{\Psi_o}$, $\underline{\nabla}^* = a\underline{\nabla}$

where a, ζ_o, Ψ_o are reference quantities which will be specified later.

Equations (2.15) and (2.16) can be written as:

$$\zeta^* = \frac{\Psi_o}{\zeta_o a^2} \nabla^{*2} \Psi^* \qquad (2.17)$$

$$\frac{\Psi_o}{a^2} \frac{1}{\rho} \left[\frac{\partial \Psi^*}{\partial \rho} \frac{\partial \zeta^*}{\partial \theta} - \frac{\partial \Psi^*}{\partial \theta} \frac{\partial \zeta^*}{\partial \rho} \right] = \frac{\mu_p}{\rho_p (1-\varepsilon_o) a^2} \nabla^{*2} \zeta^* \qquad (2.18)$$

We have the two dimensionless groups: $\frac{\Psi_o}{\zeta_o a^2}$ and $\frac{\mu_p}{\Psi_o \rho_p (1-\varepsilon_o)}$

We can equate the first group to 1 which specifies $\Psi_o = aU_b$ where U_b is the velocity of rise of the bubble and a its radius.

whence: $\Psi_o = aU_b$

$$\zeta_o = \frac{U_b}{a}$$

and $$\frac{\mu_p}{\Psi_o \rho_p (1-\varepsilon_o)} = \frac{\mu_p}{aU_b \rho_p (1-\varepsilon_o)}$$

Far from the bubble the particulate phase has a downwards velocity U_b with respect to axes moving with the bubble.

We shall therefore define a Reynolds number for the bubble rising in the particulate phase as:

$$Re = \frac{2a U_b \rho_p (1-\varepsilon_o)}{\mu_p}$$

whence the last dimensionless group becomes:

$$\frac{\mu_p}{\Psi_o \rho_p (1-\varepsilon_o)} = \frac{2}{Re}$$

The final set of equations is:

$$\zeta^* = \nabla^{*2} \Psi^* \tag{2.19}$$

$$\frac{1}{\rho}\left[\frac{\partial \Psi^*}{\partial \rho}\frac{\partial \zeta^*}{\partial \theta} - \frac{\partial \Psi^*}{\partial \theta}\frac{\partial \zeta^*}{\partial \rho}\right] = \frac{2}{Re}\nabla^{*2}\zeta^* \tag{2.20}$$

We shall now specify the boundary conditions for the above equations.

2.3.4. Boundary Conditions

Equations (2.19) and (2.20) have to be solved by numerical integration. The domain of integration is taken as an area (S) limited by a curve (C). The boundary conditions for the complete determination of Ψ must specify the value of the function or the value of its normal derivative along the curve (C). This condition is sufficient (see for example Smith (84)).

In the present problem it is convenient to choose the following domain shown in Figure 2.1.

The curve (C) is divided into four parts.

(i) On the axis of the bubble (i.e. $\theta = o$ and $\theta = \pi$), due to the symmetry of the problem, $\Psi = o$ and $\zeta = o$ are obvious boundary conditions.

(ii) On the outer boundary we shall assume the flow is ideal (i.e. is a potential flow) and uniform.

Therefore Davidson's results (10) apply and:

$$\Psi = U_b r_\infty \sin\theta$$

$$\zeta = o$$

r_∞ will have to be determined in order to satisfy the above value of Ψ .

(iii) The surface of the bubble is a streamline for the particulate flow. Therefore $\Psi = 0$ for $r = a$.

No simple boundary condition can be written for the vorticity at the surface of the bubble, but it is possible to find an expression for the tangential velocity of the particles.

Clearly a non-slip condition cannot apply here and the most plausible hypothesis is that the tangential velocity is proportional to the tangential stress. The constant of proportionality is referred to by Happel and Brenner (85) as a coefficient of sliding friction which depends only on the nature of the particulate phase and of the gas inside the bubble.

Let us consider for example the typical values of the viscosities:

air bubble : $\mu_f \sim 0.02$cp

Ballotini 300 μ m : $\mu_p \sim 10$p (measured by Schügerl (37))

therefore $\frac{\mu_p}{\mu_f} \sim 50,000$

In this condition it seems reasonable to assume that the viscous stress at the bubble surface is very small and $\tau_{r\theta} = 0$ provides the last boundary condition.

$$\tau_{r\theta} = 0 \Longrightarrow r \frac{\partial}{\partial r}\left(\frac{v_\theta}{r}\right) + \frac{1}{r}\frac{\partial v_r}{\partial \theta} = 0 \qquad \text{(see Appendix 1)}$$

or in dimensionless form:

$$\rho \frac{\partial}{\partial \rho}\left(\frac{v^*_\theta}{\rho}\right) + \frac{1}{\rho}\frac{\partial v^*_\rho}{\partial \theta} = 0$$

at $\rho = 1$ $\dfrac{\partial^2 \Psi^*}{\partial \theta^2} = 0$ whence the above equation reduces to:

$$\frac{\partial^2 \Psi^*}{\partial \rho^2} = \frac{\partial \Psi^*}{\partial \rho} \quad \text{at} \quad \rho = 1 \qquad (2.21)$$

The above conditions are summarised in Table 2.1

The solution for the equation of motion with the above boundary conditions is given in Chapter 3 where the equations are put in finite difference form and the domain of integration is transformed.

2.4. Equation of motion for the fluid phase.

We are now concerned with the solution of equation (2.7) $\underline{\nabla} P_f + \underline{nf} = 0$. The first step in the solution will be to find an expression for the interaction force $\underline{nf}$.

2.4.1. Expression for the interattion force $\underline{nf}$

Anderson and Jackson (82) show that the interaction between the fluid and the particles can be reduced to the following equation by simplifying the general Basset form of the equation (see R. Clift et al. (86)).

$$\underline{nf} = \beta(\varepsilon)(\underline{u}-\underline{v}) + c(\varepsilon)(1-\varepsilon)\rho_f \frac{d}{dt}(\underline{u}-\underline{v}) + (1-\varepsilon)(\underline{\nabla}.\ \underline{\tau}_f) \qquad (2.22)$$

Anderson and Jackson neglect the effect of "history of acceleration of the particles" in equation (2.22) on the assumption that, in a fluidised bed, "any historical background will be quickly erased by the great number of particles."

The signification of each term is as follows:

(i) the first term represents the drag force acting on the particles and is the steady component.

(ii) the second term is known as "the added mass". It is proportional to the mass of fluid accelerated with the particles.

(iii) the third term represents "the reaction of gradients in the local mean fluid stress field on the particulate phase" (Jackson (81)).

We shall try to simplify equation (2.22)

(i) As in the assumptions made to derive the equations of motion, we shall neglect the stress tensor for the fluid, i.e. we neglect $(1-\varepsilon)(\underline{\nabla}\cdot\underline{\underline{\tau}}_f)$.

(ii) Let us rearrange the second term in equation (2.22)

$c(\varepsilon)(1-\varepsilon)\,\rho_f \frac{d}{dt}(\underline{u}-\underline{v})$ can be written as:

$$c(\varepsilon)(1-\varepsilon)\,\rho_f\left\{\left(\frac{\partial \underline{u}}{\partial t}+(\underline{u}\cdot\underline{\nabla})\underline{u}\right)-\left(\frac{\partial \underline{v}}{\partial t}+(\underline{v}\cdot\underline{\nabla})\underline{v}\right)\right\}$$

If we consider a steady state problem and if, as before, we neglect the change in momentum for the fluid phase, this term becomes:

$$c(\varepsilon)(1-\varepsilon)\,\rho_f(\underline{v}\cdot\underline{\nabla})\underline{v}$$

Let us now consider equations (2.11) and (2.7)

$$\rho_p(1-\varepsilon)(\underline{v}\cdot\underline{\nabla})\underline{v} = -\underline{\nabla}P_f + \rho_p(1-\varepsilon)\underline{g} + \mu_p\nabla^2\underline{v} \qquad (2.11)$$

$$\underline{\nabla} P_f + \underline{nf} = 0 \qquad (2.7)$$

By eliminating $\underline{\nabla} P_f$ and replacing $\underline{nf}$ by its expression, we get:

$$(\rho_p + c(\varepsilon)\rho_f)(1-\varepsilon)(\underline{v}.\underline{\nabla})\underline{v} = \beta(\varepsilon)(\underline{u}-\underline{v}) + \rho_p(1-\varepsilon)\underline{g} + \mu_p \nabla^2 \underline{v} \qquad (2.23)$$

Very little is known about the coefficient of the added mass, $c(\varepsilon)$. For an isolated particle starting from rest in a stagnant fluid, Basset showed that $c(\varepsilon) = 0.5$.

The only relation available, applicable to a single particle accelerating from some finite velocity, is that of Odar and Hamilton (in R. Clift et al. (86)):

$$c = 1.05 - 0.066 \left(\frac{dRe_p}{dt}\right)^2 / \left(0.12\left(\frac{dRe_p}{dt}\right)^2 + Re_p^4\right)$$

Re_p being the Reynolds number for the particle.

The maximum value of c is obviously $c = 1.05$ for large values of Re_p or when $\frac{dRe_p}{dt} \to 0$. In the case of a fluidised bed where a great number of particles are present, a total lack of information leads us to assume that in equation (2.23):

$$c(\varepsilon)\,\rho_f \ll \rho_p$$

Murray (87) discusses in detail the various contributions to the interaction force in a general two phase flow. Although he suggests that

in the case of fluidization $c(\varepsilon)$ might be important, his justification is still based on a single sphere. Furthermore his analysis is theoretical and he does not give any numerical value for $c(\varepsilon)$.

If the maximum value of $c(\varepsilon)$ is of the order of 1 for a fluidised bed as suggested in Odar and Hamilton's relation, the above assumption is valid. However for greater values of $c(\varepsilon)$ this simplification may no longer hold and in fact one would expect it to be greater since presumably particles are set in motion, i.e. $\rho_f \gg \rho_{air}$. Thus, finally equation (2.22) reduces to

$$\underline{nf} = \beta(\varepsilon)(\underline{u} - \underline{v}) \qquad (2.24).$$

2.4.2. Calculation of the gas pressure

Given the form of $\underline{nf}$ the next step in solving equation (2.7) is to compute the solution for the pressure gradient $\underline{\nabla} P_f$

We have already shown in section 2.3.1. that:

$$\rho_p(1-\varepsilon_o)(\underline{v}.\underline{\nabla})\underline{v} = -\underline{\nabla}P + \mu_p \nabla^2 \underline{v} \qquad (2.12)$$

and

$$\underline{\nabla} P = -\underline{\nabla} P_p - \underline{\nabla} P_f + \rho_p(1-\varepsilon_o)\underline{g} \qquad (2.11)$$

Equations 2.3 and 2.4 which were written in section 2.1 are symmetrical, i.e. the equations for the gas flow and the particulate flow can be interchanged.

Consequently in order to preserve the symmetry of the equations of motion we have kept the gradient term $\underline{\nabla} P_p$ in equation (2.8). It was also noted in section 1 that the state variables were to be taken as

$\underline{u}$, $\underline{v}$, P_f and ε .

At this stage we note that since nothing is known about the expression for P_p, we could have taken it as one of the independent variables (e.g. the following set $\underline{u}$, $\underline{v}$, P_f and P_p) and therefore have $\varepsilon(P_p)$ as a dependent quantity.

We can show that this leads to an unnecessary complication in the problem.

Consider equations (2.5) and (2.7).

$$\underline{\nabla} \cdot \underline{u} = o \qquad (2.5)$$

$$\underline{\nabla} P_f + \beta (\underline{u} - \underline{v}) = o \qquad (2.7) \quad \text{with now } \beta = \beta (P_p)$$

These can be written as:

$$\underline{u} = \underline{v} - \frac{1}{\beta} \underline{\nabla} P_f \qquad (2.25)$$

$$\underline{\nabla} \cdot \left(\frac{1}{\beta} \underline{\nabla} P_f \right) = o \qquad (2.26)$$

As in Jackson's theory let us put: $\gamma = \frac{\beta_o}{\beta}$

Therefore the last equation (2.26) becomes:

$$\underline{\nabla} \gamma \cdot \underline{\nabla} P_f + \gamma \underline{\nabla}^2 P_f = o \qquad (2.27)$$

and by using (2.11):

$$\underline{\nabla}\gamma\cdot(\underline{\nabla}P-\underline{\nabla}P_p+\rho_p(1-\varepsilon)\underline{g})+\gamma\underline{\nabla}\cdot(\underline{\nabla}P-\underline{\nabla}P_p+\rho_p(1-\varepsilon)\underline{g})=0$$

$$\text{or}\quad \underline{\nabla}\gamma\cdot\underline{\nabla}P-\underline{\nabla}\gamma\cdot\underline{\nabla}P_p+\underline{\nabla}\gamma\cdot\rho_p(1-\varepsilon)\underline{g}+\gamma\underline{\nabla}^2P-\underline{\nabla}^2P_p=0 \qquad (2.28)$$

Equation (2.28) is a non-linear partial differential equation. $\underline{\nabla}P$ is known from the solution of (2.12) but γ is an unknown function of P_p. It is not possible to simplify equation (2.28) as in Jackson's treatment with ε as a state variable (i.e. ε is constant except where it enters $\beta(\varepsilon)$ etc.), which would allow (2.28) to be solved by successive iterations. Consequently the choice of P_p as a state variable is not a good one.

Murray (19) suggests that the term P_p will be in general negligible on the assumption that in the particle motion around a bubble there is little interference between neighbouring particles and that the only way a particulate pressure could be transmitted is by frequent collisions.

In another work (87), where he derives the equations of motion for a general two phase flow, Murray also suggests that the particulate pressure could be incorporated into a new definition of the bulk viscosity on the assumption that the effects of such a pressure and a bulk viscosity are similar.

He therefore writes the ij component of : $-\underline{\nabla}P_p-\underline{\nabla}\cdot\underline{\tau}_p$, as

$$\nabla \left[P_p \, \delta_{ij} - \mu_p \left(\frac{\partial v_i}{\partial x_j} + \frac{\partial v_j}{\partial x_i} \right) - \left(\lambda_p - \frac{2}{3} \mu_p \right) \delta_{ij} \frac{\partial v_k}{\partial x_k} \right]$$

and using the particulate pressure and the bulk viscosity terms Murray writes:

$$\lambda_p \frac{\partial v_k}{\partial x_k} - P_p = \bar{\lambda}_p \frac{\partial v_k}{\partial x_k}$$

But in his general equations of motion applied to fluidization, he neglects the stress tensor for the particulate phase on the assumption that the voidage remains nearly constant around the bubble.
In Jackson's theory (13) no such assumption is made concerning the voidage and as noted in Section 2.3.1 nothing is known about λ_p and consequently about $\bar{\lambda}_p$. Thus Murray's expression for $\bar{\lambda}_p$ does not help at the present time.

On the other hand, Jackson (8 1) gives a lower limit for the value of $\frac{dP_p}{d\varepsilon}$ for a uniformely fluidised bed:

$$\left| \frac{dP_p}{d\varepsilon} \right|_{\varepsilon = \varepsilon_o} = \frac{\rho_f (1 - \varepsilon_o)}{\varepsilon_o^3} U_o^2$$

In the absence of any theoretical and experimental evidence concerning the value of P_p and in view of the above contradiction, we shall neglect this term in equation (2.11), bearing in mind that it might be one of the weaknesses of the solution we shall find.
Therefore the solution for the gas pressure gradient can easily be found from:

$$\rho_p(1-\varepsilon_o)(\underline{v}.\underline{\nabla})\underline{v} = -\underline{\nabla}P + \mu_p \nabla^2 \underline{v} \qquad (2.12)$$

and $$-\underline{\nabla}P = -\underline{\nabla}P_f + \rho_p(1-\varepsilon_o)\underline{g} \qquad (2.13)$$

Let us write equations (2.12) and (2.13) in dimensionless form and put $P^* = \frac{P}{P_o}$ where the reference quantity P_o is taken as the dynamic pressure of the flow of particles with a velocity U_b i.e. $P_o = \frac{1}{2}\rho_p(1-\varepsilon_o)U_b^2$

we get $$(\underline{v}^* . \underline{\nabla}^*)\underline{v}^* = -\frac{1}{2}\underline{\nabla}^* P^* + \frac{2}{Re}\nabla^{*2} v^* \qquad (2.29)$$

and $$-\underline{\nabla}^* P^* = -\underline{\nabla}^* P_f^* + \frac{2}{Fr}\underline{i} \qquad (2.30)$$

where $Fr = \frac{U_b^2}{ga}$ is the Froude number for the bubble

and $\underline{i}$ is an unit vector in the downwards direction.

2.4.3. Calculation of the Froude number

In section 2 it was assumed that the bubble shape remains circular. By doing so, however, it is impossible to satisfy the constant pressure condition around the bubble. Nevertheless it is possible to ensure that the pressure varies only slowly around the apex of the bubble.

Let us consider the tangential component of equation (2.29).

$$v_\rho^* \frac{\partial v_\theta^*}{\partial \rho} + \frac{v_\theta^*}{\rho}\frac{\partial v_\theta^*}{\partial \theta} + \frac{v_\rho^* v_\theta^*}{\rho} = -\frac{1}{2}\frac{1}{\rho}\frac{\partial P^*}{\partial \theta} + \frac{2}{Re}\frac{\partial \zeta^*}{\partial \rho}$$

at the apex of the bubble: $v_\rho^* = v_\theta^* = 0$

$$\zeta^* = 0$$

$\zeta^* = 0$ is a boundary condition on the axis of the bubble for all ρ.

Whence at the apex of the bubble we also have $\left.\frac{\partial \zeta^*}{\partial \rho}\right|_{\substack{\rho=1 \\ \Theta=0}} = 0$

Therefore we have $\left.\frac{\partial P^*}{\partial \Theta}\right|_{\substack{\rho = 1 \\ \theta = 0}} = 0$. From equation (2.30) it is

easy to see that $\left.\frac{\partial P_f^*}{\partial \theta}\right|_{\substack{\rho = 1 \\ \theta = 0}} = 0$

If we can ensure $\left.\frac{\partial^2 P_f^*}{\partial \theta^2}\right|_{\substack{\rho = 1 \\ \theta = 0}} = 0$ then the change in pressure will be

small in a region where $\theta \sim 0$.

From (2.30) we get $\frac{\partial^2 P^*}{\partial \theta^2} = \frac{\partial^2 P_f^*}{\partial \theta^2} - \frac{2\rho}{Fr} \cos\theta$

If $\left.\frac{\partial^2 P_f^*}{\partial \theta^2}\right|_{\substack{\rho = 1 \\ \theta = 0}} = 0$ then $\left[\frac{2\rho}{Fr} \cos\theta = -\frac{\partial^2 P^*}{\partial \theta^2}\right]_{\substack{\rho = 1 \\ \theta = 0}}$ (2.31)

By differentiating the tangential component of equation (2.29) with respect to θ, it becomes:

$$\frac{1}{2}\frac{1}{\rho}\frac{\partial^2 P^*}{\partial \theta^2} = \frac{2}{Re}\frac{\partial^2 \zeta^*}{\partial \rho \partial \theta} - \left\{\frac{\partial v_\rho^*}{\partial \theta}\frac{\partial v_\theta^*}{\partial \rho} + v_\rho^*\frac{\partial^2 v_\theta^*}{\partial \rho \partial \theta} + \frac{1}{\rho}\left(\frac{\partial v_\theta^*}{\partial \theta}\right)^2\right.$$

$$\left. + \frac{v_\theta^*}{\rho}\frac{\partial^2 v_\theta^*}{\partial \theta^2} + \frac{v_\rho^*}{\rho}\frac{\partial v_\theta^*}{\partial \theta} + \frac{v_\theta^*}{\rho}\frac{\partial v_\rho^*}{\partial \theta}\right\}$$

For $\rho = 1$ and $\theta = 0$ this reduces to:

$$\left[\frac{\partial^2 P^*}{\partial \theta^2} = \frac{4}{Re}\frac{\partial^2 \zeta^*}{\partial \rho \partial \theta} - 2\left(\frac{\partial v_\theta^*}{\partial \theta}\right)^2\right]_{\substack{\rho = 1 \\ \theta = 0}}$$

consequently by using (2.31)

$$Fr = \frac{1}{\left(\frac{\partial v_\theta^*}{\partial \theta}\right)^2\Big|_{\substack{\rho = 1 \\ \theta = 0}} - \frac{2}{Re}\frac{\partial^2 \zeta^*}{\partial \rho \partial \theta}\Big|_{\substack{\rho = 1 \\ \theta = 0}}}$$

We can make the following remark:

In the case of Davidson's treatment (10) i.e. $Re \to \infty$ and irrotational flow then $Fr = \frac{1}{\left(\frac{\partial v_\theta^*}{\partial \theta}\right)^2\Big|_{\substack{\rho = 1 \\ \theta = 0}}}$; also it is easy to show that $v_\theta^* = 2 \sin\theta$ and therefore $Fr = 0.250$ which is the Davies and Taylor result for a two dimensional bubble.

Since there is no analytical solution for the Stokes flow regime around a cylinder the other limiting case, i.e. $Re \to 0$, cannot be obtained simply.

Knowing the Froude number from equation (2.32) it is possible to calculate the entire field of the pressure gradient $\underline{\nabla}^* P_f^*$ using (2.29) and (2.30).

2.4.4. Voidage variations around the bubble

Once the solution for the pressure gradient is found we can solve the equation for the voidage around the bubble using equation (2.27):

$$\underline{\nabla}\,\gamma \cdot \underline{\nabla}\,P_f + \gamma \underline{\nabla}^2 P_f = 0 \qquad (2.27)$$

or in dimensionless form:

$$\underline{\nabla}^*\,\gamma \cdot \underline{\nabla}^*\,P_f^* + \gamma \underline{\nabla}^{*2}\,P_f^* = 0 \qquad (2.33)$$

We can easily solve the previous equation by the method of characteristics:

$$\text{put } a = \frac{\partial P_f^*}{\partial \rho} \qquad b = \frac{\partial P_f^*}{\partial \theta} \qquad t = \frac{\partial \gamma}{\partial \rho} \qquad q = \frac{1}{\rho}\,\frac{\partial \gamma}{\partial \theta}$$

Equation (2.33) becomes:

$$at + bq + \gamma \nabla^{*2} P_f^* = 0 \qquad (2.34)$$

$$\text{also:} \quad \frac{d\gamma}{d\theta} = t\,\frac{d\rho}{d\theta} + \rho q$$

substituting into equation (2.34) :

$$at + b\left[\frac{1}{\rho}\,\frac{d\gamma}{d\theta} - \frac{t}{\rho}\,\frac{d\rho}{d\theta}\right] + \gamma \nabla^{*2} P_f^* = 0$$

Let (c) be a curve such that in the (ρ, θ) plane

$$\begin{cases} t\left[a - \frac{b}{\rho}\frac{\partial \rho}{\partial \theta}\right] = 0 & (2.35) \\ \frac{b}{\rho}\frac{\partial \gamma}{\partial \theta} + \gamma \nabla^{*2} P_f^* = 0 & (2.36) \end{cases}$$

If $t \neq 0$ then (2.35) gives a family of curves in the (r, θ) plane along which we integrate equation (2.36) to give the values of γ .

In equation (2.36) we assume, as a boundary condition, that $\gamma = 1$ far from the bubble (i.e. $\varepsilon = \varepsilon_o$ far from the bubble).

From the Carman-Kozeny equation it is easy to show that:

$$\gamma = \frac{\varepsilon^2 (1 - \varepsilon_o)^2}{\varepsilon_o^2 (1 - \varepsilon)^2}$$

and therefore:

$$\varepsilon = \frac{\sqrt{\gamma}}{\frac{1 - \varepsilon_o}{\varepsilon_o} + \sqrt{\gamma}} \qquad (2.37)$$

Equation (2.37) allows us to calculate the voidage variation around the bubble. Although the Carman-Kozeny relation is, strictly speaking, only valid at minimum fluidisation conditions, we assume it remains correct when $\varepsilon \neq \varepsilon_o$.

Lockett and Harrison (7) also used the equation given by Richardson and Zaki (88). They found that the difference between this and Carman-

Kozeny's relation was small.

2.4.5. Solution for the gas flow

From equation (2.25) it is possible to calculate the gas flow field:

$$u_r = v_r - \frac{1}{\beta} \frac{\partial P_f}{\partial r}$$

$$u_\theta = v_\theta - \frac{1}{\beta} \frac{1}{r} \frac{\partial P_f}{\partial \theta}$$

Let us put the two components u_r and u_θ in dimensionless form.

At incipient fluidisation:

$$\beta_o = \frac{\rho_p(1-\varepsilon_o)g}{u_o} \quad \text{and} \quad \gamma = \frac{\beta_o}{\beta}$$

whence:

$$u^*_\rho = v^*_\rho - \frac{\gamma}{2} \frac{Fr}{\alpha_b} \frac{\partial P_f^*}{\partial \rho}$$

$$u^*_\theta = v^*_\theta - \frac{\gamma}{2} \frac{Fr}{\alpha_b} \frac{1}{\rho} \frac{\partial P_f^*}{\partial \theta}$$

or $\underline{u}^* = \underline{v}^* - \frac{\gamma}{2} \frac{Fr}{\alpha_b} \underline{\nabla}^* P_f^*$ (2.38) where $\alpha_b = \frac{U_b}{u_o}$

γ , Fr and $\underline{\nabla}^* P_f$ have been derived in sections 2.4.2. to 2.4.4., therefore the solution for $\underline{u}$ is completely determined.

2.5. Conclusion

Starting with the most general form of the equations of motion for the particulate and fluid phases, we have simplified these equations by making assumptions mainly on the nature of the stress tensor $\underline{\underline{\tau}}_p$, of the interaction force $n\underline{f}$ and of the particulate pressure P_p.

Although these assumptions are not all perfectly justified they give a limit to the validity of the solution we shall get for the flows of particles and fluid.

The following chapter will deal with the numerical solution of these equations and the computation of some important variables.

Boundary Conditions	Dimensionless form of the Conditions
(i) $\theta = 0 \quad a \leqslant r \leqslant r_\infty$ $\left.\begin{array}{l} \Psi = 0 \quad \dfrac{\partial \Psi}{\partial r} = 0 \\ \zeta = 0 \end{array}\right\}$ $\theta = \pi \quad a \leqslant r \leqslant r_\infty$	(i) $\theta = 0 \quad 1 \leqslant \rho \leqslant \rho_\infty$ $\left.\begin{array}{l} \Psi^* = 0 \quad \dfrac{\partial \Psi^*}{\partial \rho} = 0 \\ \zeta^* = 0 \end{array}\right\}$ $\theta = \pi \quad 1 \leqslant \rho \leqslant \rho_\infty$
(ii) $r = r_\infty \quad 0 \leqslant \theta \leqslant \pi \quad \Psi = U_b r_\infty \sin\theta$ $\zeta = 0$	(ii) $\rho = \rho_\infty \quad 0 \leqslant \theta \leqslant \pi \quad \Psi^* = \rho_\infty \sin\theta$ $\zeta^* = 0$
(iii) $r = a \quad 0 \leqslant \theta \leqslant \pi \quad \Psi = 0 \quad \dfrac{\partial \Psi}{\partial \theta} = 0$ $\tau_{r\theta} = 0 : \dfrac{\partial^2 \Psi}{\partial r^2} = \dfrac{1}{a} \dfrac{\partial \Psi}{\partial r}$	(iii) $\rho = 1 \quad 0 \leqslant \theta \leqslant \pi \quad \Psi^* = 0 \quad \dfrac{\partial \Psi^*}{\partial \theta} = 0$ $\tau_{\rho\theta}{}^* = 0 : \dfrac{\partial^2 \Psi^*}{\partial \rho^2} = \dfrac{\partial \Psi^*}{\partial \rho}$

Table 2.1. Boundary conditions for the particulate flow

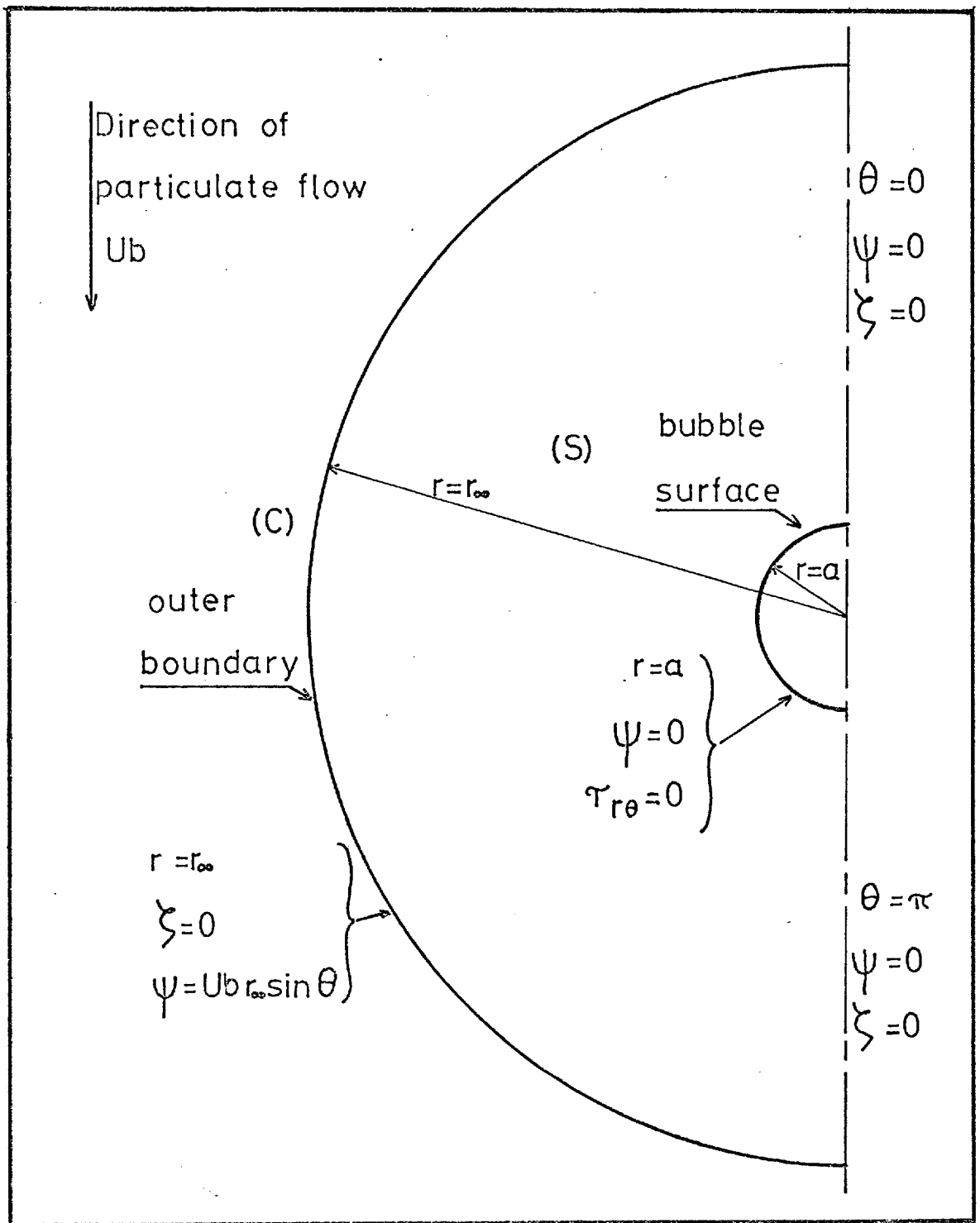


Figure 2-1 Domain of integration and boundary conditions of equations 2-15 & 2-16

CHAPTER 3

NUMERICAL SOLUTION OF THE EQUATIONS OF MOTION

The equations of motion which were derived in the preceding chapter are now transformed and put into finite difference form.

Procedures for computing variables of interest such as the pressure variations along the axis of rise of the bubble and on its surface, the drift of particles caused by the passage of the bubble, the gas and particle velocity fields, the voidage fraction, etc. ... are developed.

3.1. The transformed equations for the particulate flow

The motion of the particulate phase around a bubble rising in a two-dimensional fluidised bed is described by the following set of equations in terms of stream function and vorticity (section 2.3.3).

$$\zeta^* = \frac{1}{\rho}\frac{\partial \Psi^*}{\partial \rho} + \frac{\partial^2 \Psi^*}{\partial \rho^2} + \frac{1}{\rho^2}\frac{\partial^2 \Psi^*}{\partial \theta^2} \qquad (2.19)$$

$$\frac{\partial \Psi^*}{\partial \rho}\frac{\partial \zeta^*}{\partial \theta} - \frac{\partial \Psi^*}{\partial \theta}\frac{\partial \zeta^*}{\partial \rho} = \frac{2}{Re}\left\{\frac{\partial \zeta^*}{\partial \rho} + \rho\frac{\partial^2 \zeta^*}{\partial \rho^2} + \frac{1}{\rho}\frac{\partial^2 \zeta^*}{\partial \theta^2}\right\} \qquad (2.20)$$

The domain of integration (S) is also indicated in Figure 3.1 where r_∞ is chosen great enough so that at the outer boundary, the flow of particles is a potential flow.

To integrate equations (2.19) and (2.20), the domain (S) has to be divided into a fine grid at the nodes of which the two equations will be calculated.

An obvious choice to construct this grid would be the lines ρ = constant and θ = constant. Nevertheless it is convenient to transform the polar (ρ , θ) plane into a rectangular (ξ , η) plane and also to have a finer mesh near the surface of the bubble where the vorticity and stream-function gradients are the largest.

For this purpose we make the following transformation:

$$\rho = e^{\pi\xi} \quad \text{and} \quad \theta = \pi\eta$$

This transformation was first discussed by C.J. Apelt (89) and satisfies the requirements that (ξ, η) is a rectangular plane and that the mesh is finer near the surface of the bubble.

Equations (2.19) and (2.20) can therefore be written as:

$$E^2 \zeta^* = \frac{\partial^2 \psi^*}{\partial \eta^2} + \frac{\partial^2 \psi^*}{\partial \xi^2} \tag{3.1}$$

$$\frac{\partial \Psi^*}{\partial \xi} \frac{\partial \zeta^*}{\partial \eta} - \frac{\partial \Psi^*}{\partial \eta} \frac{\partial \zeta^*}{\partial \xi} = \frac{2}{Re} \left\{ \frac{\partial^2 \zeta^*}{\partial \eta^2} + \frac{\partial^2 \zeta^*}{\partial \xi^2} \right\} \tag{3.2}$$

where $E = \pi e^{\pi\xi}$ ($M = \frac{1}{E}$ is often referred to as the modulus of the transformation)

The boundary conditions in Table 2.1 become:

(i) $\eta = 0 \quad 0 \leqslant \xi \leqslant \xi_\infty$

$$\left.\begin{array}{l} \Psi^* = 0 \longrightarrow \dfrac{\partial \Psi^*}{\partial \xi} = 0 \\ \zeta^* = 0 \end{array}\right. \qquad (3.3)$$

$\eta = 1 \quad 0 \leqslant \xi \leqslant \xi_\infty$

(ii) $\xi = \xi_\infty \quad 0 \leqslant \eta \leqslant 1 \quad \Psi^* = e^{\pi \xi_\infty} \sin \pi\eta \qquad (3.4)$

$\zeta^* = 0$

(iii) $\xi = 0 \quad 0 \leqslant \eta \leqslant 1 \quad \Psi^* = 0 \longrightarrow \dfrac{\partial \Psi^*}{\partial \eta} = 0$

$$\tau_{\xi\eta}{}^* = 0 \longrightarrow \frac{\partial^2 \Psi^*}{\partial \xi^2} = 2\pi \frac{\partial \Psi^*}{\partial \xi}$$

The same set of equations with different boundary conditions is given by J.S. Son and T.H. Hanratty (90) for a time dependent solution of the flow past a cylinder with a non-slip condition at its surface.

3.2. Finite difference form of the equations for the particulate flow

3.2.1. Vorticity equation

Equation (3.2) is put in finite differences form using the Peaceman-Rachford alternating direction method (A.D.I.) (91).

It is beyond the scope of this work to discuss the various aspects of the different methods proposed in the literature. Stability, computer storage, rapidity of convergence would have to be studied for all the schemes to select the best one for our particulate problem.

However, it has been noted, from numerical experimentation, that the A.D.I. method is quite suitable for simulating flows around

an obstacle. It has a better stability characteristic than other methods, especially at high Reynolds numbers, and it also keeps the computer storage and time to a minimum.

The transformed grid of integration in the (ξ, η) plane is represented in Figure 3.1. In this figure:

l is the increment in the η direction

k is the increment in the ξ direction.

Approximations to the derivatives are made by using central differences, thus the values of the derivatives of the stream function and vorticity at point (i, j) are computed from the values at the four surrounding points.

In a general form we write :

$$\left.\begin{aligned}
\left(\frac{\partial f}{\partial \eta}\right)_{ij} &= \frac{1}{2l}\left\{ f_{i+1,j} - f_{i-1,j}\right\} + 0(l^2) \\
\left(\frac{\partial f}{\partial \xi}\right)_{i,j} &= \frac{1}{2k}\left\{ f_{i,j+1} - f_{i,j-1}\right\} + 0(k^2) \\
\left(\frac{\partial^2 f}{\partial \eta^2}\right)_{i,j} &= \frac{1}{l^2}\left\{ f_{i+1,j} - 2f_{i,j} + f_{i-1,j}\right\} + 0(l^2) \\
\left(\frac{\partial^2 f}{\partial \xi^2}\right)_{i,j} &= \frac{1}{k^2}\left\{ f_{i,j+1} - 2f_{i,j} + f_{i,j-1}\right\} + 0(k^2)
\end{aligned}\right] \qquad (3.6)$$

as $\lim_{l\to 0}\left\{0(l^2)\right\} = 0$ the mesh size l (resp. k) will have to be chosen small enough so that the accuracy of the calculation is not much affected by the truncation error.

However the number of equations to solve is proportional to the number of mesh points; therefore by halving the mesh length one multiplies the number of equations by four. Consequently the mesh size will have to be taken as a compromise between accuracy and computing resources.

Using the above approximations to the derivatives, equation (3.2) can be written as:

$$\frac{\Psi^*_{i,j+1} - \Psi^*_{i,j-1}}{2k}\,\frac{\zeta^*_{i+1,j} - \zeta^*_{i-1,j}}{2l} - \frac{\Psi^*_{i+1,j} - \Psi^*_{i-1,j}}{2l}\,\frac{\zeta^*_{i,j+1} - \zeta^*_{i,j-1}}{2k}$$

$$= \frac{2}{Re}\left\{\frac{\zeta^*_{i+1,j} - 2\zeta^*_{i,j} + \zeta^*_{i-1,j}}{l^2} + \frac{\zeta^*_{i,j+1} - 2\zeta^*_{i,j} + \zeta^*_{i,j-1}}{k^2}\right\} \quad (3.7)$$

The preceding elliptic equation can be regarded as the limiting solution of the corresponding time-dependent problem with some initial value. We can therefore introduce an iteration coefficient ρ_a which will be referred to in the following as the acceleration factor.

The value of this coefficient can be the same for all the iterations; however if it is changed for each iteration the converging process can be speeded up. In most cases the optimal value of ρ_a has to be found by numerical experimentation.

In our problem several values of ρ_a were tried and the best one found was used throughout the calculation.

Equation (3.7) can therefore be written as:

$$\rho_a \zeta^*_{i,j} + \frac{\Psi^*_{i,j+1} - \Psi^*_{i,j-1}}{2k} \frac{\zeta^*_{i+1,j} - \zeta^*_{i-1,j}}{2l} - \frac{\Psi^*_{i+1,j} - \Psi^*_{i-1,j}}{2l}$$

$$\frac{\zeta^*_{i,j+1} - \zeta^*_{i,j-1}}{2k} = \frac{2}{Re}\left\{\frac{\zeta^*_{i+1,j} - 2\,\zeta^*_{i,j} + \zeta^*_{i-1,j}}{l^2}\right.$$

$$\left. + \frac{\zeta^*_{i,j+1} - 2\,\zeta^*_{i,j} + \zeta^*_{i,j-1}}{k^2}\right\} + \rho_a \zeta^*_{i,j} \qquad (3.8)$$

To solve equation (3.8), one assumes that the n^{th} values in the iteration have been calculated at all the mesh points from some initial approximation $\Psi^{*(o)}_{i,j}$ and $\zeta^{*(o)}_{i,j}$ and known boundary conditions (as established in the previous section).

We can therefore write from (3.7)

$$\zeta^{*(n+1)}_{i,j} = F\,(\Psi^{*(n)},\ \zeta^{*(n)}) \qquad (3.9)$$

The solution of the set of equations (3.9) is a very lengthy process since it consists of a large number of non-linear equations. The principle of the A.D.I. method is to overcome this difficulty by dividing the step from iteration (n) to iteration (n + 1) into two half-steps.

The following procedure which is summarized in Figure 3.2 is then carried out:

(i) the derivatives in one of the directions are approximated at half step $(n + \frac{1}{2})$ while the derivatives in the other direction are approximated at the $(n)^{th}$ step which, as we already said, is assumed to be known.

(ii) The procedure is then repeated from the half step $(n + \frac{1}{2})$ to the final $(n + 1)^{th}$ step, alternating the previous directions.

The derivatives approximated at the $(n)^{th}$ step are now approximated at the $(n + 1)^{th}$ step; the derivatives in the other direction which are approximated at the half step $(n + \frac{1}{2})$ are known from stage (i).

The choice of the starting direction in the A.D.I. method depends on knowledge of the boundary condition. In the present case we know the exact value of the vorticity on the axis of the bubble ($\zeta^* = 0$) while it is unknown on the bubble surface. It is therefore more convenient to start the computation along lines r = cst, which prevents assuming an initial value for the first half step $(n) \rightarrow (n + \frac{1}{2})$. The surface vorticity is then only approximated for the second half-step $(n + \frac{1}{2}) \rightarrow (n + 1)$.

Using the grid of integration defined at the beginning of this section we can summarize the computation of the A.D.I. method as follows:

(i) At the first half step $(n) \rightarrow (n + \frac{1}{2})$ iterations are carried along lines ξ = cst.

(ii) At the second half step $(n + \frac{1}{2}) \rightarrow (n + 1)$ iterations are carried along lines η = cst.

Equation (3.8) therefore becomes:

(i) 1st half step $(n) \rightarrow (n + \frac{1}{2})$

$$\rho a \zeta^{*(n+\frac{1}{2})}_{i,j} + \frac{\psi^{*(n)}_{i,j+1} - \psi^{*(n)}_{i,j-1}}{2k} \cdot \frac{\zeta^{*(n+\frac{1}{2})}_{i+1,j} - \zeta^{*(n+\frac{1}{2})}_{i-1,j}}{2l}$$

$$- \frac{\psi^{*(n)}_{i+1,j} - \psi^{*(n)}_{i-1,j}}{2l} \cdot \frac{\zeta^{*(n)}_{i,j+1} - \zeta^{*(n)}_{i,j-1}}{2k}$$

$$= \frac{2}{Re}\left\{\frac{\zeta^{*(n+\frac{1}{2})}_{i+1,j} - 2\,\zeta^{*(n+\frac{1}{2})}_{i,j} + \zeta^{*(n+\frac{1}{2})}_{i-1,j}}{l^2}\right.$$

$$\left. + \frac{\zeta^{*(n)}_{i,j+1} - 2\,\zeta^{*(n)}_{i,j} + \zeta^{*(n)}_{i,j-1}}{k^2}\right\} + \rho_a\,\zeta^{*(n)}_{i,j}$$

which can be written as:

$$-\left\{\frac{\Psi^{*(n)}_{i,j+1} - \Psi^{*(n)}_{i,j-1}}{4kl} + \frac{2}{Rel^2}\right\}\zeta^{*(n+\frac{1}{2})}_{i-1,j} + \left\{\rho_a + \frac{4}{Rel^2}\right\}\zeta^{*(n+\frac{1}{2})}_{i,j}$$

$$+\left\{\frac{\Psi^{*(n)}_{i,j+1} - \Psi^{*(n)}_{i,j-1}}{4kl} - \frac{2}{Rel^2}\right\}\zeta^{*(n+\frac{1}{2})}_{i+1,j} = \alpha_{ij} \qquad (3.12)$$

where α_{ij} includes all the terms ζ^{*} for iteration (n) :

$$\alpha_{ij} = \left\{\frac{2}{Rek^2} - \frac{\Psi^{*(n)}_{i+1,j} - \Psi^{*(n)}_{i-1,j}}{4kl}\right\}\zeta^{*(n)}_{i,j-1} + \left\{\rho_a - \frac{4}{k^2 Re}\right\}\zeta^{*(n)}_{i,j}$$

$$+\left\{\frac{\Psi^{*(n)}_{i+1,j} - \Psi^{*(n)}_{i-1,j}}{4kl} + \frac{2}{Rek^2}\right\}\zeta^{*(n)}_{i,j+1} \qquad (3.13)$$

Equation (3.12) can be written as:

$$A_{ij}\,\zeta^{*(n+\frac{1}{2})}_{i-1,j} + B\,\zeta^{*(n+\frac{1}{2})}_{i,j} + C_{ij}\,\zeta^{*(n+\frac{1}{2})}_{i+1,j} = \alpha_{ij} \qquad (3.14)$$

with:

$$A_{ij} = -\frac{\Psi^{*(n)}_{i,j+1} - \Psi^{*(n)}_{i,j-1}}{4kl} + \frac{2}{Rel^2}$$

$$B = \rho_a + \frac{4}{Rel^2}$$

$$C_{i,j} = \frac{\Psi^{*(n)}_{i,j+1} - \Psi^{*(n)}_{i,j-1}}{4kl} - \frac{2}{Rel^2}$$

(ii) 2^{nd} half step $(n+\frac{1}{2}) \longrightarrow (n)$

The same procedure as before is applied to equation (3.8) in the other direction:

$$\rho_a \zeta_{ij}^{*(n+1)} + \frac{\Psi_{i,j+1}^{*(n)} - \Psi_{i,j-1}^{*(n)}}{2k} \quad \frac{\zeta_{i+1,j}^{*(n+\frac{1}{2})} - \zeta_{i-1,j}^{*(n+\frac{1}{2})}}{2l}$$

$$- \frac{\Psi_{i+1,j}^{*(n)} - \Psi_{i-1,j}^{*(n)}}{2l} \quad \frac{\zeta_{i,j+1}^{*(n+1)} - \zeta_{i,j-1}^{*(n+1)}}{2k}$$

$$= \frac{2}{Re} \left\{ \frac{\zeta_{i+1,j}^{*(n+\frac{1}{2})} - 2\,\zeta_{i,j}^{*(n+\frac{1}{2})} + \zeta_{i-1,j}^{*(n+\frac{1}{2})}}{l^2} \right.$$

$$\left. + \frac{\zeta_{i,j+1}^{*(n+1)} - 2\,\zeta_{i,j}^{*(n+1)} + \zeta_{i,j-1}^{*(n+1)}}{k^2} \right\} + \rho_a \zeta_{i,j}^{*(n+\frac{1}{2})}$$

which is also written as:

$$\left\{ \frac{\Psi_{i+1,j}^{*(n)} - \Psi_{i-1,j}^{*(n)}}{4kl} - \frac{2}{Rek^2} \right\} \zeta_{i,j-1}^{*(n+1)} + \left\{ \rho_a + \frac{4}{Rek^2} \right\} \zeta_{i,j}^{*(n+1)}$$

$$- \left\{ \frac{\Psi_{i+1,j}^{*(n)} - \Psi_{i-1,j}^{*(n)}}{4kl} + \frac{2}{Rek^2} \right\} \zeta_{i,j+1}^{*(n+1)} = \beta_{ij} \qquad (3.15)$$

where

$$\beta_{ij} = \left\{ \frac{\Psi^{*(n)}_{i,j+1} - \Psi^{*(n)}_{i,j-1}}{4k1} + \frac{2}{Re\,1^2} \right\} \zeta^{*(n+\frac{1}{2})}_{i-1,j} + \left\{ \rho_a - \frac{4}{Re\,1^2} \right\} \zeta^{*(n+\frac{1}{2})}_{i,j}$$

$$+ \left\{ \frac{2}{Re\,1^2} - \frac{\Psi^{*(n)}_{i,j+1} - \Psi^{*(n)}_{i,j-1}}{4k1} \right\} \zeta^{*(n+\frac{1}{2})}_{i+1,j} \qquad (3.16)$$

which we can write as before:

$$E_{i,j}\ \zeta^{*(n+1)}_{i,j-1} + F\ \zeta^{*(n+1)}_{i,j} + G_{ij}\ \zeta^{*(n+1)}_{i,j+1} = \beta_{ij} \qquad (3.17)$$

with:

$$E_{ij} = \frac{\Psi^{*(n)}_{i+1,j} - \Psi^{*(n)}_{i-1,j}}{4k1} - \frac{2}{Rek^2}$$

$$F = \rho_a + \frac{4}{Rek^2}$$

$$G_{ij} = - \frac{\Psi^{*(n)}_{i+1,j} - \Psi^{*(n)}_{i-1,j}}{4k1} - \frac{2}{Rek^2}$$

Let us also note that α_{ij} and β_{ij} can be written as:

$$\alpha_{ij} = A'_{ij}\ \zeta^{*(n)}_{i,j-1} + B'\ \zeta^{*(n)}_{i,j} + C'_{ij}\ \zeta^{*(n)}_{i,j+1}$$

$$\beta_{ij} = E'_{ij}\ \zeta^{*(n+\frac{1}{2})}_{i-1,j} + F'\ \zeta^{*(n+\frac{1}{2})}_{i,j} + G'_{ij}\ \zeta^{*(n+\frac{1}{2})}_{i+1,j}$$

where we have the following relations:

$$E'_{ij} = -A_{ij}$$

$$G'_{ij} = -C_{ij}$$

$$A'_{ij} = -E_{ij}$$

$$C'_{ij} = -G_{ij}$$

We shall discuss the solution of the set of linear equations (3.14) and (3.17) in Section (3.3).

Once the values of $\zeta_{i,j}^{(n+1)}$ have been found we can calculate the values of the stream function at each point of the grid from equation (3.1). The next section will deal with this calculation.

3.2.2. Equation for the stream function

Consider equation (3.1) : $E^2 \zeta^* = \frac{\partial^2 \Psi^*}{\partial \eta^2} + \frac{\partial^2 \Psi^*}{\partial \xi^2}$

In finite differences form this equation becomes using relations (3.6)

$$E^2 \zeta_{ij}^* = \frac{\Psi_{i-1,j}^* - 2\Psi_{i,j}^* + \Psi_{i+1,j}^*}{l^2} + \frac{\Psi_{i,j-1}^* - 2\Psi_{i,j}^* + \Psi_{i,j+1}^*}{k^2} \quad (3.18)$$

The above elliptic equation has also to be solved by an iterative technique. The method of successive overrelaxations was used. The A.D.I. method used to solve the vorticity equation could also have been employed but in regard to the simplicity of equation (3.18) the first method was preferred, although there has not been, so far, any justification as to which method is preferable, except for specific cases.

The rate of convergence to the solution of equation (3.18) is accelerated by introducing a relaxation factor ω and then a better estimate of $\Psi^*_{i,j}$ is calculated.

Equation (3.18) can be written as:

$$\Psi^*_{i,j} = \frac{1}{2\left\{\frac{1}{l^2} + \frac{1}{k^2}\right\}} \left\{ \frac{\Psi^*_{i-1,j} + \Psi^*_{i+1,j}}{l^2} + \frac{\Psi^*_{i,j-1} + \Psi^*_{i,j+1}}{k^2} - E^2 \zeta^*_{i,j} \right\}$$

Using the above remark it follows:

$$\Psi^{*(p+1)}_{i,j} = (1-\omega)\, \Psi^{*(p)}_{i,j} + \omega \bar{\Psi}^{*(p)}_{i,j} \qquad (3.19)$$

where $\Psi^{*(p+1)}_{i,j}$ is the improved estimate of $\Psi^{*(p)}_{i,j}$

and $$\bar{\Psi}^{*(p)}_{i,j} = \frac{1}{2\left\{\frac{1}{l^2} + \frac{1}{k^2}\right\}} \left\{ \frac{\Psi^{*(p+1)}_{i-1,j} + \Psi^{*(p)}_{i+1,j}}{l^2} + \frac{\Psi^{*(p+1)}_{i,j-1} + \Psi^{*(p)}_{i,j+1}}{k^2} - E^2 \zeta^{*(n+1)}_{i,j} \right\} \qquad (3.20)$$

The over-relaxation method (also referred to as the Extrapolated Liebmann method) calculates the values of $\Psi^{*(p+1)}_{i,j}$ for successive points. All the values of the stream function on the left and below (i,j) are assumed to be known for iteration $(p+1)$.

The rate of convergence depends very much on the value of the relaxation factor ω. Smith (84) reports an example in which the convergence using $\omega = 1.9$ is forty times faster than the non-extrapolated method ($\omega = 1$).

In the case of (3.18) which is a Poisson's equation, Frankel (in Smith (84)) proved that the optimum value for ω is given by the smaller root of the equation:

$$\alpha^2 t^2 - 4\alpha + 1 = 0$$

where $\alpha = \frac{\omega}{4}$

$$t = \cos \frac{\pi}{p} + \cos \frac{\pi}{q}$$

p = number of mesh points in i-direction

q = number of mesh points in j-direction

on another hand D.B. Russell (92) proposes as an optimum value:

$$\omega = \frac{2}{1 + \frac{\pi}{2} \left(\frac{1}{p^2} + \frac{1}{q^2}\right)^{\frac{1}{2}}}$$

In the present case both values were found to be close and therefore an average was taken in the computation. This was found to give a good rate of convergence.

3.3. Solution for the vorticity equation

Equations (3.14) and (3.17) constitute two sets of linear equations. Each set can be written as follows (using general notations):

$$\left.\begin{aligned}
b_1 v_1 + c_1 v_2 &= d_1 \\
a_2 v_1 + b_2 v_2 + c_2 v_3 &= d_2 \\
a_3 v_2 + b_3 v_3 + c_3 v_4 &= d_3 \\
\text{- - - - - - - - - - - - - - - - - - -} & \\
a_i v_{i-1} + b_i v_i + c_i v_{i+1} &= d_i \\
\text{- - - - - - - - - - - - - - - - - - -} & \\
a_n v_{n-1} + b_n v_n &= d_n
\end{aligned}\right] \qquad (3.21)$$

where a_i, b_i, c_i represent the coefficients in the two sets of equations and v_i represents the vorticity.

This system of linear equations could be solved by a classical Gaussian elimination.

Nevertheless we note that the matrix of the transform is tridiagonal. It is one of the great advantages of the A.D.I. method to give a matrix of this form.

It follows that:

$$\underline{M} = \begin{bmatrix}
b_1 & c_1 & 0 & 0 & \cdots & \cdots & \cdots & \cdots & \cdots & 0 \\
a_2 & b_2 & c_2 & 0 & \cdots & \cdots & \cdots & \cdots & \cdots & 0 \\
0 & a_3 & b_3 & c_3 & \cdots & \cdots & \cdots & \cdots & \cdots & 0 \\
\cdots & \cdots & \cdots & \cdots & \cdots & \cdots & \cdots & \cdots & \cdots & \cdots \\
0 & \cdots & 0 & \cdots & 0 & \cdots & a_i & b_i & c_i & 0 \\
0 & \cdots & 0 & \cdots & 0 & \cdots & \cdots & \cdots & a_n & b_n
\end{bmatrix}$$

This matrix can be partitioned into a product of an upper triangular matrix by a lower triangular matrix. It can be shown that this decomposition is always possible (D.L. Fox (94), B. Carnahan et al. (95)) provided that:

$$\left.\begin{aligned} |b_1| > |c_1| > 0 \\ |b_n| > |c_n| > 0 \\ |a_i| > |b_i| + |c_i| \end{aligned}\right\} \qquad (3.22)$$

If one of these relations is not satisfied the above authors show that the matrix $\underline{M}$ becomes singular and its inverse does not exist. Assuming (3.22) is fulfilled then:

$$\underline{M} = \underline{L} \cdot \underline{U}$$

where:

$$\underline{L} = \begin{bmatrix} \lambda_1 & 0 & \cdots & 0 \\ a_2 & \lambda_2 & \cdots & 0 \\ \cdots & \cdots & \cdots & \cdots \\ 0 & a_i & \lambda_i & 0 \\ \cdots & \cdots & \cdots & \cdots \\ 0 & \cdots & a_n & \lambda_n \end{bmatrix} \quad \text{and} \quad \underline{U} = \begin{bmatrix} 1 & \gamma_1 & \cdots & 0 \\ 0 & 1 & \gamma_2 & \cdots & 0 \\ \cdots & \cdots & \cdots & \cdots & \cdots \\ 0 & \cdots & 0 & 1 & \gamma_i & \cdots & 0 \\ \cdots & \cdots & \cdots & \cdots & \cdots & \cdots & \cdots \\ 0 & \cdots & \cdots & \cdots & 0 & 1 \end{bmatrix}$$

with the following relations :

$$\left.\begin{aligned} \lambda_1 &= b_1 \\ \lambda_i &= b_i - a_i \gamma_{i-1} \\ \gamma_i &= \frac{c_i}{\lambda_i} \end{aligned}\right] \qquad (3.23)$$

The set of linear equations (3.21) $\underline{M} \cdot \underline{V} = \underline{D}$ is therefore written as $\underline{L} \cdot \underline{U} \cdot \underline{V} = \underline{D}$.

We can, therefore, solve first $\underline{L} \cdot \underline{X} = \underline{D}$ and then $\underline{U} \cdot \underline{V} = \underline{X}$ where $\underline{X}$ is an unknown auxiliary vector.

$$\underline{U}.\underline{V} = \underline{X} \Longrightarrow \left.\begin{aligned} v_1 + \gamma_1 v_2 &= x_1 \\ v_2 + \gamma_2 v_3 &= x_2 \\ \text{- - - - - - - - - - -} & \\ v_i + \gamma_i v_{i+1} &= x_i \\ \text{- - - - - - - - - - -} & \\ v_n &= x_n \end{aligned}\right] \qquad (3.24)$$

$$\underline{L} \cdot \underline{X} = \underline{D} \Longrightarrow \left.\begin{aligned} \lambda_1 x_1 &= d_1 \\ a_2 x_1 + \lambda_2 x_2 &= d_2 \\ \text{- - - - - - - - - -} & \\ a_i x_{i-1} + \lambda_i x_i &= d_i \\ \text{- - - - - - - - - -} & \\ a_n x_{n-1} + \lambda_n x_n &= d_n \end{aligned}\right] \qquad (3.25)$$

Starting from i = 1, we have from system (3.25) :

$$x_1 = \frac{d_1}{\lambda_1}$$

$$x_2 = \frac{1}{\lambda_2}\left\{ d_2 - a_2 x_1 \right\}$$

- - - - - -

$$x_i = \frac{1}{\lambda_i}\left\{ d_i - a_i x_{i-1} \right\}$$

- - - - - -

$$x_n = \frac{1}{\lambda_n}\left\{ d_n - a_n x_{n-1} \right\}$$

Starting from i = n we have from system (3.24)

$$v_n = x_n$$

- - - -

$$v_i = x_i - \gamma_i v_{i+1}$$

- - - -

$$v_1 = x_1 - \gamma_1 v_2$$

This calculation gives therefore the solution for the vector $\underline{V} = \begin{bmatrix} v_1 \\ v_2 \\ - - \\ v_i \\ - - \\ v_n \end{bmatrix}$

It should be noted that the above calculation is an useful short way for calculating $\underline{V}$ instead of by $\underline{V} = \underline{M}^{-1} . \underline{D}$. The inverse matrix $\underline{M}^{-1}$ would not be generally a tridiagonal matrix and would therefore occupy more space than $\underline{L}$ and $\underline{U}$. Moreover the computation time of $\underline{L} . \underline{X} = \underline{D}$ and $\underline{U} . \underline{V} = \underline{X}$ is certainly shorter than the time for the inversion of $\underline{M}$ and its multiplication by the vector $\underline{D}$.

3.4. Initial conditions for the particulate flow

3.4.1. Initial values for the stream function

As noted in section 3.2.1. it is necessary to have some initial approximation to the stream function $\Psi^{*(o)}_{i,j}$ at the start of the computation. In the case of a two dimensional bubble the only solution available is the potential flow solution as given by Davidson and Harrison (10).

$$\Psi = U_b \sin\theta \left(r - \frac{a^2}{r} \right)$$

or in dimensionless form:

$$\Psi^* = \rho \sin\theta \left(1 - \frac{1}{\rho^2} \right)$$

Using the transformation given in section 3.1 it follows:

$$\psi^{*(o)} = (e^{\pi\xi} - e^{-\pi\xi}) \sin\pi\eta \qquad (3.26)$$

In the preceding chapter, in section 2.3.4, it was pointed out that r_∞ has to be chosen so that for $r = r_\infty$, $\Psi = U_b r_\infty \sin\theta$. Applied to equation (3.26) this condition means that ξ_∞ must be chosen so that $e^{-\pi\xi} \ll e^{\pi\xi}$.

In Appendix 4 the numerical values of the grid size, which were taken in the computation, are indicated.

3.4.2. Approximation of surface vorticity

It was noted in section 3.2.1. that some approximation to the surface vorticity must be calculated, when applying the second half step to equation (3.8) as an initial approximation for the calculation of the entire vorticity field at each iteration $(n) \rightarrow (n+1)$. The surface vorticity has been approximated from the values of the stream function near the surface.

A Taylor expansion of these values is as follows:

(with $\Psi^*_{i,1} = 0$ from boundary conditions).

$$\Psi^*_{i,2} = k\left(\frac{\partial \Psi^*}{\partial \xi}\right)_{i,1} + \frac{k^2}{2!}\left(\frac{\partial^2 \Psi^*}{\partial \xi^2}\right)_{i,1} + \frac{k^3}{3!}\left(\frac{\partial^3 \Psi^*}{\partial \xi^3}\right)_{i,1} + \frac{k^4}{4!}\left(\frac{\partial^4 \Psi^*}{\partial \xi^4}\right)_{i,1} + 0(k)^5 \tag{3.27}$$

$$\Psi^*_{i,3} = 2k\left(\frac{\partial \Psi^*}{\partial \xi}\right)_{i,1} + \frac{(2k)^2}{2!}\left(\frac{\partial^2 \Psi^*}{\partial \xi^2}\right)_{i,1} + \frac{(2k)^3}{3!}\left(\frac{\partial^3 \Psi^*}{\partial \xi^3}\right)_{i,1} + \frac{(2k)^4}{4!}\left(\frac{\partial^4 \Psi^*}{\partial \xi^4}\right)_{i,1} + 0(k^5) \tag{3.28}$$

$$\Psi^*_{i,4} = 3k\left(\frac{\partial \Psi^*}{\partial \xi}\right)_{i,1} + \frac{(3k)^2}{2!}\left(\frac{\partial^2 \Psi^*}{\partial \xi^2}\right)_{i,1} + \frac{(3k)^3}{3!}\left(\frac{\partial^3 \Psi^*}{\partial \xi^3}\right)_{i,1} + \frac{(3k)^4}{4!}\left(\frac{\partial^4 \Psi^*}{\partial \xi^4}\right)_{i,1} + 0(k^5) \tag{3.29}$$

Depending on the type of problem and on the accuracy required, several formulae are possible and the best one has to be found by numerical experimentation.

In the present case two, three and four-point formulae have been tried. Furthermore let us apply the equation for the stream function (3.1) at the bubble surface:

$$E^2 \zeta^*_{i,1} = \left(\frac{\partial^2 \Psi^*}{\partial \eta^2}\right)_{i,1} + \left(\frac{\partial^2 \Psi^*}{\partial \xi^2}\right)_{i,1}$$

at the bubble surface:
$$\begin{cases} E^2 = \pi^2 \\ \left(\frac{\partial^2 \Psi^*}{\partial \eta^2}\right)_{i,1} = 0 \end{cases}$$

therefore $$\zeta^*_{i,1} = \frac{1}{\pi^2} \left(\frac{\partial^2 \Psi^*}{\partial \xi^2}\right)_{i,1} \qquad (3.30)$$

We now derive the different formulae tested:

(i) two point formula.

By eliminating $\left(\frac{\partial \Psi^*}{\partial \xi}\right)_{i,1}$ from equations (3.27) and (3.28) and with a truncation error of $0(k^3)$ we get:

$$\left(\frac{\partial^2 \Psi^*}{\partial \xi^2}\right)_{i,1} = \frac{\Psi^*_{i,3} - 2\Psi^*_{i,2}}{k^2}$$

and using (3.30): $$\zeta^*_{i,1} = \frac{1}{\pi^2} \left\{ \frac{\Psi^*_{i,3} - 2\Psi^*_{i,2}}{k^2} \right\} \qquad (3.31)$$

(ii) three point formula

By eliminating $\left(\frac{\partial^3 \Psi^*}{\partial \xi^3}\right)_{i,1}$ between equations (3.27) and (3.28) we get:

$$8\Psi^*_{i,2} - \Psi^*_{i,3} = 6k\left(\frac{\partial \Psi^*}{\partial \xi}\right)_{i,1} + 2k^2\left(\frac{\partial^2 \Psi^*}{\partial \xi^2}\right)_{i,1} + 0(k^4)$$

in addition let us consider the boundary condition for the tangential stress as given in section (3.1):

$$\text{at } \xi = 0 \quad \tau^*_{\xi,\eta} = 0 \qquad \Rightarrow \left(\frac{\partial^2 \Psi^*}{\partial \xi^2}\right)_{i,1} = 2\pi \left(\frac{\partial \Psi^*}{\partial \xi}\right)_{i,1}$$

by combining the above two equations we easily get:

$$\left(\frac{\partial^2 \Psi^*}{\partial \xi^2}\right)_{i,1} = \frac{8\Psi^*_{i,2} - \Psi^*_{i,3}}{\frac{3k}{\pi} + 2k^2}$$

and using equation (3.30):

$$\zeta^*_{i,1} = \frac{1}{\pi 2}\left\{\frac{8\Psi^*_{i,2} - \Psi^*_{i,3}}{\frac{3k}{\pi} + 2k^2}\right\} \qquad (3.32)$$

This approximation is therefore given with a truncation error of $0(k^4)$.

(iii) Four point formula

By eliminating $\left(\frac{\partial^3 \Psi^*}{\partial \xi^3}\right)_{i,1}$ and $\left(\frac{\partial^4 \Psi^*}{\partial \xi^4}\right)_{i,1}$ between the three equations (3.27) to (3.29) it is easy to show that:

$$108\Psi^*_{i,2} - 27\Psi^*_{i,3} + 4\Psi^*_{i\,4} = 66k\left(\frac{\partial \Psi^*}{\partial \xi}\right)_{i,1} + 18k^2\left(\frac{\partial^2 \Psi^*}{\partial \xi^2}\right)_{i,1}$$

and by using the boundary condition for the tangential stress as above, it follows that:

$$\zeta^*_{i,1} = \frac{1}{\pi^2}\left\{ \frac{108\,\Psi^*_{i,2} - 27\,\Psi^*_{i,3} + 4\,\Psi^*_{i,4}}{\frac{33k}{\pi} + 18k^2} \right\} \qquad (3.33)$$

the truncation of error being of $0(k^5)$.

When the different formulae were tested in the calculation of equation (3.8) the following results were obtained:

(i) The two point formula (3.31) was found to be a very bad approximation, the A.D.I. procedure being divergent in this case.

(ii) Although the approximation to surface vorticity by three and four point formulae were nearly identical, it was found that the rate of convergence obtained with a four point formula was slightly faster. A trial made with a five point formula (not shown in the above derivation) showed no significant improvement on a four point formula.

It was therefore decided to use equation (3.33) as the approximation of surface vorticity.

Furthermore, to improve the convergence of the procedure it is convenient to under-relax the surface vorticity. This consists in estimating the surface vorticity at step (n + 1) from the values obtained at step (n) and the values which would be obtained in the normal way. For this we rewrite the surface vorticity as:

$$\bar{\zeta}^{*(n+1)}_{i,1} = (1-\omega_v)\,\zeta^{*(n)}_{i,1} + \omega_v\,\zeta^{*(n+1)}_{i,1} \qquad (3.34)$$

where ω_v is a relaxation factor with $0 < \omega_v \leqslant 1$.
Thus if we need a very slow variation of the surface vorticity we can set ω_v to a low value. The numerical value of ω_v has to be found by numerical experimentation (Gosman et al. (95)).

3.5 Calculation Procedure

The procedure of calculation follows directly from the derivations in the previous sections:

(i) At the start of the computation, the stream function field is assumed to be that of potential flow as indicated in section 3.4.1. The vorticity field is assumed to be $\zeta^*_{i,j} = 0$ everywhere except on the surface of the bubble where initial values are approximated by a four-point formula (section 3.4.2).

(ii) A new approximation to the stream function is then calculated by the over-relaxation method. The criterion for convergence was taken as:

$$\frac{\left|\Psi^{*\,(p+1)}_{i,j} - \Psi^{*\,(p)}_{i,j}\right|}{\left|\Psi^{*\,(p+1)}_{i,j}\right|} < \varepsilon \qquad \text{for all i and j}$$

By trial and error, the most satisfactory value for ε was found to be $\varepsilon = 10^{-3}$.

(iii) The A.D.I. method is then started for the vorticity equation. New estimations of the vorticity are calculated along lines r = cst at the first half step, whilst the values of the surface vorticity are taken equal to the original ones.

The procedure is repeated in the second direction again with the original values of the surface vorticity.

Then the new stream function field is calculated by over-relaxation and a new estimation of surface vorticity is therefore obtained by the four-point formula.

(iv) The A.D.I. method was repeated until the following criterion for convergence was satisfied:

$$\frac{\left|\zeta^{*(n+1)}_{i,1} - \zeta^{*(n)}_{i,1}\right|}{\left|\zeta^{*(n+1)}_{i,1}\right|} < \varepsilon_1$$

Recently Griffin and Meisen (96) have presented an analysis of some convergence criteria for relaxation solutions of viscous flow around a circular cylinder. The above criterion, according to these authors, is satisfactory although not the best one. In the present case it was sufficient to apply it only to surface vorticity values (i.e. at points (i,1)). In fact, if one applies this criterion to the entire field, difficulties appear at high Reynolds number due to the accumulation of roundoff errors at the rear of the bubble.

In addition it was found that at high Reynolds number (say $Re > 50$) some variables, like the drag coefficient C_D, were still oscillating even after the convergence criterion was satisfied.

In these cases the iterations were continued until C_D was steady. A value of $\varepsilon_1 = 10^{-3}$ was used throughout the calculation.

(v) After a certain fixed number of iterations the results for the streamfunction and vorticity were printed out in order to check the progress of the calculation.

(vi) At the end of calculation all the variables needed were calculated.

For example, with $\underline{v}$, γ , $\underline{u}$, the gas stream function χ the drift of a particle X, etc. ....

Thirteen cases with Reynolds numbers ranging from Re = 0.01 to Re = 200 were calculated, requiring in all about 3.2 hours of computing time on the Imperial College C.D.C. 6400 Computer.

3.6. Pressure Variations

To compare the above theory with existing ones and with experiment it is interesting to calculate important variables such as the pressure variations.

Let us consider equation (2.12) as given in the preceding chapter:

$$\rho_p(1-\varepsilon)(\underline{v}\cdot\underline{\nabla})\underline{v} = -\underline{\nabla}P + \mu_p\nabla^2\underline{v} \qquad (2.12)$$

in which, as noted, P measures the difference in pressure between two points on the same horizontal line.

We shall only concentrate on pressure variations along the axis of rise of the bubble and around its surface.

3.6.1. Pressure variations along the axis of the bubble

Let us consider the dimensionless form of equation (2.12):

$$(\underline{v}^*\cdot\underline{\nabla}^*)\underline{v}^* = -\frac{1}{2}\underline{\nabla}^*P^* + \frac{2}{R_e}\nabla^{*2}\underline{v}^* \qquad (2.29)$$

The ρ component can be written as:

$$v_\rho^* \frac{\partial v_\rho^*}{\partial \rho} + \frac{v_\theta^*}{\rho} \frac{\partial v_\rho^*}{\partial \theta} - \frac{v_\theta^{*2}}{\rho} = -\frac{1}{2} \frac{\partial P^*}{\partial \rho} + \frac{2}{Re}\left\{\frac{\partial^2 v_\rho^*}{\partial \rho^2} + \frac{1}{\rho} \frac{\partial v_\rho^*}{\partial \rho} - \frac{v_\rho^*}{\rho^2}\right.$$

$$\left. + \frac{1}{\rho^2} \frac{\partial^2 v_\rho^*}{\partial \theta^2} - \frac{2}{\rho^2} \frac{\partial v_\theta^*}{\partial \theta}\right\} \qquad (3.35)$$

In addition let us rewrite the continuity equation and vorticity component:

$$\rho \frac{\partial v_\rho^*}{\partial \rho} + v_\rho^* + \frac{\partial v_\theta^*}{\partial \theta} = 0 \qquad \text{continuity}$$

$$\zeta^* = \frac{\partial v_\theta^*}{\partial \rho} + \frac{v_\theta^*}{\rho} - \frac{1}{\rho} \frac{\partial v_\rho^*}{\partial \theta} \qquad \text{vorticity}$$

Differentiating the continuity equation with respect to ρ and the vorticity component with respect to θ and combining the two equations leads to:

$$\frac{\partial \zeta^*}{\partial \theta} = \frac{1}{\rho} \frac{\partial v_\theta^*}{\partial \theta} - \frac{1}{\rho} \frac{\partial^2 v_\rho^*}{\partial \theta^2} - 2 \frac{\partial v_\rho^*}{\partial \rho} - \rho \frac{\partial^2 v_\rho^*}{\partial \rho^2}$$

By combining the above equation and the continuity equation into (3.35) it follows that:

$$\left\{v_\rho^* \frac{\partial v_\rho^*}{\partial \rho} + \frac{v_\theta^*}{\rho} \frac{\partial v_\rho^*}{\partial \theta} - \frac{v_\theta^{*2}}{\rho}\right\} = \frac{1}{2} \frac{\partial P^*}{\partial \rho} + \frac{2}{Re}\left\{-\frac{1}{\rho} \frac{\partial \zeta^*}{\partial \theta}\right\}$$

along the axis of symetry $v_\theta^* = 0$, thus:

$$\left\{v_\rho^* \frac{\partial v_\rho^*}{\partial \rho} = -\frac{1}{2} \frac{\partial P^*}{\partial \rho} - \frac{2}{Re} \frac{1}{\rho} \frac{\partial \zeta^*}{\partial \theta}\right\}_{\theta = 0, \pi} \qquad (3.36)$$

Figure 3.3 shows the paths of integration for equation (3.36).

(i) Integration above the bubble $\theta = 0$

Equation (3.36) is integrated between A and the current point X.

$$\frac{1}{2}\left(P^*_A - P^*_X\right) + \frac{1}{2}\left(v^{*2}_{\rho A} - v^{*2}_{\rho X}\right) = -\frac{2}{Re}\int_{\rho_X}^{\rho_A} \frac{1}{\rho}\left.\frac{\partial \zeta^*}{\partial \theta}\right|_{\theta=0} d\rho$$

by taking A on the outer boundary of the flow (i.e. : $\rho_A = \rho_\infty$), then $v^*_{\rho A} = 1$ and $P^*_A = 0$.

Let us call $\Delta P^*_1 = P^*_X = P^*_X - P^*_A$, thus:

$$\Delta P^*_1 = 1 - v^{*2}_{\rho X} + \frac{4}{Re}\int_{\rho_X}^{\rho_\infty} \frac{1}{\rho}\left.\frac{\partial \zeta^*}{\partial \theta}\right|_{\theta=0} d\rho \qquad (3.37)$$

In the transformed plane the above equation can be written as:

$$\Delta P^*_1 = 1 - \frac{1}{E^2}\left\{\left.\frac{\partial \Psi^*}{\partial \eta}\right|_{\eta=o}\right\}^2 + \frac{4}{Re}\int_{\xi}^{\xi_\infty} \left.\frac{\partial \zeta^*}{\partial \eta}\right|_{\eta=0} d\xi \qquad (3.38$$

To calculate the two derivatives $\frac{\partial \Psi^*}{\partial \eta}$ and $\frac{\partial \zeta^*}{\partial \eta}$ we make use of finite differences using a four-point formula. By writing $\Psi^*_{i,j}$ in Taylor expansion around points (1, j) (i.e. around $\eta = 0$) for $i = 2, 3, 4$ it is easy to show that:

$$\left.\frac{\partial \Psi^*}{\partial \eta}\right|_{1,j} = \frac{18\,\Psi^*_{2,j} - 9\,\Psi^*_{3,j} + 2\,\Psi^*_{4,j}}{61} \qquad (3.39)$$

and:

$$\left.\frac{\partial \zeta^*}{\partial \eta}\right|_{1,j} = \frac{18\,\zeta^*_{2,j} - 9\,\zeta^*_{3,j} + 2\,\zeta^*_{4,j}}{61} \qquad (3.40)$$

In the above derivation we have made use of the boundary conditions:

$$\Psi^*_{1,j} = 0 \qquad \zeta^*_{1,j} = 0$$

The integral $\int_{\xi}^{\xi_\infty} \left.\frac{\partial \zeta^*}{\partial \eta}\right|_{1,j} d\xi$ is then calculated using the trapezoidal rule.

Note that when X is at point P (see Figure 3.3) we get the stagnation pressure (often denoted by k_o) thus:

$$k_o = 1 + \frac{4}{Re} \int_0^{\xi_\infty} \left.\frac{\partial \zeta^*}{\partial \eta}\right|_{1,j} d\xi \qquad (3.41)$$

(ii) Integration below the bubble $\theta = \pi$

Equation (3.36) is now integrated between Q and the current point Y as shown on Figure 3.3.

$$\frac{1}{2}\left(P^*_Y - P^*_Q\right) + \frac{1}{2}\left(v^{*2}_{\rho Y} - v^{*2}_{\rho Q}\right) = -\frac{2}{Re}\int_{\rho_Q}^{\rho_Y} \frac{1}{\rho}\left.\frac{\partial \zeta^*}{\partial \theta}\right|_{\theta=\pi} d\rho$$

at point Q which is the rear stagnation point $v^*_{\rho Q} = 0$ and $\rho_Q = 1$, thus:

$$\Delta P^*_3 = P^*_Y - P^*_Q = -v^{*2}_{\rho Y} - \frac{4}{Re} \int_1^{\rho_Y} \frac{1}{\rho} \frac{\partial \zeta^*}{\partial \theta} \Big|_{\theta=\pi} d\rho \qquad (3.42)$$

which can be written as:

$$\Delta P^*_3 = -\frac{1}{E^2} \left\{ \frac{\partial \Psi^*}{\partial \eta} \Big|_{\eta=1} \right\}^2 - \frac{4}{Re} \int_0^{\xi} \frac{\partial \zeta^*}{\partial \eta} \Big|_{\eta=1} d\xi$$

To calculate the derivatives we use the same type of approximation as in the above section (i). The expansion is now made around points (n, j) (i.e. around $\eta = 1$) and backwards differences are used. Therefore:

$$\frac{\partial \Psi^*}{\partial \eta}\Big|_{n,j} = \frac{-18\,\Psi^*_{n-1,j} + 9\,\Psi^*_{n-2,j} - 2\,\Psi^*_{n-3,j}}{61} \qquad (3.43)$$

$$\frac{\partial \zeta^*}{\partial \eta}\Big|_{n,j} = \frac{-18\,\zeta^*_{n-1,j} + 9\,\zeta^*_{n-2,j} - 2\,\zeta^*_{n-3,j}}{61} \qquad (3.44)$$

Again we used the boundary conditions $\Psi^*_{n,j} = 0$ and $\zeta^*_{n,j} = 0$ and the integral in (3.42) is calculated using the trapezoidal rule.

3.6.2. Pressure variations on the bubble surface

As noted in the preceding chapter, by assuming a circular shape to the bubble, it is impossible to ensure the constant pressure condition at its surface. Thus there is a theoretical pressure change around the bubble surface which we shall compute in order to compare it with Jackson's and Murray's theory of bubble motion.

Let us consider the tangential component of equation (2.29).

$$v_\rho^* \frac{\partial v_\theta^*}{\partial \rho} + \frac{v_\theta^*}{\rho} \frac{\partial v_\theta^*}{\partial \theta} + \frac{v_\rho^* v_\theta^*}{\rho} = -\frac{1}{2}\frac{1}{\rho}\frac{\partial P^*}{\partial \theta} + \frac{2}{Re}\left\{\frac{\partial^2 v_\theta^*}{\partial \rho^2} + \frac{1}{\rho}\frac{\partial v_\theta^*}{\partial \rho} - \frac{v_\theta^*}{\rho^2} + \frac{1}{\rho^2}\frac{\partial^2 v_\theta^*}{\partial \theta^2} + \frac{2}{\rho^2}\frac{\partial v_\rho^*}{\partial \theta}\right\} \qquad (3.45)$$

The same type of derivation is used as in the previous section 3.5.1. We differentiate the continuity equation with respect to θ and the vorticity component with respect to ρ. Combining the two equations:

$$\frac{\partial \zeta^*}{\partial \rho} = \frac{\partial^2 v_\theta^*}{\partial \rho^2} + \frac{1}{\rho}\frac{\partial v_\theta^*}{\partial \rho} - \frac{v_\theta^*}{\rho^2} + \frac{2}{\rho^2}\frac{\partial v_\rho^*}{\partial \theta} + \frac{1}{\rho^2}\frac{\partial^2 v_\theta^*}{\partial \theta^2}$$

Using the above equation and the continuity equation, (3.45) becomes:

$$v_\rho^* \frac{\partial v_\theta^*}{\partial \rho} + \frac{v_\theta^*}{\rho}\frac{\partial v_\theta^*}{\partial \theta} + \frac{v_\rho^* v_\theta^*}{\rho} = -\frac{1}{2}\frac{1}{\rho}\frac{\partial P^*}{\partial \theta} + \frac{2}{Re}\frac{\partial \zeta^*}{\partial \rho}$$

at the surface of the bubble $v_\rho^* = 0$ and $\rho = 1$, thus:

$$v_\theta^* \frac{\partial v_\theta^*}{\partial \theta} = -\frac{1}{2}\frac{\partial P^*}{\partial \theta} + \frac{2}{Re}\frac{\partial \zeta^*}{\partial \rho} \qquad (3.46)$$

This equation can be integrated from the front stagnation point P to a current point S on the surface as shown on Figure 3.3.

$$\Delta P_2^* = P_S^* - P_P^* = v_{\theta P}^{*2} - v_{\theta S}^{*2} + \frac{4}{Re}\int_0^\theta \left.\frac{\partial \zeta^*}{\partial \rho}\right|_{\rho=1} d\theta$$

at the stagnation point P, $v^*_{\theta P} = 0$ therefore:

$$\Delta P_2^* = - v^{*2}_{\theta S} + \frac{4}{Re} \int_0^{\theta} \left. \frac{\partial \zeta^*}{\partial \rho} \right|_{\rho = 1} d\theta \qquad (3.47)$$

In the transformed plane this can be written as:

$$\Delta P_2^* = - \frac{1}{E^2} \left\{ \left. \frac{\partial \Psi^*}{\partial \xi} \right|_{\xi = 0} \right\}^2 + \frac{4}{Re} \int_0^{\eta} \left. \frac{\partial \zeta^*}{\partial \xi} \right|_{\xi = 0} d\eta \qquad (3.48)$$

The same type of calculation for the derivatives $\frac{\partial \Psi^*}{\partial \xi}$ and $\frac{\partial \zeta^*}{\partial \xi}$ is used as in the previous sections.

By expanding $\Psi^*_{i,j}$ and $\zeta^*_{i,j}$ around points (i, 1) (i.e. around $\xi = 0$) we have:

$$\left. \frac{\partial \Psi^*}{\partial \xi} \right|_{i,1} = \frac{18 \Psi^*_{i,2} - 9 \Psi^*_{i,3} + 2 \Psi^*_{i,4}}{6k} \qquad (3.49)$$

$$\left. \frac{\partial \zeta^*}{\partial \xi} \right|_{i,1} = \frac{-11 \zeta^*_{i,1} + 18 \zeta^*_{i,2} - 9 \zeta^*_{i,3} + 2 \zeta^*_{i,4}}{6k} \qquad (3.50)$$

The boundary condition $\Psi^*_{i,1} = 0$ has been used and the integral in (3.48) is again calculated by the trapezoidal rule.

The entire pressure drop around the surface gives the value of the pressure at the rear stagnation point (often denoted as k_1).

$$\Delta P_2^* = P^*_Q - P^*_P = \frac{4}{Re} \int_0^{\pi} \left. \frac{\partial \zeta}{\partial \xi} \right|_{\xi = 0} d\eta$$

for $v^*_{\theta Q} = 0$

as $P^*_P = k_o$ thus:

$$P^*_Q = k_1 = k_o + \frac{4}{Re} \int_0^{\pi} \left. \frac{\partial \zeta}{\partial \xi} \right|_{\xi = 0} d\eta \qquad (3.51)$$

3.7. Drag Coefficient

In addition to the pressure variations it is equally interesting to know the variation of the drag coefficient as a function of the Reynolds number. This can be compared with the experimental data for gas bubbles rising in a viscous liquid.

We define the drag coefficient as:

$$C_D = \frac{\text{drag force}}{\text{cross section area} \times \frac{1}{2} \rho_p (1-\varepsilon) U_b^2}$$

For a gas bubble rising in a liquid the total drag coefficient C_D arises from two effects: $C_D = C_{DV} + C_{DP}$

C_{DV} : the viscous drag coefficient

C_{DP} : the pressure drag coefficient (i. e. the normal stress contribution)

In the present case with a zero tangential-stress boundary condition:

$$C_{DV} = \int_0^{\pi} \frac{\tau_{r\theta} \left| \right. r = a}{\frac{1}{2} \rho_p (1-\varepsilon) U_b^2} d\theta = 0$$

Thus the only contribution is due to the pressure drag coefficient.

$$C_D = C_{DP}$$

As indicated in Appendix 1 the normal stress is defined as:

$$\tau_{rr} = P - 2\mu_p \frac{\partial v_r}{\partial r}$$

As shown on Figure 3.3 the pressure drag force will be :

$$F = \int_0^{\pi} r\, \tau_{rr} \cos\theta \, d\theta$$

and therefore the pressure drag coefficient

$$C_{DP} = \frac{\int_0^{\pi} r\, \tau_{rr} \cos\theta \, d\theta}{\frac{1}{2} \rho_p (1-\epsilon) U_b^2}$$

or in dimensionless quantities:

$$C_{DP} = \int_0^{\pi} P_S^* \cos\theta \, d\theta - \frac{8}{Re} \int_0^{\pi} \left. \frac{\partial v_\rho^*}{\partial \rho} \right|_{\rho=1} d\theta$$

In addition we have $\left. \frac{\partial v_\rho^*}{\partial \rho} \right|_{\rho=1} = \left. \frac{\partial^2 \Psi^*}{\partial \rho \, \partial \theta} \right|_{\rho=1}$ and therefore in the transformed plane:

$$C_{DP} = \pi \int_0^1 P_S^* \cos(\pi\eta) \, d\eta - \frac{8}{\pi Re} \int_0^1 \left. \frac{\partial^2 \Psi^*}{\partial \xi \, \partial \eta} \right|_{\xi=0} d\eta \qquad (3.52)$$

The second derivative in equation (3.52) is calculated by a twelve-point formula as shown on Figure 3.4

We can, in fact write $\frac{\partial^2 \Psi^*}{\partial \xi \, \partial \eta} = \frac{\partial}{\partial \xi}\left(\frac{\partial \Psi^*}{\partial \eta}\right)$ and $\frac{\partial}{\partial \xi}$ is calculated by a four-point formula as done in the calculation of the pressure variations, while $\frac{\partial \Psi^*}{\partial \eta}$ is simulated by central difference.

Thus:

$$\frac{\partial}{\partial \xi}\left(\frac{\partial \Psi^*}{\partial \eta}\right) = \frac{-11 \left.\frac{\partial \Psi^*}{\partial \eta}\right|_{i,1} + 18 \left.\frac{\partial \Psi^*}{\partial \eta}\right|_{i,2} - 9 \left.\frac{\partial \Psi^*}{\partial \eta}\right|_{1,3} + 2 \left.\frac{\partial \Psi^*}{\partial \eta}\right|_{i,4}}{6k}$$

with $\left.\frac{\partial \Psi^*}{\partial \eta}\right|_{i,j} = \frac{\Psi^*_{i+1,j} - \Psi^*_{i-1,j}}{2l}$

The two integrals in C_{DP} are then calculated using the trapezoidal rule.

3.8. Particle Drift

As mentioned in Chapter 1 one important variable, that may be used in the comparison between theory and experiments, is the particle drift, i. e. the particle displacement caused by the rising bubble as seen by a stationary observer.

A summary of previous works concerning the calculation of particle drift in the two limiting cases of potential flow and Stokes's flow is given in the first chapter. Experimental results are given in a later section.

We concentrate here on the theoretical drift obtained with the solution of the vorticity and stream function equations.

For this, let us consider a bubble rising with steady velocity in the fluidised bed and let us call:

(i) O, x, y, the coordinate systems with axes fixed with respect to the bubble.

(ii) O', X, Y, the coordinate system with axes fixed with respect to the particles.

Furthermore let us consider the origin of time t = 0 when O and O' coincide.

Thus, (O, x, y) is moving with an upwards velocity U_b with respect to (O', X, Y) and the following relations hold:

$$\left.\begin{aligned} X &= x + U_b t \\ Y &= y \\ t &= \frac{X-x}{U_b} \end{aligned}\right\} \quad (3.53)$$

Up to now we have been considering the solution of the particle flow past a cylinder with respect to the system (O, x, y) (i.e. a Laplacian point of view).

We have $\frac{dx}{dt} = v_x = -\frac{\partial \Psi}{\partial y}$

and from (3.53) :

$$\frac{dX}{dt} = \frac{dx}{dt} + U_b$$

whence:

$$dX = \left\{ -\frac{\partial \Psi}{\partial y} + U_b \right\} dt \qquad (3.54)$$

We also have $v_\theta = r\frac{d\theta}{dt} = \frac{\partial \Psi}{\partial r}$

$$\text{or :} \quad dt = \frac{r\,d\theta}{\frac{\partial \Psi}{\partial r}}$$

Using the expression for dt into equation (3.54) leads to :

$$dX = \left\{ -\frac{\partial \Psi}{\partial y} + U_b \right\} \frac{r d\theta}{\frac{\partial \Psi}{\partial r}} \qquad (3.55)$$

The drift X at a particular instant t is given by the integration of equation (3.54) from t = 0 to t.

$$X = \int_0^t \left\{ -\frac{\partial \Psi}{\partial y} + U_b \right\} dt \qquad (3.56)$$

In the above equation t can be positive or negative. When the bubble is well under point O' then $t \rightarrow -\infty$, when it is well above $t \rightarrow +\infty$.

In terms of polar coordinates the drift is given by (3.55)

$$X = \int_{\frac{\pi}{2}}^{\theta} \left\{ -\frac{\partial \Psi}{\partial y} + U_b \right\} \frac{r d\theta}{\frac{\partial \Psi}{\partial r}} \qquad (3.57)$$

From Figure 3.5 it is easy to establish the following relations:

$$v_y = v_r \sin\theta + v_\theta \cos\theta$$

$$v_x = v_r \cos\theta - v_\theta \sin\theta$$

Using the stream function Ψ, the above relations become:

$$\frac{\partial \Psi}{\partial x} = -\frac{1}{r} \frac{\partial \Psi}{\partial \theta} \sin\theta + \frac{\partial \Psi}{\partial r} \cos\theta$$

$$\frac{\partial \Psi}{\partial y} = \frac{1}{r}\frac{\partial \Psi}{\partial \theta}\cos\theta + \frac{\partial \Psi}{\partial r}\sin\theta$$

Replacing $\frac{\partial \Psi}{\partial y}$ in equation (3.57) gives :

$$X = \int_{\frac{\pi}{2}}^{\theta} \left\{ \frac{U_b r}{\frac{\partial \Psi}{\partial r}} - r\sin\theta - \frac{\frac{\partial \Psi}{\partial \theta}}{\frac{\partial \Psi}{\partial r}}\cos\theta \right\} d\theta \qquad (3.58)$$

The particle drift in the x direction with respect to point O' is given by equation (3.58) for any angle θ. The complete drift being obtained by :

$$X = \int_{\frac{\pi}{2}}^{0} \left\{ ---- \right\} d\theta + \int_{\frac{\pi}{2}}^{\pi} \left\{ ---- \right\} d\theta$$

The derivatives $\frac{\partial \Psi}{\partial r}$ and $\frac{\partial \Psi}{\partial \theta}$ are easily computed from the solution for the stream function Ψ .

Furthermore we have :

$$Y = y$$

$$\text{or} \quad Y = r\sin\theta \qquad (3.59)$$

$$\text{and} \quad t = \frac{X - r\cos\theta}{U_b} \qquad (3.60)$$

The complete position of the particle with respect to axes O', X, Y, is therefore determined by X and Y. The parameter t gives the time at which a particular position (X, Y) is reached, the origin being when the particle is in O'.

Equations (3.58) to (3.60) can easily be written in the dimensionless form in which they are used in the computer program :

$$X^* = \int_{\frac{\pi}{2}}^{\theta} \left\{ \frac{\rho}{\frac{\partial \Psi^*}{\partial \rho}} - \rho \sin\theta - \frac{\frac{\partial \Psi^*}{\partial \eta}}{\frac{\partial \Psi^*}{\partial \rho}} \cos\theta \right\} d\theta$$

$$Y^* = \rho \sin\theta$$

$$\tau = X^* - \rho \cos\theta$$

3.9. Gas flow stream function

Once the solution for Ψ (and therefore for $\underline{v}$) has been obtained from the vorticity and stream function equations using the A.D.I. and the over-relaxation methods, the calculation of the gas velocity is straight forward using equation (2.38) as derived in Chapter 2

$$\underline{u}^* = \underline{v}^* - \frac{\gamma}{2} \frac{Fr}{\alpha_b} \underline{\nabla}^* P_f^* \qquad (2.38)$$

$$\text{with} \quad \underline{\nabla}^* P_f^* = \underline{\nabla}^* P^* + \frac{2}{Fr} \underline{i} \qquad (2.30)$$

Knowing the value of the gas velocity at each point of the grid, it is also interesting to calculate the corresponding stream function χ. For this we shall assume that, at the outer boundary of the flow, χ is known from the potential flow solution as given by Davidson and Harrison (10) :

$$\chi = \frac{U_b}{\alpha_b} r \sin\theta \left\{ (\alpha_b - 1) - \frac{a^2}{r^2} (\alpha_b + 1) \right\}$$

for $r = r_\infty$: $\frac{a^2}{r^2} \ll 1$ and therefore χ simplifies to :

$$\chi_\infty = U_b \frac{\alpha_b - 1}{\alpha_b} r_\infty \sin\theta$$

or in dimensionless form:

$$\overset{*}{\chi}_{i,n} = \overset{*}{\chi}_\infty = \frac{\alpha_b - 1}{\alpha_b} \rho_\infty \sin\theta \qquad (3.61)$$

Between two points (i, j) and (i, j+1) (Figure 3.6) the variation of the gas stream function $\Delta\chi$ represents the flow of gas through $(r_{j+1} - r_j)$. Along the radial direction there is no flow due to the r component of the velocity $\underline{u}$. Therefore :

$$\Delta\chi = \chi_{i,j+1} - \chi_{i,j} = \int_{r_j}^{r_{j+1}} u_\theta \, dr$$

To calculate this integral we shall assume a linear variation of the gas velocity between r_j and r_{j+1} :

$$u_\theta = \frac{u_{\theta,j+1} - u_{\theta,j}}{r_{j+1} - r_j} (r - r_j) + u_{\theta,j}$$

When obtaining the actual numerical values for u_θ , this was found to be a good approximation.

Therefore:

$$\chi_{i,j+1} - \chi_{i,j} = \frac{1}{2} (u_{\theta,j+1} - u_{\theta,j}) (r_{j+1} - r_j) .$$

Or in dimensionless form:

$$\overset{*}{\chi}_{i,j+1} - \overset{*}{\chi}_{i,j} = \frac{1}{2} (\overset{*}{u}_{\theta,j+1} - \overset{*}{u}_{\theta,j}) (\rho_{j+1} - \rho_j) \qquad (3.62)$$

Thus starting from $j+1 = n$ where the values of $\overset{*}{\chi}_{i,n}$ are known from equation (3.61) it is possible to calculate the values of $\chi_{i,j}$ for all the field.

3.10. Conclusion

The numerical procedure to obtain the solution of the equation of motion has been derived in this chapter. This allows the computer program to be written to calculate all the variables needed to compare with already existing theories and with the experimental data.

One of the main theoretical results concerns the drift of a particle. A great part of the experimental work has been devoted to the study of particle movement for bubbles at various Reynolds numbers.

A summary of the equations which have been used for the calculation of the different variables is indicated in Table 3.1 and in the following chapters a description of the theoretical results obtained is given.

TABLE 3.1

SUMMARY OF THE MAIN EQUATIONS

Stream function equation (S.O.R. method):

$$E^2 \zeta^* = \frac{\partial^2 \Psi^*}{\partial \eta^2} + \frac{\partial^2 \Psi^*}{\partial \xi^2}$$

Vorticity equation (A.D.I. method):

$$\frac{\partial \Psi^*}{\partial \xi} \frac{\partial \zeta^*}{\partial \eta} - \frac{\partial \Psi^*}{\partial \eta} \frac{\partial \zeta^*}{\partial \xi} = \frac{2}{Re} \left\{ \frac{\partial^2 \zeta^*}{\partial \eta^2} + \frac{\partial^2 \zeta^*}{\partial \xi^2} \right\}$$

Pressure variations:

- axis above the bubble $\Delta P_1^* = 1 - \frac{1}{E^2} \left\{ \frac{\partial \Psi^*}{\partial \eta} \Big|_{\eta=0} \right\}^2 + \frac{4}{Re} \int_{\xi}^{\xi_\infty} \frac{\partial \zeta^*}{\partial \eta} \Big|_{\eta=0} d\xi$

- axis below the bubble $\Delta P_3^* = - \frac{1}{E^2} \left\{ \frac{\partial \Psi^*}{\partial \eta} \Big|_{\eta=1} \right\}^2 - \frac{4}{Re} \int_{0}^{\xi} \frac{\partial \zeta^*}{\partial \eta} \Big|_{\eta=1} d\xi$

- on the bubble surface $\Delta P_2^* = - \frac{1}{E^2} \left\{ \frac{\partial \Psi^*}{\partial \xi} \Big|_{\xi=0} \right\}^2 + \frac{4}{Re} \int_{0}^{\eta} \frac{\partial \zeta^*}{\partial \xi} \Big|_{\xi=0} d\eta$

Drag coefficient: $$C_{DP} = \pi \int_0^1 P_s^* \cos(\pi\eta) d\eta - \frac{8}{\pi Re} \int_0^1 \frac{\partial^2 \Psi^*}{\partial \xi \partial \eta} \Big|_{\xi=0} d\eta$$

Particle drift:

$$X^* = \int_{\frac{\pi}{2}}^{\theta} \left\{ \frac{\rho}{\frac{\partial \Psi^*}{\partial \rho}} - \rho \sin\theta - \frac{\frac{\partial \Psi^*}{\partial \eta}}{\frac{\partial \Psi^*}{\partial \rho}} \cos\theta \right\} d\theta$$

$$Y^* = \rho \sin\theta$$

$$\tau = X^* - \rho \cos\theta$$

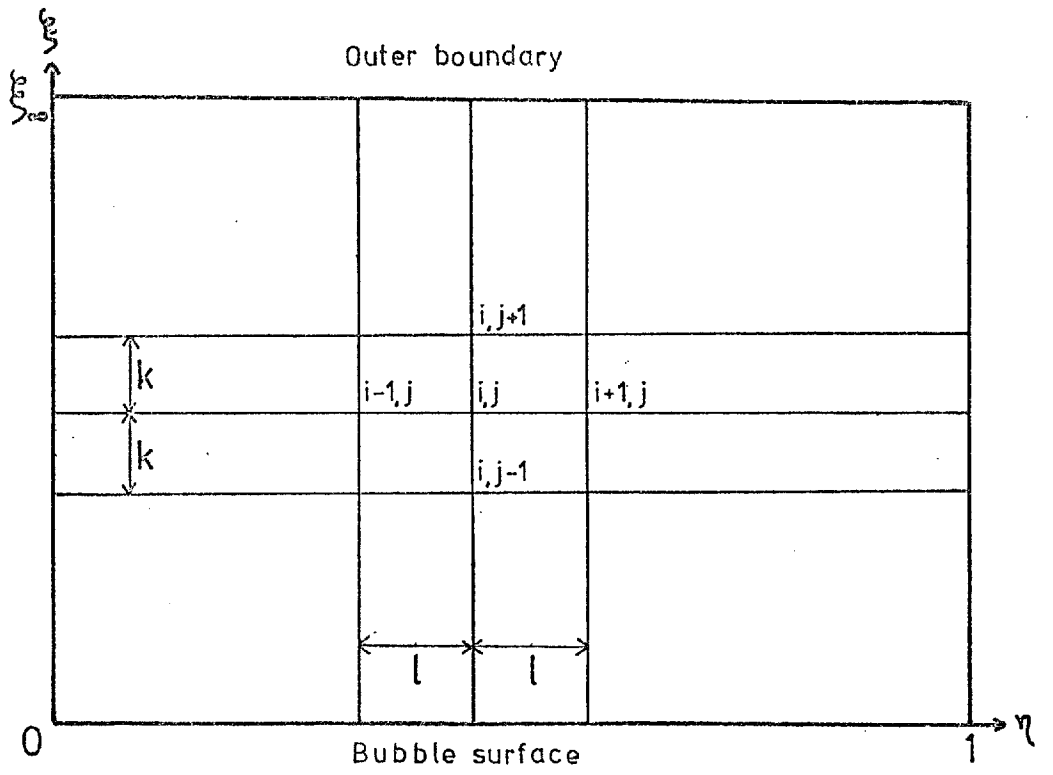


Figure 3-1 Grid of integration

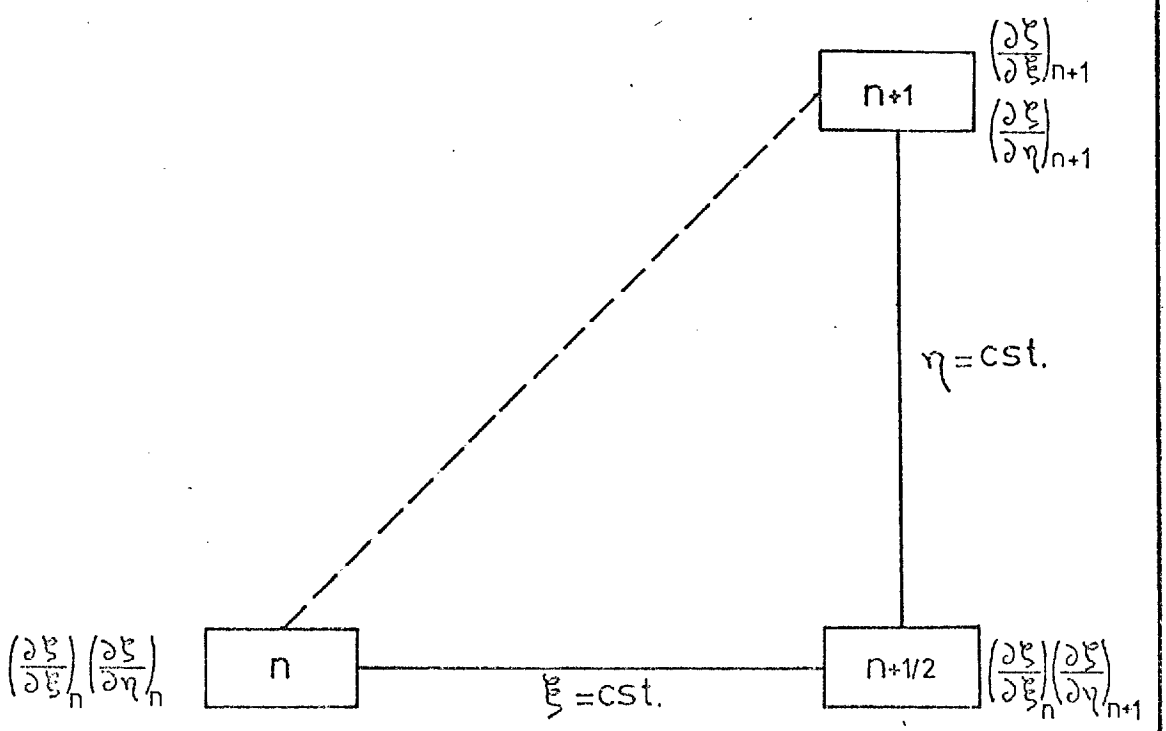


Figure 3-2 Procedure of iteration in the ADI method.

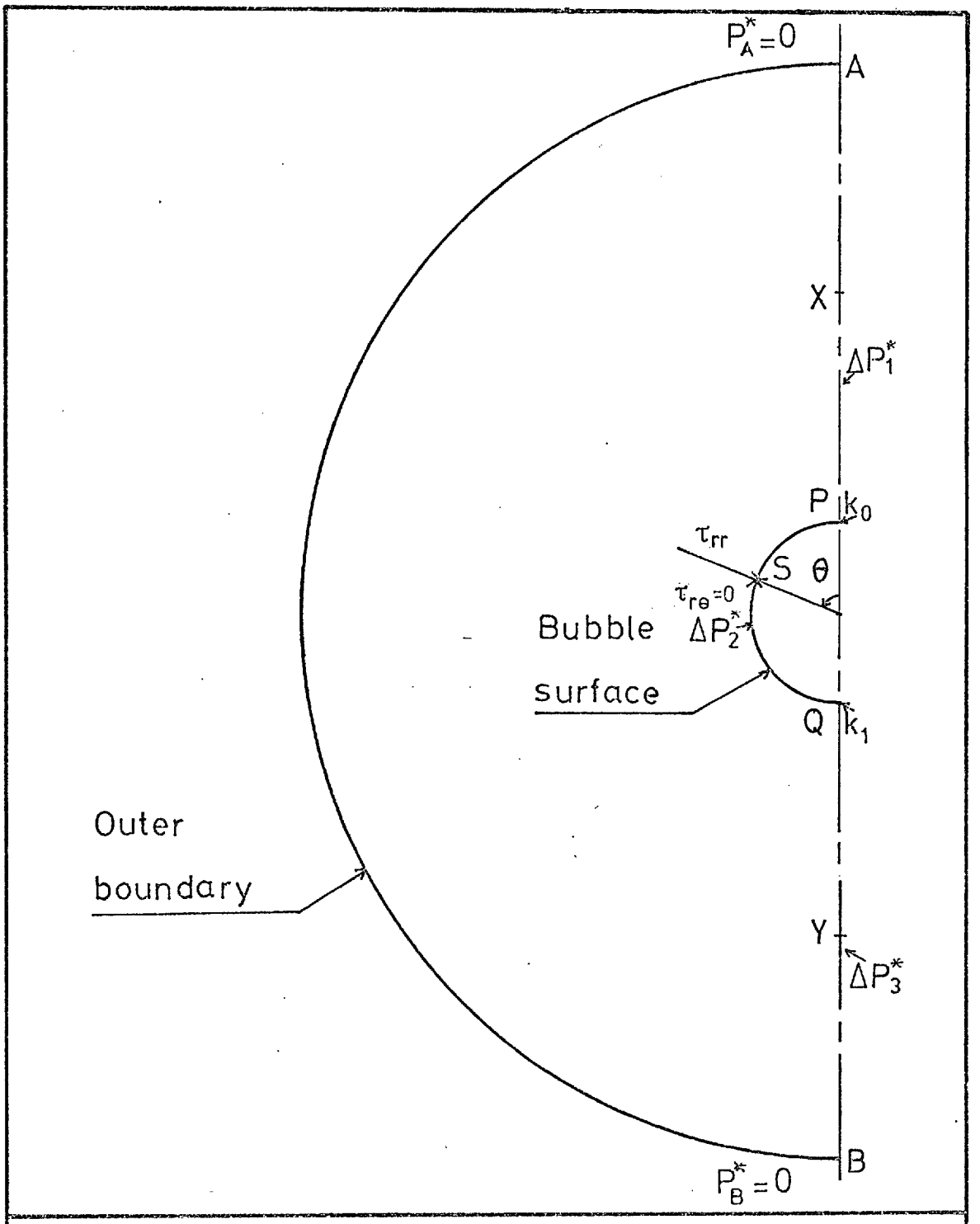


Figure 3-3 Pressure variations and drag coefficient calculation.

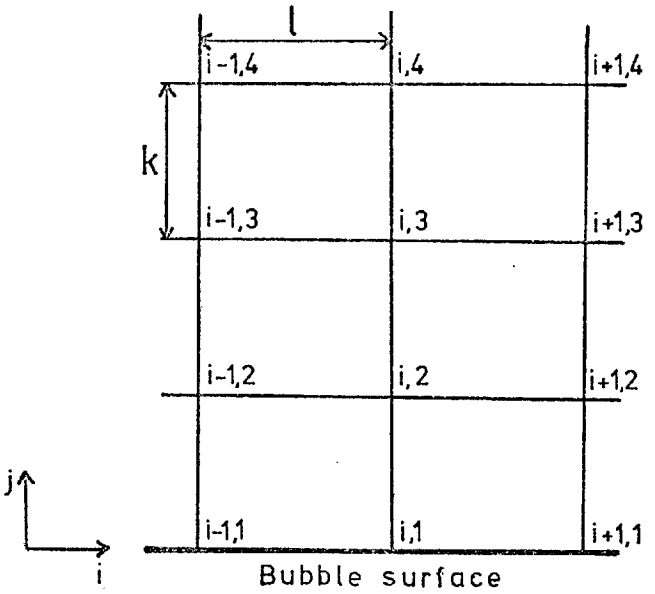


Figure 3-4 Calculation of second derivative in equation 3-52

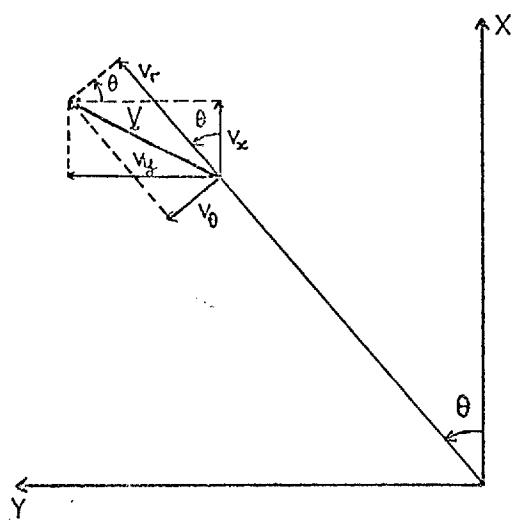


Figure 3-5
Velocity components

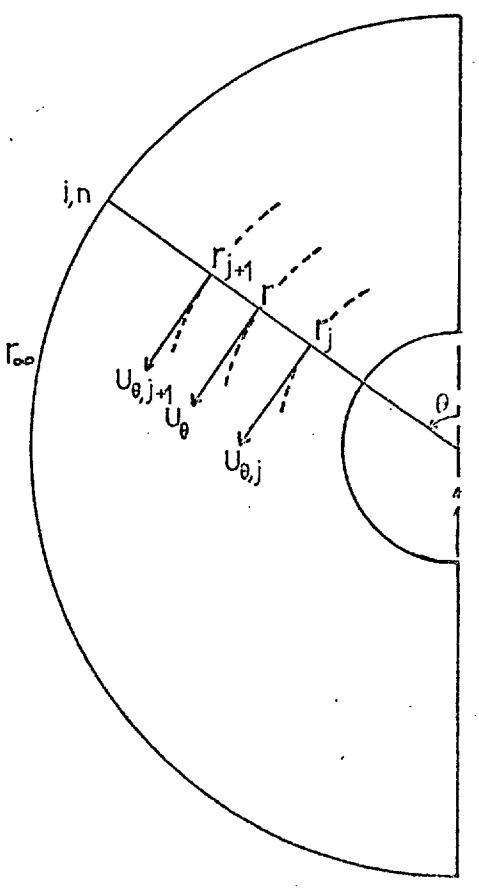


Figure 3-6 Evaluation of the gas stream-function

CHAPTER 4

EXPERIMENTAL

4.1 Experimental set-up

The two dimensional fluidised bed used throughout the experiments was constructed with two pieces of Armour plate glass, 1.27 cm thick. The dimensions of the apparatus were: 128 cm height x 48 cm large, the two plates being held 1.27 cm apart by two cork spacers. The apparatus was maintained on the sides of the plates by a set of "G. cramps".

Compressed air was supplied from a main line. It was first passed through a filter and then through a reducing valve. To prevent any oil from the main compressor being entrained in the apparatus, a second filter was installed on the line after the valve.

Clean air was then passed through a set of three rotameters with flow rate ranges as indicated below:

rotameter 1	1 - 10 l/mn
rotameter 2	5 - 60 l/mn
rotameter 3	12 - 120 l/mn

The air pressure measurement necessary for the calibration of the rotameters was recorded on a pressure gauge. Air was then passed through an humidifier necessary to keep electrostatic forces in the fluidised bed to a minimum. By controlling the temperature of the water it was also possible to maintain the air temperature to a constant value which is important in the measurement of interstitial air velocity as will be shown later. Air was finally injected in the bed through

the distributor made of a piece of porous plastic (Vyon) fixed to a brass vessel. In order to measure the pressure drop across the packing of particles, a hole was drilled, 12 cm from the distributor and connected to one end of a manometer filled with mercury.

An additional hole (12 cm from distributor) was drilled and used to inject artificial bubbles by a solenoid valve, the necessary air was being supplied from a separate compressed air cylinder.

Three sizes of Ballotini glass spheres were used in the experiments. Their characteristics are given in Table 4.1

Ballotini grade	Size range μ m	Density ρ_p (g/cm^3)	Apparent viscosity μ_p (poise)	Kinematic viscosity ν_p (cm^2/sec)	Minimum of fluid-isation U_o (cm/sec)
7	505-700	2.86	9.5(1)	3.32	34.3*
8	440-530	2.86	12(2)	4.2	25.6*
10	210-325	2.86	9(2)	3.14	8.9*

* values obtained from a curve : pressure drop v. s. superficial velocity

(1) viscosity value calculated by Grace (44)

(2) viscosity value measured by Schügerl (37)

Table 4.1 Characteristics of particles

4.2 Method of measurements

As indicated in the first chapter, particle displacements and gas velocity variations at the vicinity of a rising bubble were measured. The two.kinds of experiments were carried out separately with the two methods which will be now described.

(i) Particle movements

Particles in the fluidised bed were followed with the aid of black tracer particles (coloured with Nigrosine alcohol soluble dye). They were photographed with a Milliken D.B.M.5 high speed camera operated at 400 frames per second. Kodak Plus-X Negative films were used.

Depending on the size of the particles, the area filmed on the bed varied from 16 x 12 cm. for Ballotini grade 7 to 10 x 8 cm for Ballotini grade 10.

It was necessary to perform two kinds of experiments:

(a) In the first case, single artificial bubbles were injected through the solenoid valve. A typical experiment was carried out as follows: the high speed camera was first started and about one second later a bubble was injected. It was therefore ensured that, when the bubble was in the field of view, the camera was operating at a constant speed. A timing unit built in the camera, impressed the edge of the film with a frequency of 100 Hz. It was therefore possible to check the constancy and the value of the camera speed. The indicated value of 400 frames per second was found to be exact and reliable.

In all cases,to obtain stable bubbles,it was necessary to maintain the velocity of gas inside the bed below the minimum of fluidisation defined from the pressure drop v. s. flow rate curve. The flow rate was then adjusted so that the injected bubbles neither increased nor contracted. If this was not done,bubbles became elongated and particles falling from the roof caused the splitting of the bubble in

several parts. When the gas velocity was maintained below the minimum velocity of fluidisation, bubbles did not tend to elongate and splitting occurred less frequently.

In order to achieve a reasonable comparison with theory, it is important that the bubble shape does not depart too much from the assumed circular shape. In the case of bubble splitting, both sides were examined and each side considered as a separate bubble (Figure 4.1).

Furthermore only relatively small bubbles could be injected. It was not found possible to inject large bubbles which would remain stable.

This means that the Reynolds number ($Re = \frac{2aU_b(1-\varepsilon_o)}{\nu_p}$) for artificially injected bubbles remained small (< 20). In order to get bubbles with higher Reynolds number, a second set of experiments was performed.

(b) In this second part, the velocity of fluidising gas was maintained above minimum fluidisation velocity. Natural bubbles were thus rising from the distributor plate. The high speed camera was started and occasionally a single bubble, free from visible interaction from any neighbouring bubbles, was filmed. Those bubbles were much more stable than artificial ones and some of them had a high Reynolds number (~ 100). "Fingering" of particles could appear on the bubble sides but in most cases they did not produce any bubble splitting. Otherwise the bubble picture is the same as indicated on Figure 4.1.

In all cases the particle displacements were followed with the

aid of a P.C.D. digital motion analyser. Experimental results are presented in Chapter 5.

(ii) Gas velocity measurements

1) Choice of method

As indicated previously, gas velocities in a fluidised bed have been measured by two kinds of experiments:

- in the particulate phase, by following the displacement of gas tracer (Anwer (97), Rowe and Partridge (79)).

- in the bubble phase, throughflow velocities have been measured using a hot-wire anemometer placed inside an artificial bubble made of a fine wire gauze (Judd (98), Leung (99)).

The first method using the displacement of a gas tracer layer caused by a rising bubble, can only give results for measurements done on the axis of the bubble when there is only one component of the velocity; it is therefore a limited method. Furthermore as seen in Anwer's experimental results, the tracer gas tends to diffuse through the bed and one can hardly expect to measure a "point" variation of the velocity.

In the second method one introduces in the fluidised bed an artificial body which will deform the flow of particles; as seen in the second chapter the tangential shear stress on the bubble surface is zero. By introducing a solid surface one certainly modifies this boundary condition.

In this work by measuring the velocity of tracer particles falling from the bubble roof it has been possible to estimate a value for the throughflow velocity (Chapter 7).

However most attention has been devoted to the measurement of

gas velocity variations within the particulate phase. The experimental results are presented in Chapter 6 and the following discussion is concerned with the method of measurement which was used.

In order to obtain a reliable and precise measurement of the gas velocity it was decided to use a shielded hot-wire anemometer. Anemometry is one of the most successful and precise methods for the measurements of fluid velocity; once a proper calibration of the probe has been made, it gives a direct reading of the velocity - this is the main reason for which this method was selected.

It is obviously impossible to use an unprotected sensor within the bed since the movement of the particles would cause impacts on the wire and break it immediately. A shielding cage was therefore built around the wire and its description is given in the next paragraph. Commercial shielded hot wires (described for example in Ower and Pankurst (100)) are big (of the order of 1 cm or more) and would have therefore disturbed the flow. By using a standard probe and building a cage around it, the final dimensions were 3 x 3mm; this was assumed not to disturb the flow. When actually making the experiments, no bubbles induced by the presence of this foreign body could be seen.

As has already been mentioned, a precise calibration of the probe is required, and the procedure is described in Appendix 2.

2) Description of the anemometry system

The basic system used was a DISA 55 M 10 constant temperature anemometer with a standard 55 F11 probe, the sensor of which was 3 mm long. In Appendix 2 a description of the theory and a justification of the choice of constant temperature operation are given.

The protective cage around the sensor was made of a stainless steel wire, 190μ m (gauge 36) diameter, spiral-wound. The pitch in the spiral was calculated so that the whole voidage of the cage was close to that of the fluidised bed (i.e. $\sim \dot{0}\dot{4}$). The pitch was therefore 110 μm and was tested using a wire of known dimension of 114 μm (gauge 40) which could not pass between two loops of the spiral. The wire diameter of 190 μm was first chosen so that no particle in the smallest range of Ballotini (210 μm - 325 μm) could enter the cage and thus obstruct it or break the wire. Another possibility would have been to use a hot-film probe: in our problem the thin sensor film would certainly have been quickly erased by the friction of the particles.

By making the cage, as described above, (i.e. with a voidage of 0(0.4)) one ensures that the flow through it, is similar to that in the bulk of the particles, i.e. there is no preferential flow either inside or outside the cage.

The cage was cemented on both sides on two insulator plates made of epoxy resin laminate ("paxoline") which were fixed on the two leads of the probe. Care was taken to ensure that the protective cage and the two leads were not in contact.

The actual probe is pictured on plate 4.1.a and an enlargement of the protective cage on plate 4.1.b.

As noted previously the probe used was a standard DISA 55 F11 probe, and the characteristics are listed below in Table 4.2

Length of sensor	3mm
wire material	tungsten
wire diameter	5 μm
approximate wire resistance	8 Ω
overheating ratio(1)	0.8
maximum wire temperature	300°C

(1) See Appendix 2

Table 4.2. Hot wire probe characteristics

The probe was connected to the measurement bridge by a standard support (DISA 55 A 44) and a 5m cable.

3) Experimental set-up

In order to perform the measurements a set of holes (65 cm from distributor, 6.5 cm apart) were drilled in the rear plate of the bed. They provided housing for a plug in which the probe was fixed. Measurements could thus be done at various distances from the bubble center. A description of the experimental set-up is given in Figure 4.2. Before any experiment was started, the probe was calibrated (see Appendix 2), and the controls on the 55 M system were adjusted. The adjustment of the bridge balance was done by applying a square-ware current to the probe, which was exposed to a constant flow, the value of which was the maximum possible in the fluidised bed. Then, the controls were adjusted so that the response signal to the square-ware current did not show any damped oscillations on the screen of an oscilloscope connected to one of the output sockets

of the bridge ([7] on Figure 4.2). The gain and the H.F. filter of the system were then stepwise increased and further adjustments of the controls were performed at each step until adequate compensation to the oscillations could not be accomplished any more. The maximum values of the gain and H.F. filter were therefore reached. In all measurements within the fluidised bed, the interstitial gas Reynolds number (defined as $Re_f = \frac{d_p u}{\nu_f}$) remained small (< 100 in all cases). Therefore there is no turbulent component of the velocity and no particular demand on the bandwidth of the system is required. Thus by backing off the gain and H.F. filter switches, the system was offering a particularly stable operation.

The fluidised bed used in the experiments has already been described previously. The same camera (Milliken D.B.M. 5) as for the particle paths recordings was used and was operated at 64 frames per second.

As indicated on Figure 4.2 an injection unit [4] was employed to give a pulse of a given interval to a solenoid valve [11]. The air injected by the valve was supplied from a separate compressed air cylinder. The valve was fixed directly on the bed wall, so that when a pulse was given, a bubble was immediately injected into the bed. The injection unit was also connected to a U.V. recorder [5] and when a pulse was produced, a mark was made on the paper output of the recorder. Furthermore a flash [9] was connected to the injection unit and was illuminated when a pulse was produced; simultaneously a mark was recorded on the film in the camera. It was therefore ensured that the bubble rise in the bed, the output recording and the

camera were synchronized.

In a typical experiment the camera was first started so that it reached a steady speed before any bubble was injected. At the same time the U.V. recorder was started by an operator. A few seconds later a bubble was injected in the bed and at the same moment a flash discharge was produced and a mark made on the recorder output. When the bubble reached the top of the bed, the camera and recorder were stopped. The whole sequence of the recording was between 6 and 7 seconds.

As in the experiments for the particle movements, the flow of interstitial gas had to be maintained slightly under the minimum fluidisation velocity so that an injected bubble neither dilated nor contracted. By doing so,bubbles were much more stable.

Furthermore before any experiment was started, the fluidising air was turned on and allowed to bubble in the humidifier for some time. This ensured that temperature and humidity within the bed were constant and equal to those values obtained when calibrating the probe.

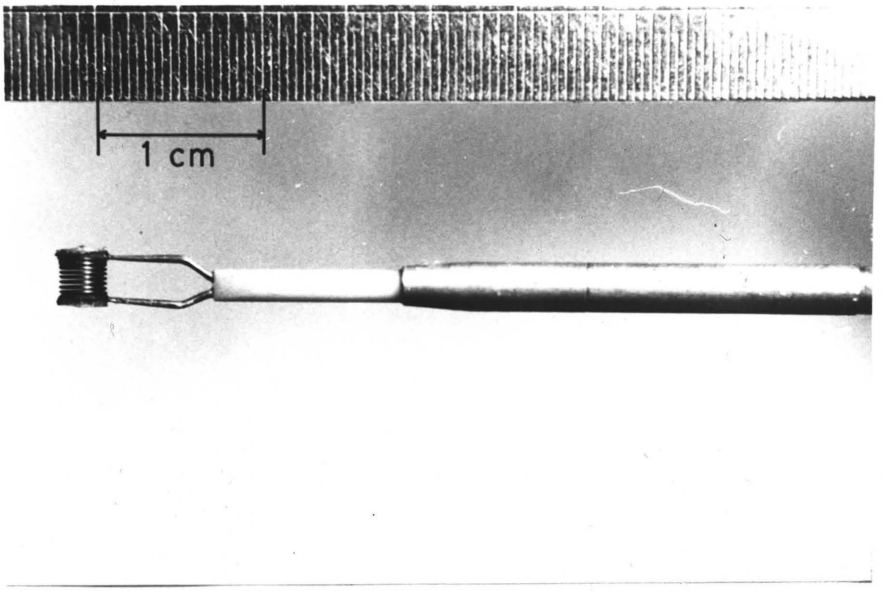


PLATE 4.1.a

Hot-wire probe

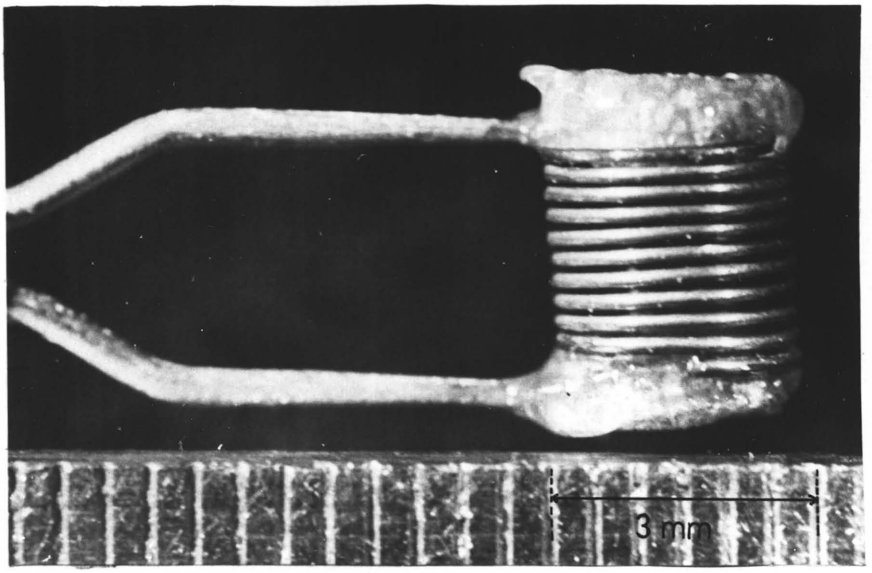
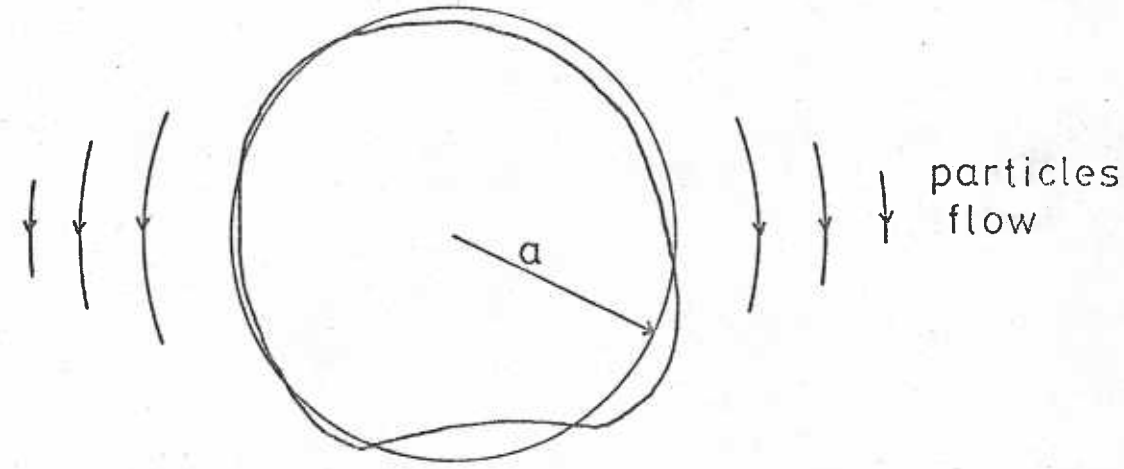
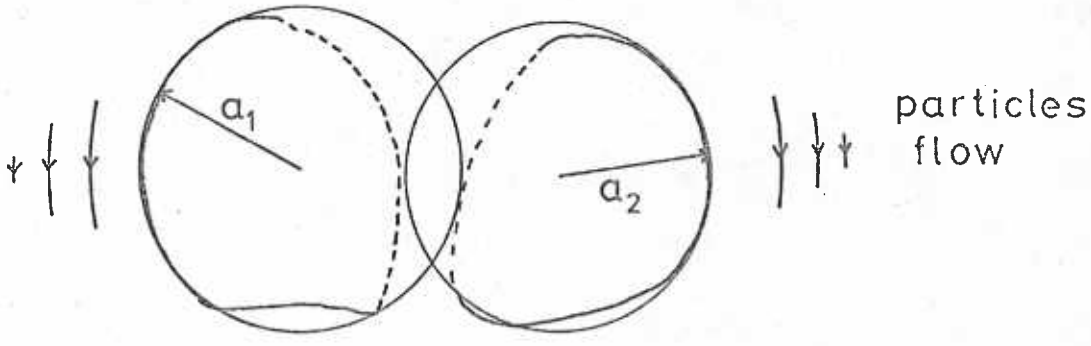


PLATE 4.1.b

Enlargement of the shielding cage

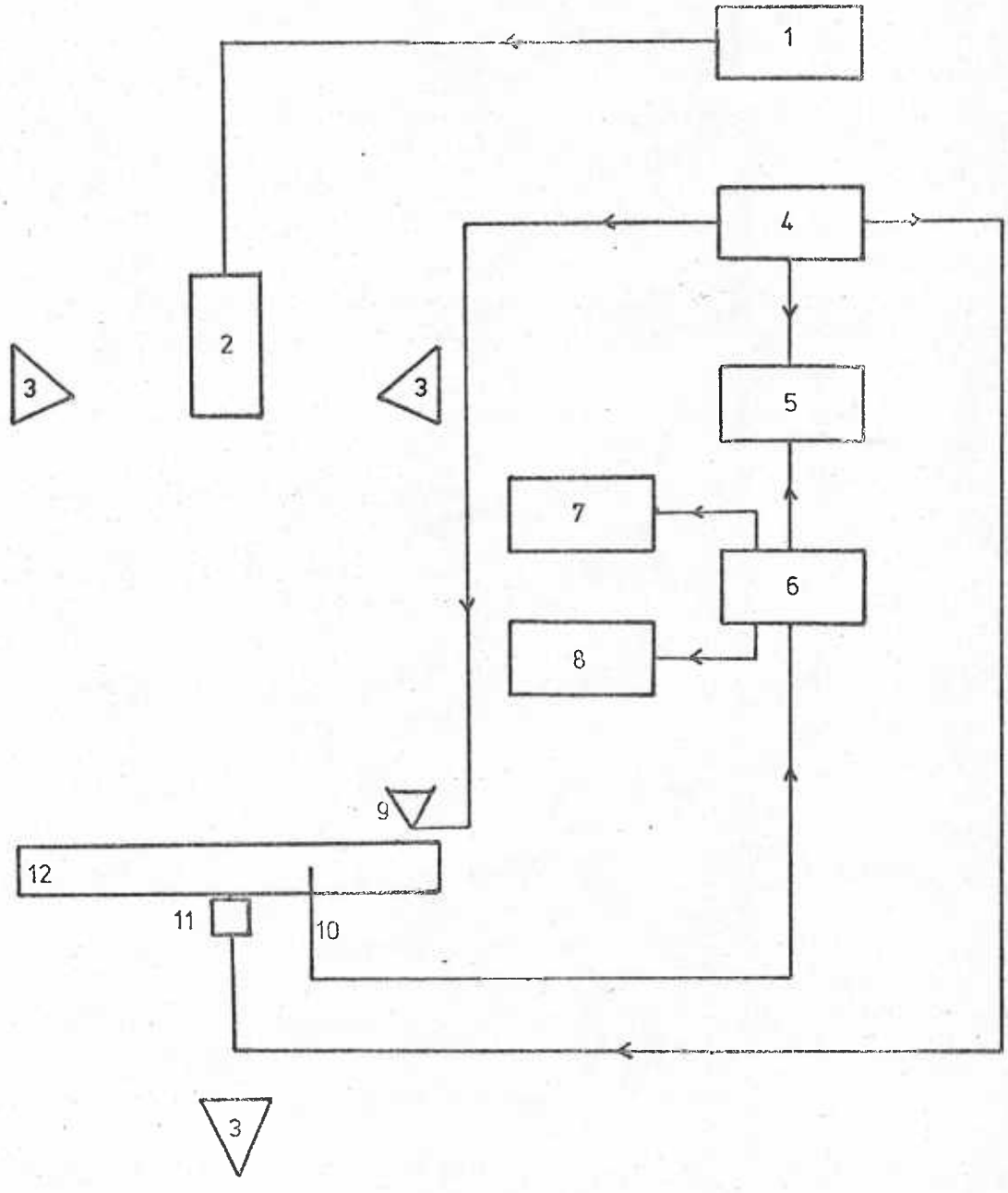


Single bubble (1.5 times real size)



Bubble splitting
(1.4 times real size)

Figure 4.1 Analysis of particle motion.



1_Camera power unit
2_Camera
3_Lights
4_Injection unit
5_U.V. recorder
6_Anemometer
7_Oscilloscope
8_Digital voltmeter
9_Flash
10_Hot-wire probe
11_Solenoide valve
12_Fluidised bed

Figure 4.2 Gas velocity measurements: experimental set-up

CHAPTER 5

THEORETICAL AND EXPERIMENTAL RESULTS FOR THE PARTICULATE FLOW

In the first part of this chapter, theoretical results obtained for the motion of the particulate phase from the equations of motion developed and discussed in Chapters 2 and 3 are presented. These results are compared with existing theories assuming the inviscid behaviour of the dense phase. The main features of these theories are recalled in Appendix 3.

In the second part, experimental results for the particle motion are compared with the theoretical predictions.

5.1 Theoretical results

5.1.1. Solution for the stream function and vorticity

Let us recall the set of equations derived in Chapter 2 and which governs the behaviour of the particulate phase when a certain viscosity is attributed to it. In terms of the dimensionless vorticity and stream-function the equations of motion are respectively:

$$\zeta^* = \nabla^{*2}\Psi^* \qquad (2.19)$$

$$\frac{1}{\rho}\left\{\frac{\partial \Psi^*}{\partial \rho}\,\frac{\partial \zeta^*}{\partial \theta} - \frac{\partial \Psi^*}{\partial \theta}\,\frac{\partial \zeta^*}{\partial \rho}\right\} = \frac{2}{Re}\,\nabla^{*2}\zeta^* \qquad (2.20)$$

$$\text{with} \quad Re = \frac{2a\, U_b\, (1 - \varepsilon_o)}{\nu_p}$$

These two equations are solved for the particle flow around a cylindrical bubble with the boundary conditions listed in Table 2.1.

The solutions for the vorticity ζ^* and the stream function Ψ^* obtained for the following Reynolds numbers: 0.1, 1, 10, 25 and 100, are shown on Figures 5.1 to 5.5. The value indicated on each contour refers to the value of ζ^* or Ψ^* and for each Reynolds number the contours were plotted for the same values of ζ^* and Ψ^*.

For low Reynolds numbers the solution is symmetrical with respect to the equatorial plane of the bubble. Figure 5.1 shows that, since convective effects are small, vorticity develops only in the radial direction. As the Reynolds number increases and due to convective effects, vorticity develops towards the rear of the bubble and the streamlines come closer to each other and to the bubble. This is a well-known result in other problems of streaming flow past an obstacle.

However as can be seen on Figure 5.5, there are no vortices formed in the rear of the bubble even for Reynolds numbers as high as 100; this is due to the perfect-slip boundary condition which was assumed on the bubble surface. (Table 2.1). In comparison vortices are obtained in the case of a no-slip condition for Re = 10 (in Son and Hanratty (90)). Experimentally, closed streamlines have been observed for a Reynolds number as low as 6 in the case of liquid flow past a circular cylinder (Taneda in Batchelor (101)). Following Batchelor we can say very crudely that in the present case there is sufficient vorticity generated at the rear of the bubble to satisfy the requirements of the perfect-slip condition, so that no backward flow is induced near the surface.

Furthermore as can be seen from Figures 5.3 to 5.5 the flow of particles for Reynolds number $10 < Re < 100$ is only slightly non-symmetrical and much less than it would be for a no-slip condition (for which some contours are shown in Batchelor (101) p. 258).

Outside the wake region closed streamlines along which particles circulate have never been observed experimentally in fluidised beds. We think it is important to emphasize that those particles which would circulate along closed streamlines must not be physically identified with particles circulating within the bubble wake. The theoretical model developed in this work assumes that the bubble is perfectly circular and does not include a wake. Therefore if vortices appeared in the theoretical model, they would not represent physically the particles in the bubble wake. What has been said above is thus some additional justification for the zero tangential shear stress boundary condition assumed in Chapter 2.

Once the solution for the stream function is obtained it is easy to calculate the components of the particle velocity from the relations:

$$v_r = -\frac{1}{r}\frac{\partial \Psi}{\partial \theta} \qquad (5.1)$$

$$v_\theta = \frac{\partial \Psi}{\partial r} \qquad (5.2)$$

(i) On the bubble surface $v_r = 0$ and the tangential velocity can easily be calculated from (5.2) using a finite-difference formula as described in Chapter 3. In dimensionless form:

$$v^*_\theta = \frac{\partial \Psi^*}{\partial \rho} = \frac{18\,\Psi^*_{i,2} - 9\,\Psi^*_{i,3} + 2\,\Psi^*_{i,4}}{6\,\pi k} \quad \text{at} \quad \rho = 1$$

The variations of the dimensionless tangential velocity v^*_θ along the bubble surface are shown on Figure 5.6 as a function of the surface angle and for different Reynolds numbers. As expected from the form and closeness of the streamlines shown in Figures 5.1 to 5.5, the tangential velocity decreases when the Reynolds number decreases and as streamlines move apart. The velocity is symmetrical with respect to $\theta = 90^o$ for potential flow and for low Reynolds number (Stokes's flow). For intermediate values of the Reynolds number the maximum velocity is situated on the upper surface of the bubble ($\theta < 90^o$).

(ii) It is equally interesting to plot the variations of the particle velocity along selected streamlines. This is shown in Figure 5.7a (potential flow and Stokes's flow) and on Figure 5.7b (Re = 25). On these figures the values of $v^* = (v^{*2}_\rho + v^{*2}_\theta)^{\frac{1}{2}}$ are plotted for different values of the stream function contours. ($\Psi^* = 0$ has been plotted for clearness but refers to the previous section).

Figure 5.7a shows that the velocity field is symmetrical for Stokes's flow but, as expected, the values of particle velocity are lower than for potential flow.

As can be seen from Figure 5.7b, at intermediate Reynolds number, the maximum particle velocity along the streamlines does not occur at $\theta = 90^o$ but moves from $\theta = 72^o$ for $\Psi^* = 0$ to $\theta \sim 90^o$ for $\Psi^* = 1$ and then to about $\theta = 114^o$ for $\Psi^* = 3$.

All the results above refer to a set of axes moving steadily with the bubble. If one observes the motion of a particle when referred to axes fixed with respect to the fluidised bed, it will describe a curve which, in previous chapters, has been referred to as the drift.

5.1.2 Drift of particles

The set of equations describing the motion of particles with respect to a fixed set of axes has been derived in Chapter 3 (section 3.8).

The resulting curves for different Reynolds numbers are represented on Figures 5.8 to 5.12. On each of these figures the curves refer to the following values of the dimensionless stream function: $\Psi^* = 0.1,\ 1,\ 2,\ 3$.

The parameter on the curves represents the dimensionless time τ as calculated in Chapter 3. The origin (i.e. $\tau = 0$) has been taken at the central passage of the bubble and the value of $\tau = 1$ represents the position of the particle when the bubble has moved one radius above position 0. In each case the corresponding curve for potential flow has also been drawn.

In the case of potential flow the net predicted movement is upwards and curves are symmetrical with respect to the equatorial plane of the bubble. These curves are often referred to as "elastica".

At intermediate Reynolds number, the gross feature of the curves obtained is the prediction of a net upward movement for particles close to the bubble (say $\Psi^* < 2$) and a net downward movement for particles further away ($\Psi^* > 2$). The "looping" of particles obtained for potential flow disappears gradually when the Reynolds number decreases and vanishes for $Re < 10$. In addition, for $Re > 10$

only particles close to the bubble describe a loop, otherwise as has already been noted, the movement is downward.

The case for Stokes's flow is well represented by the curves for Re = 0.01 shown on Figure 5.8. In this last case all curves are symmetrical. In addition it can be seen that the total drift for particles close to the bubble axis is very large and it can be shown (Lamb, Hydrodynamics (105)) that it is in fact infinite. This result has already been mentioned in Chapter 1 in connection with Gabor's analysis (72).

It can also be noted that in all cases of Reynolds numbers the final points on the curves (corresponding to $\theta = 0$ and $\theta = \pi$) could not be calculated numerically. For these values the particle is at infinity on its streamline and therefore outside the grid of integration as defined in Chapter 3.

The total drift volume can be written as:

$$D = \int_{-\infty}^{+\infty} \rho \, X^* \, d\Psi^* \qquad (5.3)$$

and what has been noted previously implies that the net drift volume could not be calculated. However the drift volumes obtained for the two limiting cases of Stokes's flow and potential flow are well-known results:

(i) in the case of Stokes's flow it has been said previously that the drift X^* is infinite. Therefore, according to (5.3), the drift volume is infinite.

(ii) in the case of potential flow, it is easy to show from the

expression of X^* as defined in Appendix 3 that $D = \pi\rho\, a^2$ which is the mass of liquid displaced by the circular cylinder.

Thus the above results imply that the predicted mixing of particles in a fluidised bed is more important for Stokes's flow than for potential flow.

Another interesting result is to plot the variations of the particle velocity along its path line. This is shown on Figures 5.13a and 5.13b for potential flow, Stokes's flow and Re = 25, and it is seen that the particle velocity presents two maxima. This can easily be understood qualitatively if one considers the theoretical path lines as they were described above (Figures 5.8 to 5.12). Consider for example the case Re = 25 and $\Psi^* = 0.1$ shown in Figure 5.11 : the particle starts from rest when $\tau \sim -\infty$ and then accelerates when it is pushed upwards by the bubble. When the bubble reaches the region of the central position (say $\tau = -1$) the particle begins to describe a small loop and deccelerates to reach a minimum value. It is then carried upwards with the bubble and therefore accelerates again. The velocity reaches a maximum and then decreases again until the particle comes at rest when $\tau \sim +\infty$.

A useful way of visualizing the displacement of particles caused by the bubble is to calculate the deformation of an initially horizontal layer of particles. This can easily be calculated from the drift curves described above.

In the present case the undisturbed horizontal line was assumed to be situated three radii above the center of the bubble, i.e. at points corresponding to $\tau = 3$ on the drift curves. Thus these curves were recalculated taking $\tau = 3$ as a new origin $\tau' = 0$ and all points $\tau' = 0$

were taken on the same horizontal line. Then lines of equal τ' were calculated and are shown on Figures 5.14 to 5.16 for three cases of Reynolds number, Re = 1, 10, 100. Some streamlines for the particle motion have also been represented and are indicated by their dimensionless value. It is perhaps easier to see from these figures that the net displacement of particles (upwards and downwards) increases when the Reynolds number decreases.

5.1.3. Drag coefficient

The drag coefficient C_D predicted from the present theory is calculated in Chapter 3 (section 3.7). It has been shown that the only contribution to C_D arises from the pressure drag coefficient C_{DP} which was calculated by equation(3.52). The variation of C_D as a function of Reynolds number is shown on Figure 5.17. The drag coefficients for gas bubbles in liquids as well as the theoretical models for solid cylinders and spheres are also plotted. Hadamard's model ($Re < 1$) and Moore's model ($Re > 10$) refer to tangentially-free spheres.

It was thought interesting to plot Parlange's model (102) for spherical-cap bubbles ($Re \geq 100$). In his closed wake model Parlange assumes that the bubble occupies only a small part of the closed region and has no effect on the hydrodynamics of the wake; this is not true for a bubble rising in a fluidised bed. Nevertheless this model corresponds to a high-M liquid ($M = \frac{g \mu_1^4}{\rho_1 \sigma_1^3}$, where σ_1 is the surface tension of the liquid against the gas) and to a bubble rising according to Davies and Taylor's relation. This seems to be the case in a fluidised bed as will be seen later.

However it can be seen from Figure 5.17 that predicted values of C_D are higher than those obtained in the present theory. On this figure, solid curves refer to theoretical models, dotted curves to experimental data (references to be found in Harper (103)).

Most of the experimental data in the literature refer to three-dimensional bubbles. Two sets of experiments by Haberman and Morton (in Harper (103)) are shown in Figure 5.17 for a high and a low value of the dimensionless number M. Data by Tritton (in Batchelor (101)) for a rigid cylinder are also given.

For values of Re greater than 0.5 the drag coefficient obtained in the present theory is, as expected, lower than the one obtained for a no-slip condition on the bubble surface. However for low values of the Reynolds number the drag coefficient becomes higher than Oseen's approximation for a rigid cylinder. It is very difficult to suggest a satisfactory explanation for this behaviour.

Among the liquid-like properties of a fluidised bed some authors have attributed to it a certain surface tension (e.g. Gelperin and Einstein (40)). The same type of analogy as for viscosity (Chapter 1) has been derived: it is possible to obtain the same mathematical expression for the variation of σ_1 with temperature in a liquid as for the variations of σ_1 with the fluidising fluid velocity U.

However very few numerical values have been calculated for σ (Furukawa and Ohmae (32) for three-phase fluidisation) and the introduction of such a parameter seems quite arbitrary. But if one admits the order of magnitude of Furukawa and Ohmae's data for medium sized particles, then:

$$\rho_p \sim 3 g/cm^3 \quad \text{(e.g. Ballotini)}$$

$$(\sigma_l =)\ \sigma_p \sim 100 \text{ dynes/cm}$$

$$\mu_p \sim 10 \text{ poises}$$

thus $M = \dfrac{g \mu_p^4}{\rho_p \sigma_p^3} = 3$ which corresponds to a liquid with a

rather high M value. This helps to situate on Figure 5.17 the experimental data which could be obtained for a gas bubble in a fluidised bed. Nevertheless such data seem very difficult to obtain since:

- the true shape of the bubble has to be taken into account
- viscosity data, particle velocity and pressure measurements are still very few and unprecise.

Finally, from the theoretical results, a good representation of C_D for low Reynolds numbers is given by the following relation:

$$C_D = \frac{7.32}{Re} \qquad Re \leqslant 1$$

with an error of 4% for Re = 1.

This can be compared with other theoretical predictions:

rigid sphere : $\dfrac{24}{Re}$ (Stokes's law)

tangentially-free sphere: $\dfrac{16}{Re}$ (Hadamard Rybczynski's result)

rigid cylinder : $\dfrac{8\pi}{Re \ln \left(\frac{7.4}{Re}\right)}$ (Oseen's approximation Batchelor (101))

5.1.4 Variations of the bubble Froude number

An expression for the Froude number ($Fr = \frac{U_b^2}{ga}$) has been derived in Chapter 2 (section 2.4.3). This was done by ensuring that pressure variations remained small on the surface of the bubble near the apex of the bubble. The variation of the Froude number as a function of the Reynolds number is represented in Figure 5.18. The Davies and Taylor result for potential flow, $Fr = 0.250$, is the asymptotic value when Re is large and is represented by a dotted line.

As can be seen, there is a predicted maximum for the Froude number of $Fr = 0.35$ corresponding to $Re \sim 5$. For lower values of the Reynolds number, the value of the Froude number decreases sharply while it tends towards the Davies and Taylor result for high Reynolds number as explained in section 2.4.3. It is worth remarking that an analytical result can be obtained for low Reynolds numbers in the three-dimensional case as: $Fr = \frac{1}{3} Re$ (Appendix 5).

The occurrence of the maximum can be understood qualitatively by considering the expression derived in Chapter 2:

$$Fr = \frac{1}{\left[\left(\frac{\partial v_\theta^*}{\partial \theta} \right)^2 - \frac{2}{Re} \frac{\partial^2 \zeta^*}{\partial \rho \, \partial \theta} \right]_{\substack{\rho = 1 \\ \theta = 0}}}$$

On Figure 5.6, $\left. \frac{\partial v_\theta^*}{\partial \theta} \right|_{\substack{\rho = 1 \\ \theta = 0}}$ represents the slope at the origin of the curve $v_\theta^*(\theta)$. Therefore it can be seen that the decrease

of $\frac{\partial v_\theta^*}{\partial \theta}$ is greater when Re decreases from 100 to 10 (say) than when it decreases from 1 to 0.1. One can also see from the vorticity contours (Figures 5.1 to 5.5) that vorticity variations with Re are smaller for $Re > 10$ (say) than for $Re < 10$.

Thus when the Reynolds number decreases from high values where the Davies and Taylor result applies, the main contribution to the Froude number arises from $\frac{\partial v_\theta^*}{\partial \theta}$ which decreases rapidly with decreasing Re; consequently Fr increases. For lower Reynolds number the second term in the denominator becomes greater while the variations in $\frac{\partial v_\theta^*}{\partial \theta}$ are smaller. Thus Fr decreases.

Some experimental points obtained in this work for bubbles in a fluidised bed are also plotted on Figure 5.18. These results were obtained from experiments carried out to measure the gas velocity variation around a bubble (described in Chapter 6). In these experiments, the bubble Reynolds number and the Froude number were calculated using measured values of the bubble velocity and bubble radius as well as viscosity and density data as given in Table 4.1.

As often happens in this type of measurement there is a large scatter. In addition the experimental points represent the Froude number for artificially injected bubbles and thus the range of Reynolds number obtained is very narrow ($10 < Re < 30$). However it can be seen, as many authors have already reported, that the Davies and Taylor result is a good average value for the bubble velocity.

In the present case the experimental results are inconclusive as far as the variation of Fr with Re is concerned, and experiments would have to be conducted to cover a much wider range of bubble Reynolds

numbers to provide a real test of the theory.

5.1.5 Voidage variations

The variations of voidage around the bubble have been calculated from the calculated particle velocity field using Jackson's method as explained in Chapter 2 (section 2.4.4). The voidage is given from Carman Kozeny's equation by:

$$\varepsilon = \frac{\sqrt{\gamma}}{\frac{1-\varepsilon_o}{\varepsilon_o} + \sqrt{\gamma}} \quad \text{with} \quad \gamma = \frac{\beta_o}{\beta}$$

Some integration paths and lines $1/\gamma$ = const are shown on Figures 5.19 to 5.22 for increasing Reynolds number. Figure 5.22 refers to Jackson's solution (11).

It can be seen from these figures that the region which cannot be reached by integration of the differential equation in γ becomes very large when Re decreases, the corresponding variations of γ being much smaller.

For Re = 1 the minimum value obtained is $1/\gamma = 0.90$ (i.e. $\varepsilon = 0.413$), for Re = 10: $(1/\gamma)_{min} = 0.70$ ($\varepsilon = 0.444$), for Re = 100: $(1/\gamma)_{min} = 0.50$ ($\varepsilon = 0.571$).

In order to get a solution for the gas flow in this inaccessible region, it was assumed that the voidage fraction was constant and equal to the value obtained on the border of the region. This was taken in each case as a first approximation (e.g. $1/\gamma = 0.5$ for Re = 100, $1/\gamma = 0.8$ for Re = 10).

Nevertheless it should be emphasized that Jackson's method of obtaining the solution for the voidage ε in cases of low Reynolds

numbers is not very satisfactory since no solution is obtainable for a large region above the equatorial plane in addition to that below the bubble.

The variation of the voidage fraction on the vertical axis above the bubble is represented on Figure 5.23 for Reynolds numbers between 0.1 and 100. As before it can be seen that voidage changes are small for low Reynolds number and increase with increasing Re.

Experimental data obtained by Lockett and Harrison (7) are also plotted on this figure. As can be seen, the agreement with Jackson's theory and with the present theory for a typical intermediate Reynolds number (say Re = 10) is very poor and shows the need for many more measurements.

Nevertheless it is interesting to note the very small variations in voidage that are predicted at low Reynolds numbers.

5.2 Experimental results

Experiments were performed by recording the displacement of coloured tracer particles with the aid of a high-speed camera. Results as they were obtained directly from analyzing the cine-films are first presented and show the particle movement with respect to stationary axes. Then results are given in terms of streamlines (with respect to axes moving with the bubble).

5.2.1 Results with respect to stationary axes

Paths of particles are shown on Figures 5.24a to 5.26b. For each size of particles two typical results are presented:

- figure (a) concerns artificially injected bubbles

- figure (b) concerns natural bubbles.

The reason for which these two kinds of experiments have been performed has already been explained in Chapter 4 : broadly speaking they were carried out to test the difference in behaviour of the particulate phase between minimum fluidisation conditions and the fully fluidised state.

For each figure theoretical models for potential flow and for the nearest calculated Reynolds number have been plotted. It was in fact impossible to compute all the theoretical values of Re corresponding to experimental results. Furthermore the experimental value of the Reynolds number is calculated from the measured bubble radius and bubble velocity and from viscosity data which are unprecise. Thus the experimental value indicated on the figures is only approximate.

Examination of these results shows the difference betwe en injected and natural bubbles.

(i) Natural bubbles are more stable and thus generally larger. They also rise more rapidly than the injected bubbles so that the Reynolds number is greater.

In addition the displacement of the particles is much greater. In one case (Ballotini grade 8) complete looping of particles starting their motion near the bubble axis was observed (Figure 5.25b). For smaller particles this looping was not observed since bubbles tended to be more unstable and particles situated near the bubble axis fell through the roof rather than flowing around the sides. Larger sized particles (Ballotini grade 7) ended their motion before being carried upwards in the bubble wake.

(ii) For injected bubbles the net movement of particles is downwards and qualitatively similar to that observed by Gabor (69, 72). Looping of particles was never observed in this case. In fact all particles situated near the bubble axis at the inception of their movement were falling through the bubble roof. This caused frequent splitting and elongating for injected bubbles. Although some of Gabor's experiments concern natural bubbles (72), these bubbles are much smaller than the ones for which looping was observed as indicated in the previous section. Therefore we suggest that Gabor's experiments were not appropriate to provide a real test of the potential flow theory.

Furthermore for injected bubbles the movement of particles extends to about two bubble radii. For natural bubbles it extends much farther to about 5 bubble radii.

Comparison with the theoretical models leads to the following conclusions:

a) Naturally occurring bubbles

For particles starting their movement very close to the bubble axis, potential flow is a reasonably good solution. Experimental values of the Reynolds number are quite high (~ 50) and in this case looping of particles is observed. Furthermore it can be seen from Figure 5.25b that the experimental looping is symmetrical with respect to the equatorial plane of the bubble as predicted from the potential flow theory. The theory developed in this work and incorporating the effects of viscosity in the particulate phase does not represent adequately the movement of such particles.

For particles starting their movement farther from the axis, potential flow is not satisfactory since experimental movement of the

particles is not symmetrical and looping is not observed. The present theory describes, at least qualitatively, the movement of those particles. However it predicts a greater downward movement than obtained experimentally.

b) Injected bubbles

For these bubbles the present theory gives a better qualitative description of the particle movement than potential flow. However in this case all movement vanishes very rapidly when moving away from the bubble and ceases for $\frac{r}{a} > 2$. This suggests that a Newtonian behaviour is not realistic in this case and confirms Schügerl's distinction (39) between a semi-fluidised bed and a fully developed bed.

The analysis of the cine-films also permits the calculation of the particle velocity along its path line. Variations of the particle velocity as a function of its position on the path line represented by the angle θ are shown on Figures 5.27 to 5.29. On these figures each broken line refers to a particle. Only results concerning natural bubbles have been plotted since they can usefully be compared with theoretical predictions.

The important result shown on these figures is that the maximum velocity occurs at $\theta > 90^{\circ}$. These results can usefully be compared with theoretical predictions (Figures 5.13a and 5.13b) which show that there is either one maximum at $\theta = 90^{\circ}$ for potential flow, or, at lower Reynolds numbers, two maxima for $\theta < 90^{\circ}$ and $\theta > 90^{\circ}$. The first maximum is not observed on the experimental curves which suggests that potential flow is a better representation of the particle velocity at least for particles situated close to the bubble axis. For these particles (the upper broken curves on Figures 5.27 to 5.29 the

maximum value for the velocity is situated closer to $\theta = 90^{o}$ as in potential flow theory. However for all curves the theoretical and experimental maxima do not coincide.

Tuot and Clift (104) suggested that the maximum particle velocity occurs on the lower part of the bubble, in interpreting their measurements of heat transfer coefficients around injected bubbles. Their results show that the flow of particles is highly asymmetric. They also suggest that Gabor's model of Bingham - plastic (72) is consistent with their observations. This last result is confirmed by the present experiments on injected bubbles where it has been shown that a Newtonian behaviour is unrealistic.

5.2.2 Results with respect to axes moving with the bubble

By using relations (3.53) defined in Chapter 3, it is easy to calculate the streamlines corresponding to the particle paths shown on Figures 5.24a to 5.26b, i.e. :

$$\left.\begin{aligned} x &= X - U_b t \\ y &= Y \end{aligned}\right\} \qquad (3.53)$$

X, Y refer to stationary axes and therefore represent point coordinates on the particle path.

x, y refer to axes moving with the bubble and represent point coordinates on the streamlines.

The transformed figures in terms of streamlines are shown on Figures 5.30a to 5.32b. On these figures the calculated theoretical streamlines corresponding to the nearest estimated Reynolds number are also plotted. Lines $\tau' = \text{const}$ as defined at the beginning of this

chapter (section 5.1.2) are also shown for the corresponding Reynolds number and for potential flow. The line $\tau' = 0$ corresponds to an undisturbed horizontal layer of particles situated three radii above the bubble center.

It can be seen that the duration of the movement of particles (i.e. the length of the experimental streamline) is much smaller for injected bubbles than for natural bubbles. In other words the radius of influence of the bubble is less important for injected bubbles. This result was already obtained by considering the particle path lines which showed that particle motion vanished for particles situated more than about two radii from the bubble.

The results for natural bubbles are more useful since an important part of the streamline is obtained experimentally.

(i) As far as the predicted asymmetry of the particle flow is concerned, no asymmetry can reasonably be found from those results. This is not necessarily in contradiction with the experimental results of Tuot and Clift (104) who suggested that the flow of particle is highly asymmetric. Their results concern injected bubbles and the different behaviour of these bubbles and natural ones has already been emphasized.

The difference between potential flow and flow at, say, Re = 25 or Re = 50, falls within experimental error, i.e. there is often a difference in abscissa, positive or negative, between the starting and the terminating positions of the particle. This renders quantitative comparison difficult since it is not possible to attribute a dimensionless stream function value to a particular experimental streamline.

Furthermore the asymmetry for those intermediate Reynolds numbers is not very pronounced.

(ii) The total drift of particles obtained experimentally is much less than that predicted by all Newtonian theories, as can be seen from Figures 5.24a to 5.26b, showing particle path lines. Thus lines $\tau' = \text{const}$ differ sensibly from theoretical predictions for $\tau' \geqslant 3$, i.e. for positions situated below the equatorial plane of the bubble.

A more conclusive and quantitative result can be obtained from the particle velocity as it moves on its streamline. These results are shown on Figures 5.33a to 5.35b where the vertical component of the particle velocity v_x^* has been plotted as a function of the particle distance from the bubble center at the central passage of the bubble ($\theta = 90^o$). From these figures it is very clear that:

(i) The movement of particles for injected bubbles does not extend more than two bubble radii from the bubble center.

(ii) There is no influence of the Reynolds number as shown on figures concerning natural bubbles (Figures 5.33b, 5.34, 5.35b).

(iii) For particles close to the bubble axis (say $y^* < 1.5$) potential flow is the best representation of the variations in particle velocity. For particles further away all theories are close and fall within experimental error. In this former case experimental results are therefore inconclusive.

(iv) In the case of artificial bubbles, no theory describes adequately the variations of the particle velocity.

5.3 Conclusion

General conclusions concerning results for both the particulate phase and the gas phase are given in Chapter 8. However as far as the particulate phase is concerned it is possible to summarize the main results as follows:

(i) no improvement has been obtained by introducing a Newtonian viscosity in the equation of motion.

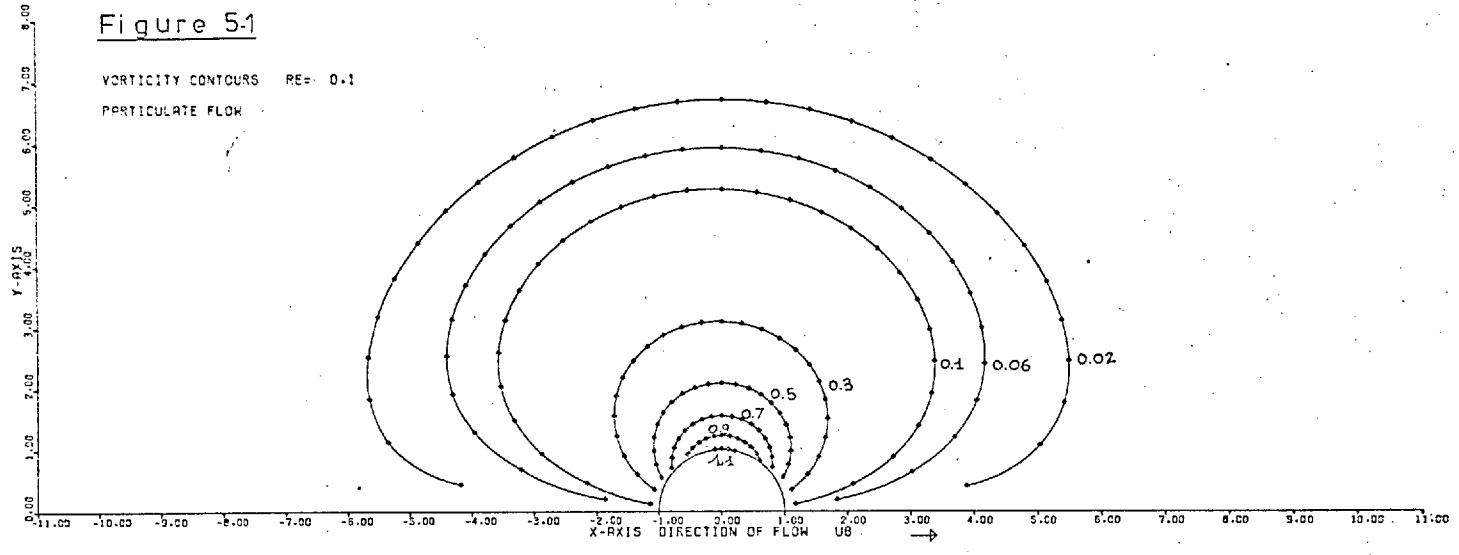
(ii) the difference between a semi-fluidised bed and fully developed bed has been shown experimentally.

(iii) in the case of natural bubbles, complete looping of particles situated near the bubble axis has been observed.

(iv) the experimental drift obtained is much lower than that predicted by Newtonian theories.

On a theoretical point of view, a general solution has been presented for the flow around a circular cylinder with a zero tangential shear-stress at the cylinder surface. We believe that these results might be of some interest since they are not presented elsewhere particularly in what concerns the drift of a particle where only potential flow solution is available.

Figure 5-1


VORTICITY CONTOURS RE= 0.1
PARTICULATE FLOW
Y-AXIS
X-AXIS DIRECTION OF FLOW U8
0.02
0.06
0.1
0.3
0.5
0.7
0.9
1.1

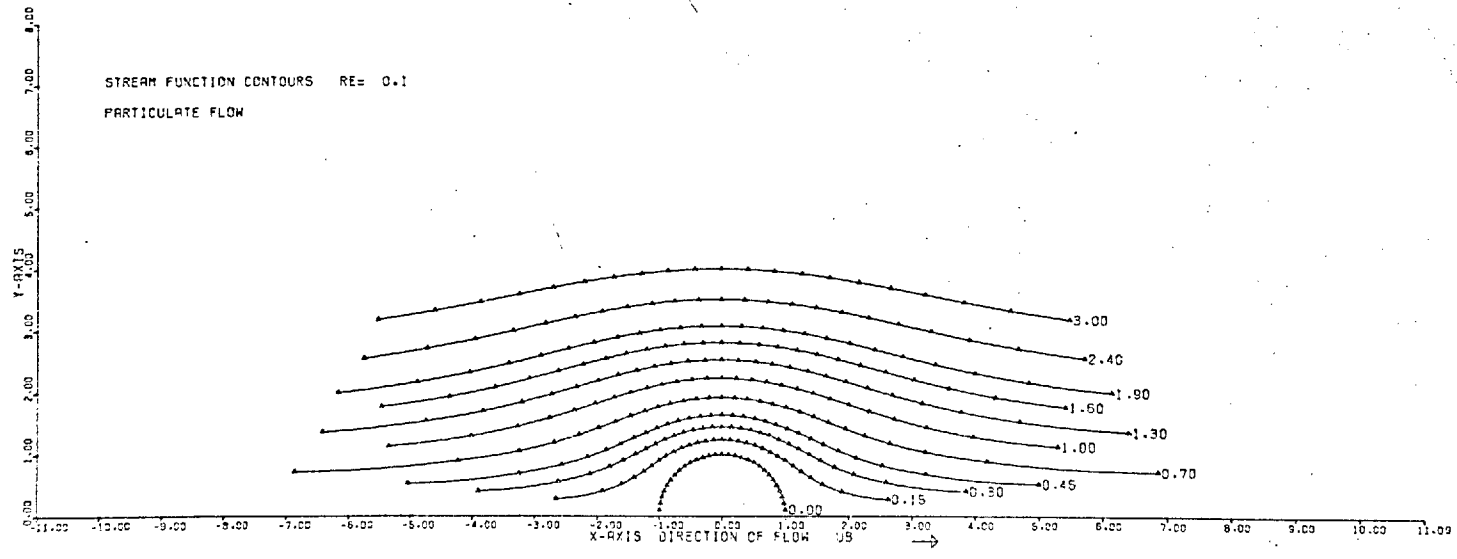
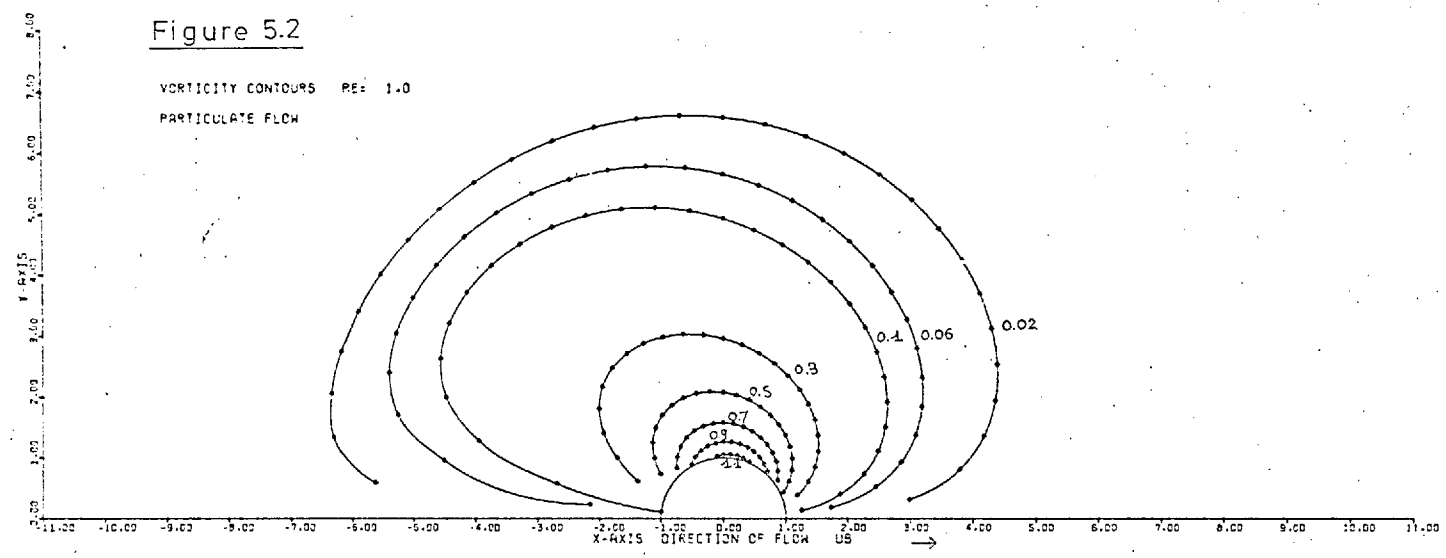

STREAM FUNCTION CONTOURS RE= 0.1
PARTICULATE FLOW
Y-AXIS
X-AXIS DIRECTION OF FLOW U8
3.00
2.40
1.90
1.60
1.30
1.00
0.70
0.45
0.30
0.15
0.00

Figure 5.2


VORTICITY CONTOURS RE= 1.0
PARTICULATE FLOW
0.02
0.06
0.1
0.3
0.5
0.7
0.9
1.1
Y-AXIS
X-AXIS DIRECTION OF FLOW US

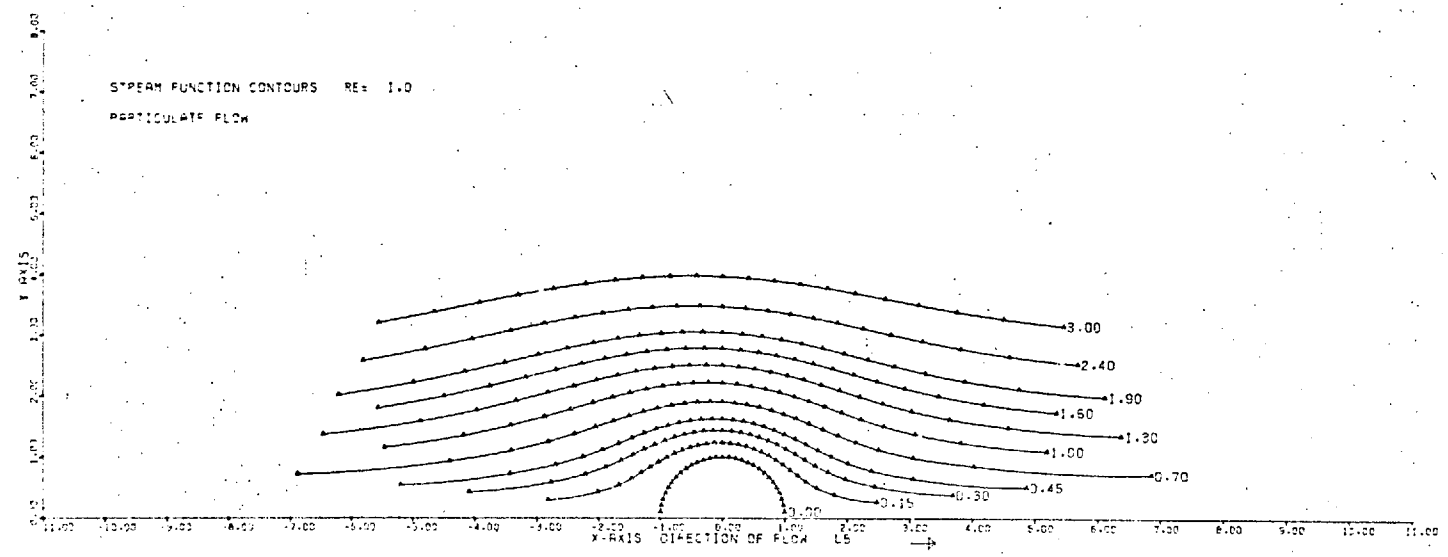
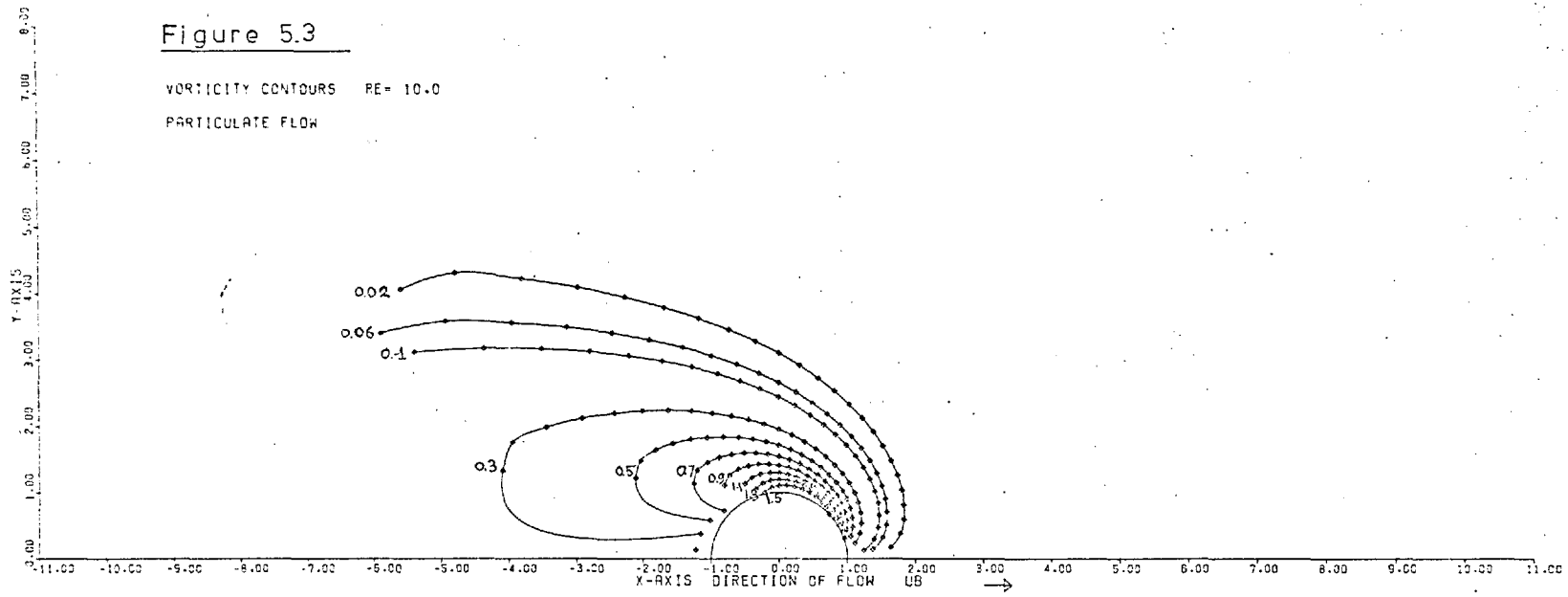

STREAM FUNCTION CONTOURS RE= 1.0
PARTICULATE FLOW
3.00
2.40
1.90
1.60
1.30
1.00
0.70
0.45
0.30
0.15
0.00
Y-AXIS
X-AXIS DIRECTION OF FLOW US

Figure 5.3


VORTICITY CONTOURS RE= 10.0
PARTICULATE FLOW
0.02
0.06
0.1
0.3
0.5
0.7
0.9
1.1
1.3
1.5
Y-AXIS
X-AXIS DIRECTION OF FLOW U8

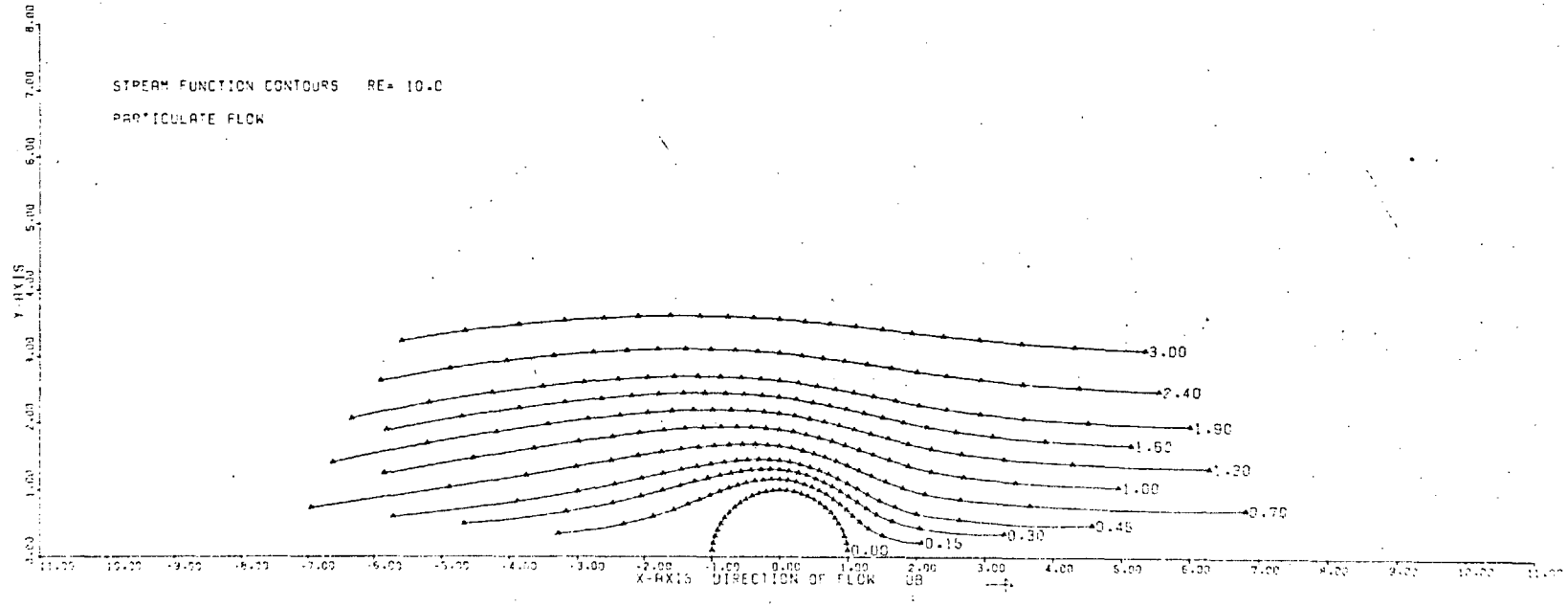
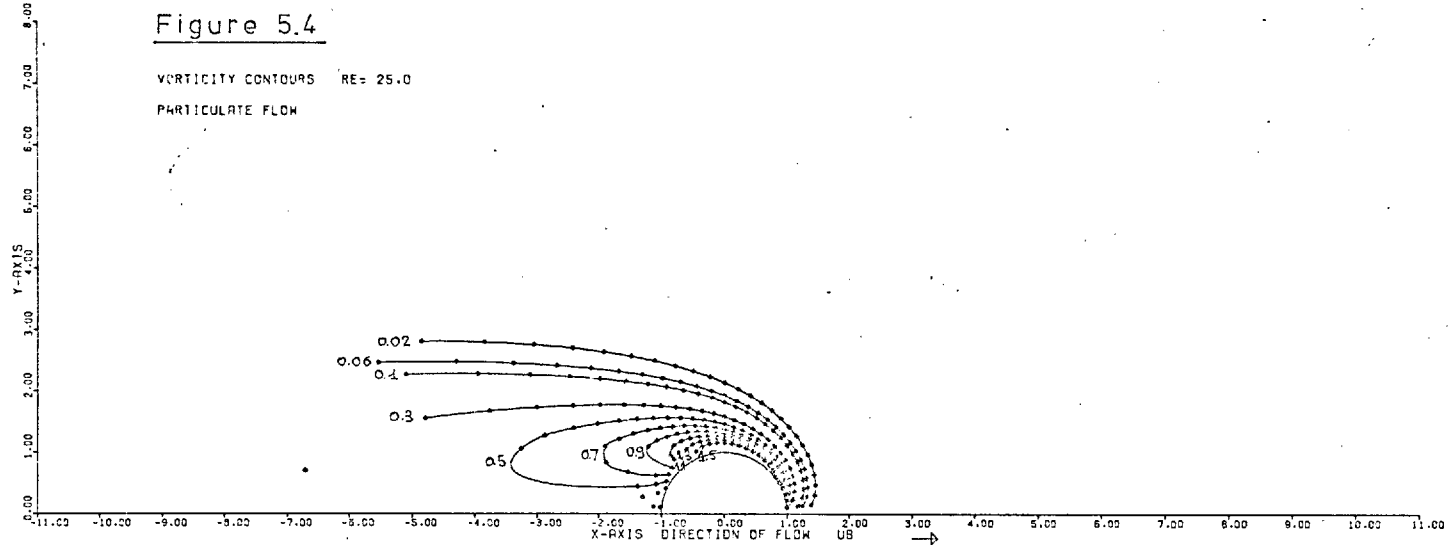

STREAM FUNCTION CONTOURS RE= 10.0
PARTICULATE FLOW
3.00
2.40
1.90
1.60
1.20
1.00
0.70
0.45
0.30
0.15
0.09
Y-AXIS
X-AXIS DIRECTION OF FLOW U8

Figure 5.4


VORTICITY CONTOURS RE= 25.0
PARTICULATE FLOW
Y-AXIS
X-AXIS DIRECTION OF FLOW UB
0.02
0.06
0.1
0.3
0.5
0.7
0.9

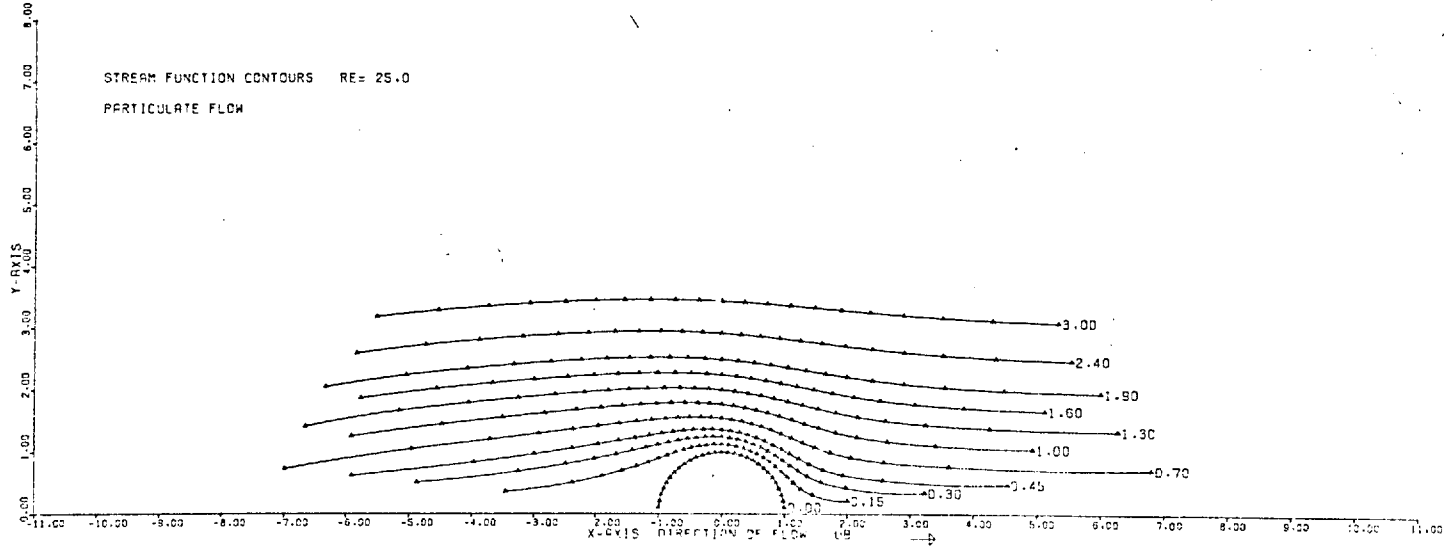
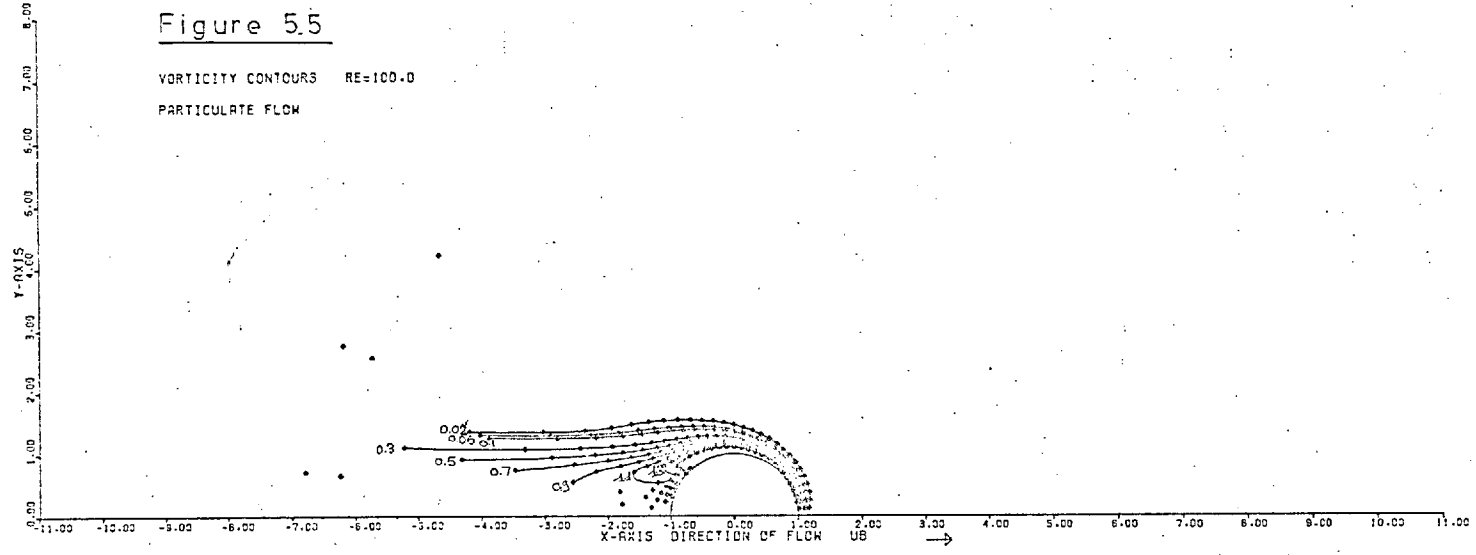
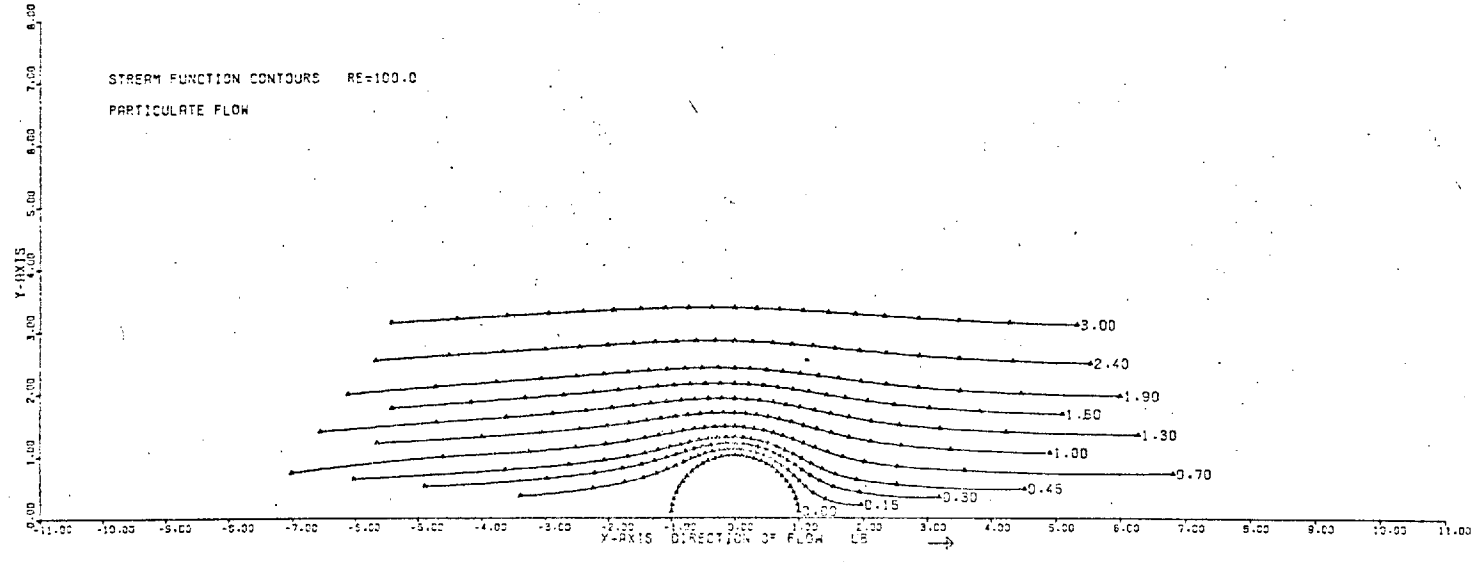

STREAM FUNCTION CONTOURS RE= 25.0
PARTICULATE FLOW
Y-AXIS
X-AXIS DIRECTION OF FLOW UB
3.00
2.40
1.90
1.60
1.30
1.00
0.70
0.45
0.30
0.15
0.00

Figure 5.5


VORTICITY CONTOURS RE=100.0
PARTICULATE FLOW
Y-AXIS
X-AXIS DIRECTION OF FLOW U8
0.3
0.5
0.7


STREAM FUNCTION CONTOURS RE=100.0
PARTICULATE FLOW
Y-AXIS
X-AXIS DIRECTION OF FLOW U8
3.00
2.40
1.90
1.60
1.30
1.00
0.70
0.45
0.30
0.15

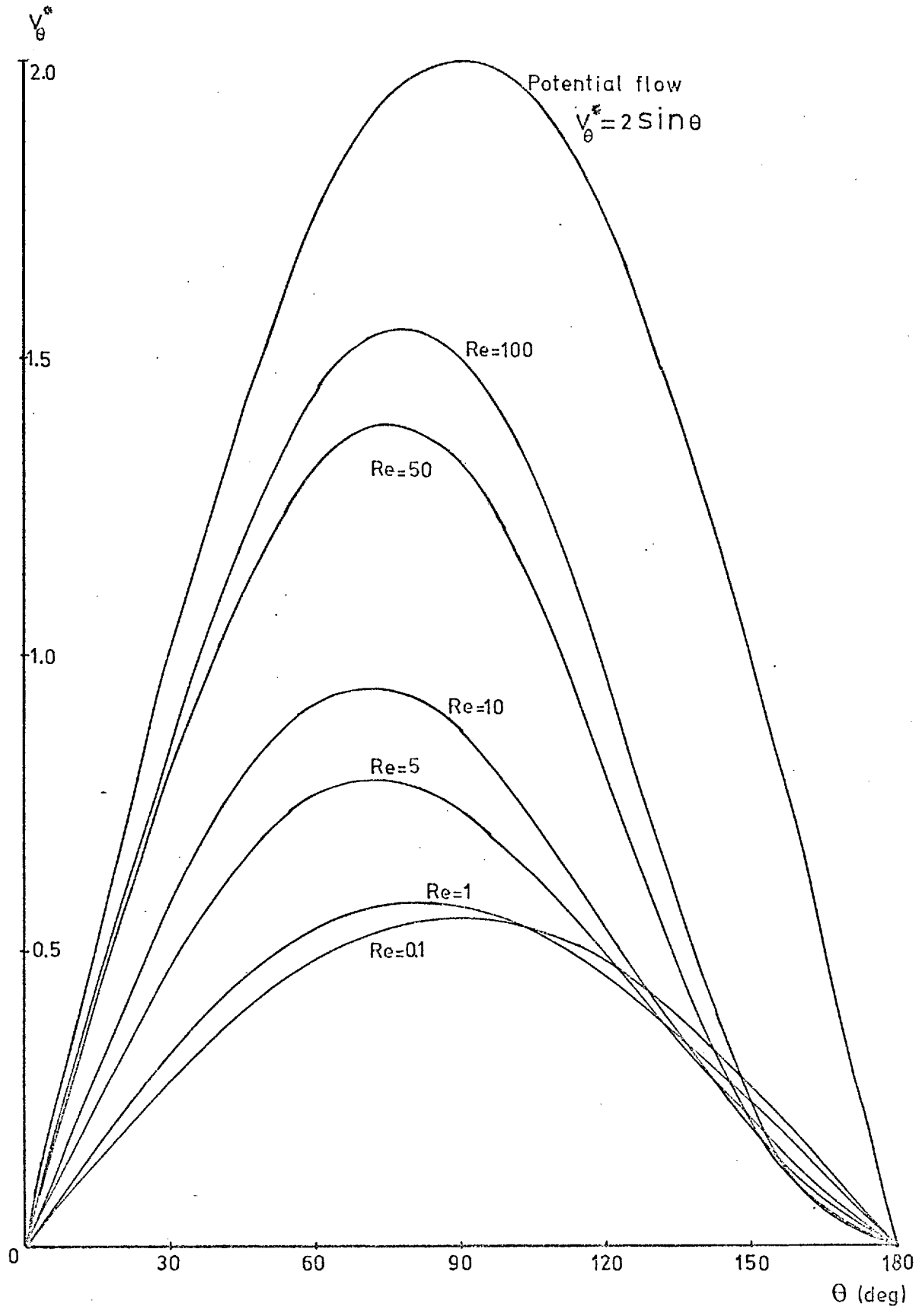


Figure 5.6 Variation of the tangential velocity of particles at the bubble surface.

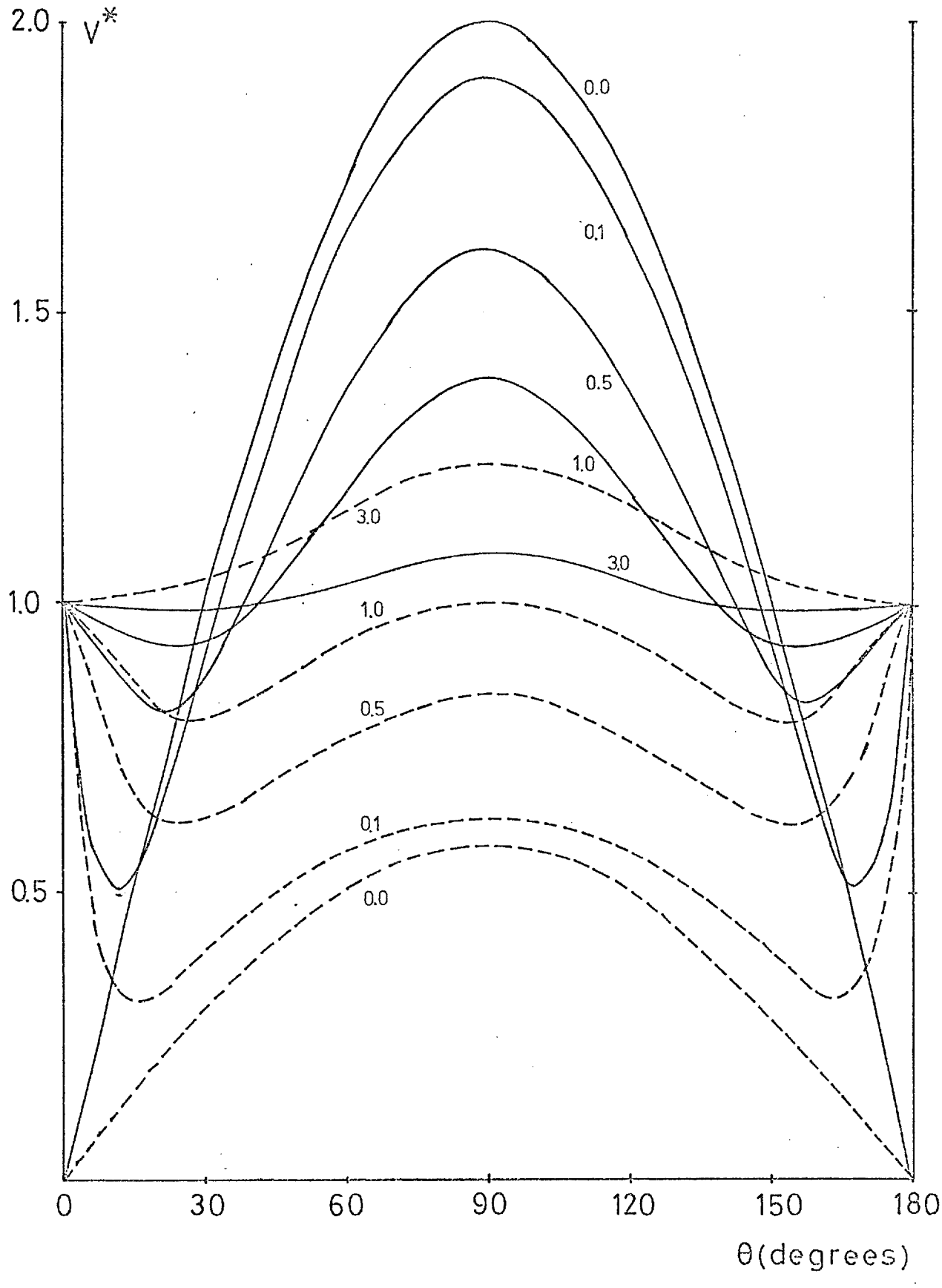


Figure 5.7.a Variations of particle velocity along streamlines. ——— Potential flow

– – – – Stokes's flow

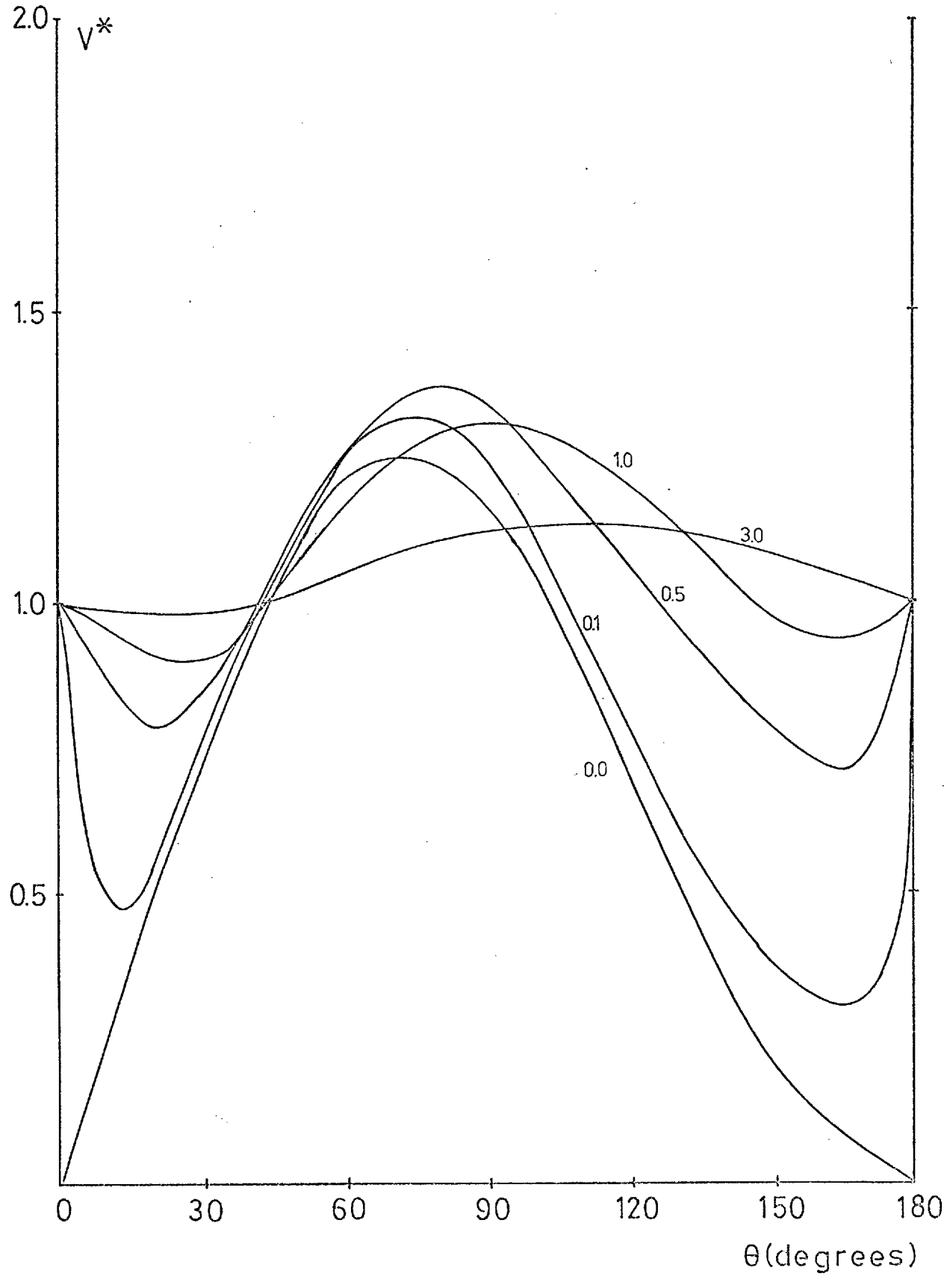


Figure 5.7.b Variations of particle velocity along streamlines. Re=25

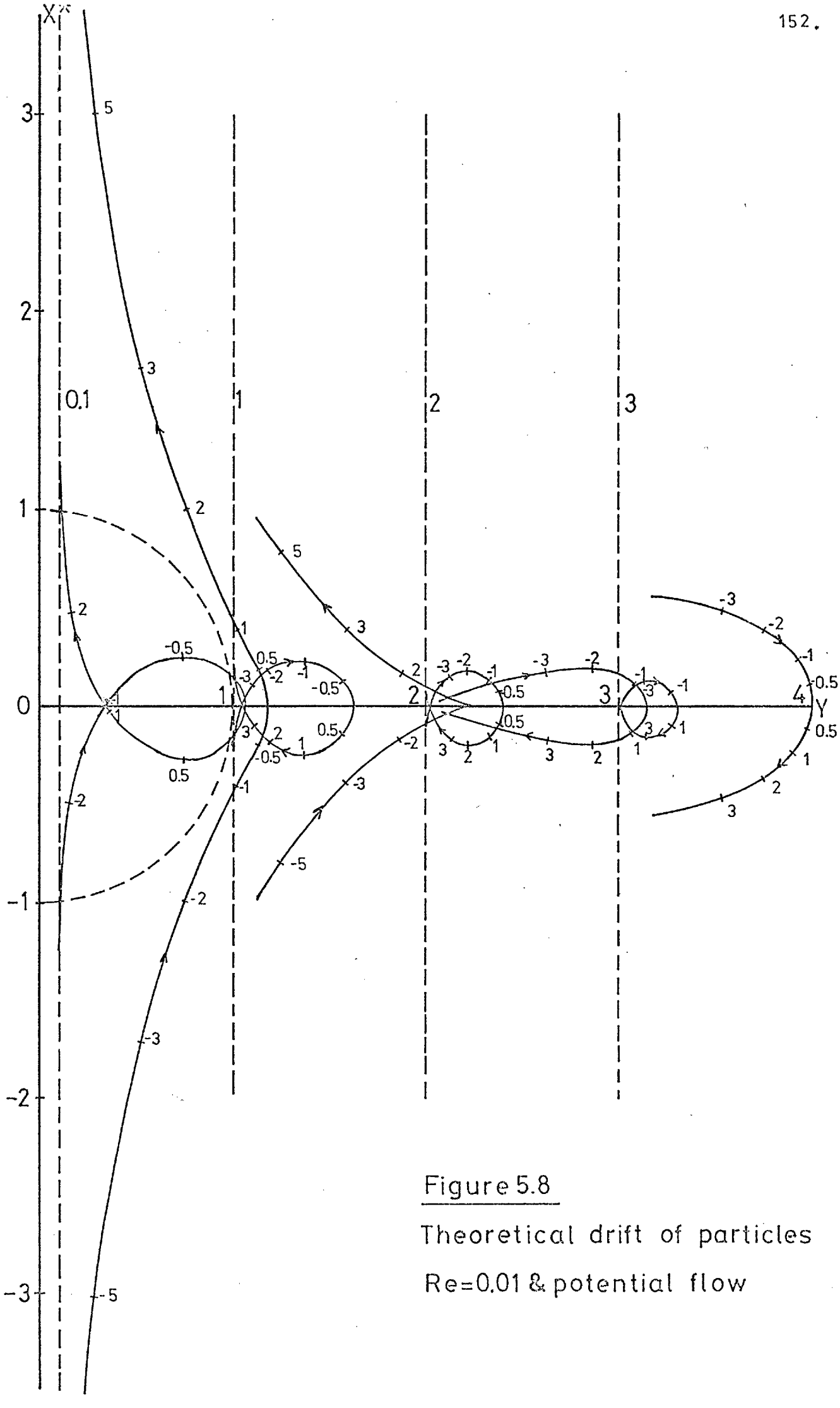


Figure 5.8

Theoretical drift of particles

Re=0.01 & potential flow

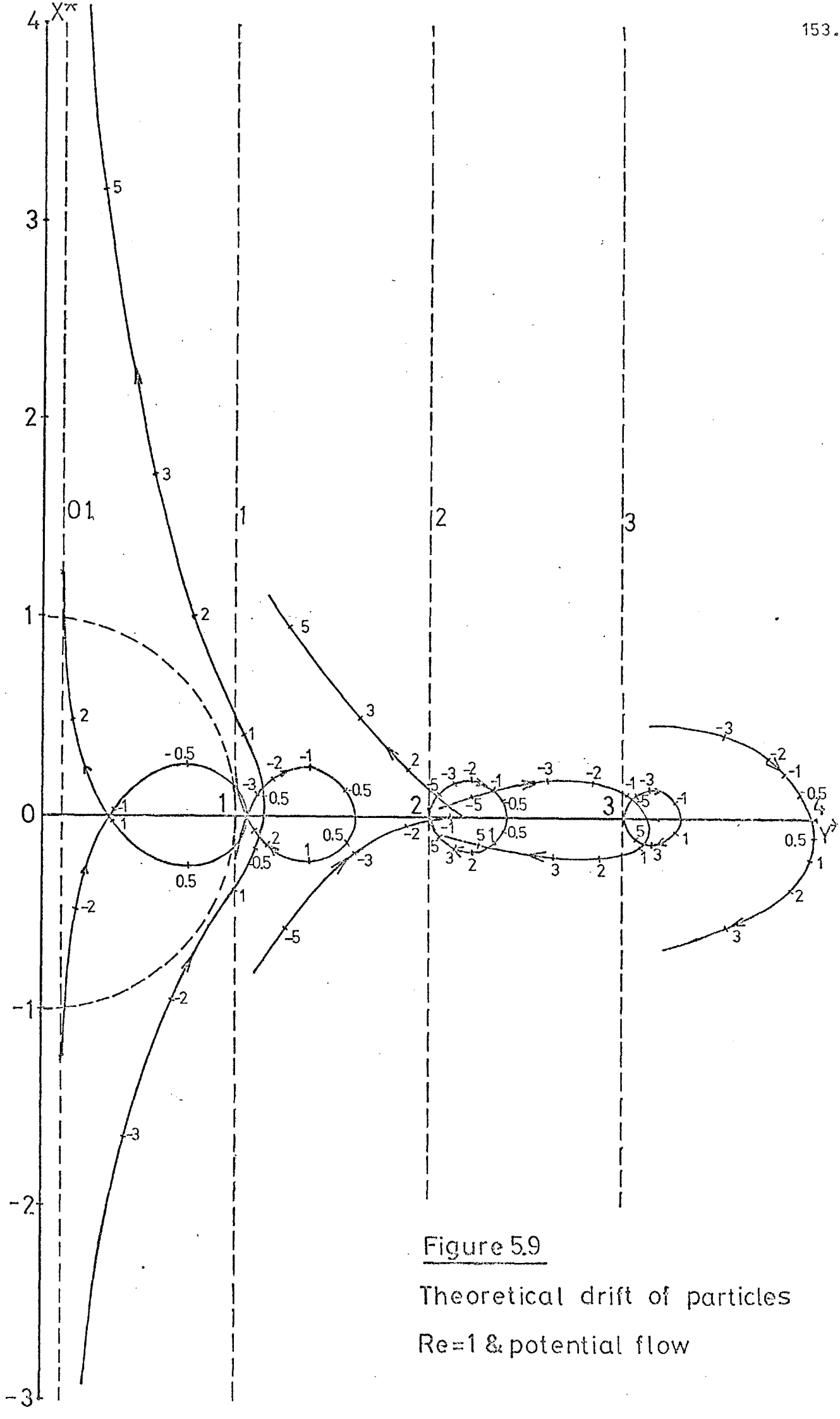


Figure 5.9

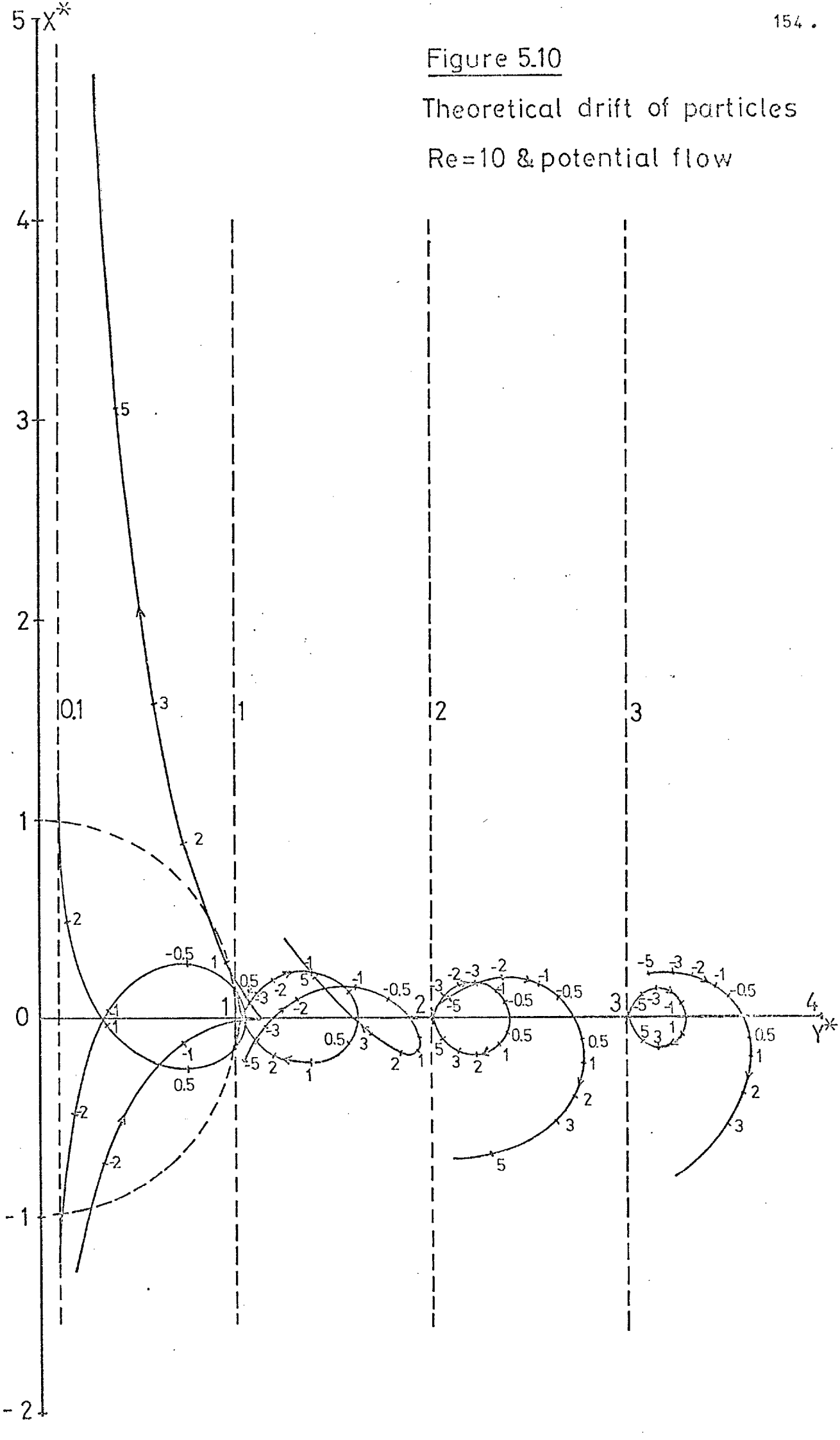
Theoretical drift of particles

Re=1 & potential flow

Figure 5.10

Theoretical drift of particles

Re=10 & potential flow



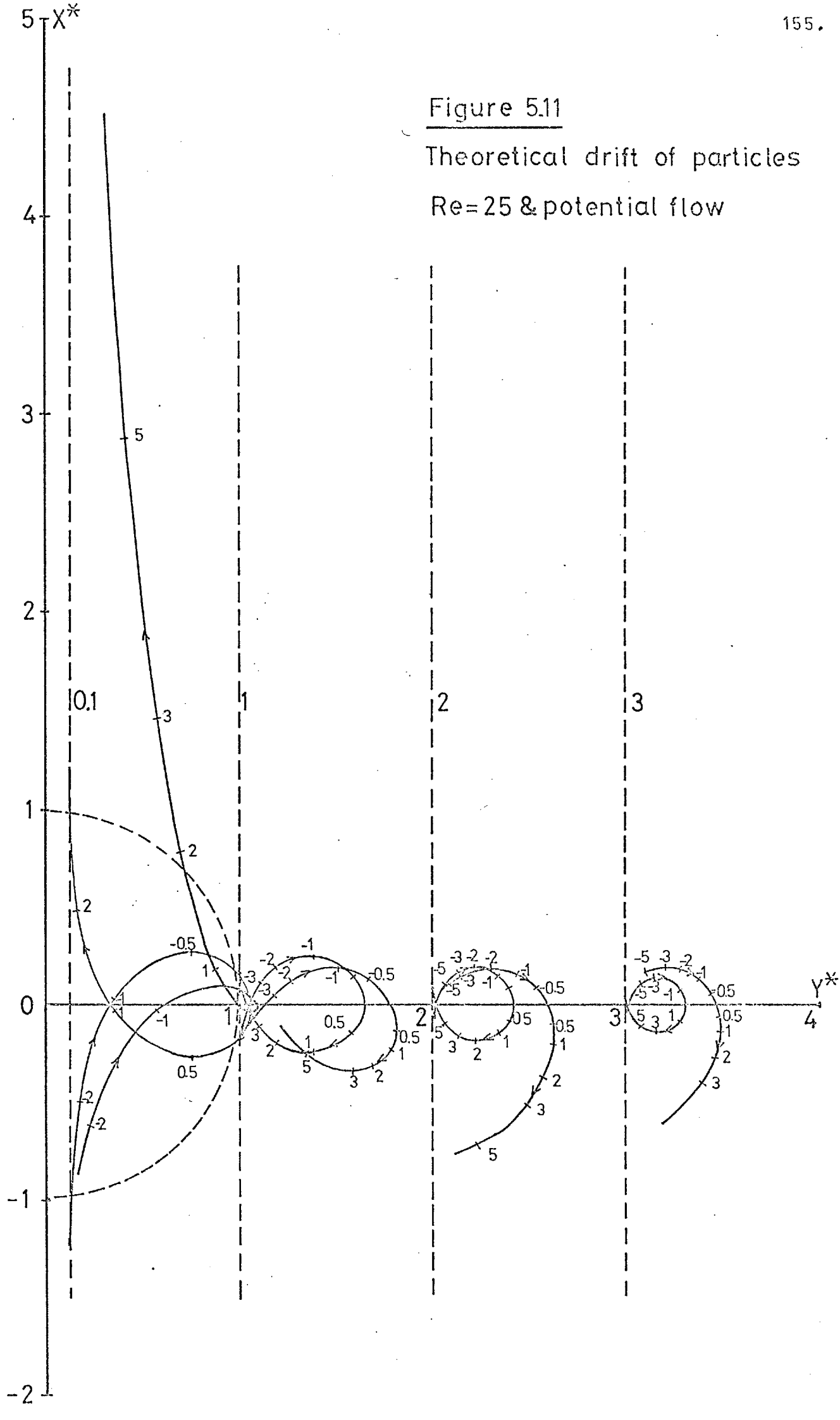


Figure 5.11

Theoretical drift of particles

Re=25 & potential flow

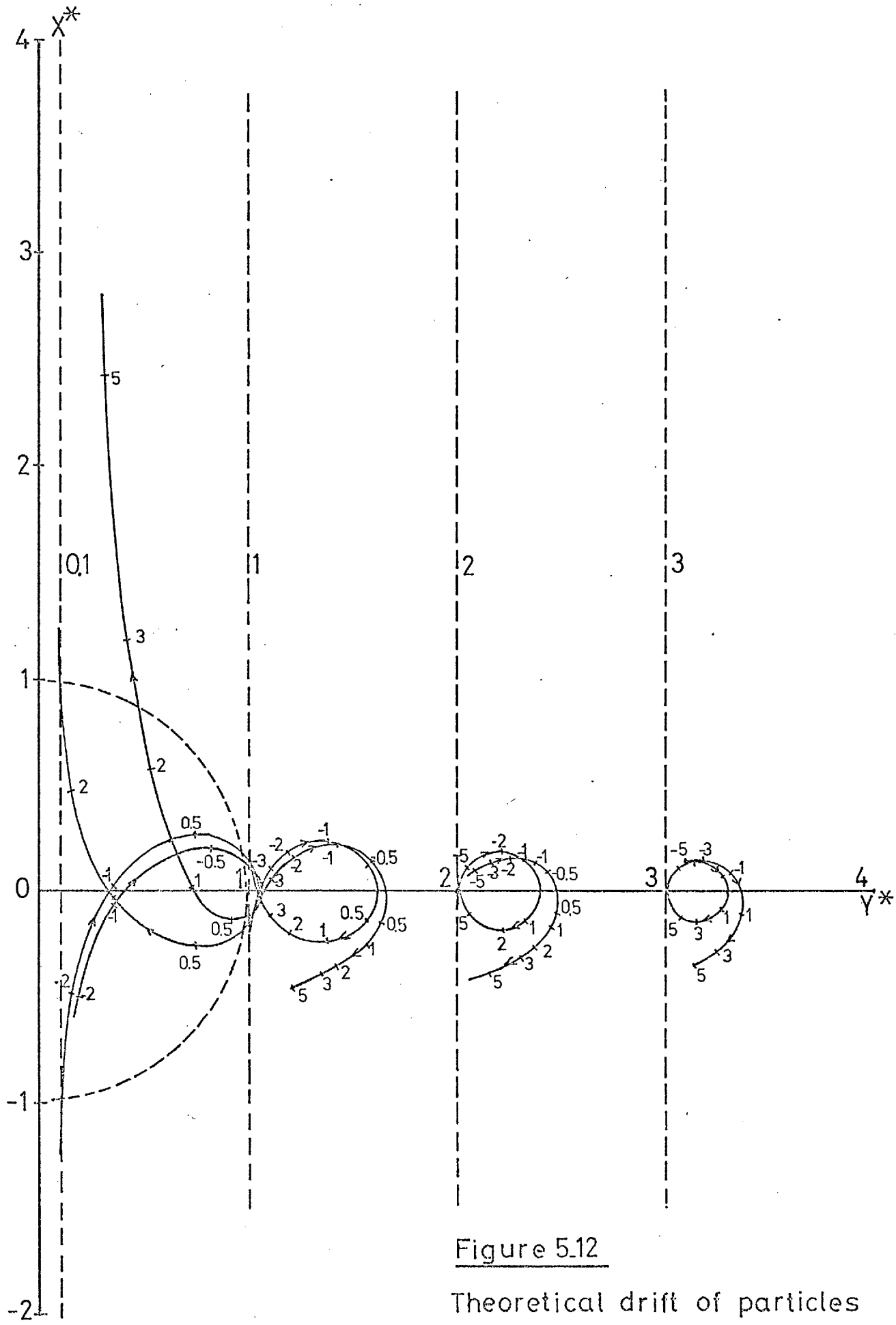


Figure 5.12

Theoretical drift of particles

Re=100 & potential flow

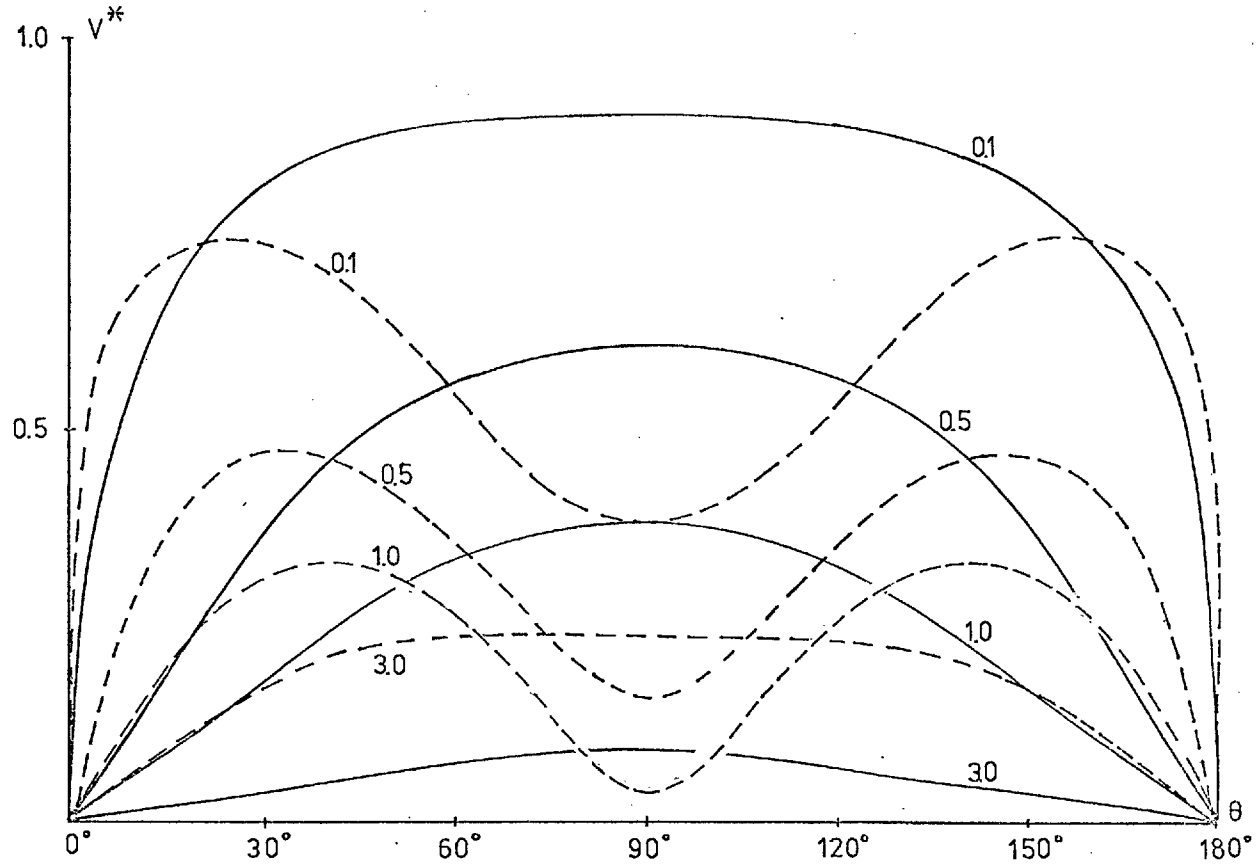


Figure 5.13.a Velocity along path lines ——— Potential flow

---- Stokes flow

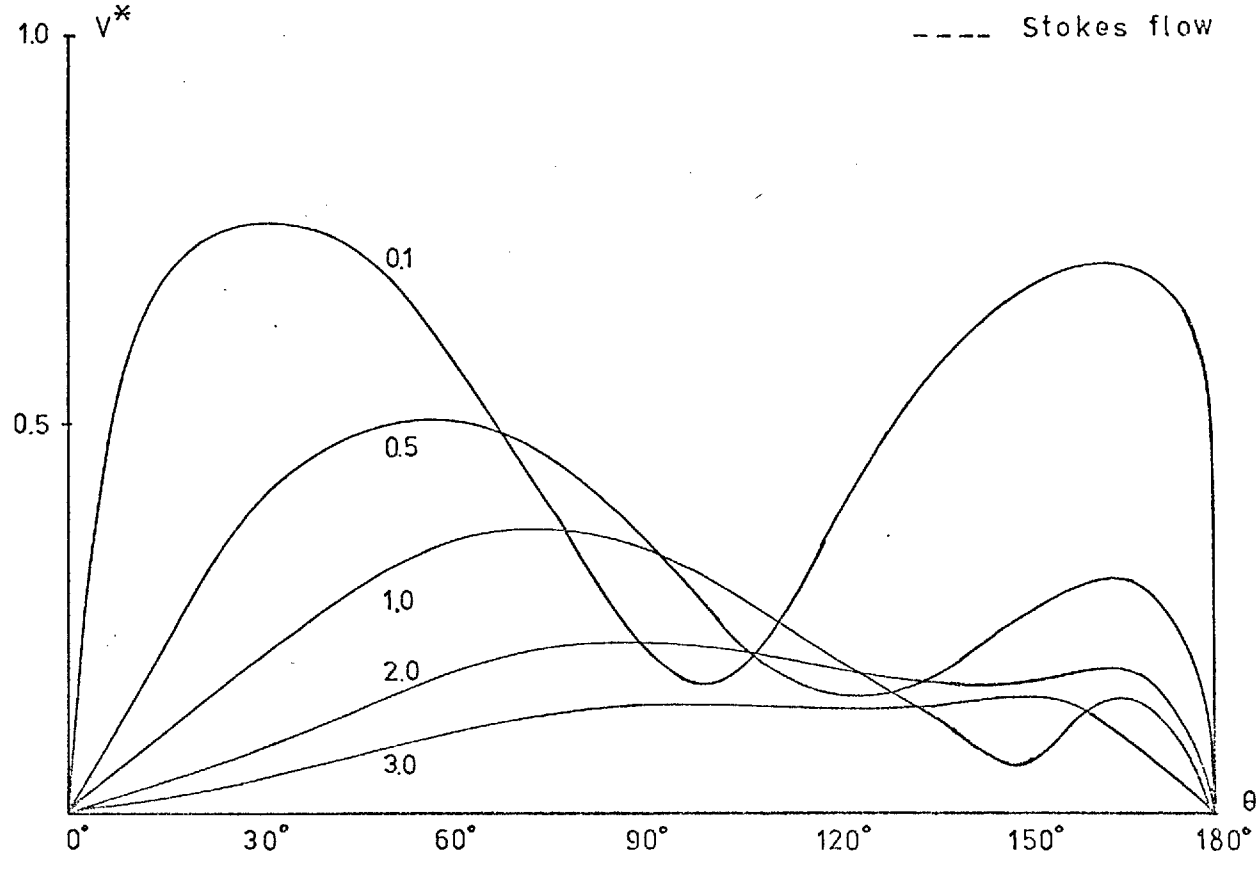


Figure 5.13.b Velocity along path lines Re=25

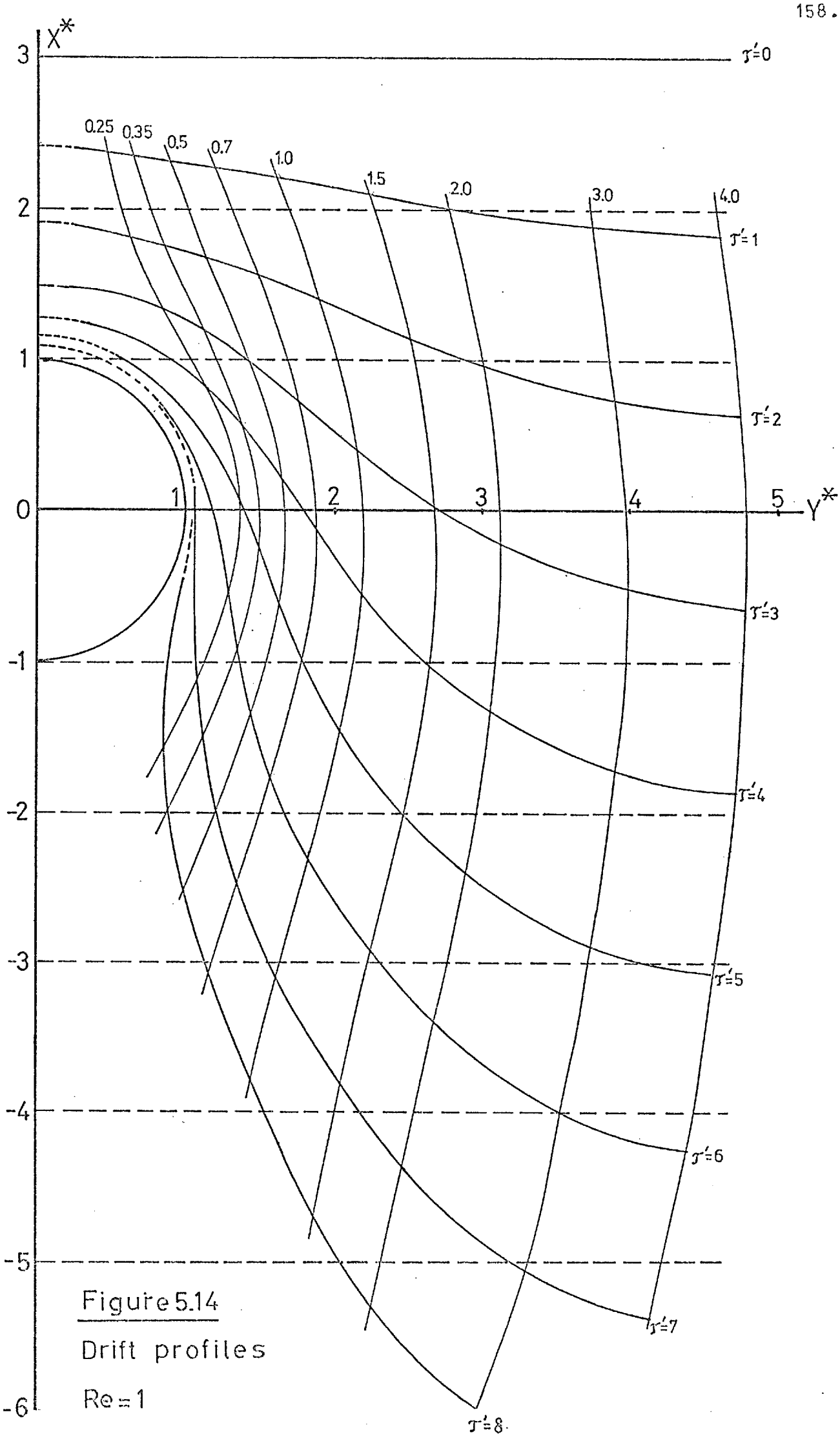


Figure 5.14

Drift profiles

Re = 1

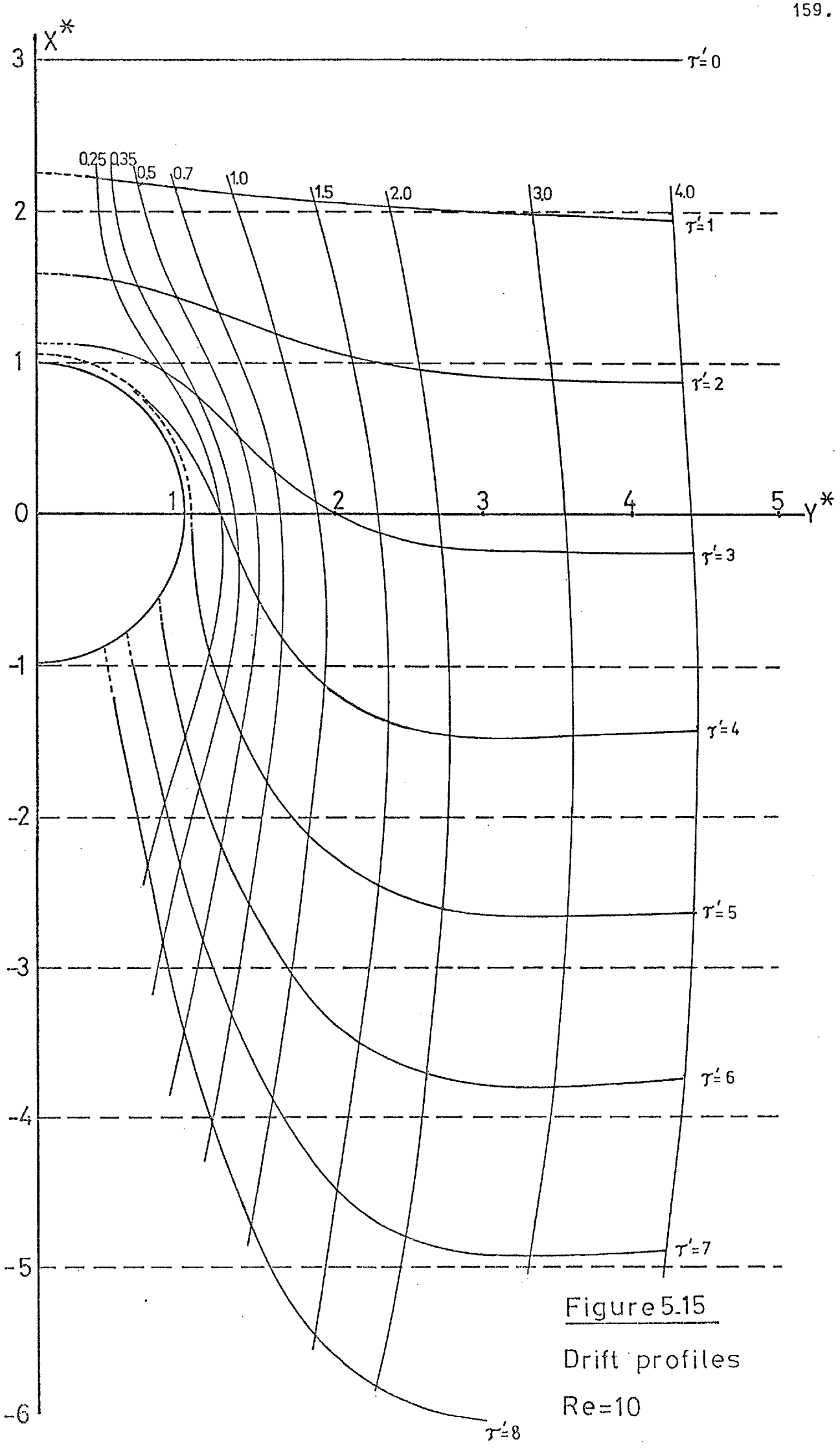


Figure 5.15

Drift profiles

Re=10

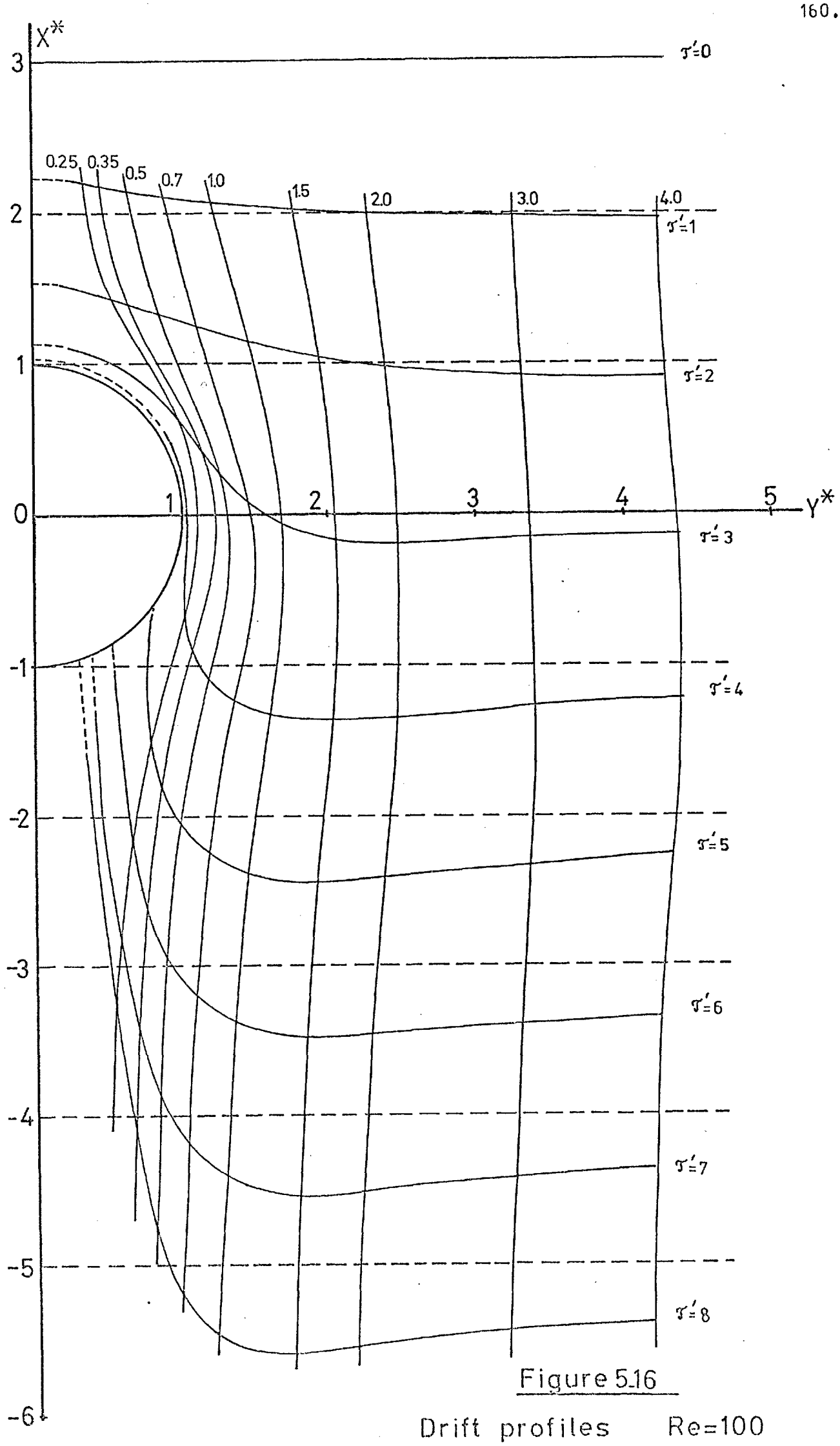


Figure 5.16

Drift profiles Re=100

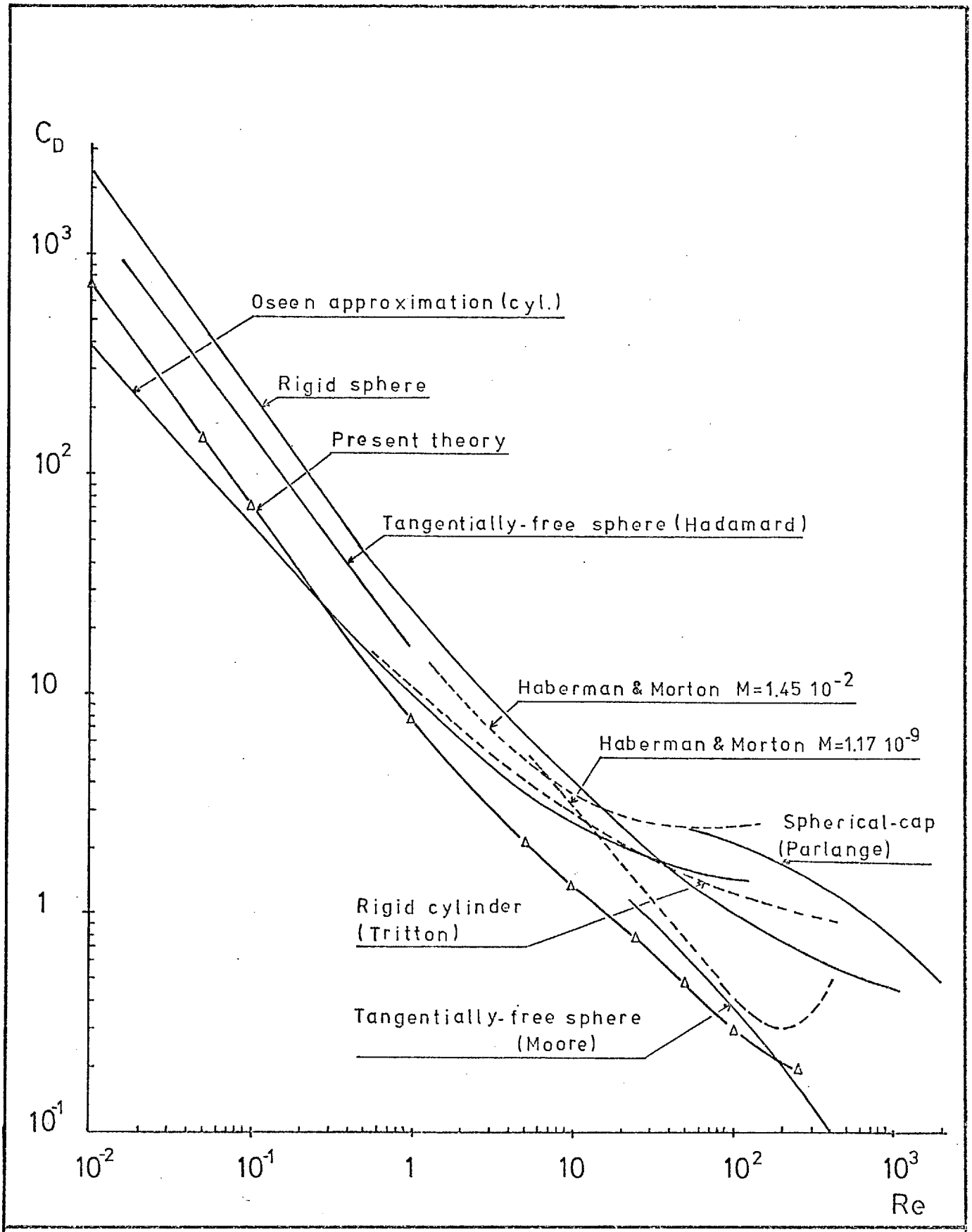


Figure 5.17 Drag coefficient as a function of the Reynolds number.

_____ theory

\- - - - - experiments

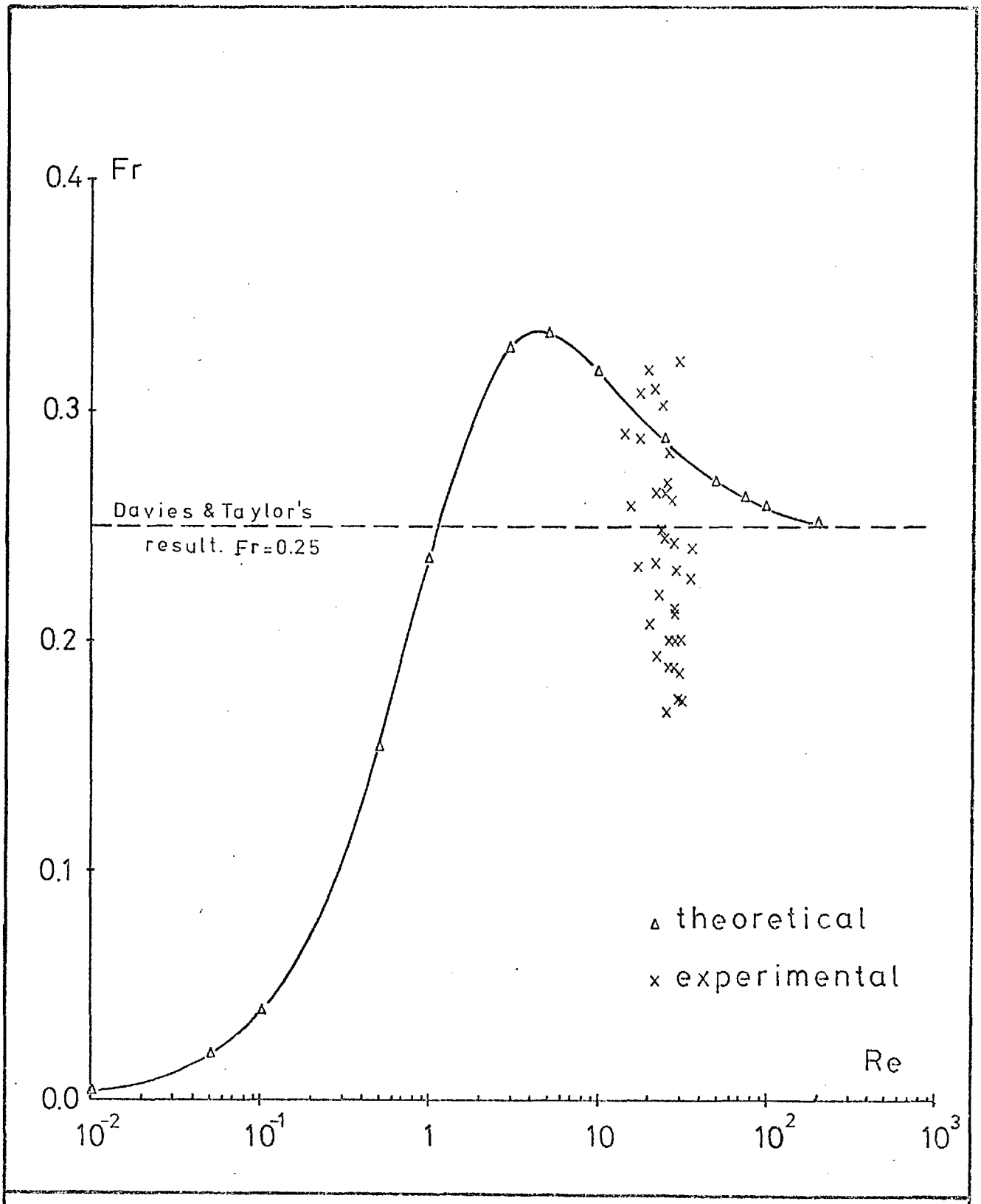


Figure 5.18 Variation of the Froude number as a function of the Reynolds number for a bubble rising in a 2-D fluidised bed.

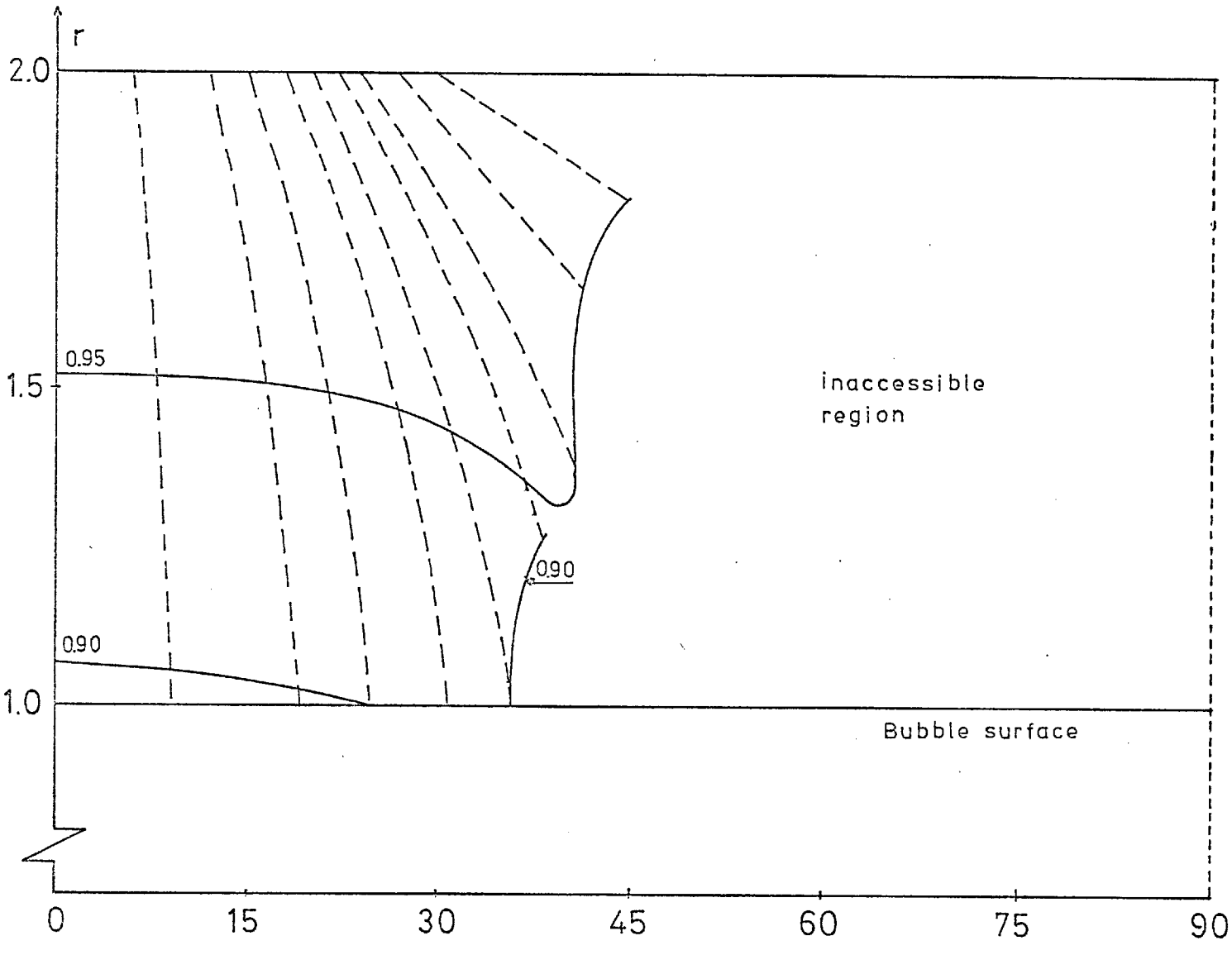


Figure 5_19

Re=1

___ lines $1/\gamma$=cst

___ integration path

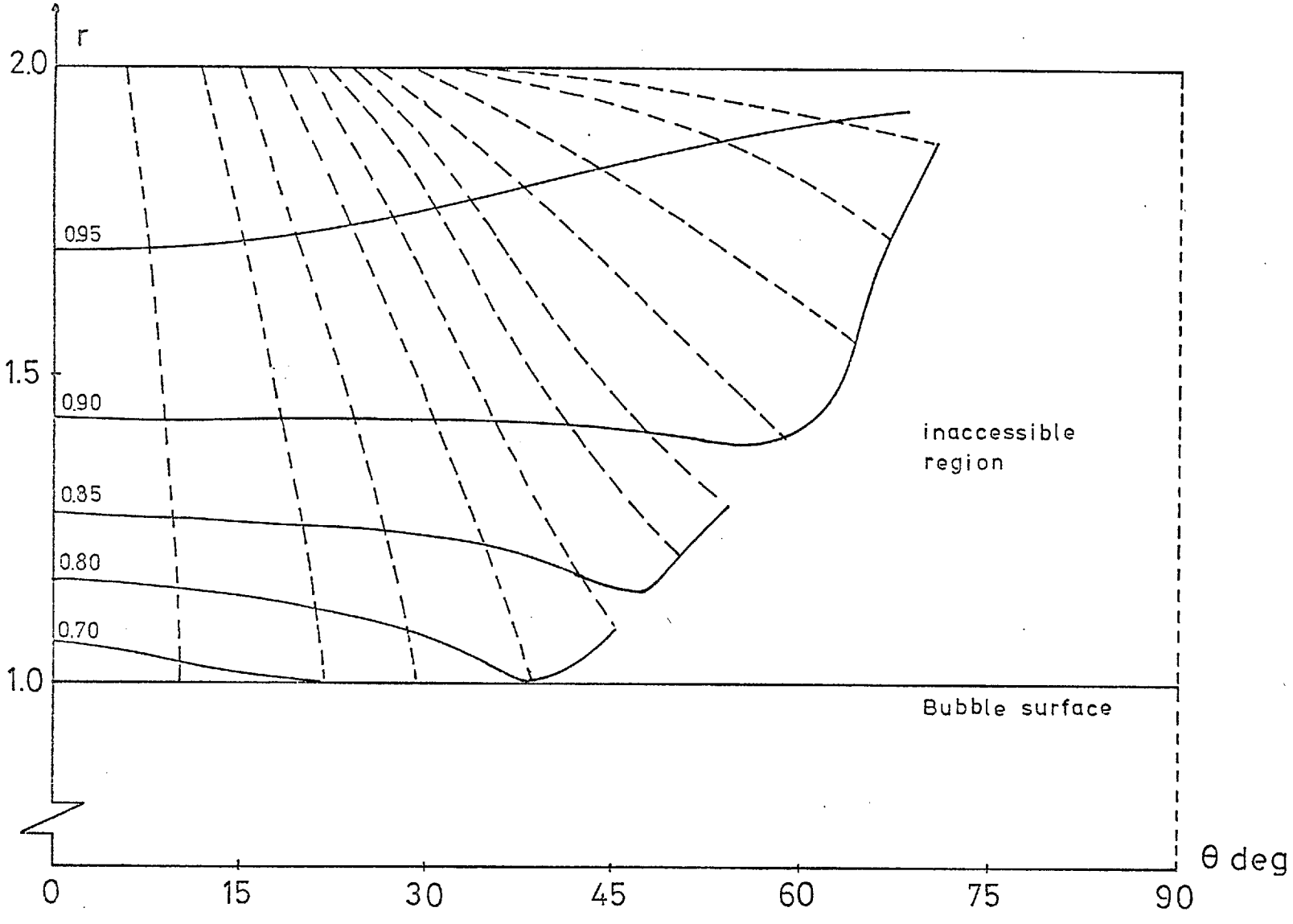


Figure 5.20

Re=10

—— lines $1/\psi$=cst

– – – integration path.

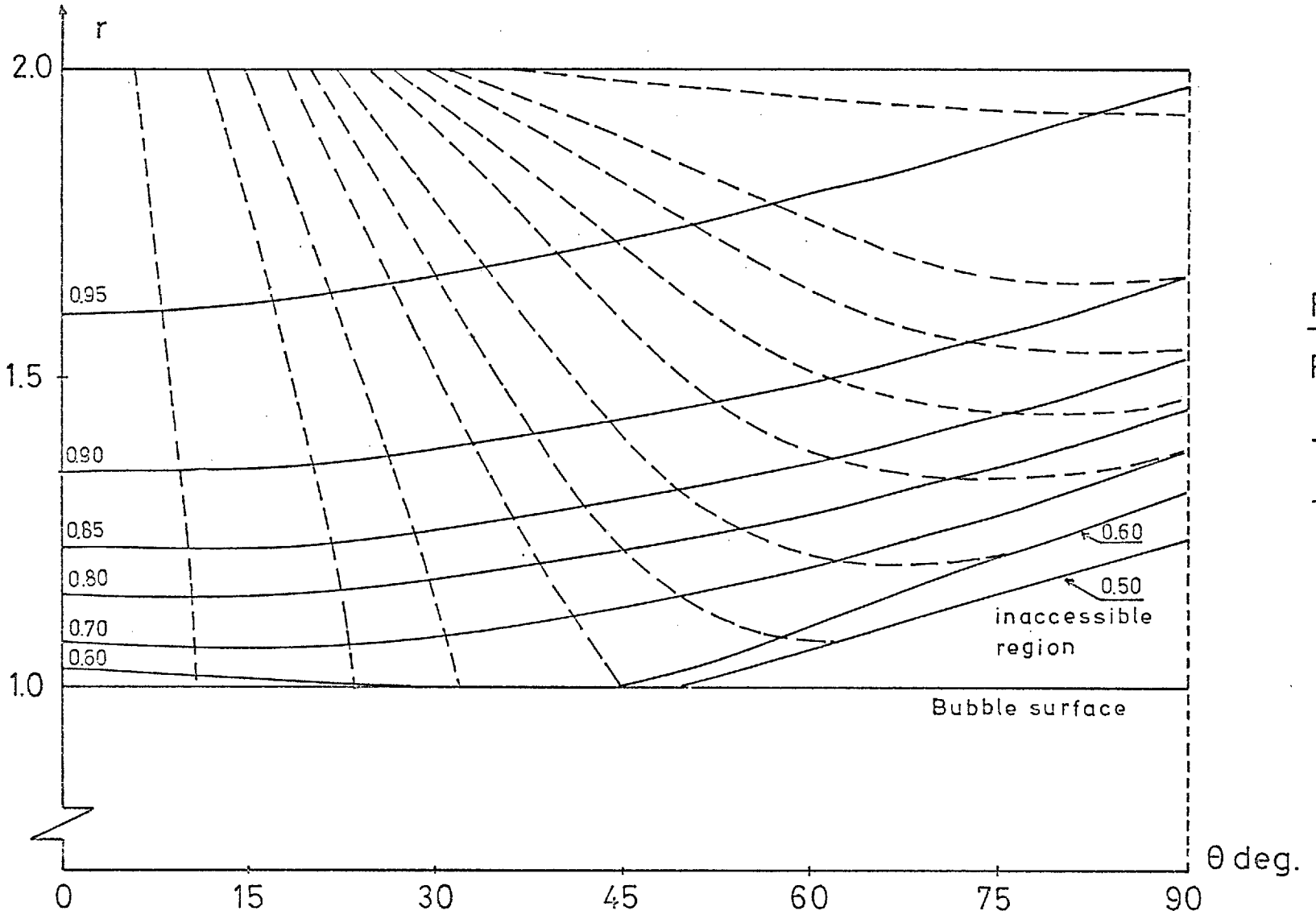


Figure 5.21

Re=100

___ lines $1/\psi$=cst

--- integration path

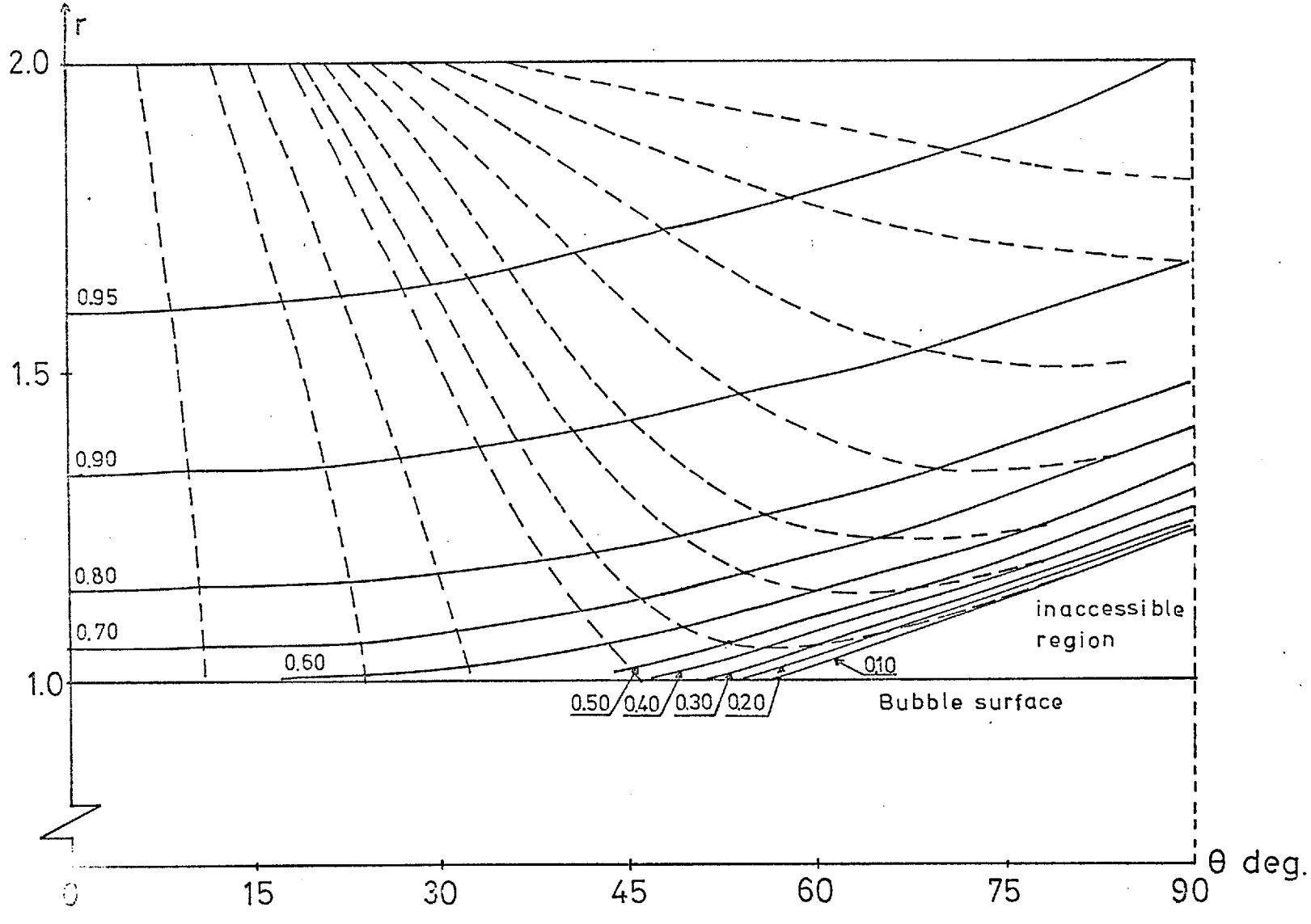


Figure 5.22

Jackson's solution

___ lines $1/\gamma$=cst

--- integration path

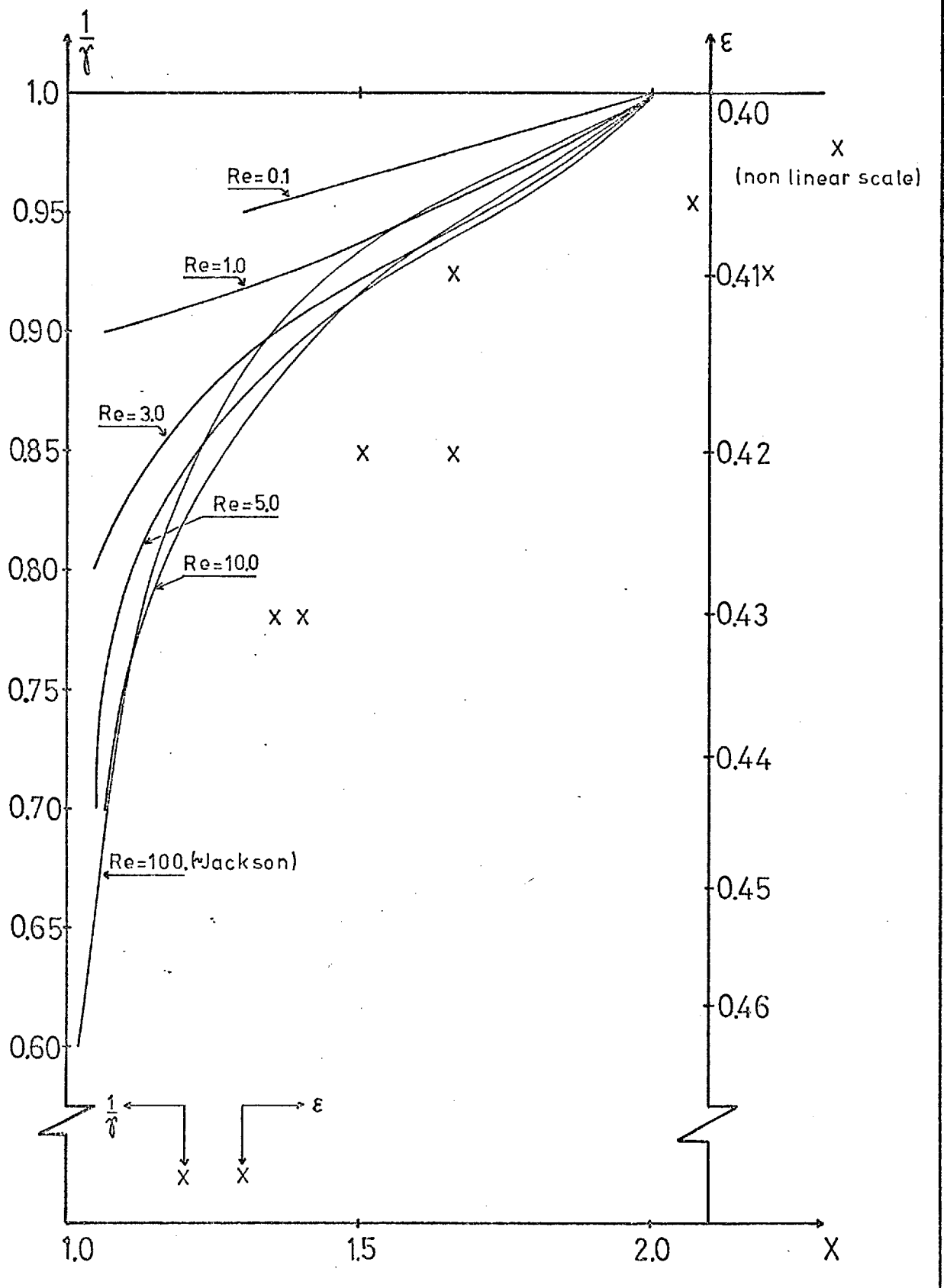


Figure 5.23

Variations of the function $\frac{1}{\gamma}=\frac{\beta}{\beta_0}$ and of the voidage ε on the axis of the bubble. ($\theta=0$)

x : experimental Lockett & Harrison (7)

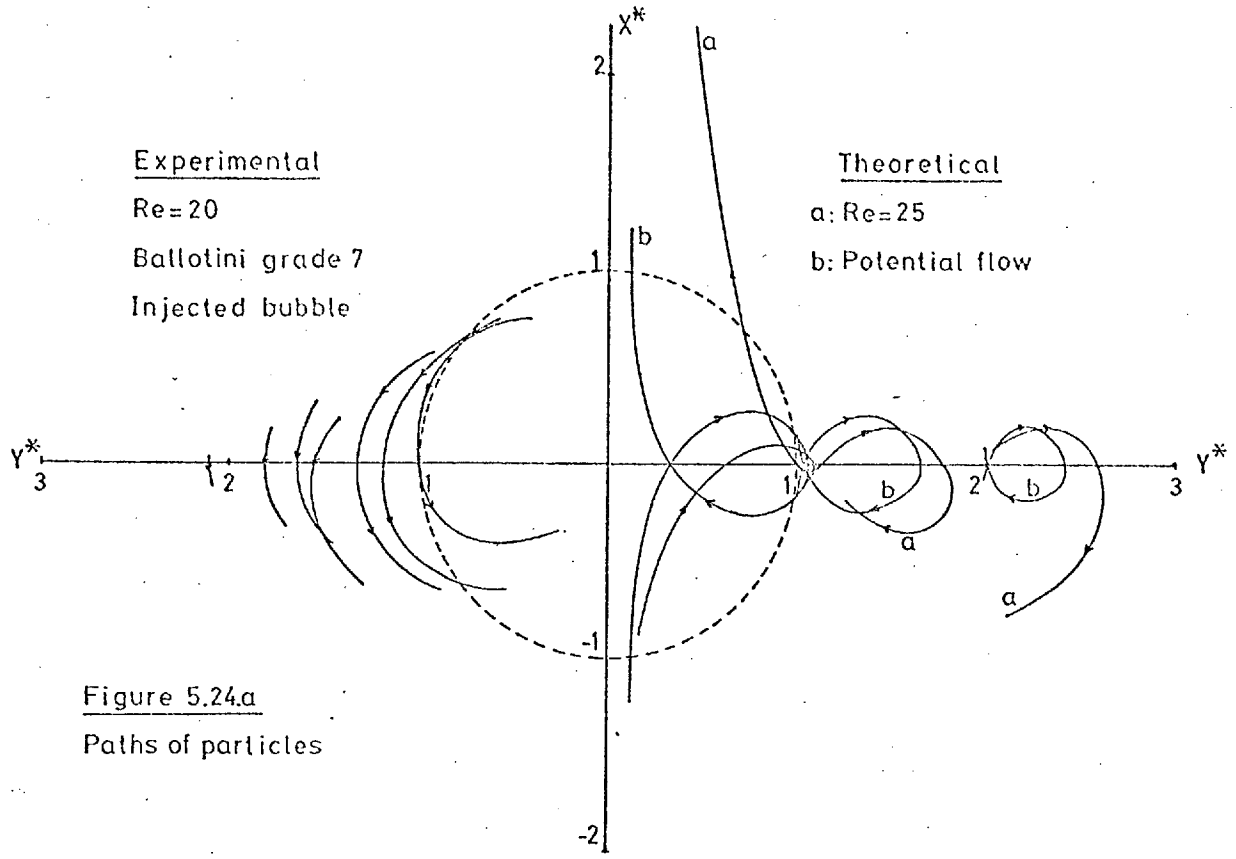


Figure 5.24.a
Paths of particles

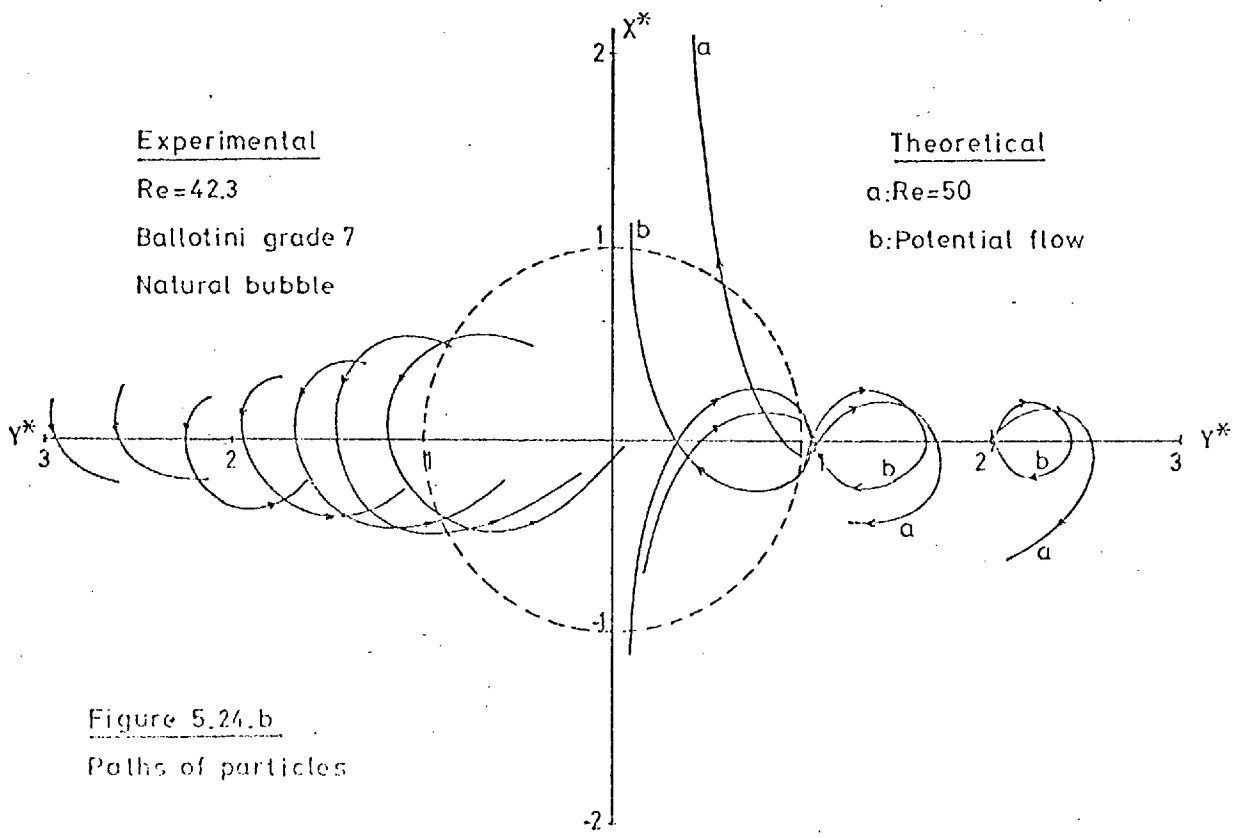


Figure 5.24.b
Paths of particles

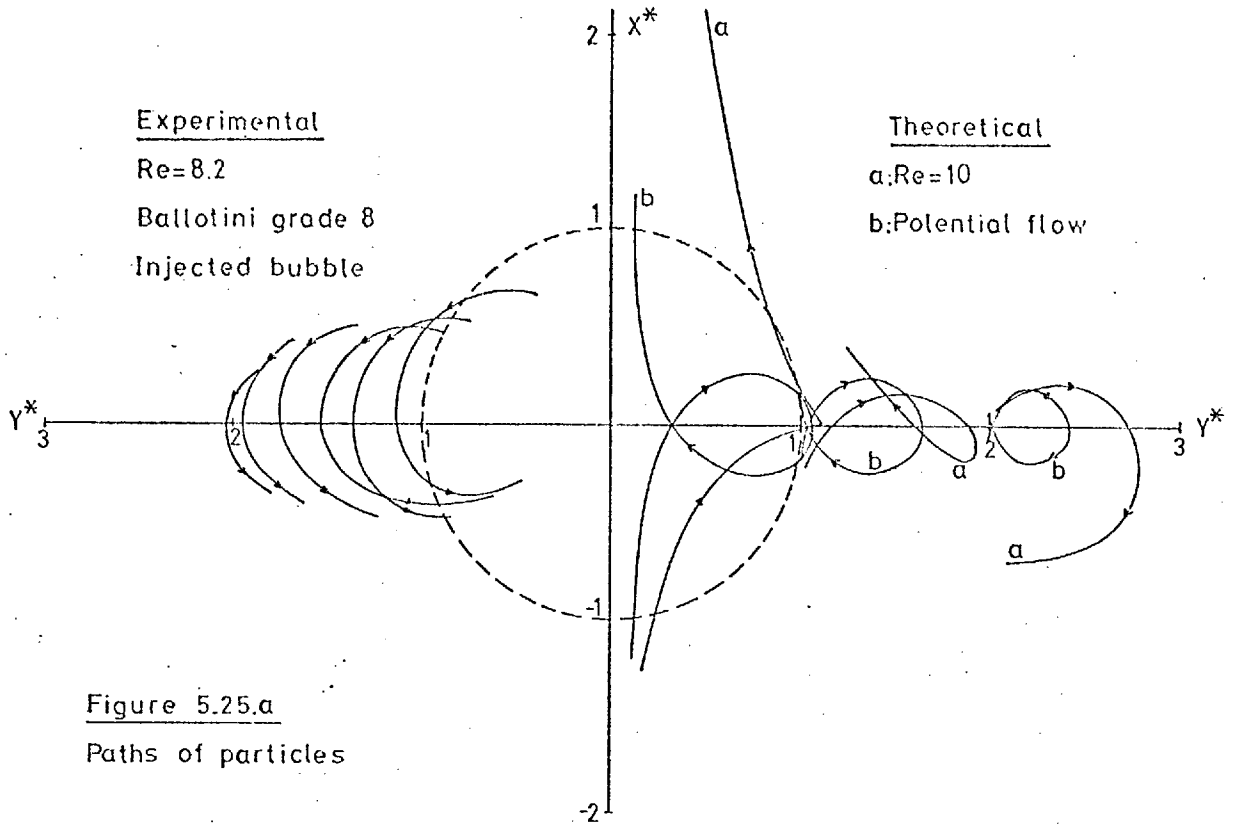


Figure 5.25.a
Paths of particles

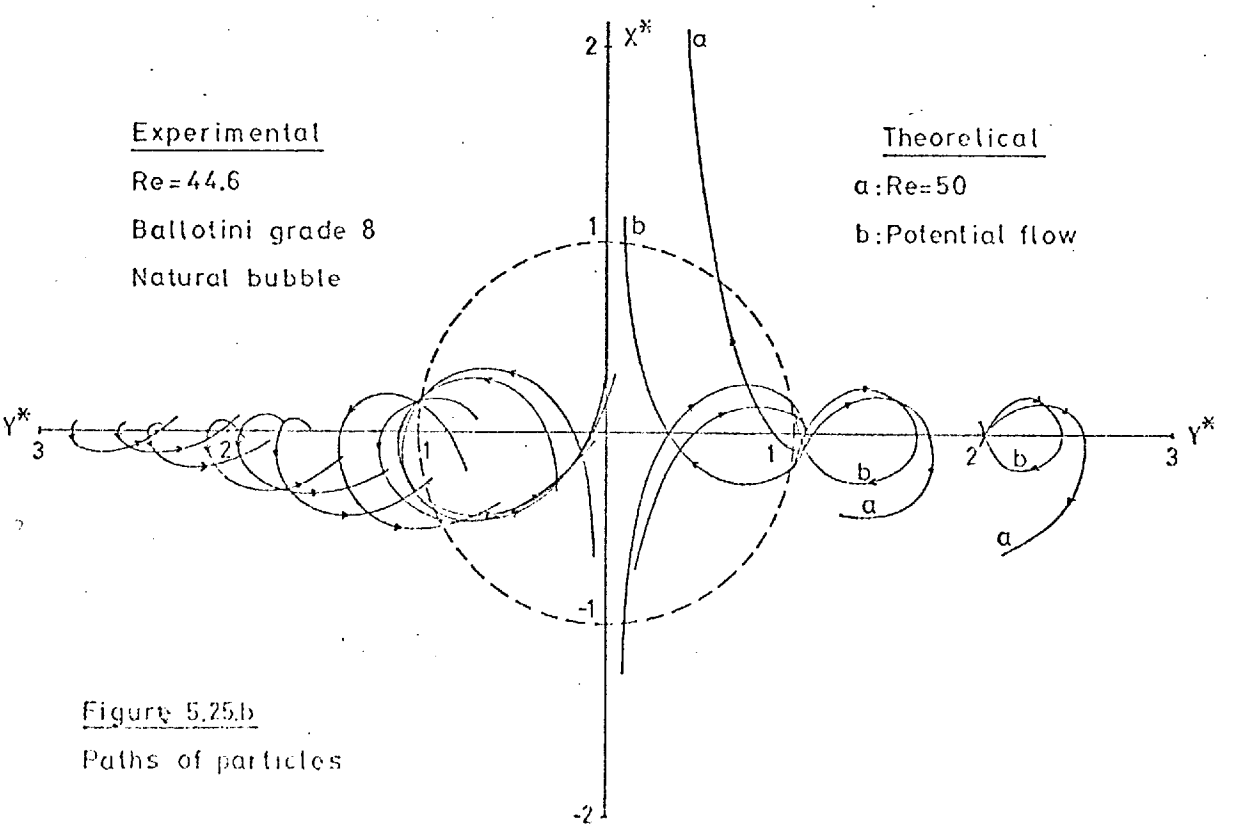


Figure 5.25.b
Paths of particles

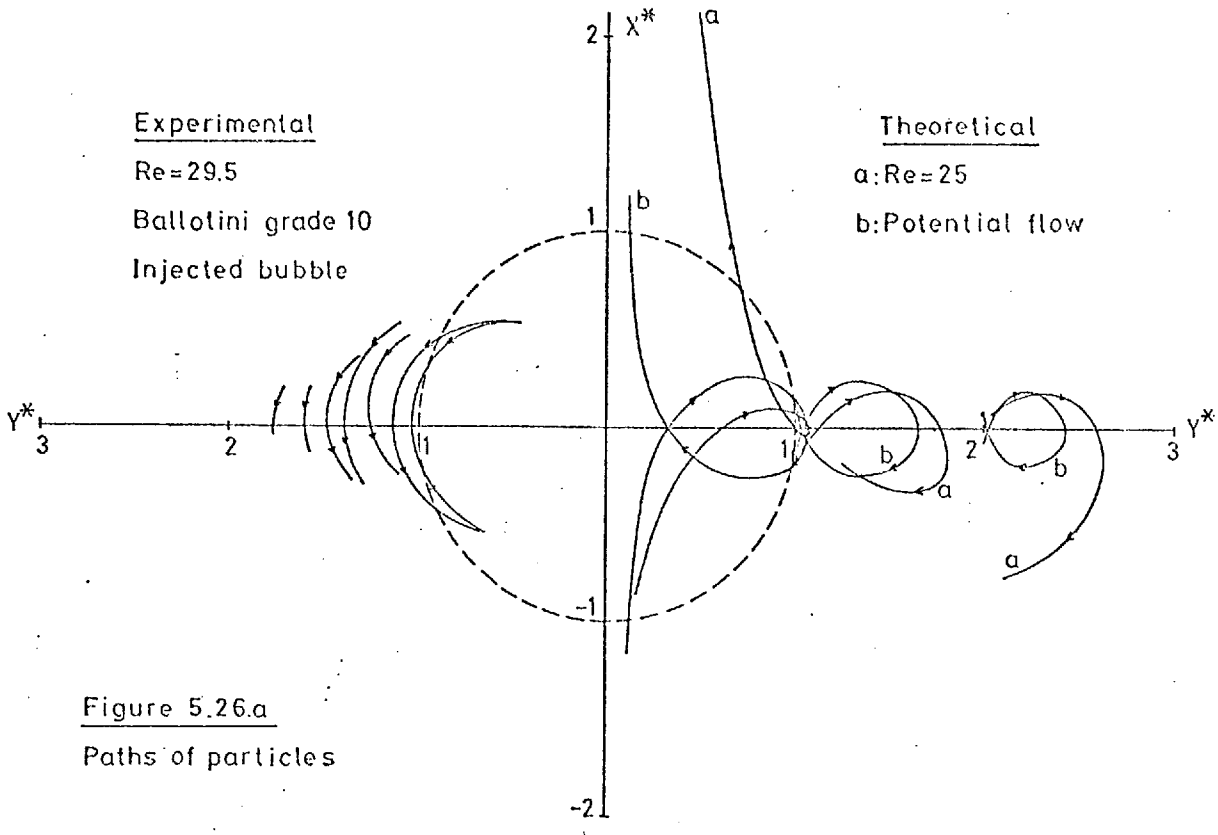


Figure 5.26.a
Paths of particles

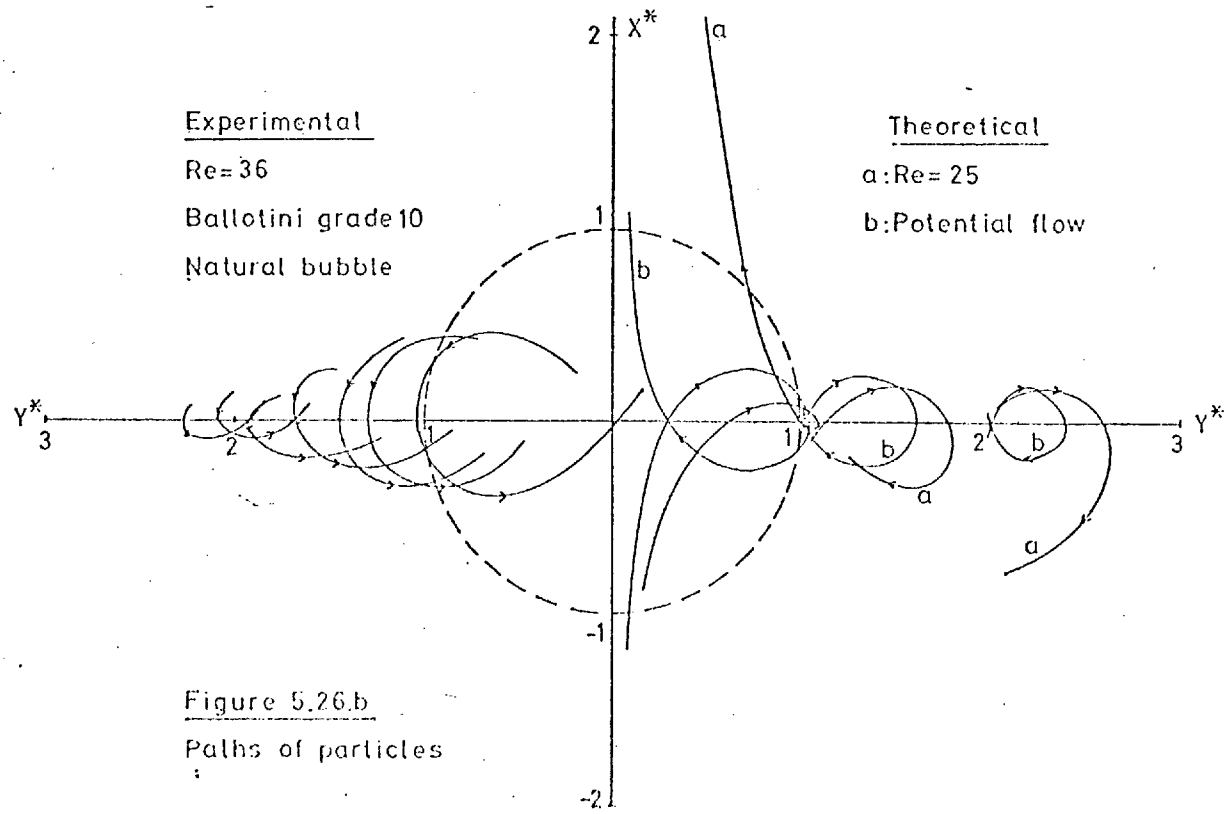


Figure 5.26.b
Paths of particles

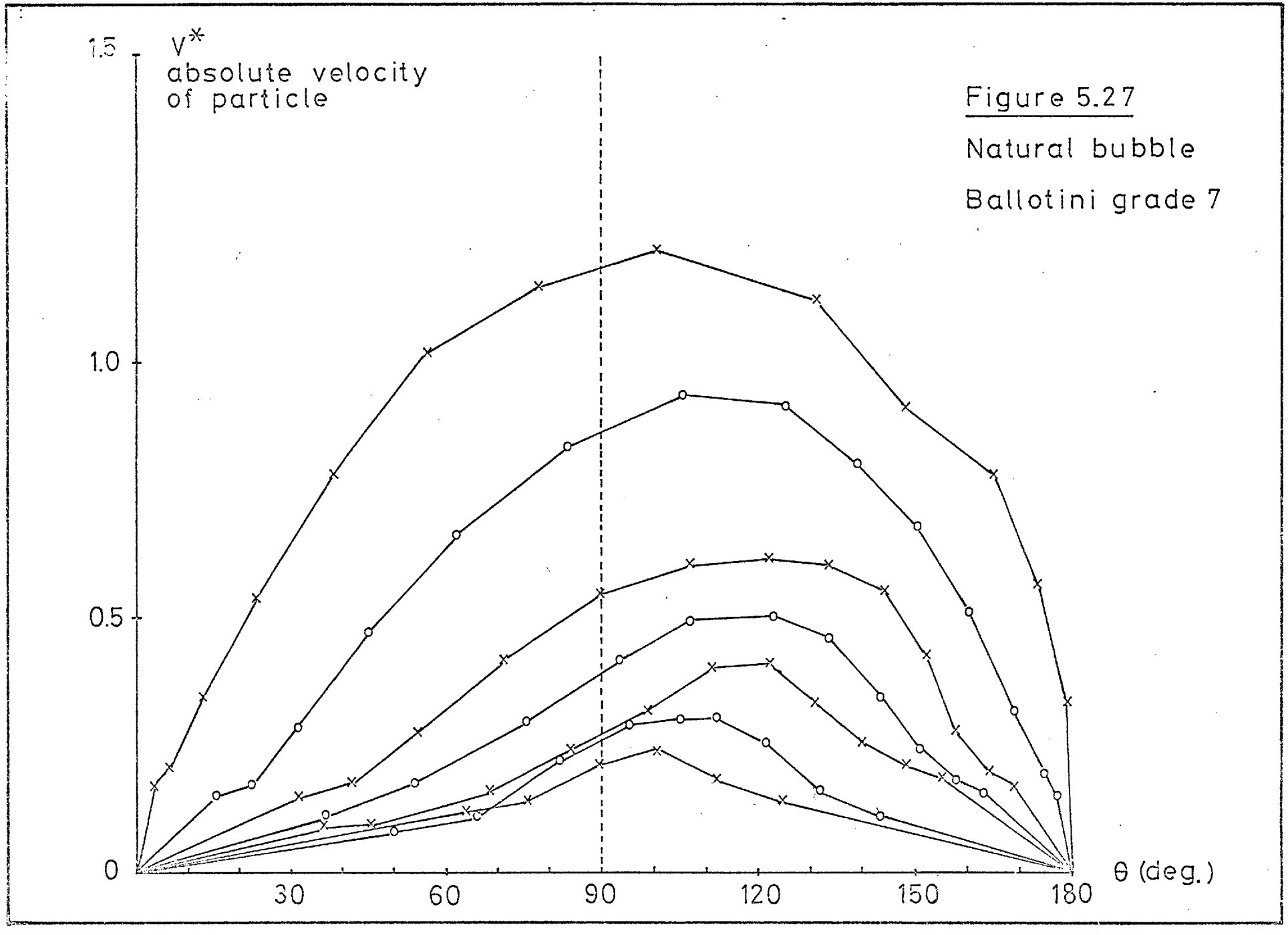


Figure 5.27

Natural bubble

Ballotini grade 7

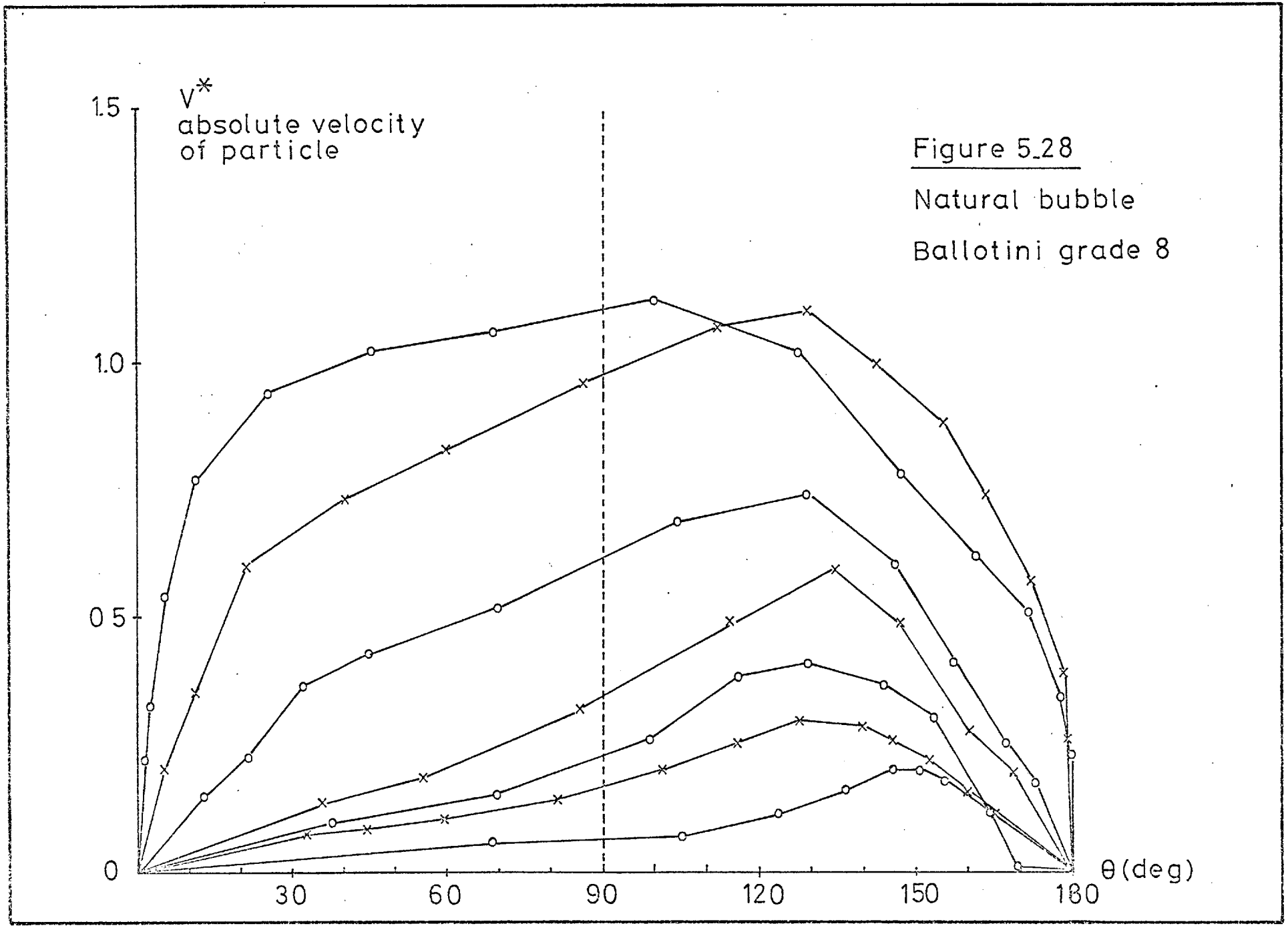


Figure 5.28

Natural bubble

Ballotini grade 8

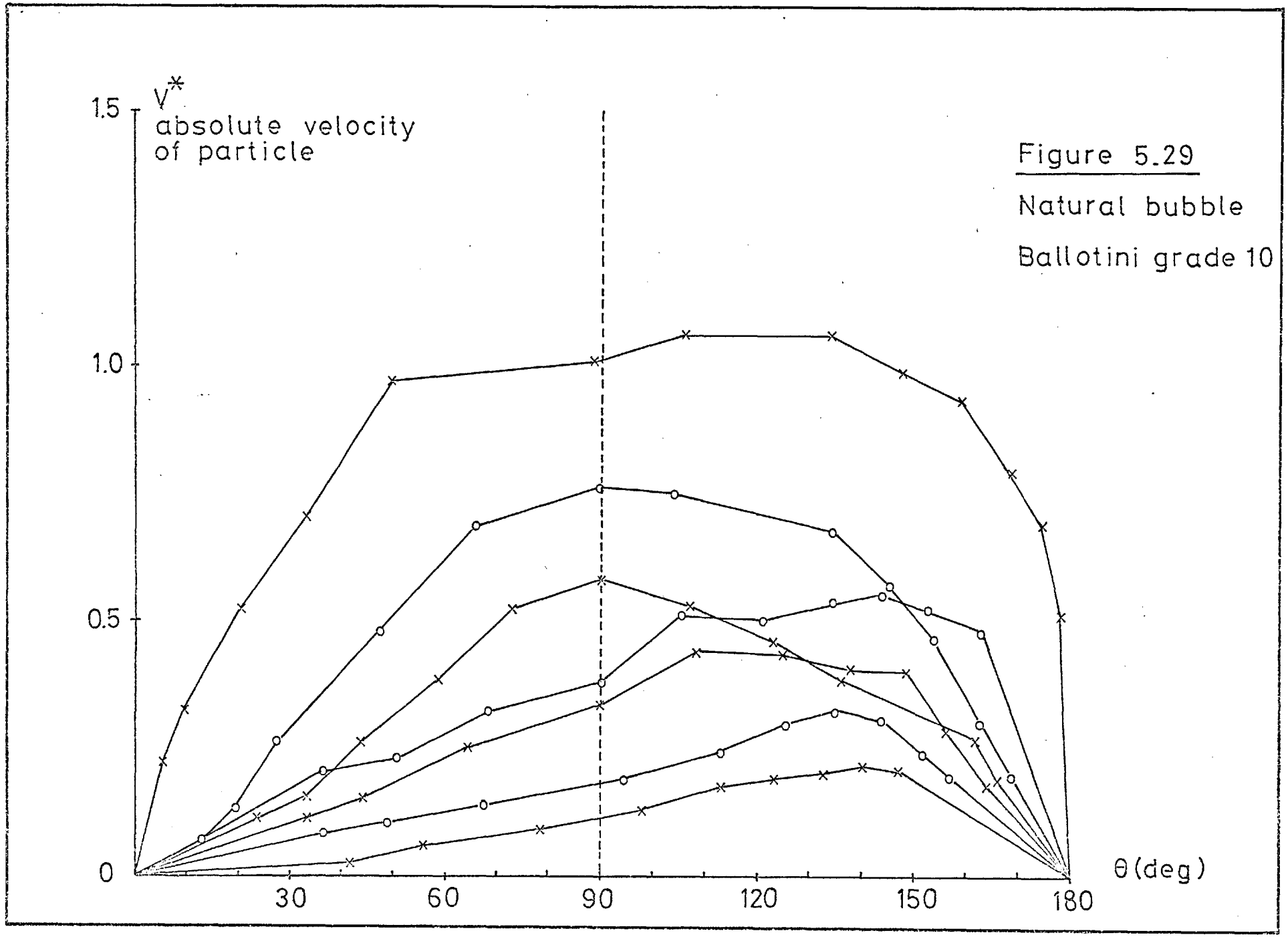


Figure 5.29

Natural bubble

Ballotini grade 10

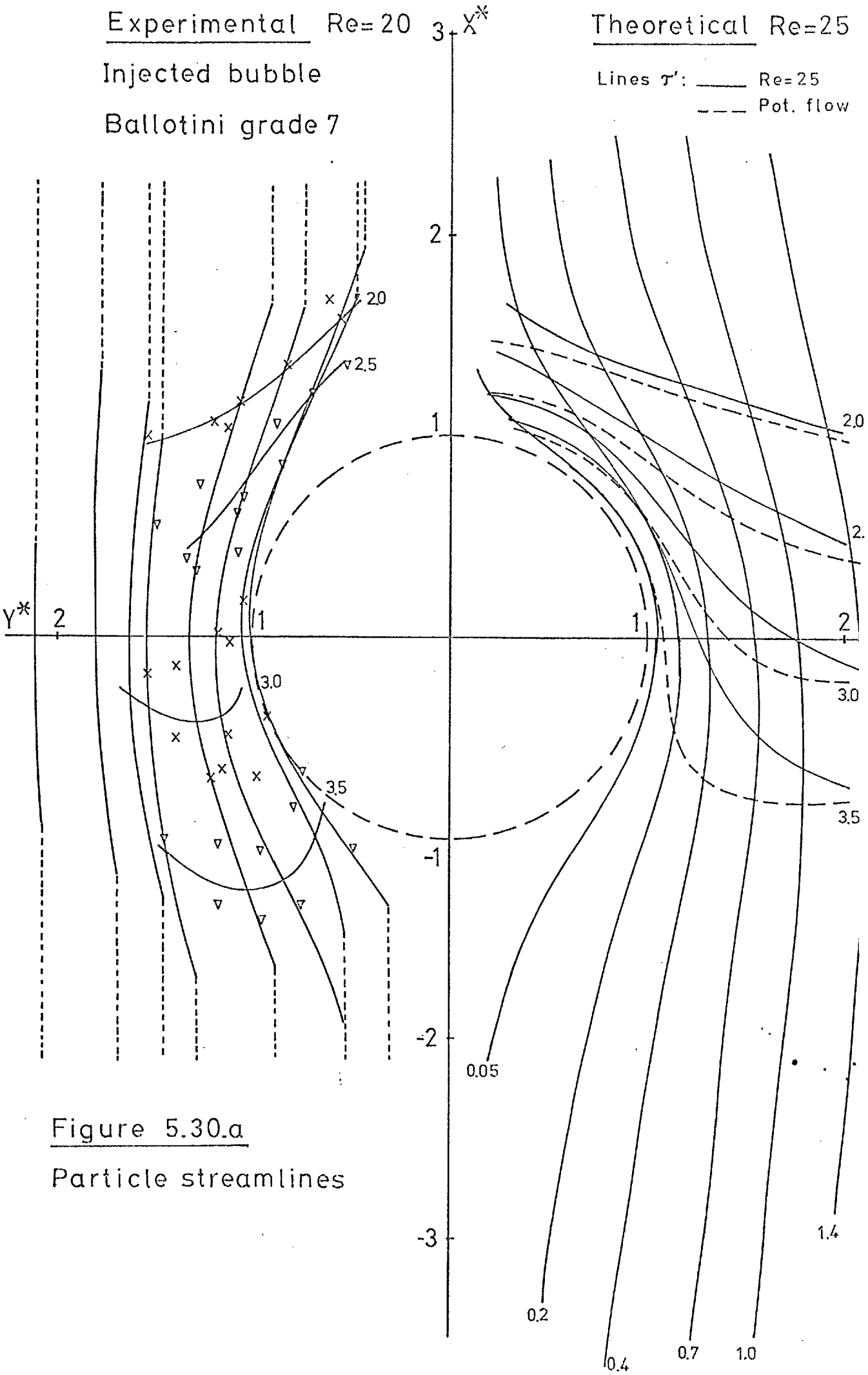


Figure 5.30.a

Particle streamlines

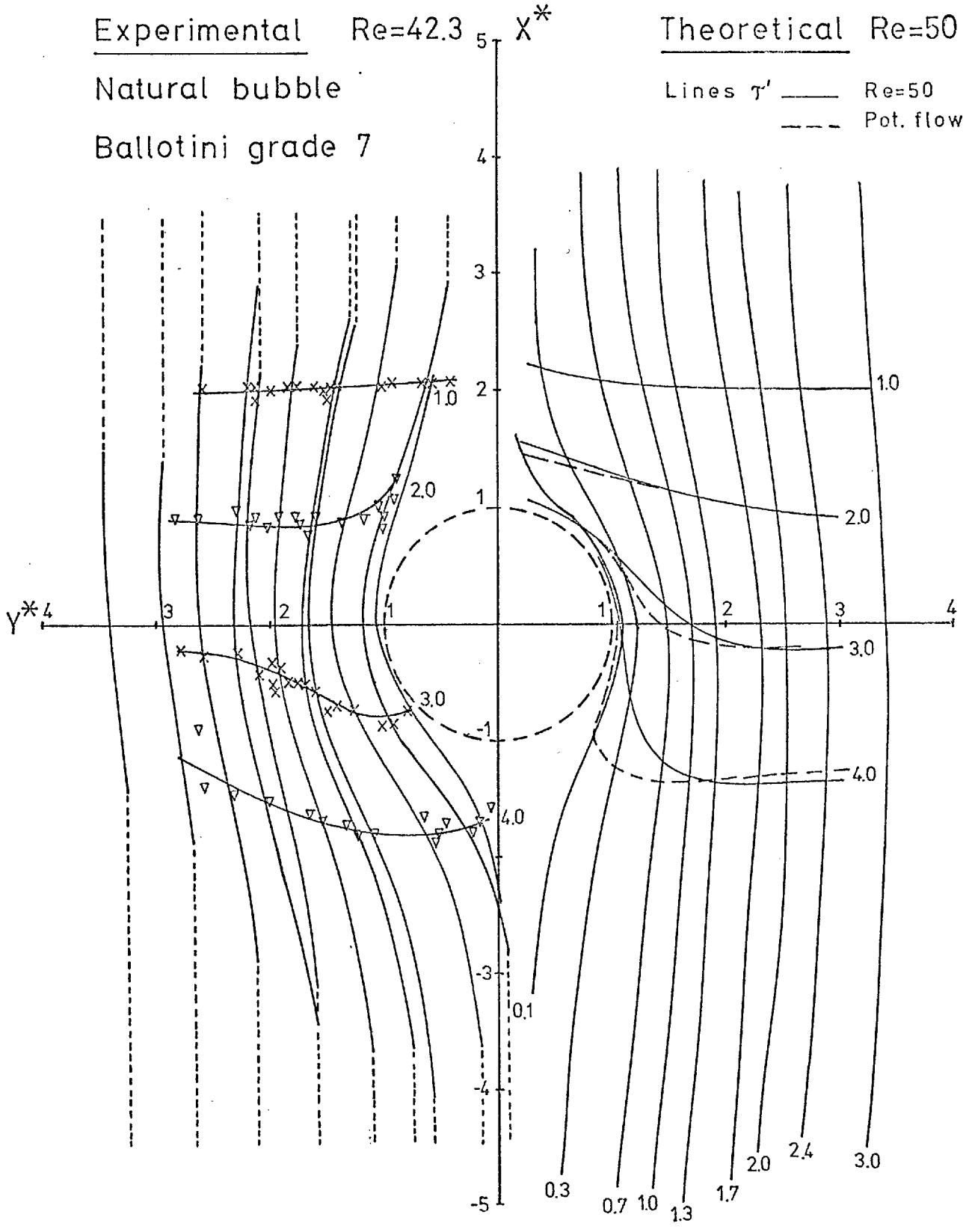


Figure 5.30.b

Particle streamlines

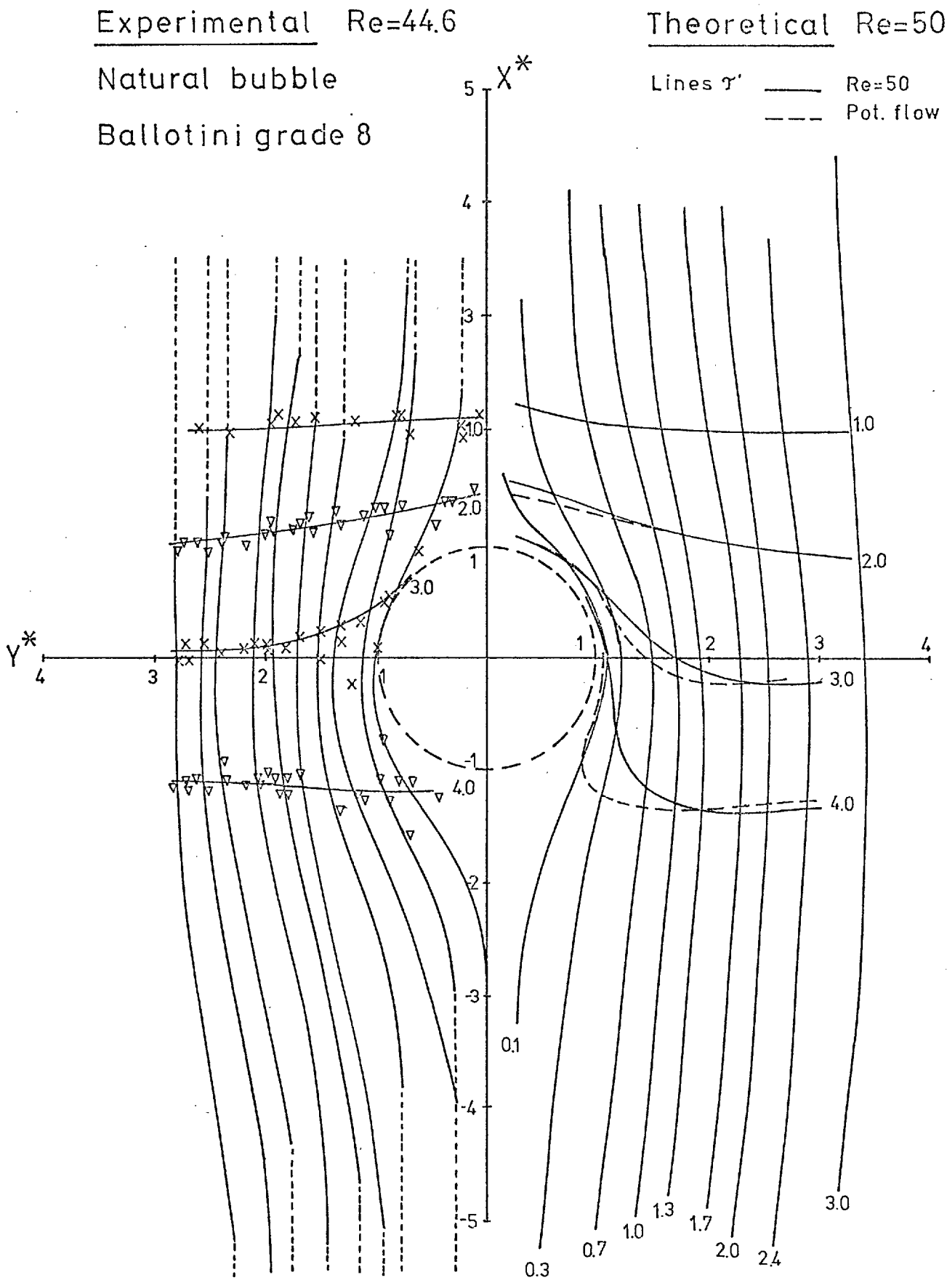


Figure 5.31

Particle streamlines

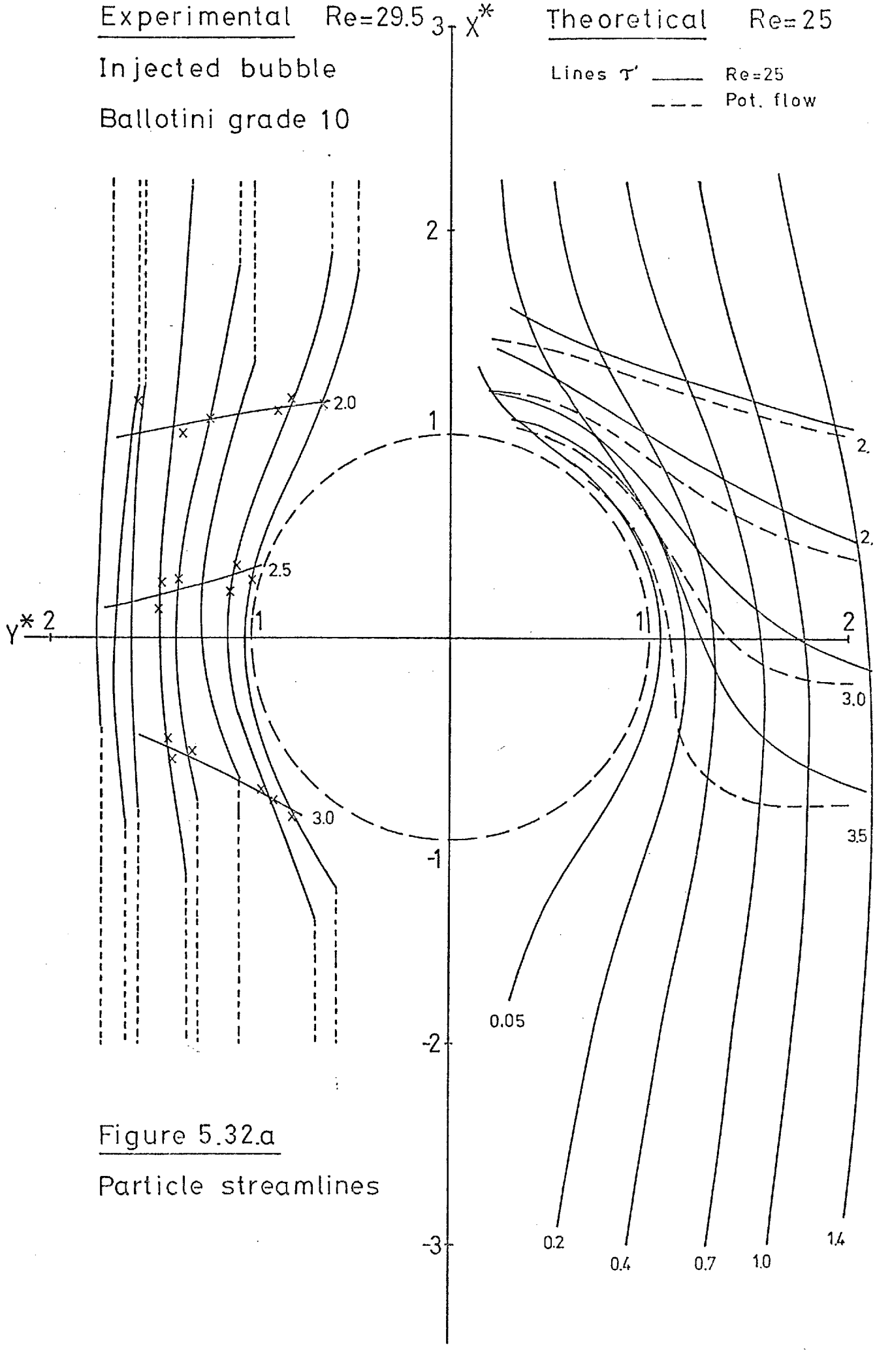


Figure 5.32.a

Particle streamlines

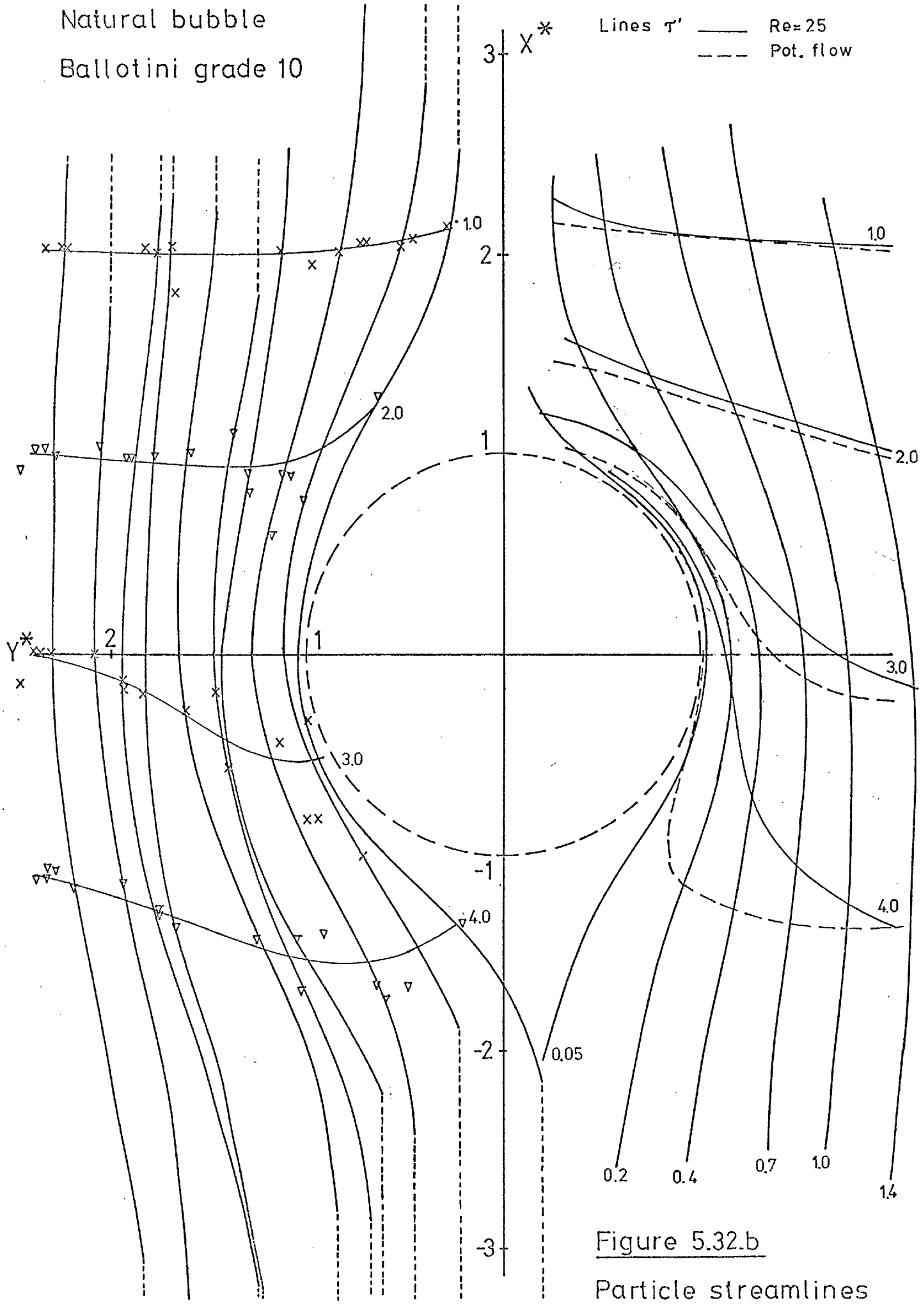


Figure 5.32.b

Particle streamlines

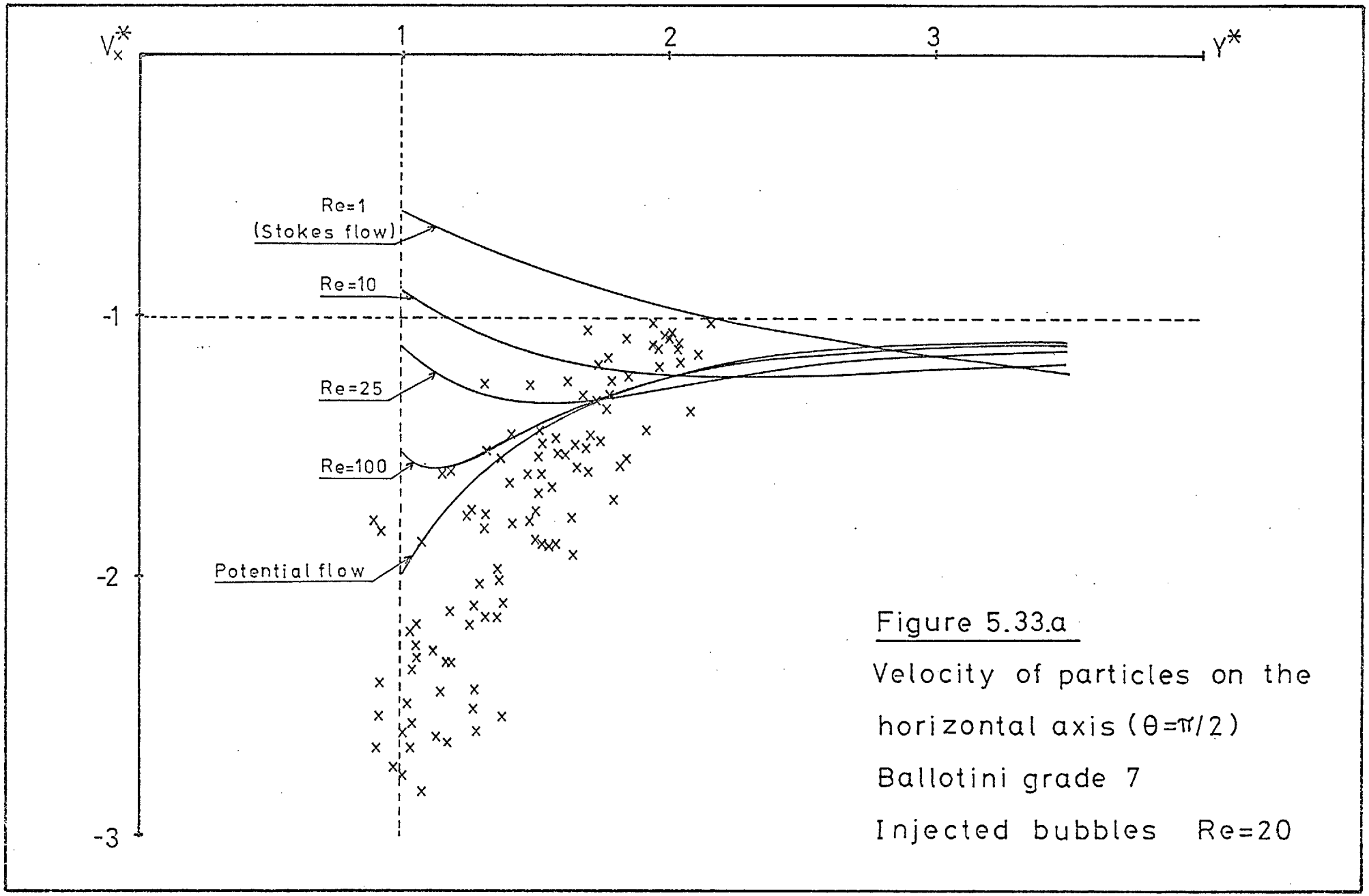


Figure 5.33.a

Velocity of particles on the horizontal axis ($\theta=\pi/2$)

Ballotini grade 7

Injected bubbles Re=20

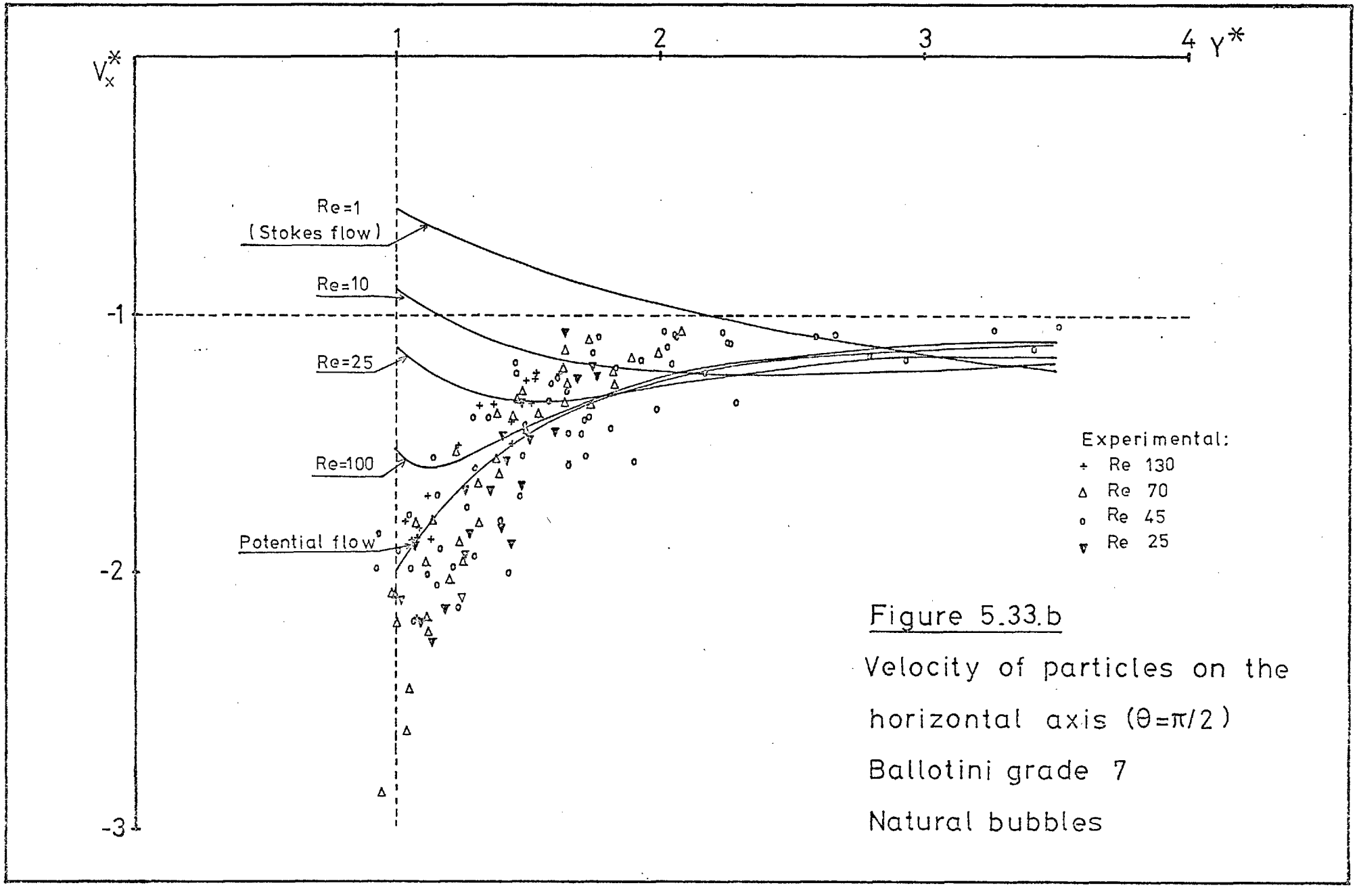


Figure 5.33.b

Velocity of particles on the horizontal axis ($\theta=\pi/2$)

Ballotini grade 7

Natural bubbles

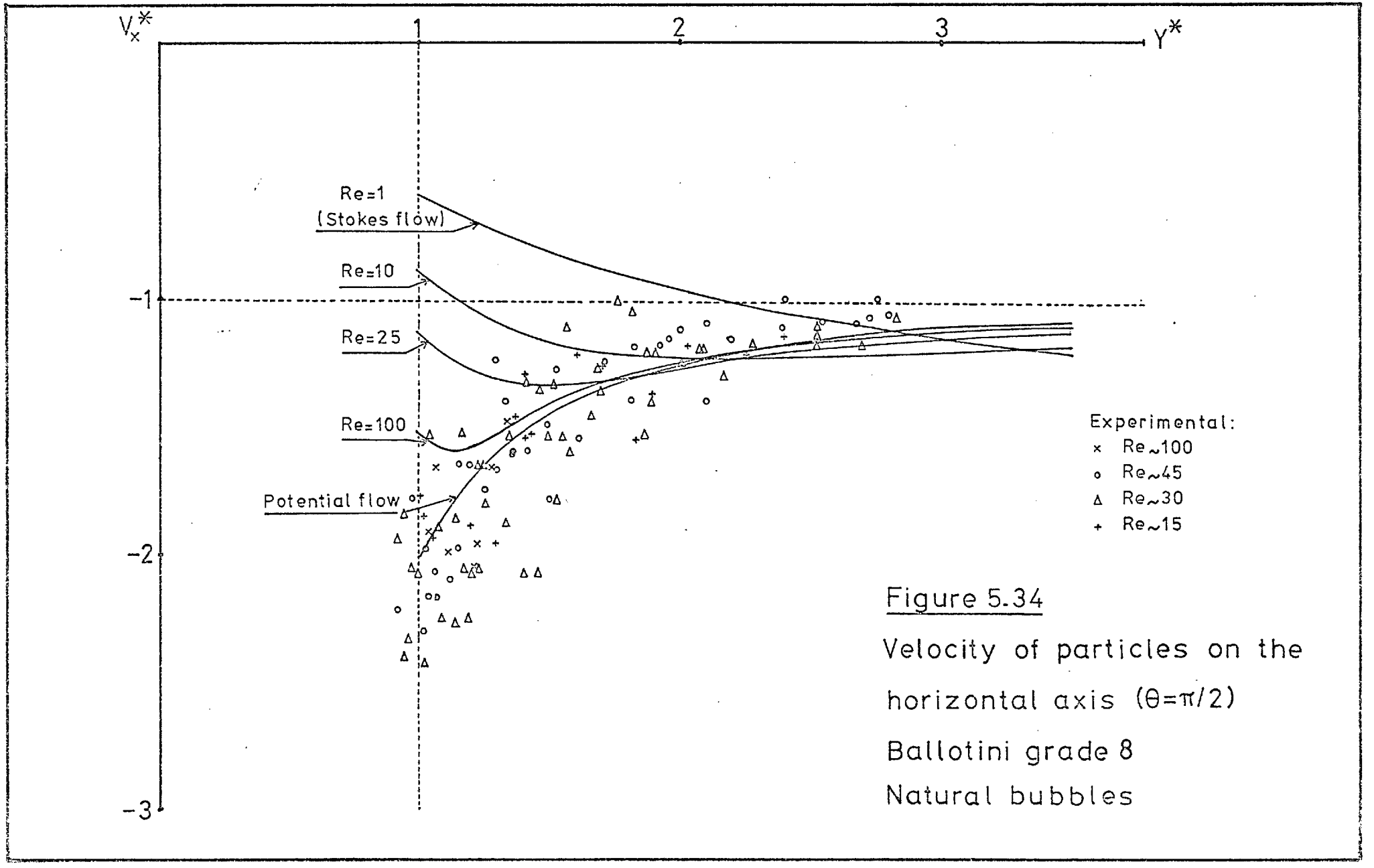


Figure 5.34

Velocity of particles on the horizontal axis ($\theta=\pi/2$)

Ballotini grade 8

Natural bubbles

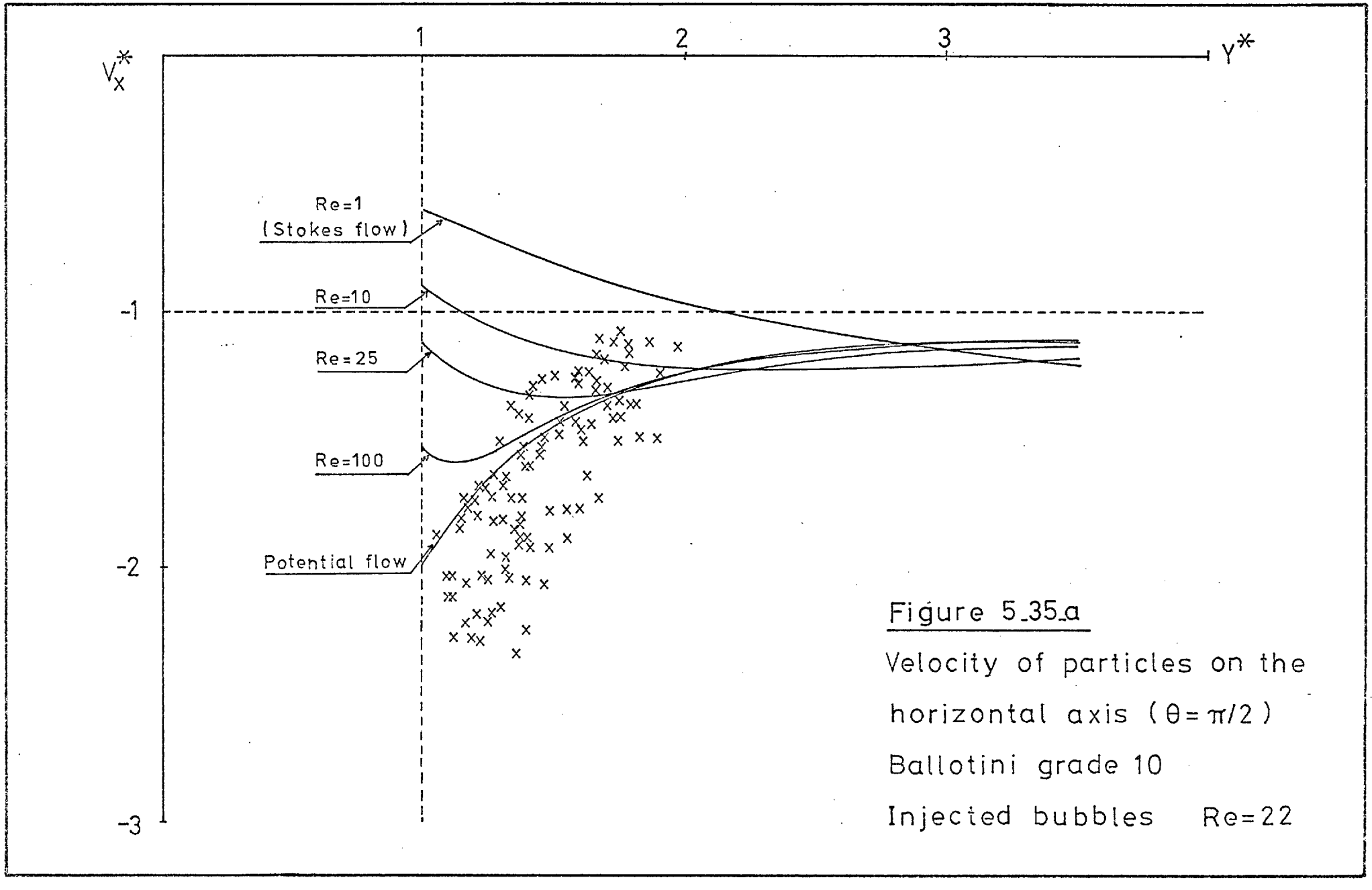


Figure 5.35.a

Velocity of particles on the horizontal axis ($\theta = \pi/2$)

Ballotini grade 10

Injected bubbles Re=22

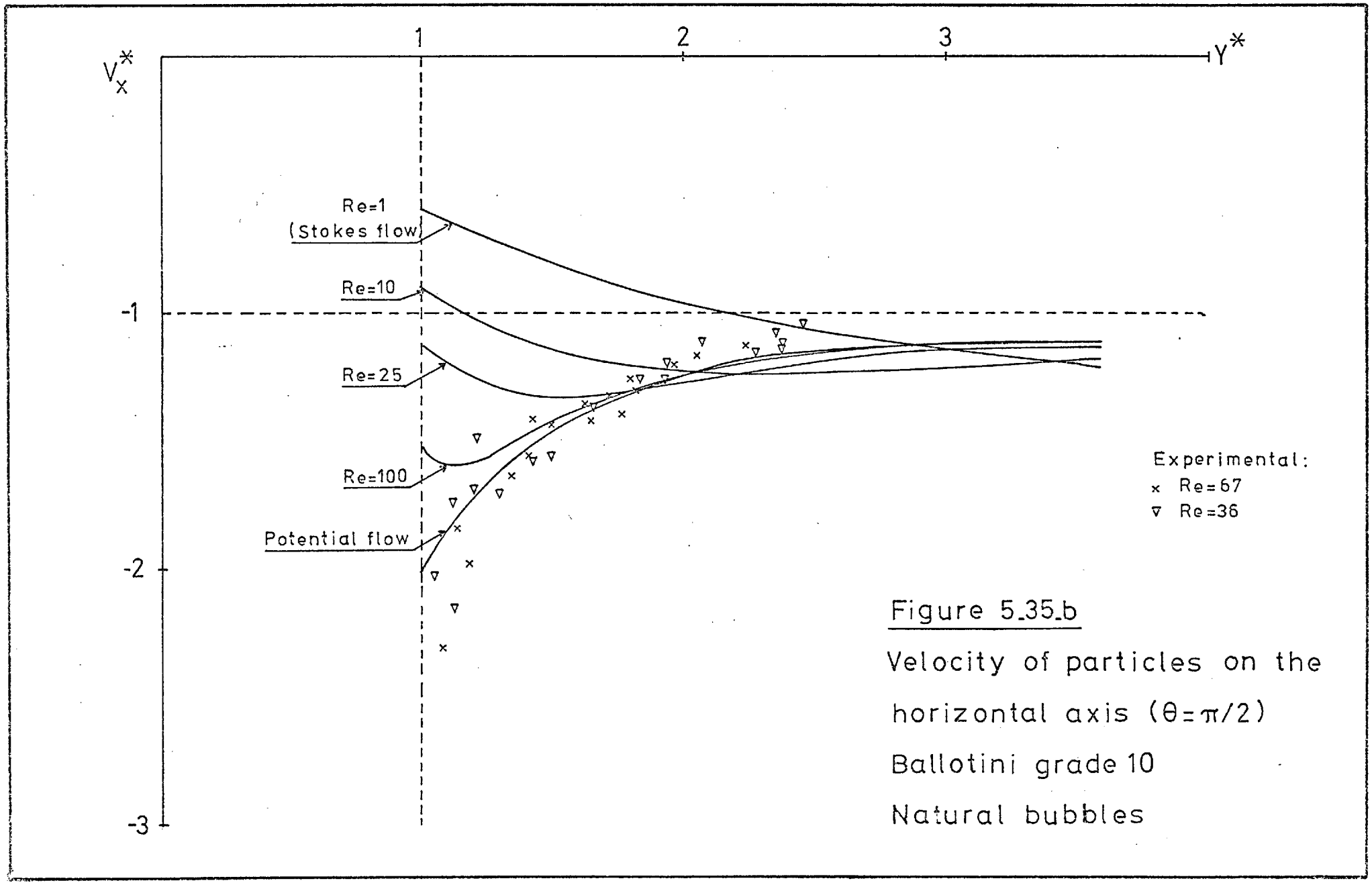


Figure 5.35.b

Velocity of particles on the horizontal axis ($\theta = \pi/2$)

Ballotini grade 10

Natural bubbles

CHAPTER 6

THEORETICAL AND EXPERIMENTAL RESULTS FOR THE GAS FLOW

The structure of this chapter is identical to that of Chapter 5 in which the results for the particulate flow were discussed.

In the first part of this chapter, theoretical results for the gas flow obtained from the viscous theory derived in Chapters 2 and 3 are presented and compared with predictions from other theories.

In the second part, the experimental results obtained with the aid of the measurement technique based on hot-wire anemometry, and described in Chapter 4, are presented and compared with theoretical predictions.

6.1 Theoretical results

The gas flow field is easily calculated when the solutions for the particle velocity and the gas pressure gradient are known. The momentum equation for the gas phase reduces to: (Chapter 2)

$$\underline{u} = \underline{v} - \frac{1}{\beta} \underline{\nabla} P_f \qquad (2.25)$$

or in the dimensionless form:

$$\underline{u}^* = \underline{v}^* - \frac{\gamma}{2} \frac{Fr}{\alpha_b} \underline{\nabla}^* P_f^* \qquad (2.38)$$

The solutions for the ratio of particle fluid drag coefficients $\gamma = \frac{\beta_o}{\beta}$ and for the Froude number, $Fr = \frac{U_b^2}{ga}$, as a function of the bubble Reynolds number, have been discussed in the previous chapter (sections 5.1.3. and 5.1.4).

We shall, therefore, be concerned first with the solution of the pressure field and then with the solution for the gas velocity obtained from (2.38).

6.1.1 Solution for the pressure field

The gas pressure gradient can be calculated from equations (2.29) and (2.30) which were derived in Chapter 2:

$$(\underline{v}^* \cdot \underline{\nabla}^*)\,\underline{v}^* = -\frac{1}{2}\,\underline{\nabla}^*\,P^* + \frac{2}{Re}\,\nabla^{*2}\,\underline{v}^* \qquad (2.29)$$

$$\text{with} \quad -\underline{\nabla}^* P^* = -\underline{\nabla}^* P_f^* + \frac{2}{Fr}\,\underline{i} \qquad (2.30)$$

where $\underline{i}$ is a downwards unit vector.

By combining equation (2.29) with the continuity and the vorticity equations, it has been shown in Chapter 3 (section 3.6) that the two components of the pressure field can be calculated by:

$$\frac{1}{2}\,\frac{\partial P^*}{\partial \rho} = \left\{ v_\rho^*\,\frac{\partial v_\rho^*}{\partial \rho} + \frac{v_\theta^*}{\rho}\,\frac{\partial v_\rho^*}{\partial \theta} - \frac{v_\theta^{*2}}{\rho} \right\} + \frac{2}{Re}\,\frac{1}{\rho}\,\frac{\partial \zeta^*}{\partial \theta} \qquad (6.1)$$

$$\frac{1}{2}\,\frac{1}{\rho}\,\frac{\partial P^*}{\partial \theta} = -\left\{ v^*_\rho \frac{\partial v^*_\theta}{\partial \rho} + \frac{v^*_\theta}{\rho}\frac{\partial v^*_\theta}{\partial \theta} + \frac{v^*_\rho\, v^*_\theta}{\rho} \right\} + \frac{2}{Re}\,\frac{\partial \zeta^*}{\partial \rho} \qquad (6.2)$$

In the computer programme the velocity and vorticity derivatives are simulated by finite difference formulae as described in Chapter 3. Thus the two components of the pressure gradient are calculated from the two equations (6.1) and (6.2).

In order to achieve a useful comparison with existing theories and with experiments, the above equations were integrated along selected paths, i.e. on the axis of rise of the bubble and on the bubble surface.

a) Pressure variations on the axis of the bubble (section 3.6.1)

Theoretical predictions of the dynamic pressure:

$$\frac{P'_f}{\rho_p(1-\varepsilon_o)ga} + \rho \cos\theta$$

are shown on Figure 6.1.

It must be noted that on this figure the gas pressure P'^*_f has been normalized with respect to $\rho_p(1-\varepsilon_o)ga$ and is therefore related to the gas pressure obtained from the solution of equation (2.30) by:

$$\frac{P'_f}{\rho_p(1-\varepsilon_o)ga} = \frac{P_f}{\frac{1}{2}\rho_p(1-\varepsilon_o)U_b^2} \times \frac{\frac{1}{2}\rho_p(1-\varepsilon_o)U_b^2}{\rho_p(1-\varepsilon_o)ga}$$

$$\text{or:} \quad P'^*_f = P^*_f \cdot \frac{Fr}{2} \qquad (6.3)$$

Three cases obtained from the present theory, Re = 0.01, 1, 10 as well as predictions from Davidson's (10), Jackson's (11) and

Murray's (12) theories are plotted on Figure 6.1. In the case of Jackson's and Murray's theories the results refer to a bubble rising with a velocity given by the Davies and Taylor approximation ($U_b = \frac{1}{2} (ga)^{\frac{1}{2}}$).

Ahead of the bubble, i.e. along $\theta = 0$, all the predictions fall below Davidson's theory. In addition it can be seen that the pressure variations obtained from the viscous theory are significantly different from Jackson's prediction only for low Reynolds numbers (say $Re < 10$). Stokes's flow is again well represented by the curve for $Re = 0.01$.

For low Reynolds numbers, the predicted point of zero pressure is situated above the centre of the bubble. When Re increases this point moves towards the bubble center. Stewart (42) uses this result to estimate a value for the particulate phase viscosity . (His argument is developed in Chapter 1, section 1.2.1).

In the rear of the bubble ($\theta = 180^{\circ}$), the viscous theory predicts a larger change in pressure for very low Reynolds numbers than Davidson's theory. It must also be noted that the recovery in pressure is much slower than Davidson's prediction. This is partly due to round off errors which are accumulated in the computation in the rear of the bubble and at large distance from the bubble center.

It is interesting to compare these theoretical predictions with some experimental data by Motamedi (106) and Littman and Homolka (6). Both sets of results are in good agreement together. They also show that the change in pressure is greater at the rear of the bubble than it is at the bubble nose. This is predicted by the viscous theory

developed in this work.

However the experimental value of the Reynolds number calculated for Motamedi's results is Re = 104 and therefore his results do not coincide with theoretical predictions since the curve for Re =100 is very close to Jackson's theory. On the other hand the value of Re = 104 in Motamedi's results seems very high. It was obtained for Ballotini grade 10, also studied in this work, and for artificially injected bubbles. The average bubble velocity and radius from his results predicts a Froude number $(\frac{U_b^2}{ga})$ of about 1, in contradiction with many other published data (e.g. Littman and Homolka (112)) and with the present experimental results which suggest that Fr = 0.25 (Davies and Taylor's result) is a good approximation.

Despite this, intermediate values of the Reynolds number (say Re = 10) still predict values which are too low. The agreement is better with Stokes's flow (Re = 0.01). This is the only result to predict the larger dynamic pressure change at the rear of the bubble than Davidson's prediction that has been found experimentally. In addition the point of zero pressure on the axis of the bubble is also well predicted by Stokes's solution and the recovery in dynamic pressure can extend experimentally up to 8 bubble radii below the rear stagnation point (Littman and Homolka (6)).

Nevertheless, it is not very clear physically why Stokes's solution fits experimental data at least as well as Davidson's theory. As Jackson's solution, which is based on the interaction between the particle momentum and the pressure gradient, fails, it would suggest

that interparticle forces are of major importance in determining the pressure field around the bubble while particle momentum has a negligible effect. However it has been shown in Chapter 5 that Stokes's solution is not an adequate representation of the particulate flow. Thus, presumably, Davidson's approach which assumes that the percolation of gas through the particles is governed by Darcy's law should be preferred. This is also Littman and Homolka's conclusion from their experimental results (6). They show that the pressure field is Laplacian and therefore that voidage variations near the bubble are small.

b) Pressure variations on the bubble surface.

In this case only theoretical predictions are shown on Figure 6.2. In this figure the dynamic pressure as defined in the previous section $(P'^{*}_{f} + \rho \cos\theta)$ is plotted as a function of the surface angle.

The experimental value of the gas pressure P'^{*}_{f} is known to be constant on the bubble surface and thus Davidson's theory for the gas motion which includes this boundary condition is presumably the best representation.

Furthermore Figure 6.2 shows the failure of Murray's or Jackson's solution for which the predicted dynamic pressure at the rear stagnation point is equal to that of the front stagnation point.

It can also be seen that in the case of the viscous theory the pressure variations are small near the front stagnation point (say $\theta < 30^{o}$) as expected from the Davies and Taylor-type approximation which was enforced.

The minimum pressure occurs on the side of the cylinder for intermediate Reynolds numbers while it is situated at the rear stagnation point for $Re \ll 1$. These results are thus qualitatively identical to those obtained for a rigid cylinder (Batchelor (101)).

6.1.2 Stream lines of gas flow

Once the solution for the pressure gradient has been obtained from equations (6.1) and (6.2), it is easy to calculate the gas velocity field using equation (2.38) as given at the beginning of this chapter.

An important result concerns the variation of the radial component of the gas velocity. This is shown on Figure 7.3 in the next chapter in connection with the calculation of the bubble throughflow velocity.

However the predicted results for the gas flow field are best visualized when presented in terms of a gas stream function χ. This calculation is discussed in Chapter 3 (section 3.9) and the results are shown on Figures 6.3 to 6.5 for three cases of Reynolds numbers: Re = 0.01, 10, 100. On these figures Davidson's solution (10) is also plotted for the same values of the dimensionless stream function and, as in Jackson's theory (11), only the upper part of the bubble is plotted since it has been shown in the previous chapter that the solution is very doubtful below the equatorial plane of the bubble. For each Reynolds number two values of α_b, $\alpha_b = 0.5$ and $\alpha_b = 1.5$ are plotted.

For all cases of Reynolds number, the patterns of the gas stream lines are qualitatively similar to those obtained by Jackson (11). It

can be seen from Figures 6.4 and 6.5 that the gas flow is certainly asymmetric with respect to the horizontal equatorial plane of the bubble. In the case of Stokes's flow this asymmetry is less apparent and the streamlines resemble those obtained in Davidson's solution.

A more valuable comparison can be made by plotting on the same graph the different cloud sizes obtained for various values of the Reynolds number and for an identical value of α_b ($\alpha_b > 1$). Four cases are shown on Figures 6.6a to 6.6d with α_b = 1.25, 1.50, 2 and 5. Davidson's solution for the cloud size is also plotted on these figures.

As expected the cloud dimension decreases when α_b increases. For large Reynolds number it is close to Jackson's solution. In the case of low Reynolds numbers (say $Re < 5$) the predicted cloud sizes are larger than in Davidson's theory. For Stokes's solution the cloud is well represented by a circle while for higher Reynolds numbers it is asymmetrical, as in Jackson's solution.

The same kind of comparison can be achieved by plotting the variations with α_b of the dimensionless cloud radius $\frac{r_c}{a}$ as measured on the axis above the bubble for different Reynolds numbers. On this figure the two marked experimental points correspond to measurements carried out in this work. They are discussed in the next section.

All the experimental results to be found in the literature show that Davidson's solution is an upper value for the cloud size, which is better represented by Jackson's theory (or by Murray's theory which is very close to Jackson's theory in this case). Thus Stokes's

flow also predicts a cloud size which is too large and which disagrees with the experimental results. On the contrary the cloud dimension obtained for intermediate Reynolds numbers ($10 < Re < 50$) agrees fairly well with experimental data (Figure 6.7).

6.2. Experimental results

Measurements of the interstitial gas velocity around artificially injected bubbles were carried out using the method described in Chapter 4 and Appendix 2. The position of the hot-wire probe could be varied in the fluidised bed so that measurements could be performed on the bubble axis and around the bubble sides. Two typical outputs from the U.V. recorder (Chapter 4) are shown on Figures 6.8a and 6.8b and are discussed below.

6.2.1. Measurements on the bubble axis

Figure 6.8a refers to a typical measurement when the probe is situated on the bubble axis. The output curve can be divided into several portions:

- point A corresponds to the injection pulse given on the injection unit. At the same time the synchronization flash is discharged and the solenoid valve is opened.

- section AB of the curve represents the injection effect on the probe. When a bubble is injected into the bed, there is an upward movement of the particles and an increase in gas velocity as shown on the output.

- section BC corresponds to the bubble travelling within the bed towards the probe. The total length AC represents about 40 cm in

the fluidised bed from the injection point to the probe.

- section CD represents the rise in gas velocity when the bubble approaches the probe. The maximum velocity is reached at point D which corresponds to the apex of the bubble.

- section DG represents the period when the probe is inside the bubble and corresponds to a sharp decrease in the gas velocity acting on the probe. This can be easily understood if one considers that inside the bubble the voidage is nearly unity and that consequently the gas tends to flow around the cage rather than to flow through it. Thus, as far as quantiative measurements are concerned, section DG is not useful and does not permit the measurement of the through flow velocity. The increase in velocity between points E and F corresponds to particles falling from the bubble roof on the cage thus creating a "knife" of particles where the voidage fraction is less than unity.

- section GH represents the decrease in velocity from the rear stagnation point of the bubble, until the velocity reaches a steady value equal to the value preceding the injection of the bubble.

The zero gas flow level has been drawn on the bottom part of the curve and thus the distance d represents the interstitial velocity far from the bubble. This is the value which has been taken in the calculation of the dimensionless parameter $\alpha_b = \frac{U_b}{u_o}$.

The central passage of the bubble as noted on the output has been determined from the cine films.

It must be noted that the curve on the U.V recorder represents the value of the vertical component of the interstitial gas velocity

with respect to stationary axes. It is easy to calculate the gas velocity with respect to axes moving with the bubble once the velocity of the bubble has been determined from the cine films.

Some experimental results are shown on Figures 6.9 to 6.13. On each figure the curves predicted by Davidson's (10), Jackson's (11) or Murray's (12) theories have been drawn. In the case of the viscous theory, Stokes's solution (Re = 0.01) and an intermediate value of the Reynolds number are also plotted.

The conclusions appear to depend on the particle size.

(i) Considering Figures 6.9 to 6.11 which concern bigger Ballotini (grade 7 and 8, i.e. 600 μm and 430 μm) for which $\alpha_b < 1$ it can be seen that there is a large scatter in the results especially for measurements above the bubble. This is mainly due to the injection effect of the bubble. In many cases the recovery in velocity was not completed and thus data for a distance greater than, say, three bubble radii are somewhat doubtful.

However for distances smaller than three bubble radii, it can be seen that most of the experimental points lie between Davidson's and Murray's theoretical curves. The maximum value predicted by Davidson's theory on the bubble surface is not obtained experimentally. As far as the viscous theory is concerned, theoretical predictions for the intermediate value of Re plotted, underestimate the values of gas velocity.

Below the bubble, although Davidson's theory predicts values of the gas velocity which are too high, it is a better representation of the experimental results than Murray's theory which fails badly in this case.

(ii) For smaller Ballotini (grade 10, i.e. 270 μm), the parameter α_b is greater than one and therefore there is a cloud of gas around the bubble. Two sets of experimental results are given on Figures 6.12 and 6.13.

In this case of small particles for which $\alpha_b > 1$, Murray's theory is a better representation of the gas velocity than Davidson's prediction.

The agreement is very good with Murray's theory for measurements above the bubble. In addition, with these particles, the recovery in velocity after the bubble injection was achieved in almost all cases and thus scattering of the results is less important.

The agreement is not so satisfactory for measurements below the bubble. It can be seen that the decrease in the gas velocity is sharper than predicted. However the maximum velocity obtained from Murray's theory at the rear stagnation point agrees very well with experimental results.

Although the viscous theory for an intermediate Reynolds number agrees fairly well with experimental results it does not really improve Murray's theory in this case.

Results on Figures 6.12 and 6.13 also permit the calculation of the dimensions of the gas cloud on the bubble axis. The dimension of the cloud corresponds to the points where $u_x = 0$. It can be seen from these figures that the dimension obtained experimentally at the rear of the bubble is very small and due to the bubble wake. This is in agreement with published data. At the front of the bubble experimental and theoretical predictions are compared in Table 6.1.

Experimental			Theoretical cloud radius $\frac{r_c}{a}$			
Re	α_b	$\frac{r_c}{a}$	Davidson	Murray	Present theory Re=25	Present theory Re=0.01 (Stokes)
22.8	1.50	1.75	2.24	1.81	1.82	3.39
26.1	2.00	1.50	1.73	1.53	1.48	2.51

Table 6.1 Gas cloud size comparison

Agreement with Murray's theory or with the present theory for Re = 25.0 (which corresponds to the experimental values of Re) is quite good. Davidson's solution and Stokes's solution overestimate the cloud size.

Finally it is possible to draw the following conclusions from the experiments:

(i) All the experiments prove that the flow of gas on the bubble axis is not symmetrical with respect to the center of the bubble as predicted by Davidson's theory, especially for smaller particles (Ballotini grade 10).

(ii) Comparison with theoretical predictions shows a difference between large particles and small ones. In the present work large particles correspond to $\alpha_b < 1$ and small particles to $\alpha_b > 1$.

- for small Ballotini and $\alpha_b < 1$ Murray's theory is a good representation
- for large Ballotini and $\alpha_b > 1$ Murray's theory fails below the bubble and Davidson's prediction is the best estimate.

This result seems surprising since one expects that Darcy's law for the percolation of fluid holds better for small particles where the interstitial Reynolds number $Re_i = \frac{U_o \, d_p}{(1-\varepsilon_o)\, \nu_f \, \varepsilon_o}$ is smaller. On Table 6.2, the values of Re_i have been calculated from the data given in Table 4.1 (Chapter 4) at minimum fluidisation conditions.

Ballotini	U_o cm/sec	d_p (mean) cm	Re_i
7	34.3	0.0600	57.2
8	25.6	0.0500	35.5
10	8.9	0.0270	6.3
in this table $\nu_f = 15\ 10^{-2}$ cm^2/sec (air at 20°C)			

Table 6.2 Values of the interstitial Reynolds number

The above table shows that Re_i is ten times larger for Ballotini grade 7 than it is for Ballotini grade 10. Therefore if Davidson's theory fits better the experimental data for larger particles this is not due presumably to the size of the particles.

In fact it can be seen from Figures 6.9 to 6.13 that the difference between particles is only important in the rear of the bubble. The cloud dimension obtained for Ballotini grade 10 is much smaller in the rear of the bubble than above it. This has also been proved using injection of NO_2 gas tracer (e.g. Anwer and Pyle (80)). Therefore we suggest that the difference between particles tested in this work and the theoretical models is due to the bubble wake which

has been neglected.

(iii) For small Ballotini with $\alpha_b > 1$ the gas cloud dimension above the bubble is well predicted by Murray's theory or by the present theory.

6.2.2. Velocity measurements around the bubble

When the hot wire probe is situated away from the bubble axis, the output of the U.V. recorder is different from that illustrated on Figure 6.8a since the probe does not penetrate inside the bubble. A typical output is shown on Figure 6.8b.

- The first part of the curve from A to C has already been discussed in the previous section. It is worth remarking again that the recovery in velocity after the injection effect is not perfect, as has been emphasized previously.

- Section CD corresponds to the effect of the bubble when it passes near the probe. As the probe does not enter the bubble, this curve represents the actual variations of the interstitial gas velocity. As in the previous measurements on the bubble axis, the position of the central passage of the bubble was determined from the cine films.

Experiments were carried out only for large particles (Ballotini grade 7 and 8) where it is possible to determine, from the cine films, the exact position of the probe with respect to the bubble center. In the case of smaller Ballotini, splitting occurred for almost all the bubbles and thus the position of the probe could not be determined with precision. On the other hand, for these smaller particles, more experiments were done on the bubble axis which is important for the determination of the cloud size (preceding section).

Results for measurements around bubbles are shown in Figures 6.14 to 6.22. On each figure the vertical component of the interstitial gas velocity u_x^* relative to the bubble, is plotted versus x^*, that is as a function of the distance from the horizontal equatorial plane of the bubble. The position of the probe with respect to the bubble axis is represented by the dimensionless horizontal distance y^* and indicated on each graph. In fact, although the probe was in fixed positions with respect to the injection point of the bubble, the latter, very often, does not rise on the vertical line which explains the various values of y^* obtained on the graphs and which emphasizes the importance of determining the exact position of the probe.

As expected, when the distance y^* increases, the variations in the gas velocity become smaller. In practice the variations are not significant for $y^* > 4$. It is worth remarking that this distance is the double of the limit found previously for particle movement around injected bubbles (Chapter 5). Each graph refers to a single bubble and therefore the value of α_b is different for each. It is obviously difficult to repeat exactly the same experiment since bubbles are not generally reproducible. In the present experiments: $0.4 < \alpha_b < 0.7$, and for each graph theoretical curves are plotted for the value of α_b which was determined experimentally.

Predictions from the viscous theory are plotted for the Reynolds number nearest to the experimental value. Re is determined experimentally from the measurements of the bubble radius and velocity as obtained from the cine films and is therefore only approximate. For some results, two theoretical curves for Re = 10 and Re = 25

were plotted and it can be seen that the difference between them is small (Figures 6.18 and 6.19) so that the results are not in any case very sensitive to the inaccuracy in the Reynolds number.

For both sets of particles most of the experimental results lie between Jackson's and Davidson's predictions and very often agree better with Davidson's prediction especially for larger Ballotini (grade 7). This confirms the results obtained for measurements along the bubble axis of the gas velocity (previous section) and of the gas pressure (e.g. Littman and Homolka (6)). Thus in the present case Darcy's law is presumably the best representation of the percolation of the fluid. However it must be emphasized that no experiments have been performed around bubbles with small particles and the present results are not sufficient to conclude on the effect of the particle size.

As far as the viscous theory is concerned it does not describe adequately the experimental results in a region close to the bubble. In all cases variations of the gas velocity are underestimated by the viscous theory, which suggests that the reduction in voidage as predicted by Jackson's method (Chapter 5, section 5) does not occur.

6.3. Conclusions

General conclusions are drawn in Chapter 8. However as far as the gas flow field is concerned it is possible to point out the following remarks:

(i) Theoretical predictions for the gas cloud dimension when $\alpha_b > 1$ show that the cloud is larger than Davidson's prediction when the Reynolds number is small and decreases when Re increases.

(ii) Pressure variations are well predicted by Stokes's flow solution.

(iii) Experimental measurements along the bubble axis and around the bubble show that Davidson's theory is a good representation of the gas velocity field for large particles (Ballotini grade 7 and 8).

(iv) For smaller Ballotini (grade 10) the cloud size is well represented by Murray's theory and by the present theory.

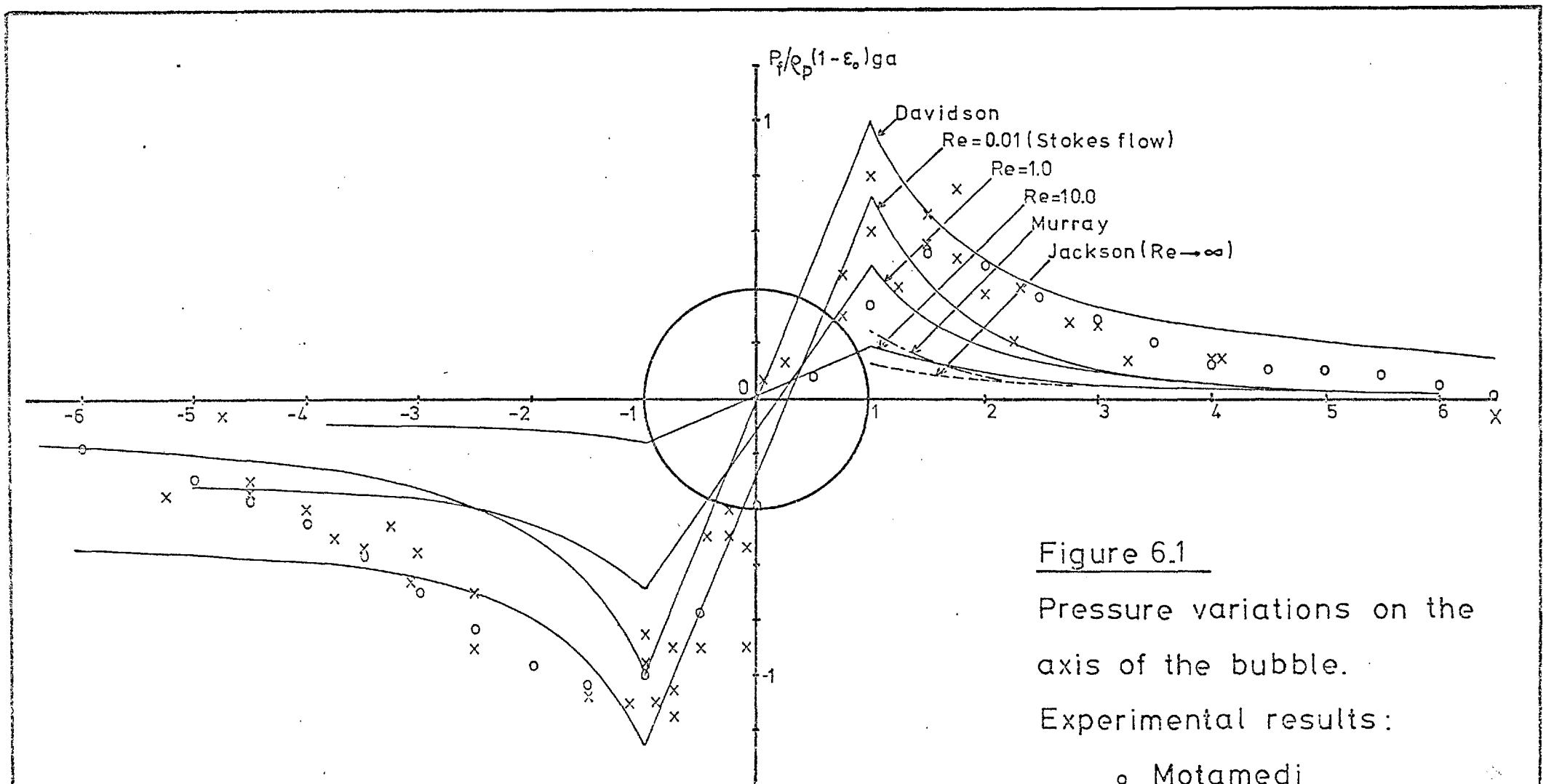


Figure 6.1

Pressure variations on the axis of the bubble.

Experimental results:

- o Motamedi (averaged Re=104)
- x Littman & Homolka

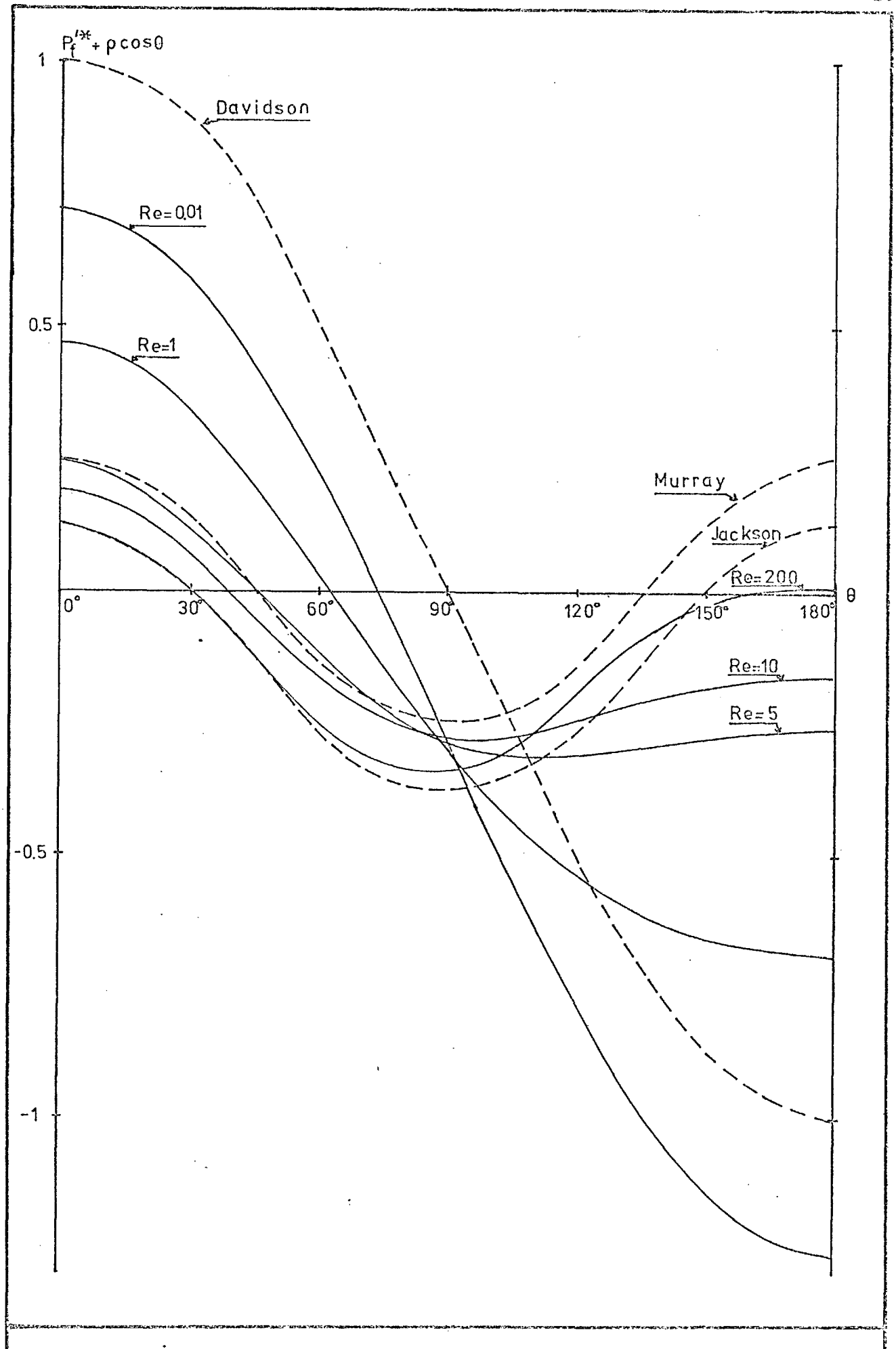


Figure 6.2 Variations of the dynamic pressure on the bubble surface.

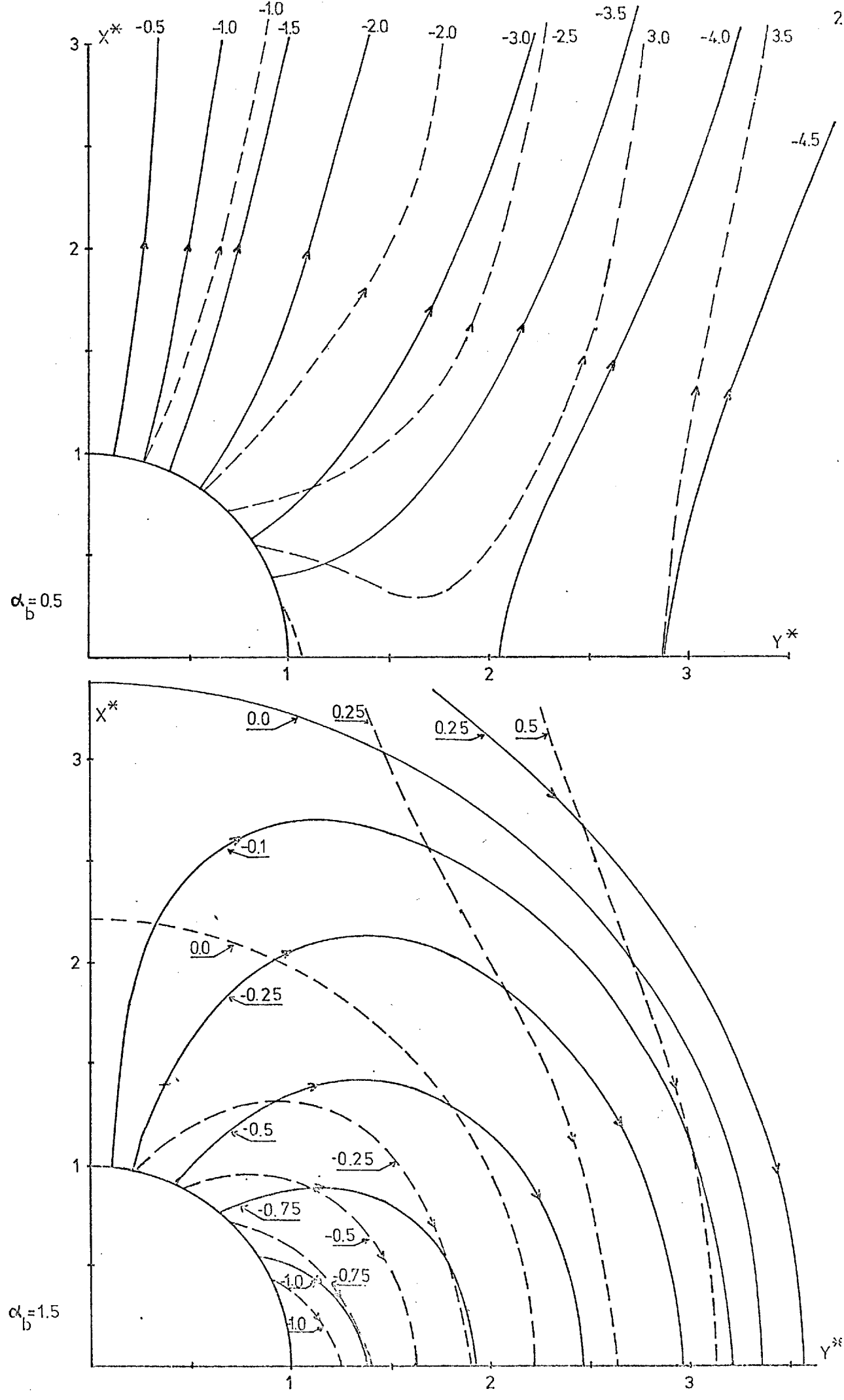
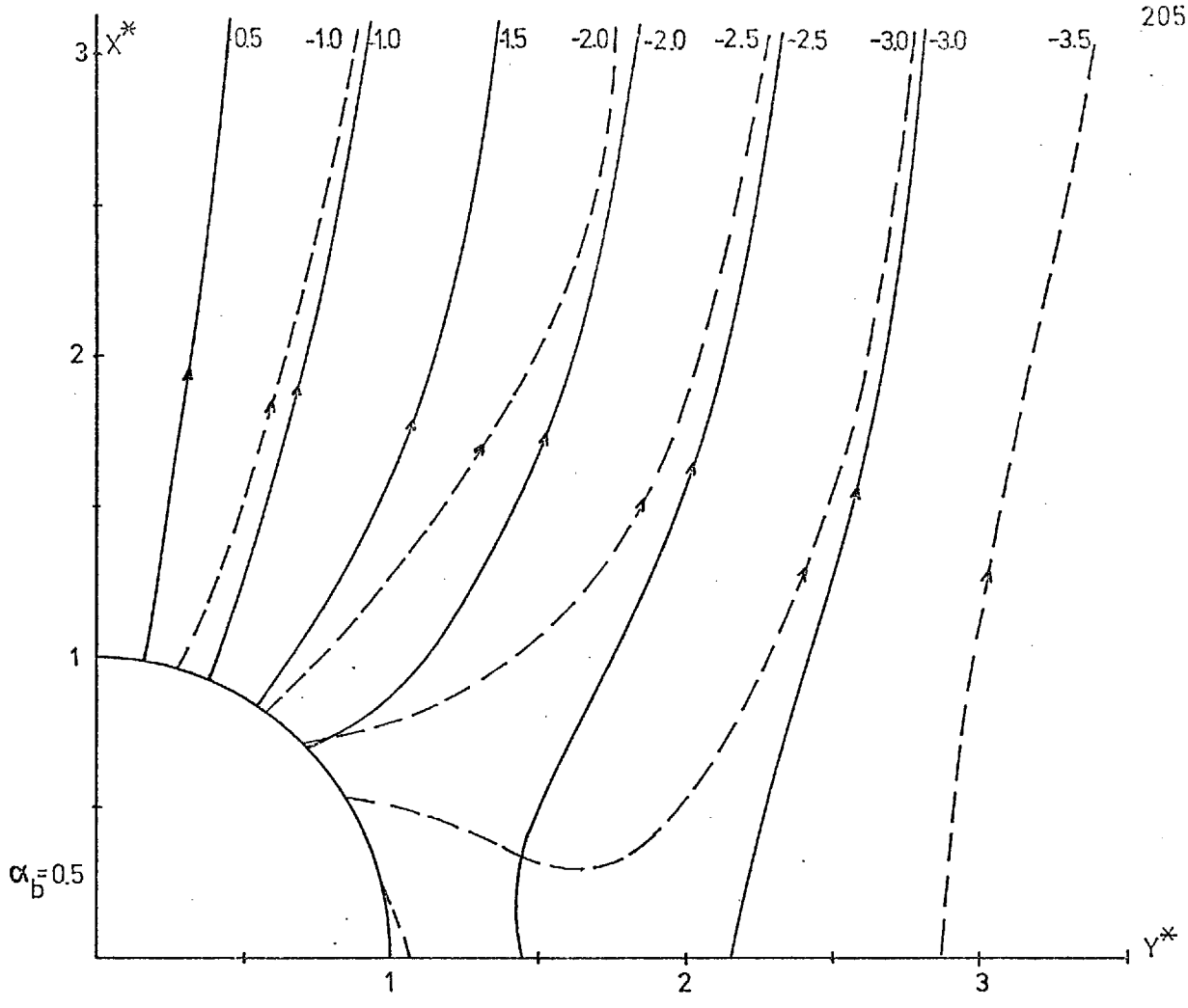


Figure 6.3 Gas streamlines



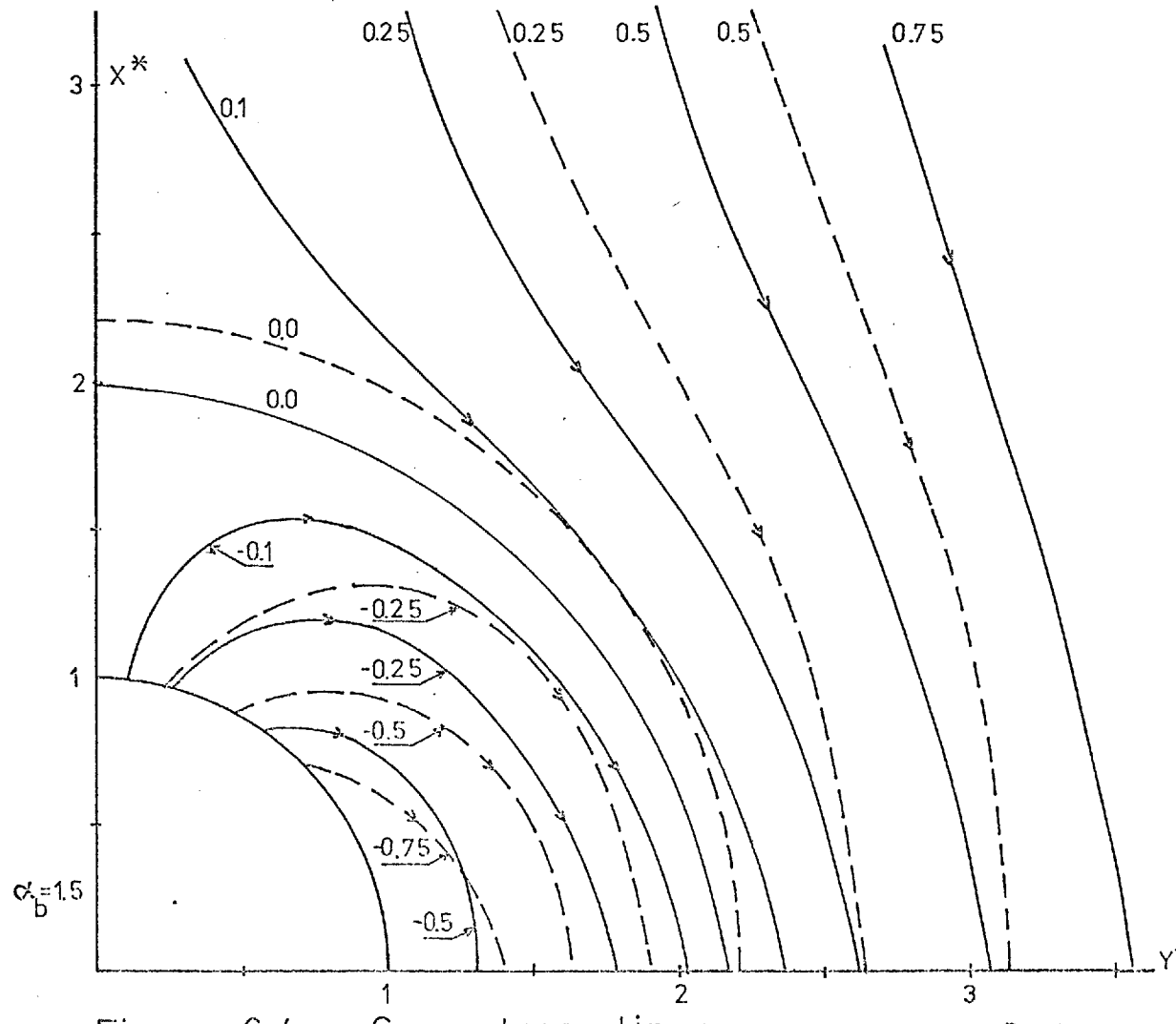
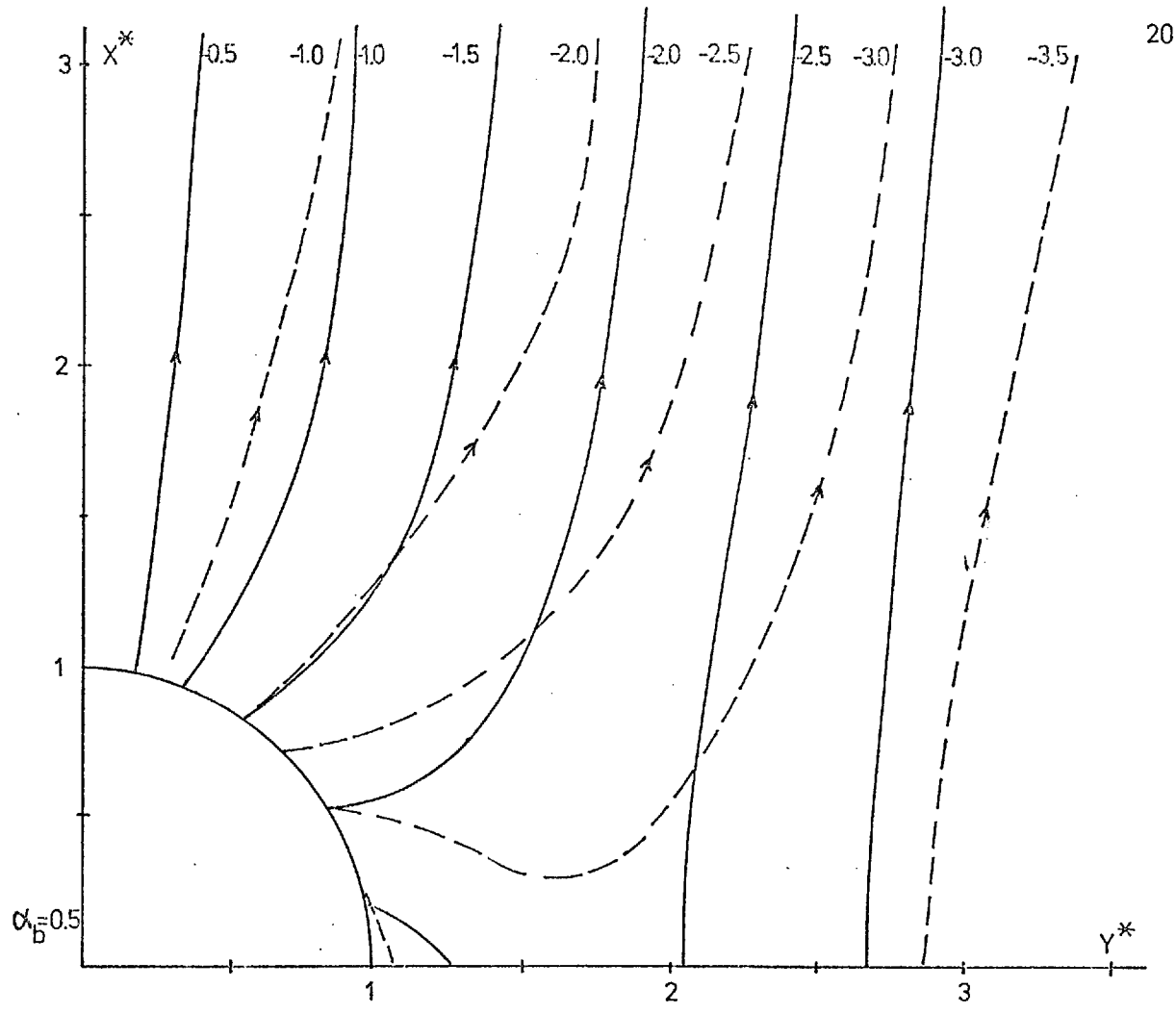


Figure 6.4 Gas streamlines

—— Re=10

– – – Davidson



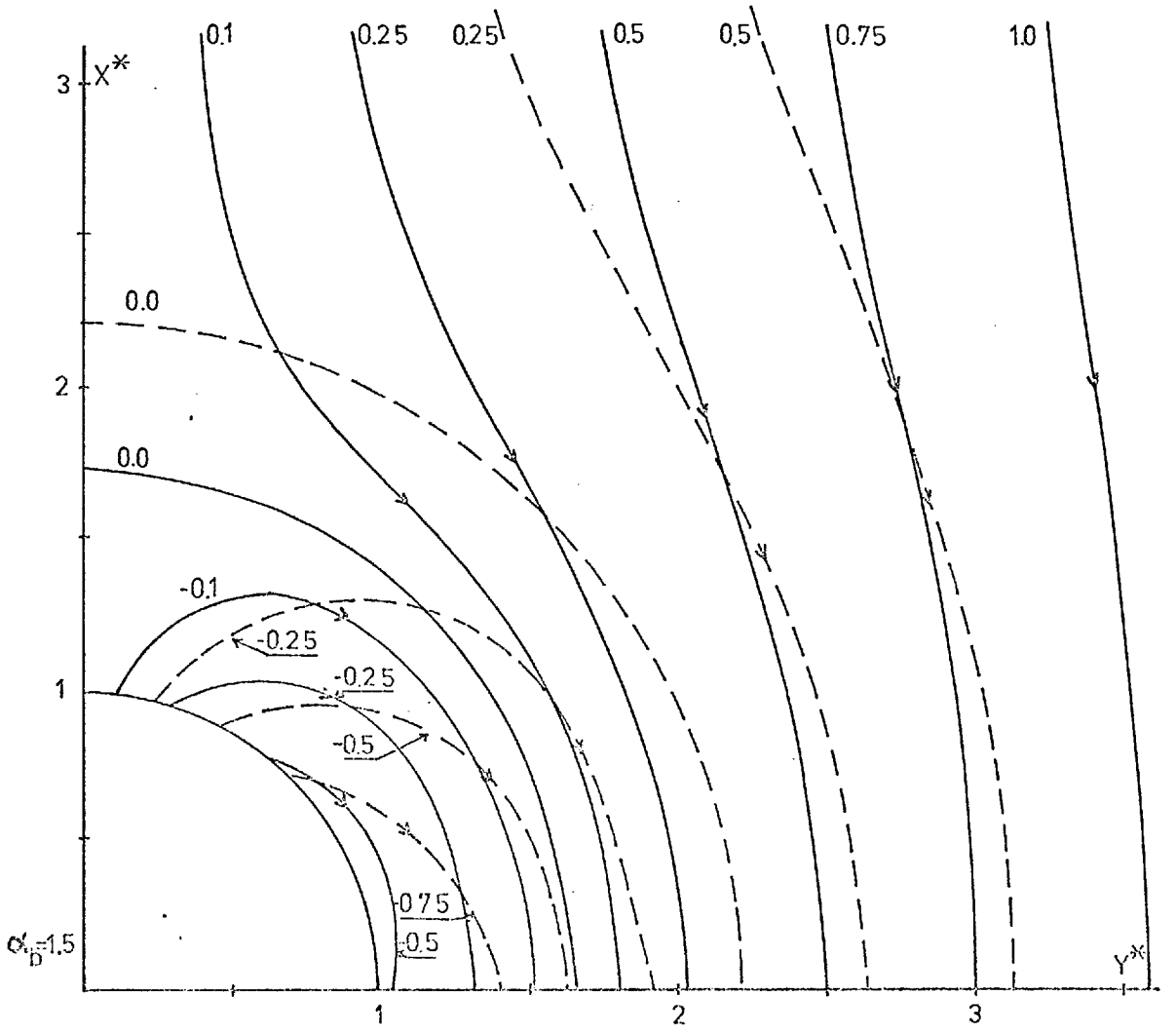


Figure 6.5 Gas streamlines

Re=100

Davidson

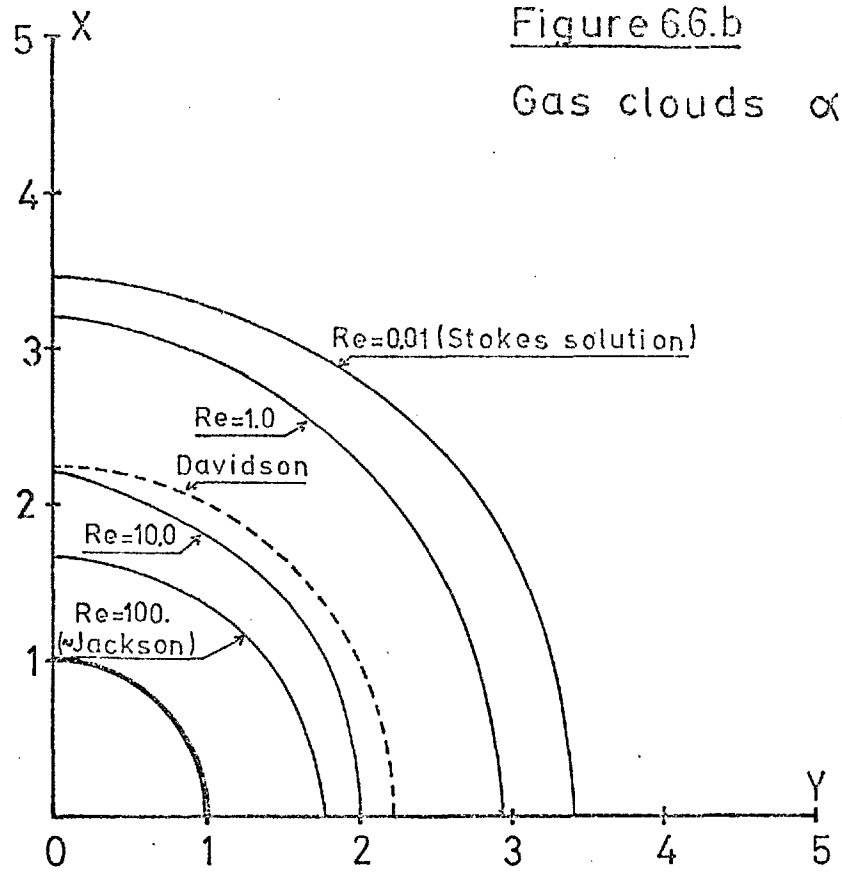


Figure 6.6.b

Gas clouds $\alpha_b = 1.50$

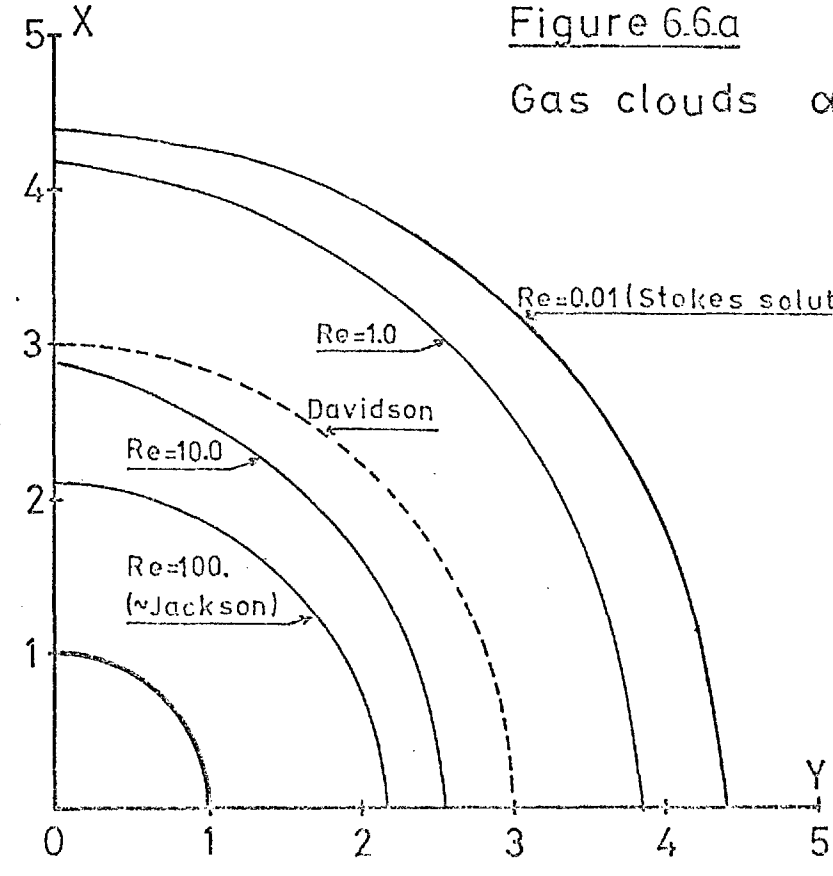


Figure 6.6.a

Gas clouds $\alpha_b = 1.25$

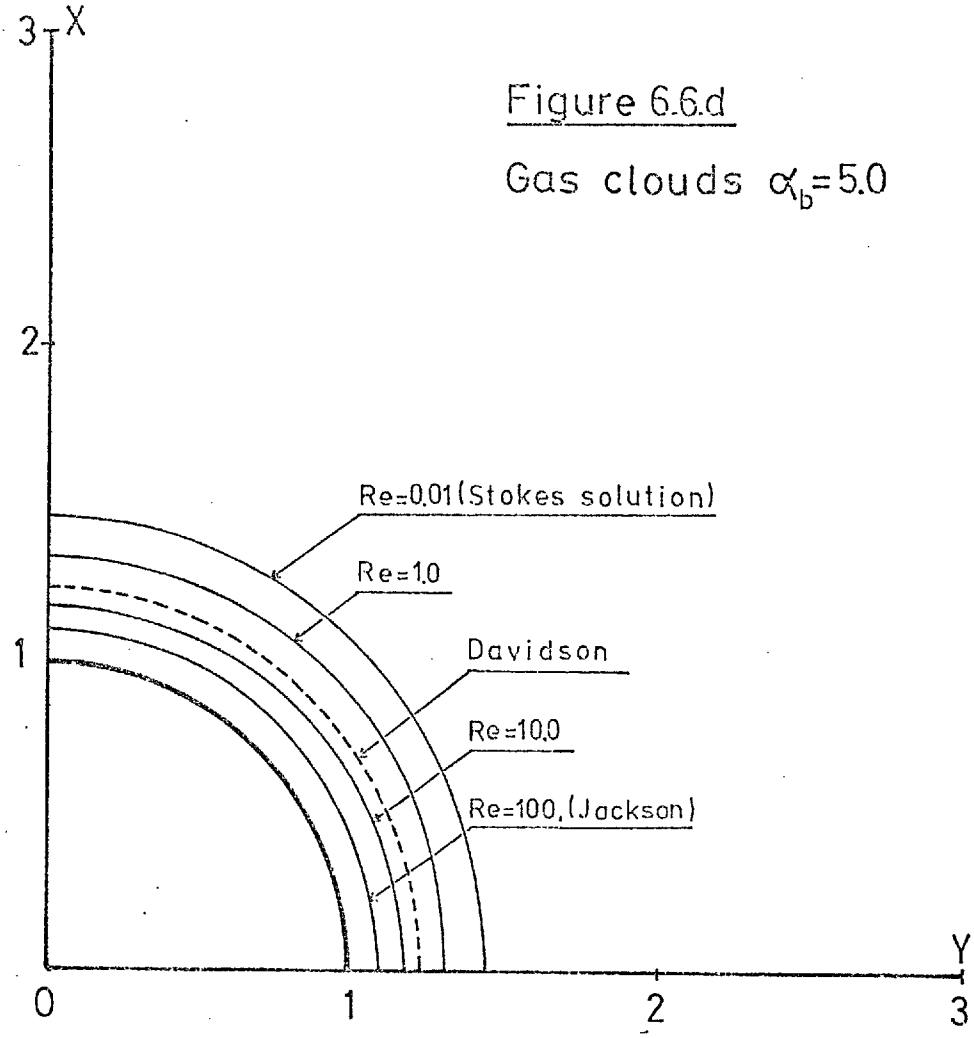


Figure 6.6.d

Gas clouds $\alpha_b = 5.0$

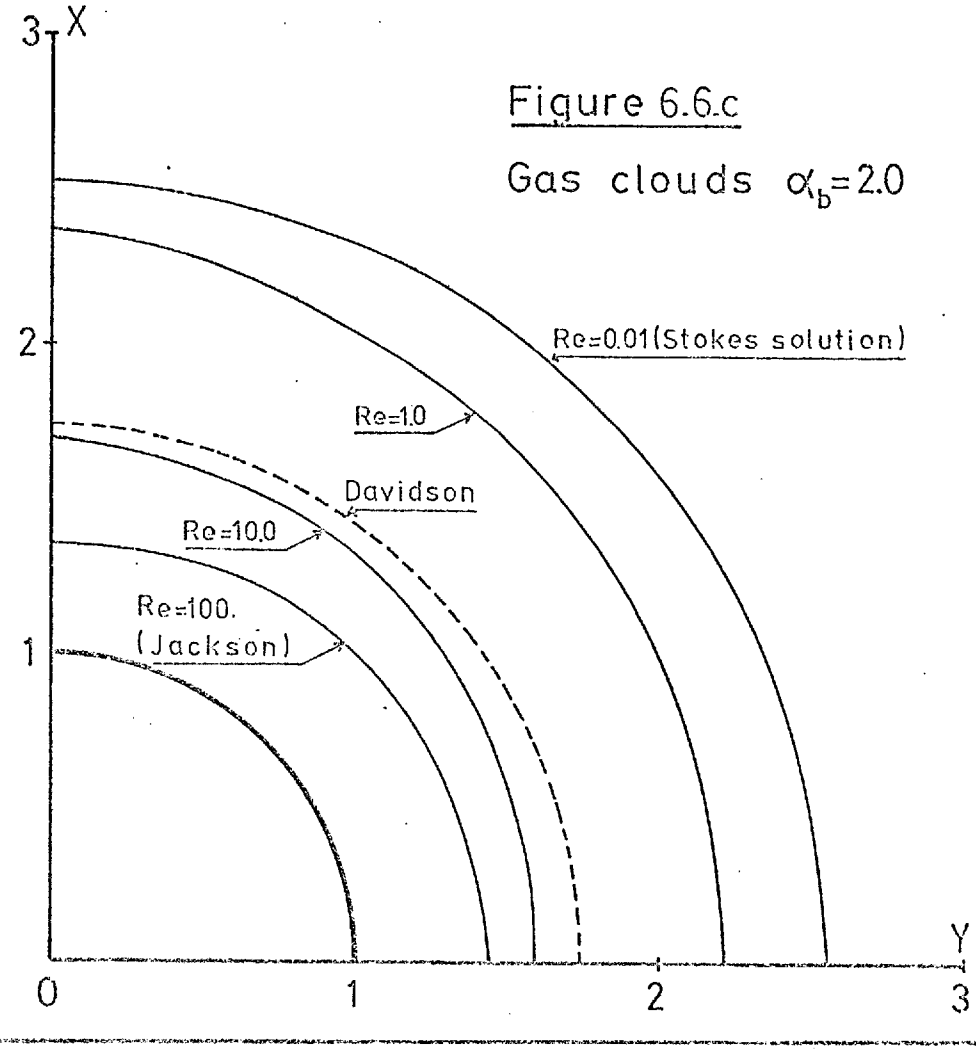


Figure 6.6.c

Gas clouds $\alpha_b = 2.0$

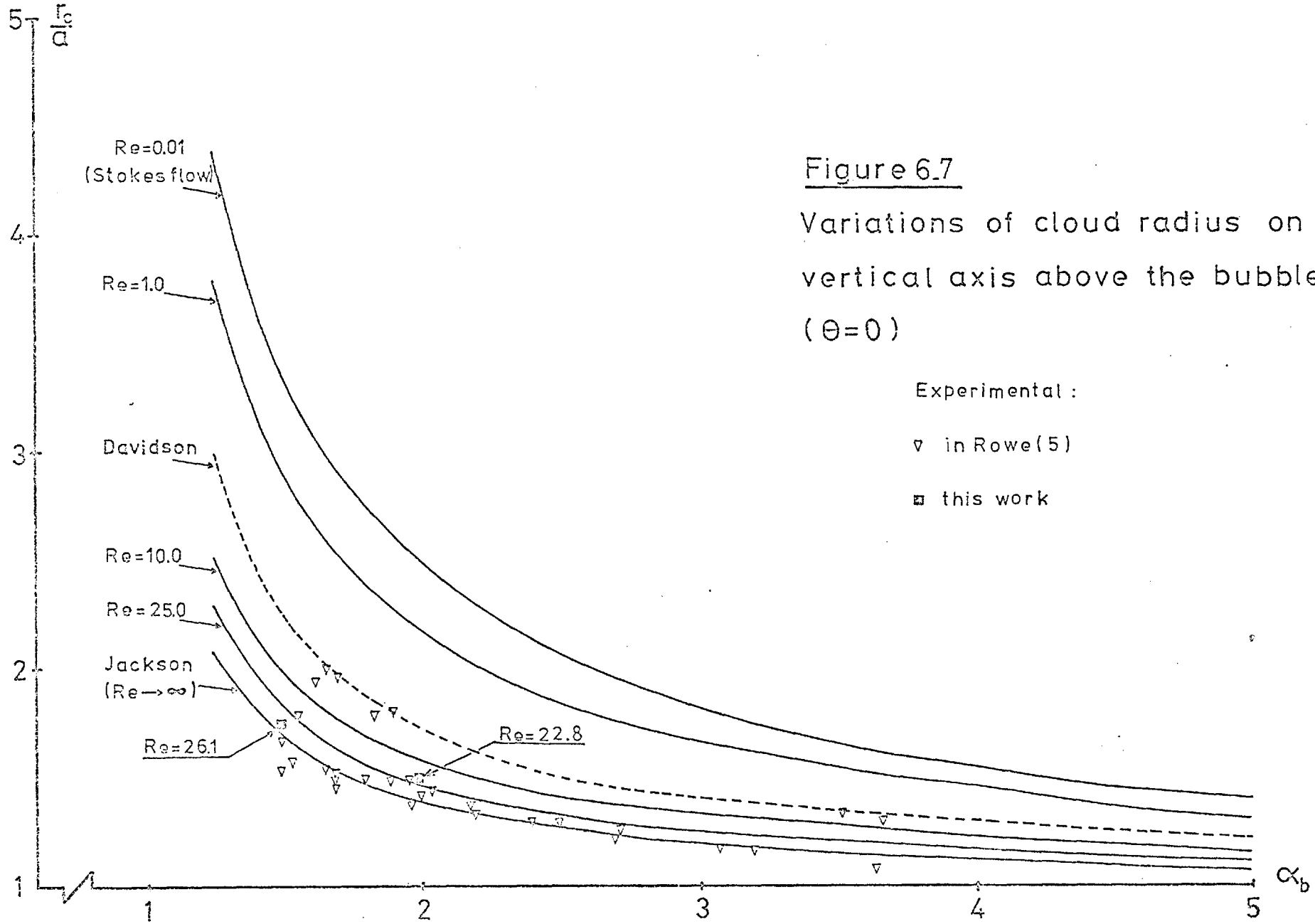


Figure 6.7

Variations of cloud radius on the vertical axis above the bubble. ($\theta=0$)

Experimental :

▽ in Rowe(5)

▣ this work

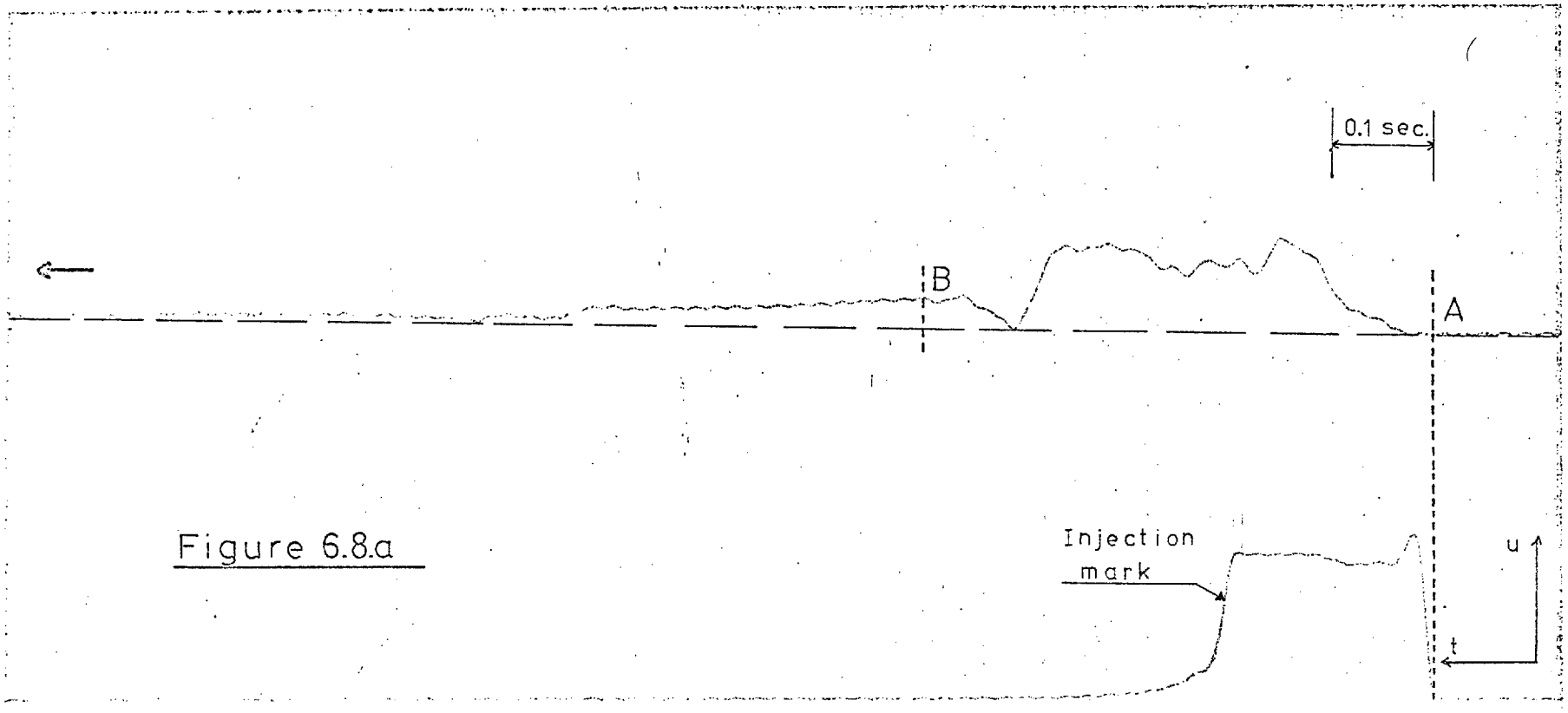
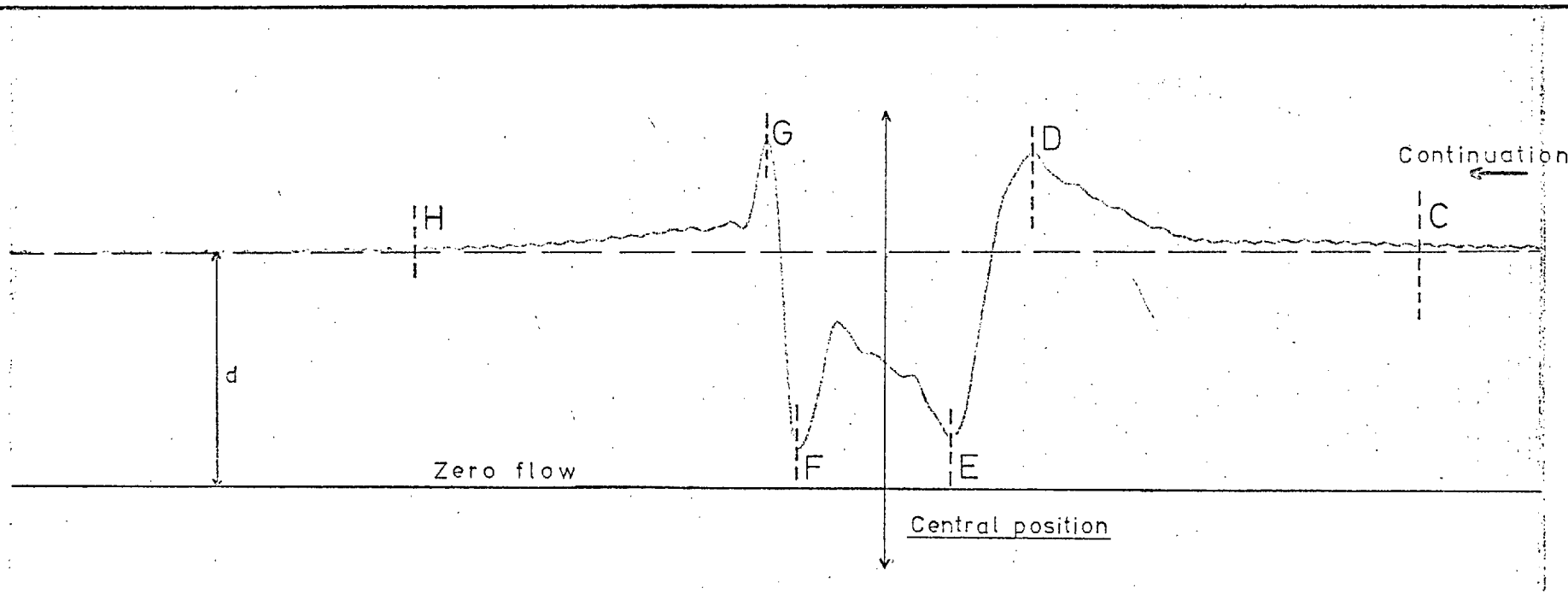

0.1 sec.
B
A
Injection
mark
u
t

Figure 6.8a


G
D
Continuation
H
C
d
Zero flow
F
E
Central position

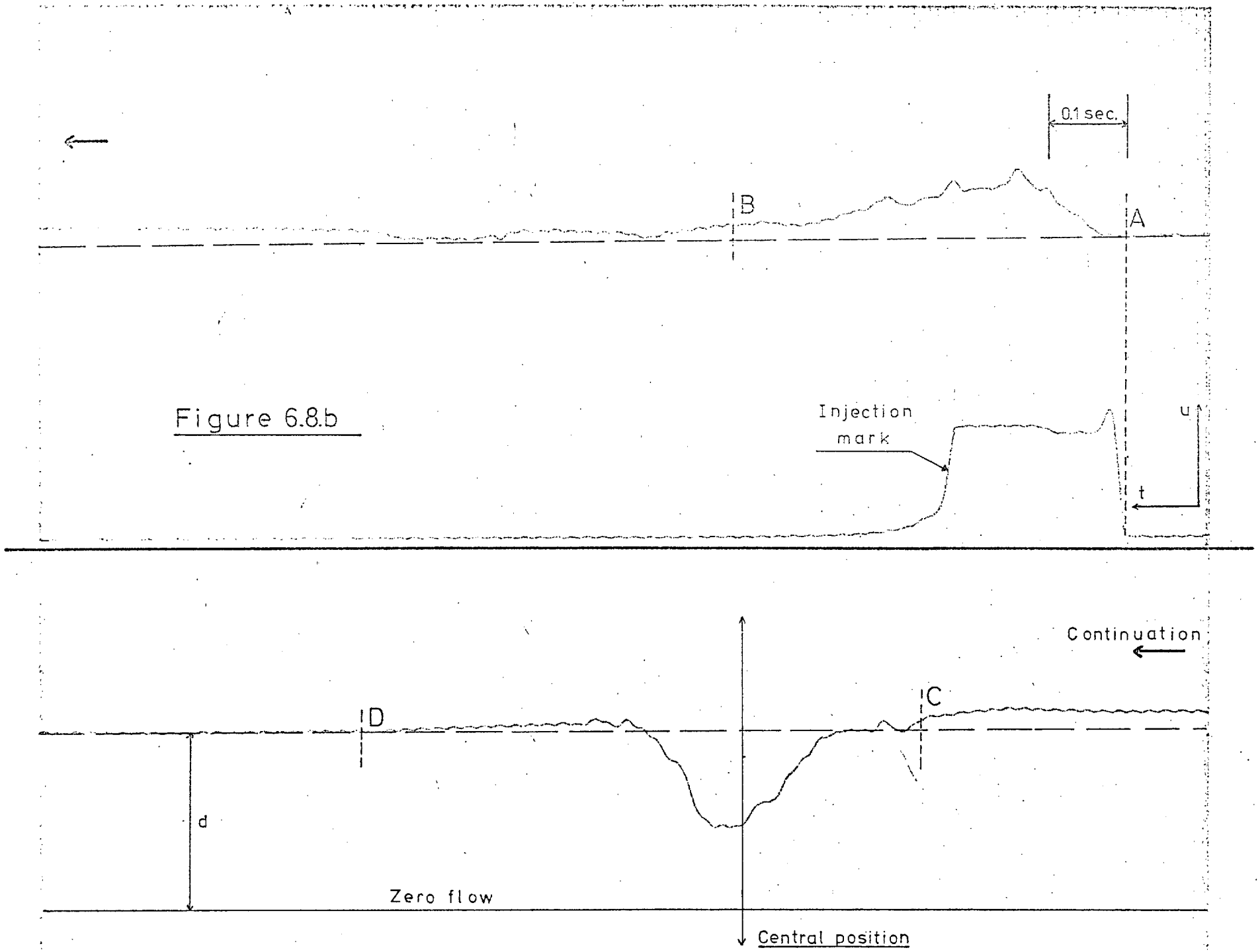
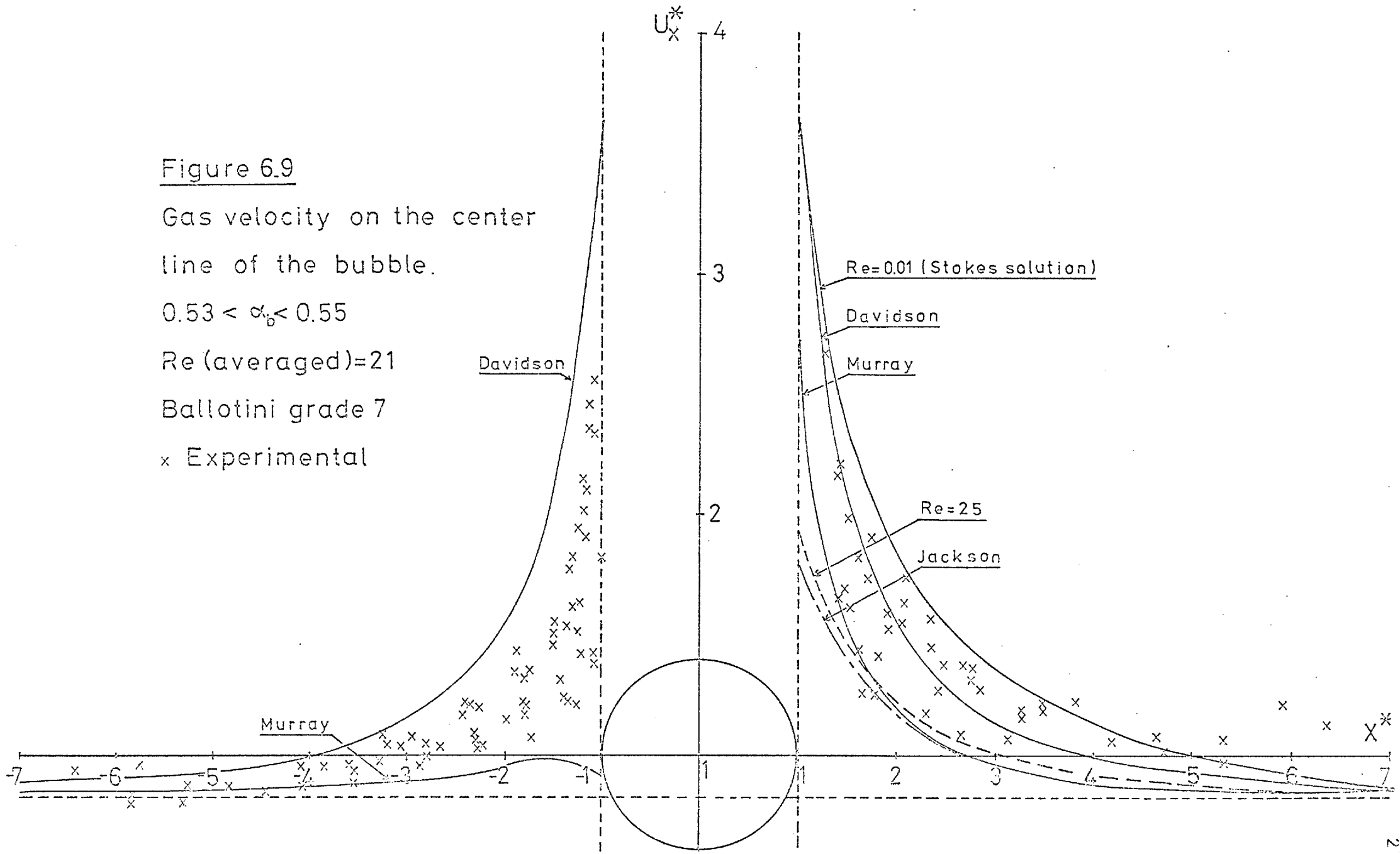

0.1 sec.
B
A
Injection
mark
u
t
Continuation
C
D
d
Zero flow
Central position

Figure 6.8.b


Figure 6.9
Gas velocity on the center line of the bubble.
0.53 < α_b < 0.55
Re (averaged)=21
Ballotini grade 7
× Experimental
U_x^*
X^*
Davidson
Murray
Re=0.01 (Stokes solution)
Davidson
Murray
Re=25
Jackson
Murray

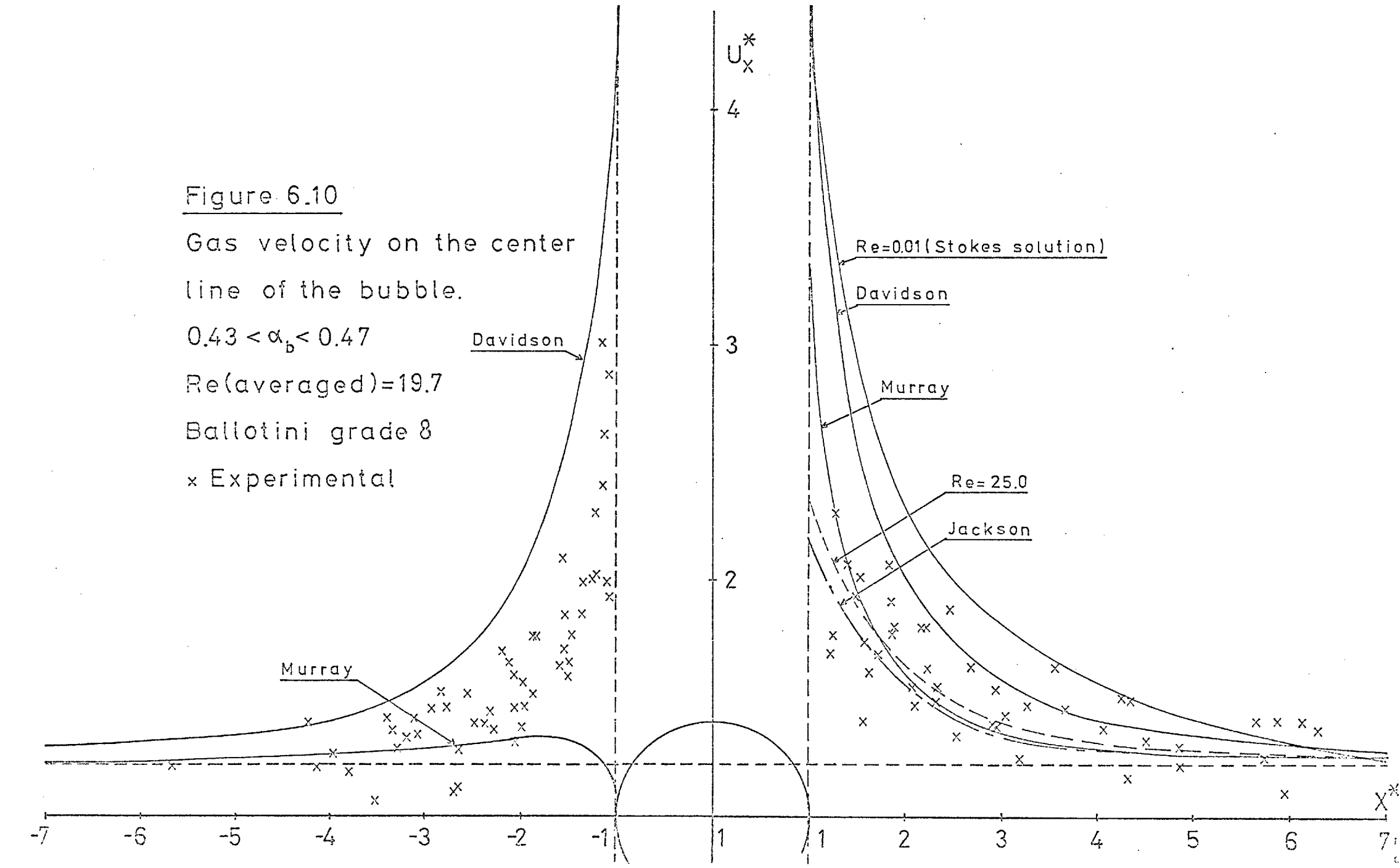

Figure 6.10
Gas velocity on the center line of the bubble.
$0.43 < \alpha_b < 0.47$
Re(averaged)=19.7
Ballotini grade 8
× Experimental
U_x^*
X^*
Davidson
Murray
Re=0.01(Stokes solution)
Davidson
Murray
Re=25.0
Jackson
4
3
2
-7
-6
-5
-4
-3
-2
-1
1
1
2
3
4
5
6
7

Figure 6.11

Gas velocity on the center line of the bubble.

$0.48 < \alpha_{l_b} < 0.52$

Re(averaged)=18.7

Ballotini grade 8

× Experimental

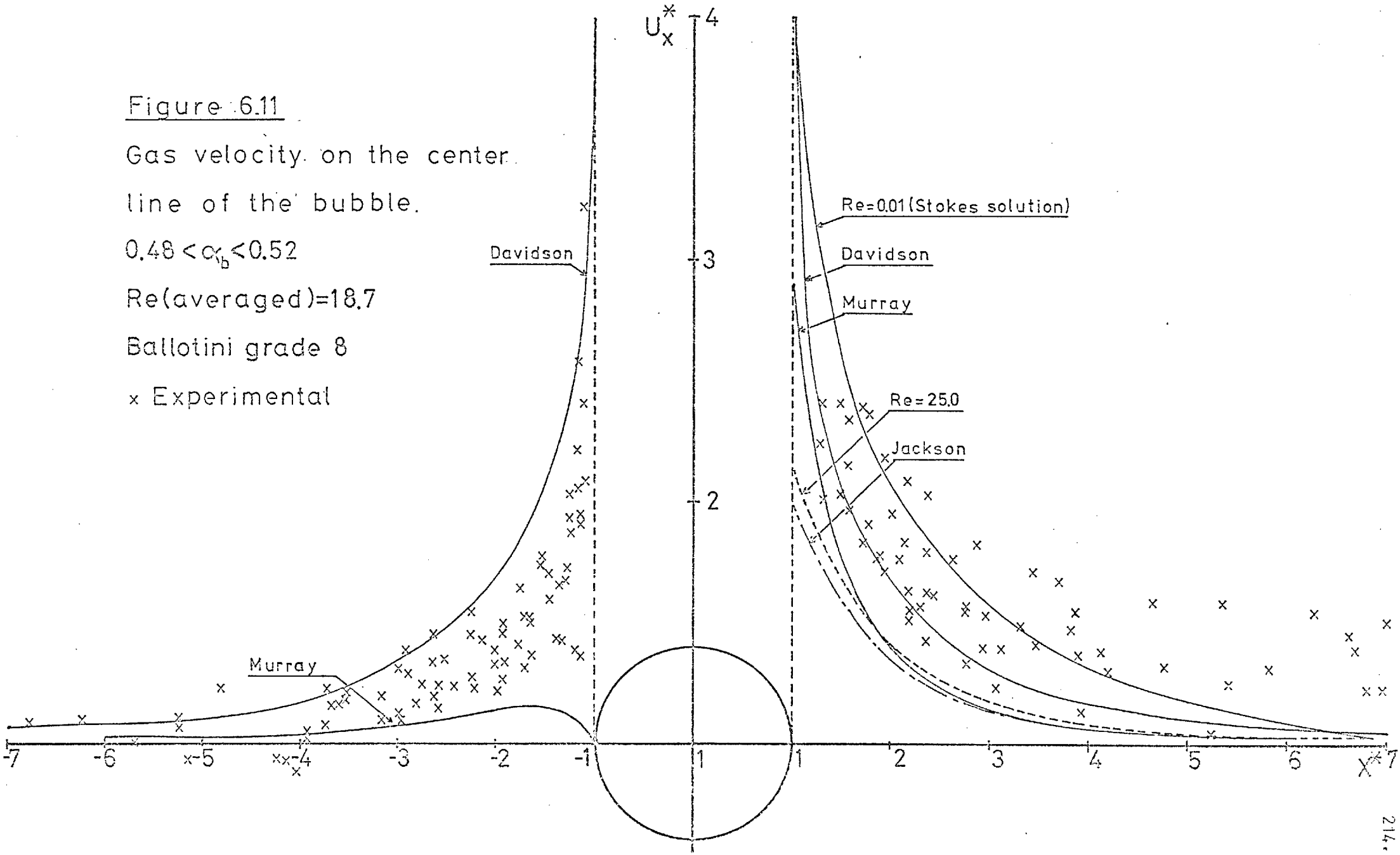


Figure 6.12

Gas velocity on the center line of the bubble.

$1.40 < \alpha_b < 1.60$

Re (averaged) = 26.1

Ballotini grade 10

x Experimental

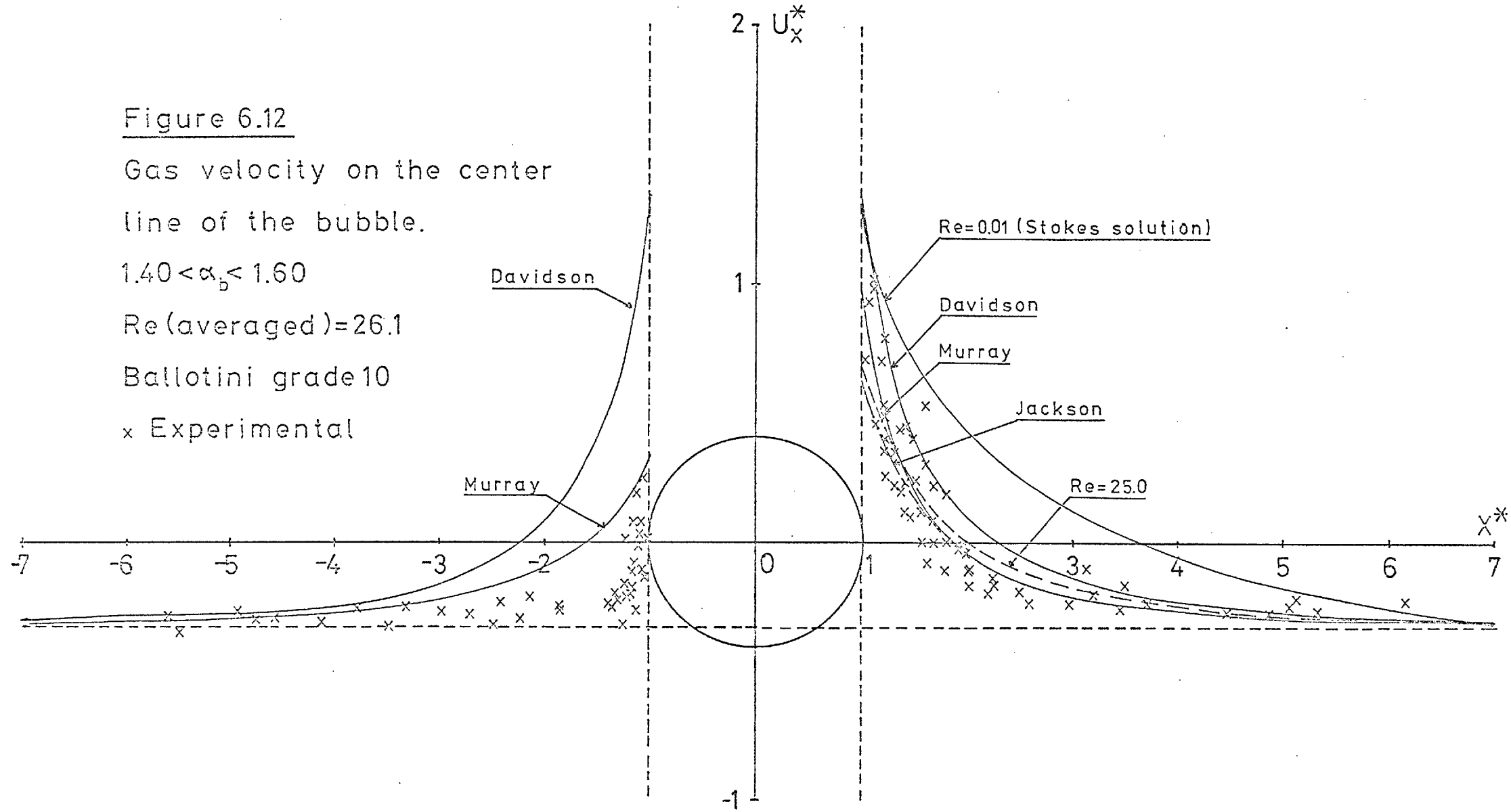


Figure 6.13

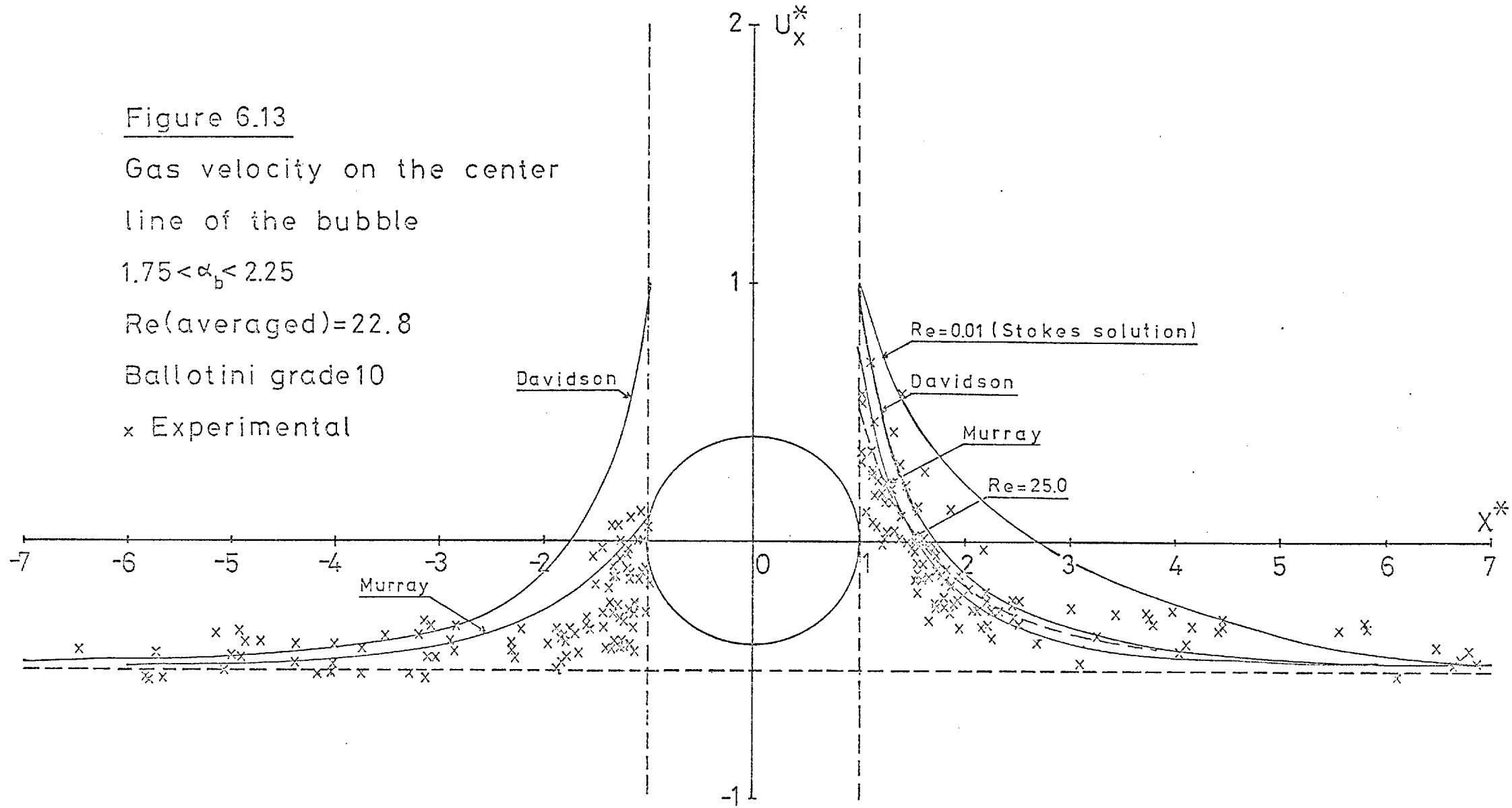
Gas velocity on the center line of the bubble

$1.75 < \alpha_b < 2.25$

Re(averaged)=22.8

Ballotini grade10

× Experimental



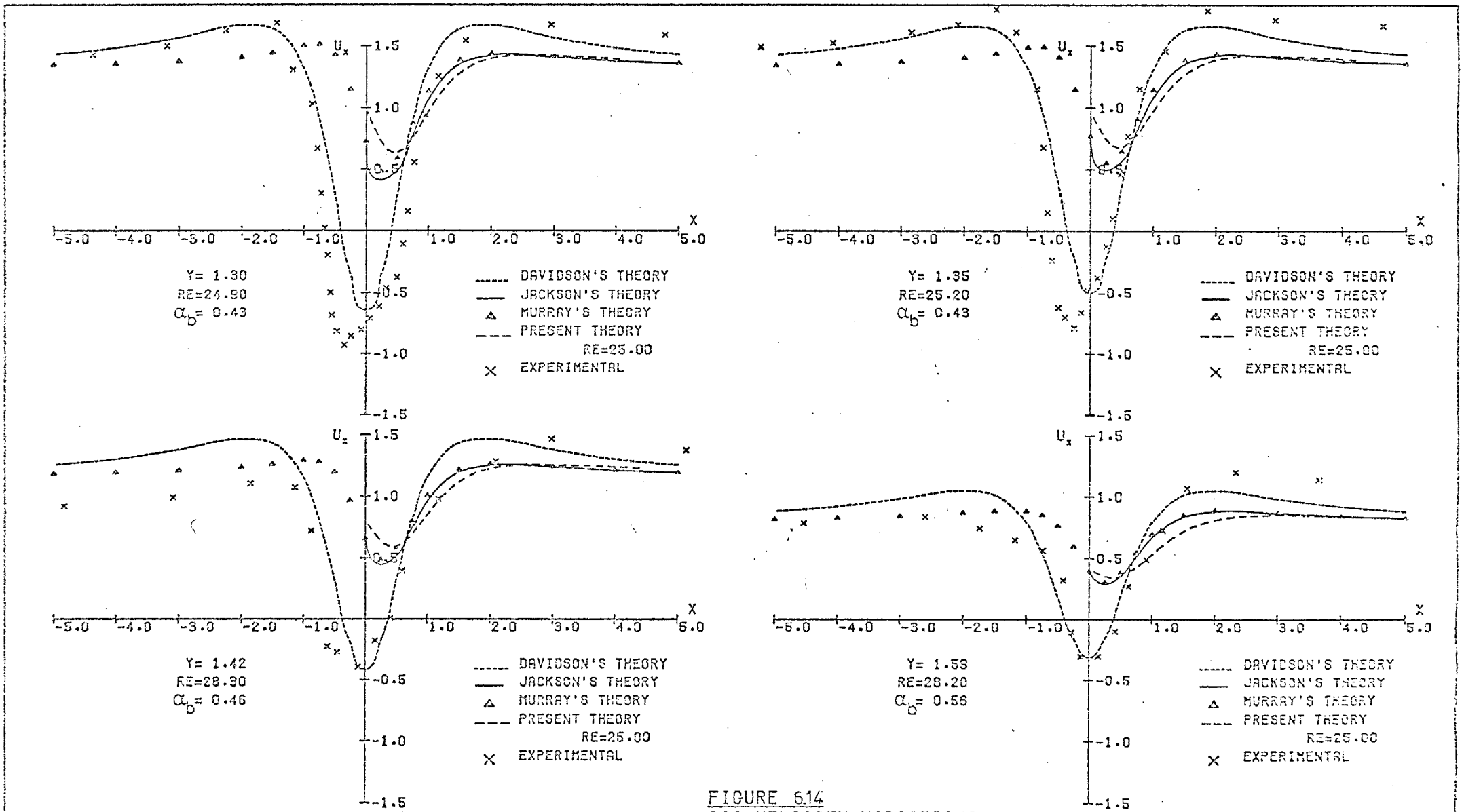
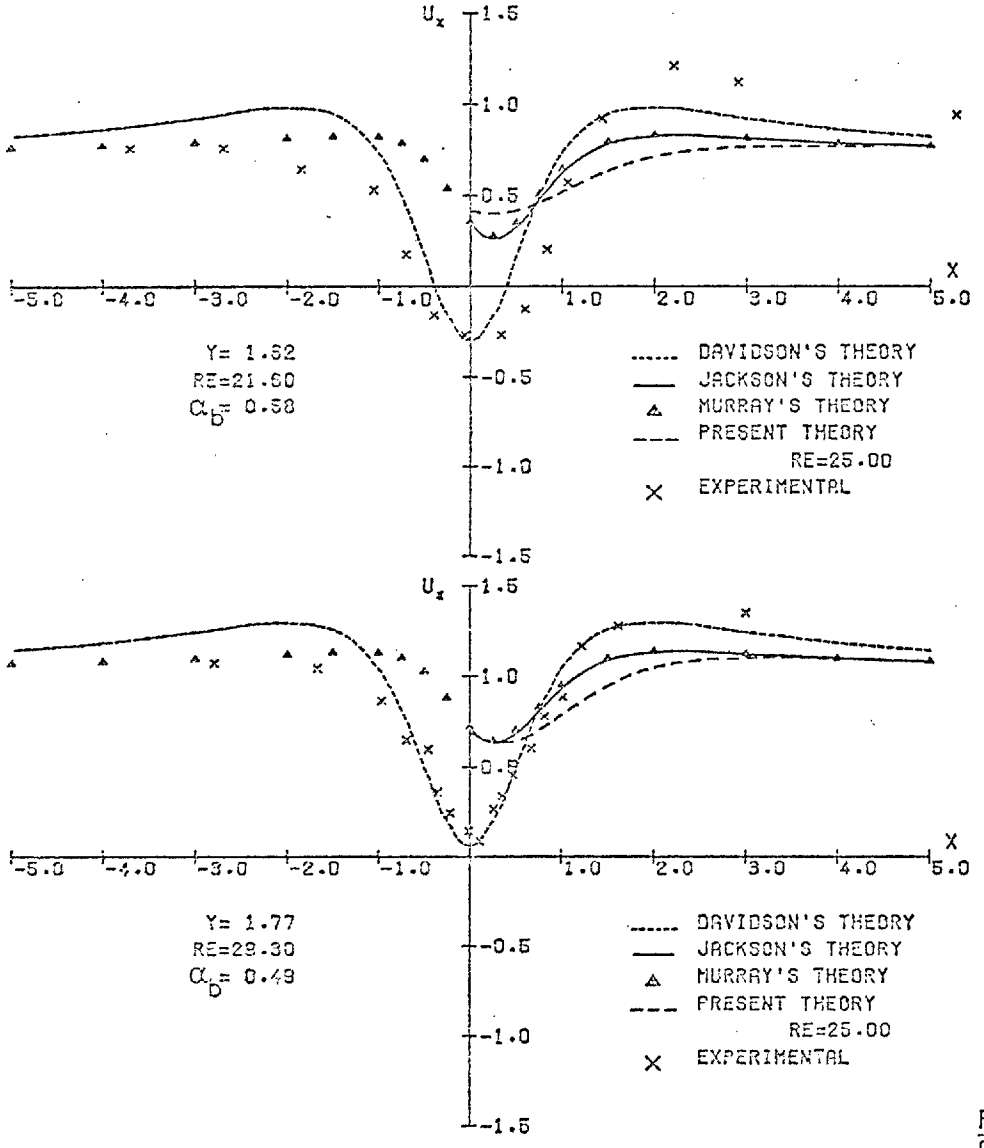


FIGURE 6.14
GAS VELOCITY VARIATIONS
BALLOTINI GRADE 7



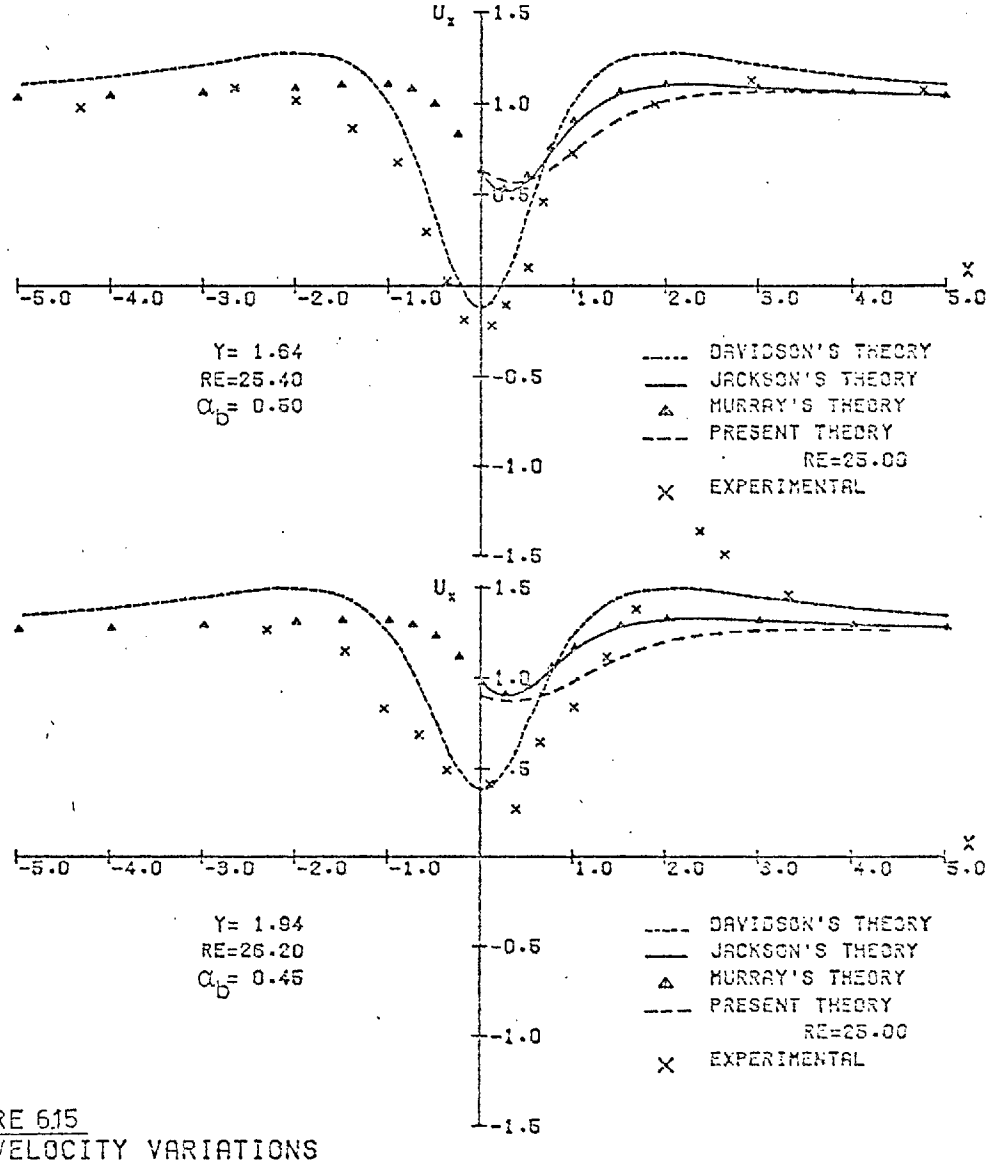


FIGURE 6.15
GAS VELOCITY VARIATIONS
BALLOTINI GRADE 7

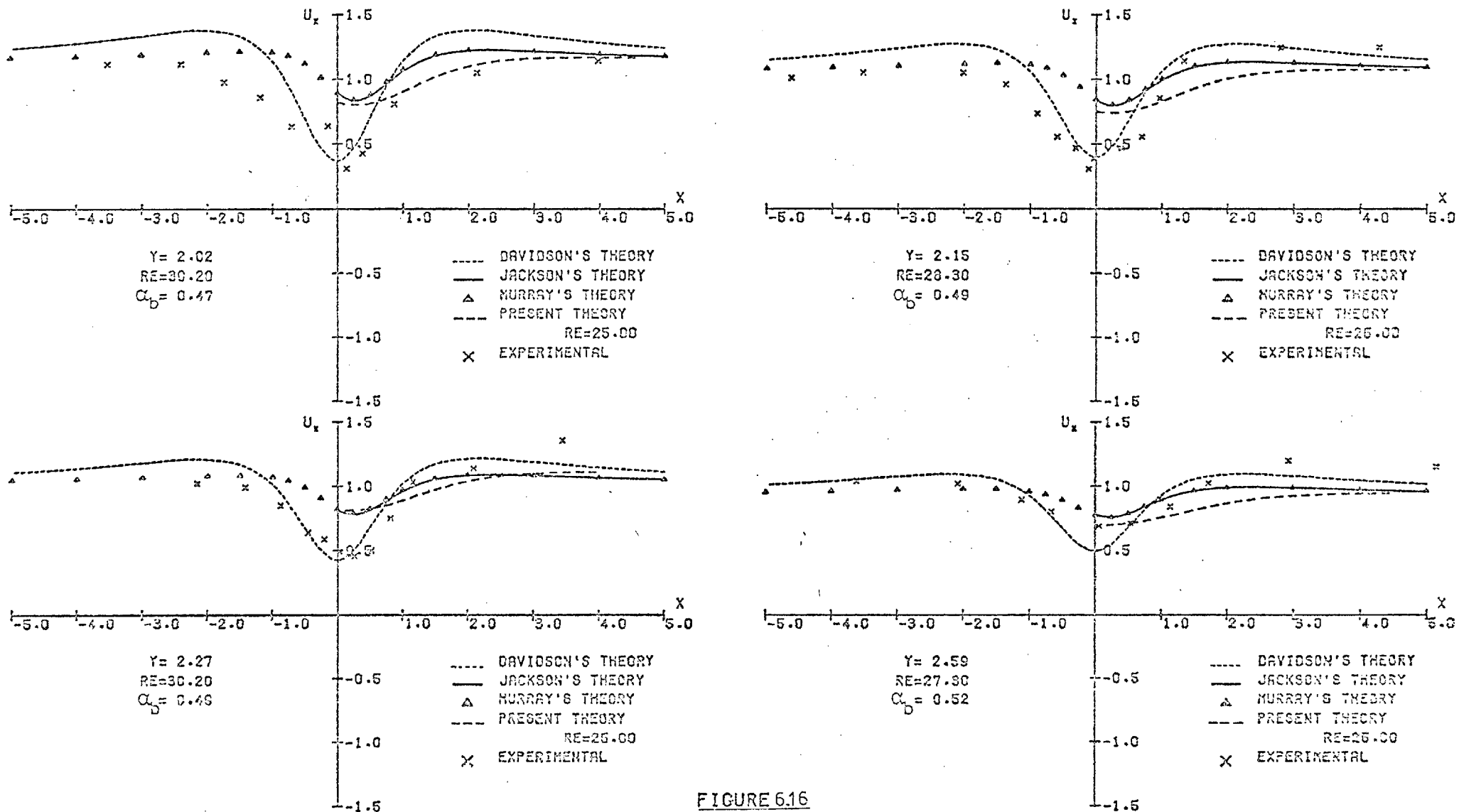


FIGURE 6.16
GAS VELOCITY VARIATIONS
BALLOTINI GRADE 7

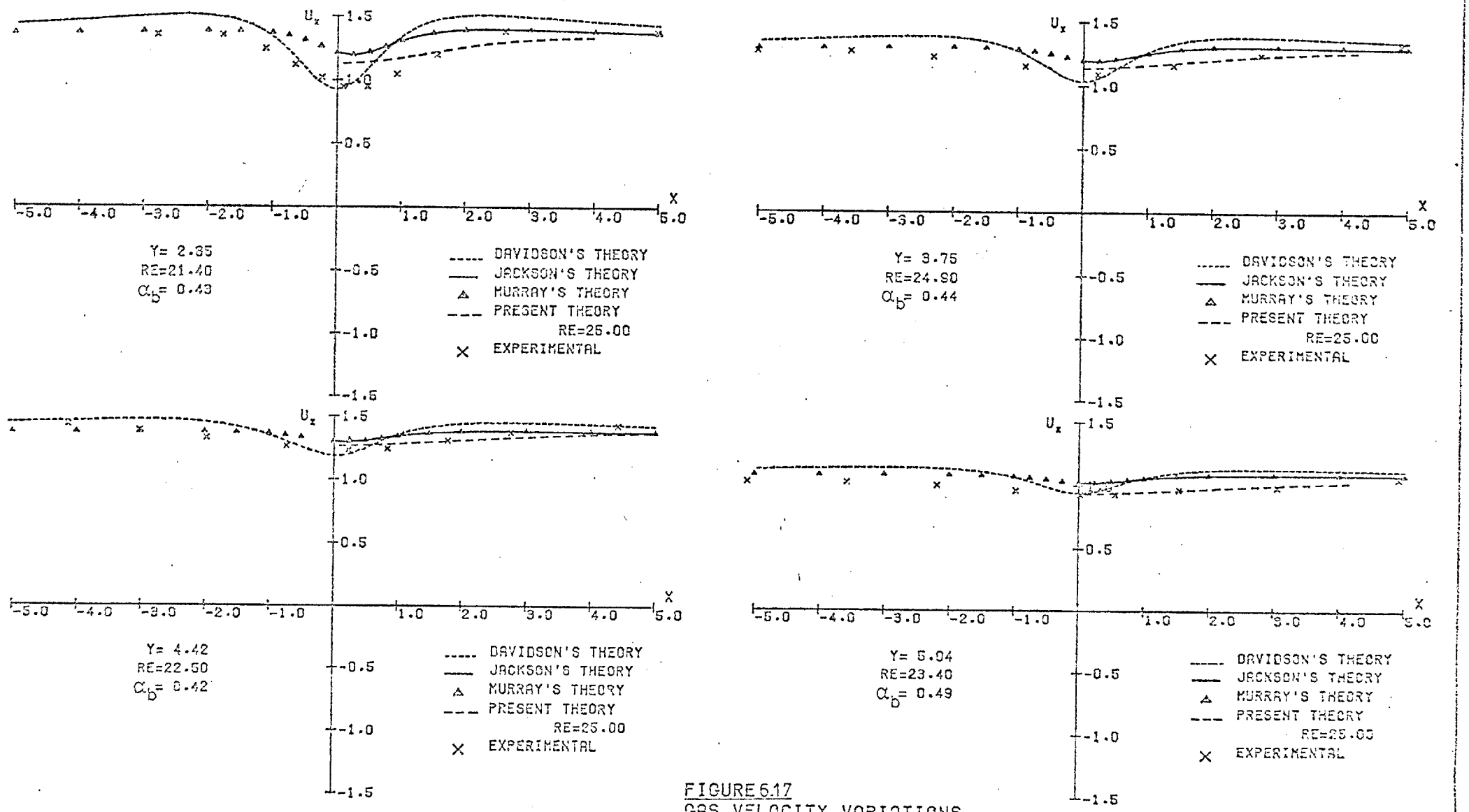
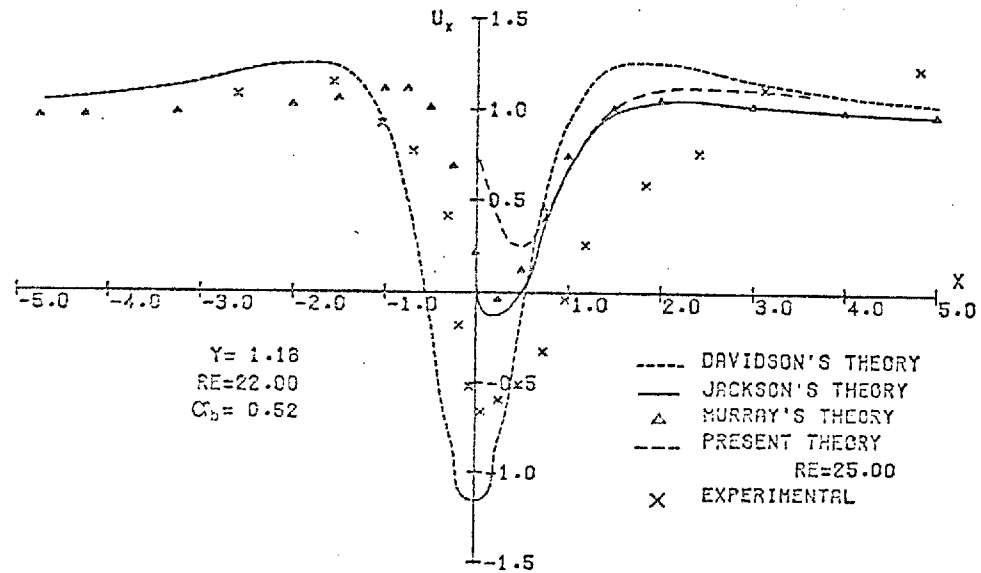
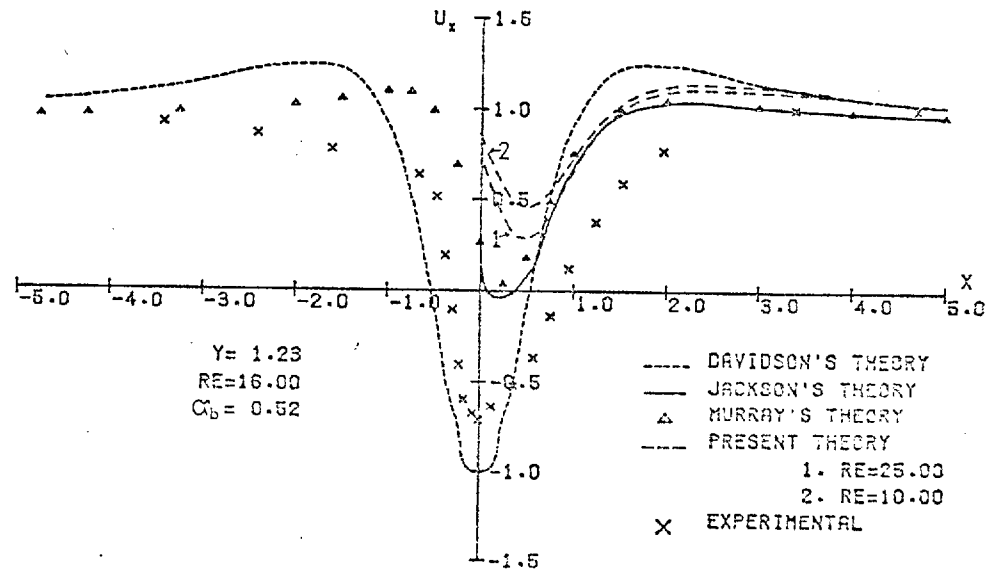
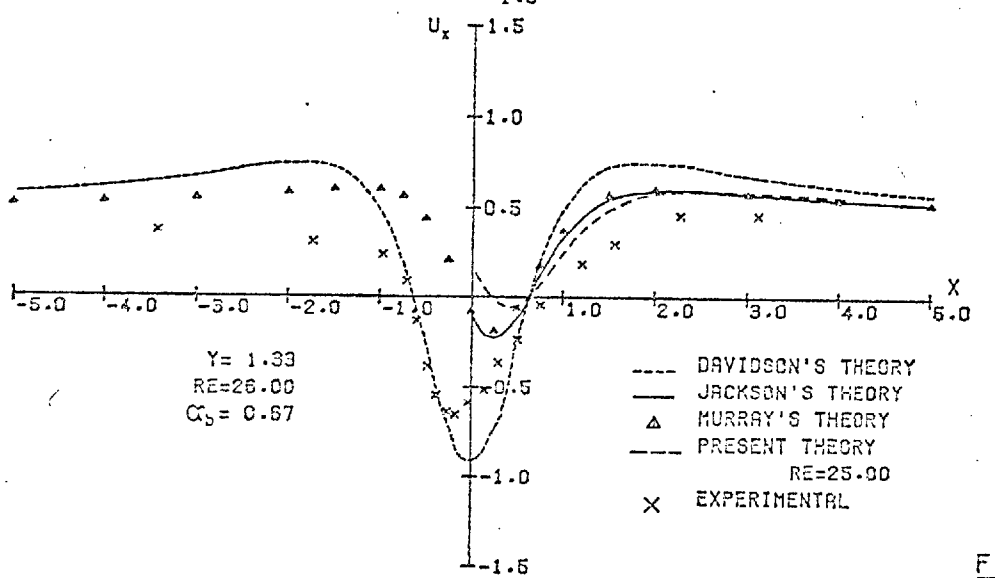


FIGURE 6.17
GAS VELOCITY VARIATIONS
BALLOTINI GRADE 7







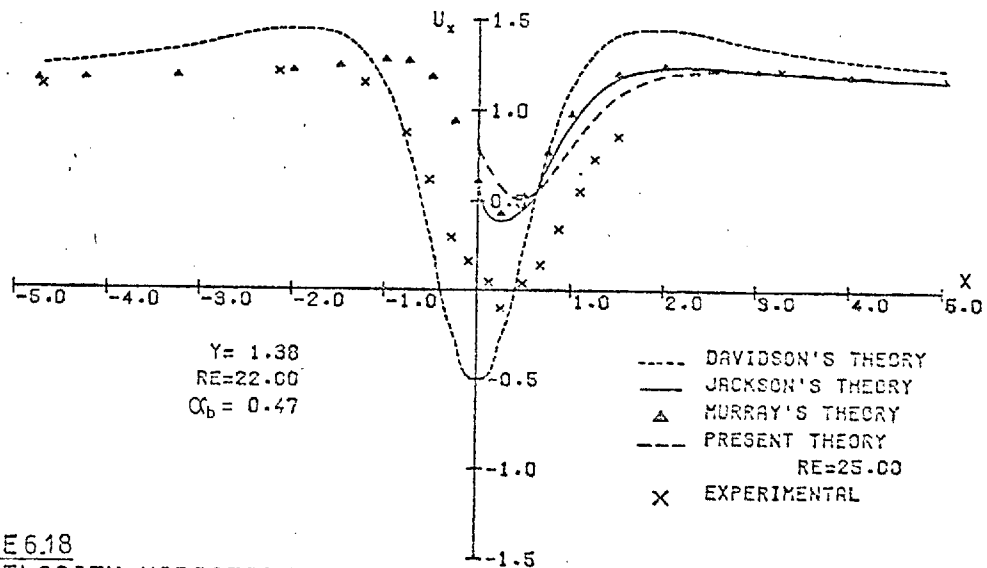
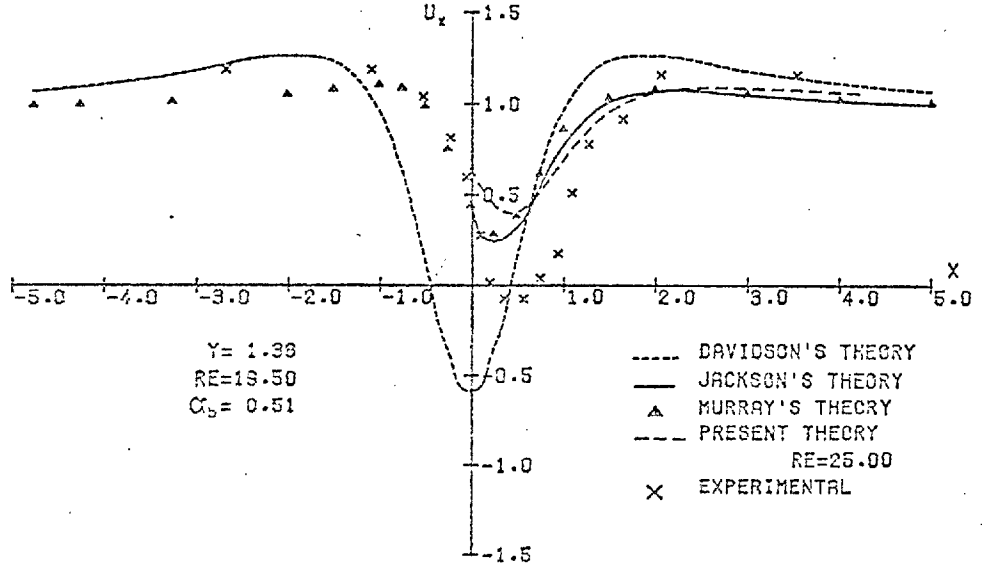
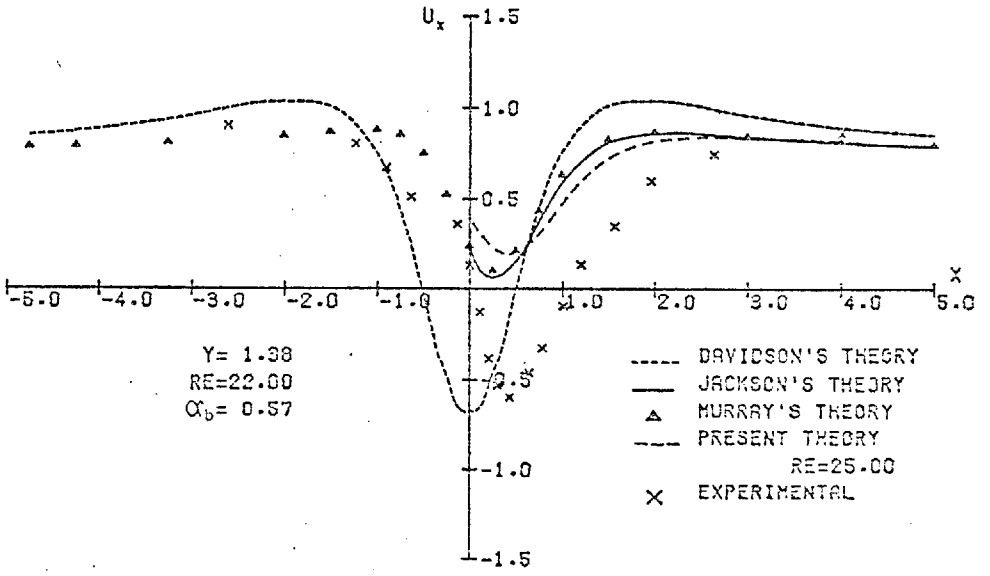
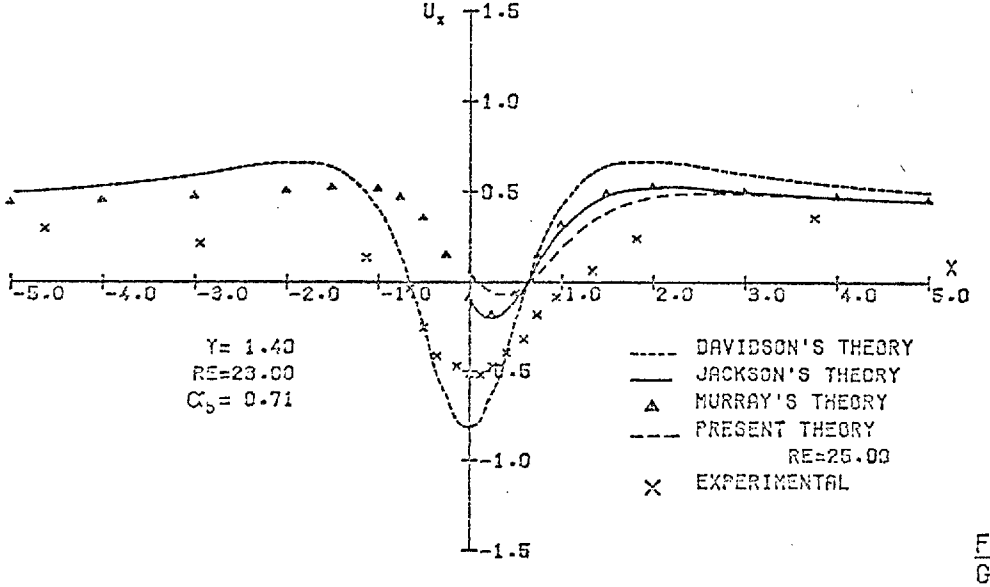


FIGURE 6.18
GAS VELOCITY VARIATIONS
BALLOTINI GRADE 8







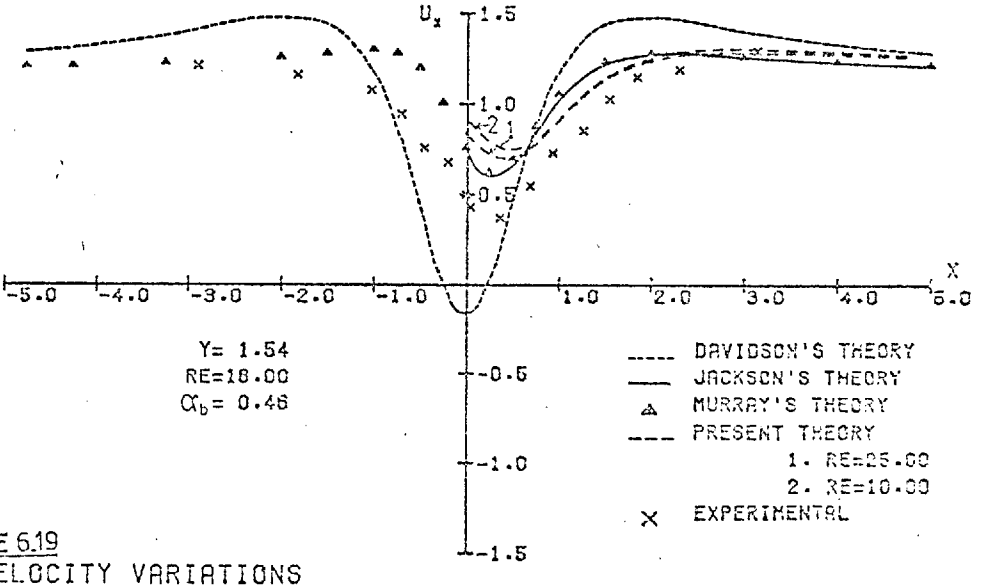


FIGURE 6.19
GAS VELOCITY VARIATIONS
BALLOTINI GRADE 8

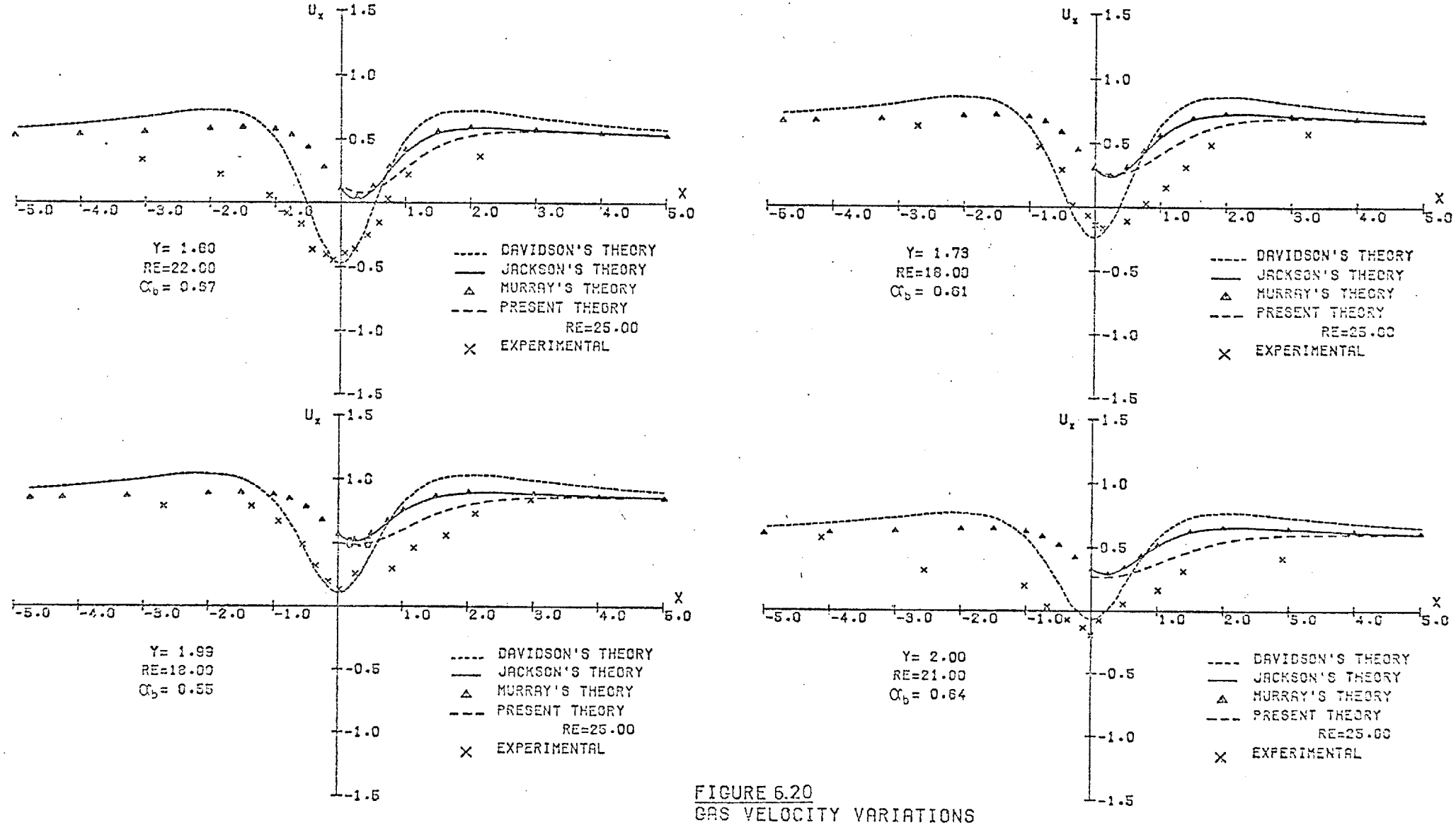


FIGURE 6.20
GAS VELOCITY VARIATIONS
BALLOTINI GRADE 8

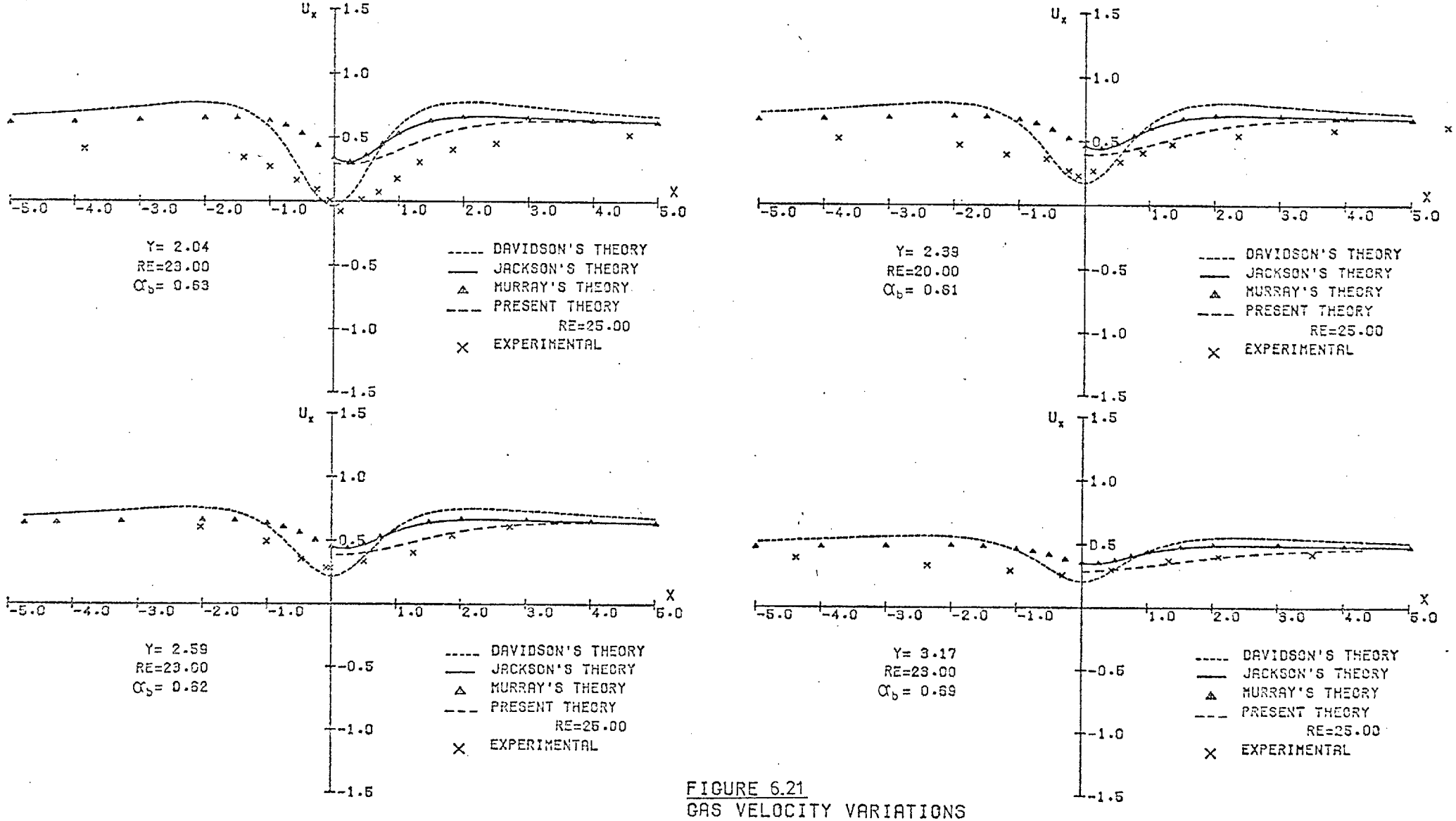


FIGURE 6.21
GAS VELOCITY VARIATIONS
BALLOTINI GRADE 8

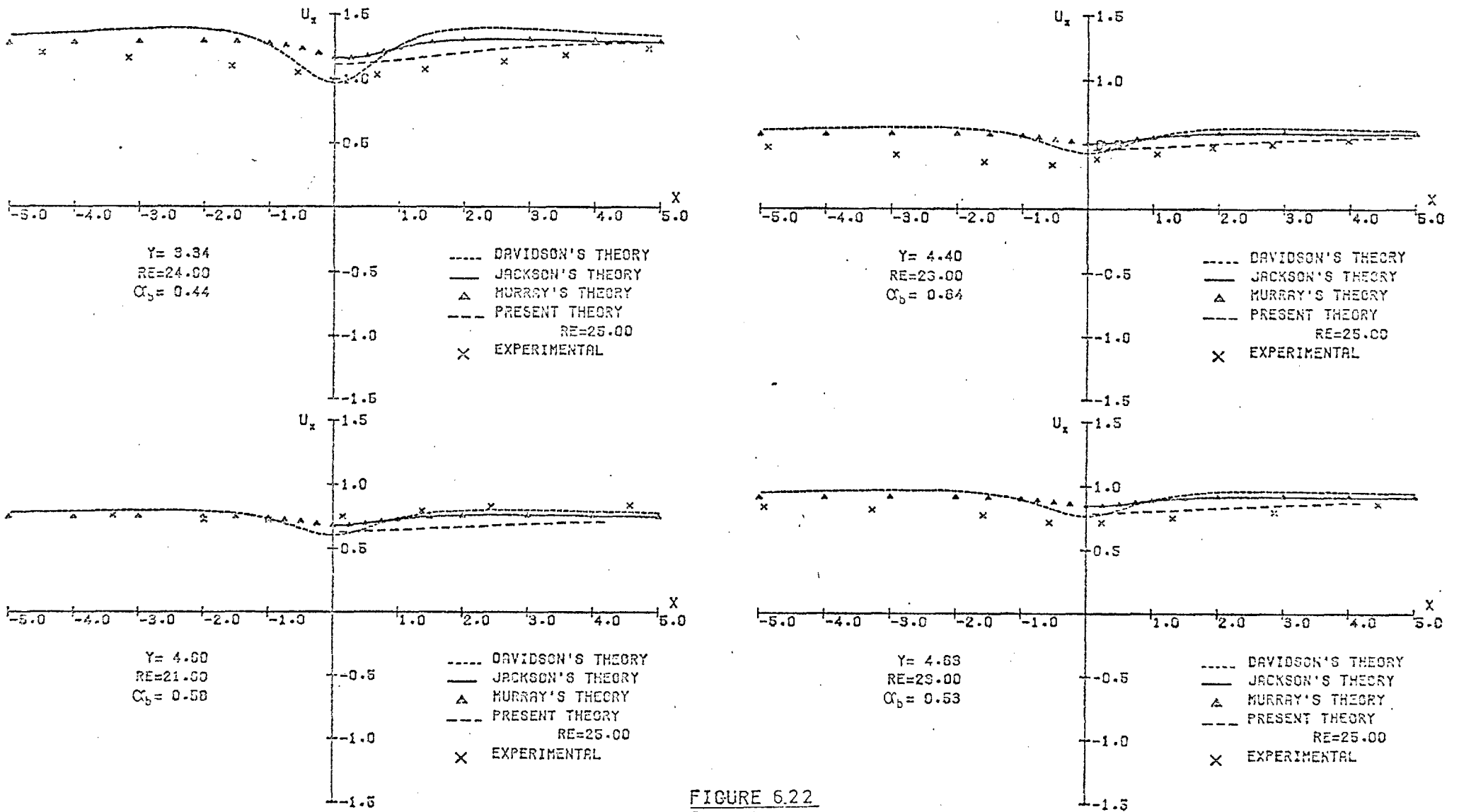


FIGURE 6.22
GAS VELOCITY VARIATIONS
BALLOTINI GRADE 8

CHAPTER 7

INDIRECT MEASUREMENT OF THE BUBBLE THROUGH-FLOW VELOCITY

Although theories of bubble motion in a fluidised bed assume there is no particle flowing through the bubble, experimental evidence shows that a number of particles detach from the bubble roof and fall into the bubble wake.

It was therefore thought that the velocity of these particles might give an estimation of the velocity of gas percolating through the bubble.

7.1 Theory

For this let us consider the movement of an isolated particle M with a mass m. It is falling from rest under gravity but experiences a resistance from a steady flow of air, the velocity of which is U. The purpose is then to find how the velocity of the particle, V_p, is related to time t.

The distance axis 0Z is taken in the downward direction and is fixed with respect to the fluidised bed (V_p is the absolute velocity of the particle). In addition t = 0 when the particle M coincides with 0. (Figure 7.1).

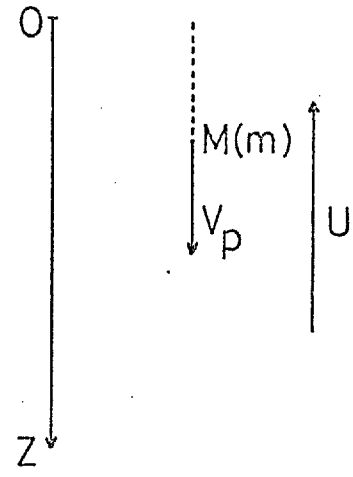


Figure 7.1

The following forces act on the particles:

(i) its weight $f_1 = mg = \frac{4}{3}\pi r_p^3 \rho_p g$

(ii) the Archimedes's force $f_2 = -\frac{4}{3}\pi r_p^3 \rho_f g$

(iii) the viscous resistance of the fluid $f_3 = -6\pi r_p \mu_f \left\{\frac{dZ}{dt} + U\right\}$

(iv) the drag force of the fluid on the particle $f_4 = -\frac{1}{2}\pi r_p^2 \rho_f C_{D_p} \left\{\frac{dZ}{dt} + U\right\}^2$

In the expressions of the viscous resistance and of the drag force, the velocity entering the equations is the relative velocity between the particle and the fluid, i.e. $\frac{dZ}{dt} + U$

= absolute velocity of the particle + absolute velocity of the fluid. Furthermore Basset's history term has been neglected

Now, we have:

$$m \frac{d^2Z}{dt^2} = \sum_{i=1}^{4} f_i$$

whence:

$$m\frac{d^2Z}{dt^2} = \frac{4}{3}\pi r_p^3 \rho_p g - \frac{4}{3}\pi r_p^3 \rho_f g - 6\pi r_p \mu_f \left\{\frac{dZ}{dt} + U\right\}$$

$$- \frac{1}{2}\pi r_p^3 \rho_f C_{Dp} \left\{\frac{dZ}{dt} + U\right\}^2 \qquad (7.1)$$

with the initial conditions: $t = 0 \quad Z = 0$

$$t = 0 \quad \frac{dZ}{dt} = V_p = 0 \qquad (7.2)$$

Relations (7.1) and (7.2) describe the complete motion of the falling particle. In addition, in all cases of gas fluidisation, $\rho_p \gg \rho_f$ and therefore we shall neglect Archimedes's force in comparison with the particle weight.

Let us put:

$$T = \frac{dZ}{dt} + U$$

$$A = \frac{3}{8}\,\frac{1}{r_p}\,\frac{\rho_f}{\rho_p}$$

$$B = \frac{9}{2}\,\frac{\mu_f}{\rho_p\, r_p^2}$$

Relations (7.1) and (7.2) become:

$$\frac{dT}{dt} = g - BT - AC_{Dp}\, T^2 \qquad (7.3)$$

$$t = 0 \qquad T = U$$

Let us also define the Reynolds number for the particle as:

$$Re_p = \frac{d_p \rho_f T}{\mu_f}$$

Depending upon the value of Re_p, we can consider three different regions for the behaviour of the particle:

(i) $Re_p < 0.5$ laminar region (Stokes's law)

(ii) $0.5 < Re_p < 1000$ intermediate region

(iii) $Re_p > 1000$ turbulent region (Newton's law)

In Stokes's law the momentum term will be negligible as compared with the viscous term, while in Newton's law the converse will be true.

Let us consider the three different solutions.

7.1.1 Laminar region : $Re_p < 0.5$

Equation (7.3) reduces to : $\frac{dT}{dt} = g - BT$

and $t = 0 \quad T = U$

Therefore it is easy to find $T = \frac{g}{B}(1 - e^{-Bt}) + Ue^{-Bt}$ (7.4)

and when $t \longrightarrow \infty \quad T \rightarrow \frac{g}{B} = \frac{2g \rho_p r_p^2}{9 \mu_f}$ which is Stokes's equation

for the free-falling velocity of a particle.

7.1.2 Turbulent region : $Re_p > 1000$

Equation (7.3) becomes: $\frac{dT}{dt} = g - AC_{Dp} T^2$

In this case C_{Dp} is almost independent of the Reynolds number and equal to 0.44, whence:

$$\frac{dT}{dt} = g - 0.44AT^2 = g - k' T^2 \quad \text{with } k' = 0.44A$$

By separating the variables, this equation can easily be integrated:

$$T = \frac{U\sqrt{kg} + g \tanh\{\sqrt{kg}\, t\}}{\sqrt{kg} + Uk \tanh\{\sqrt{kg}\, t\}} \qquad (7.5)$$

and when $t \to \infty$ $\quad T \longrightarrow \sqrt{\frac{2gr_p \rho_p}{0.33\, \rho_f}}$

7.1.3 Intermediate region : $0.5 < Re_p < 1000$

This case is more difficult since there is no analytical solution for equation (7.3). The numerical method which we have followed is due to Heywood (107). One can easily obtain the following relations between the drag coefficient C_{Dp} and the Reynolds number Re_p :

$$C_{Dp}\, Re_p^2 = \frac{4}{3}\, g\, \frac{\rho_p - \rho_f}{\mu_f^2}\, \rho_f\, d_p^3$$

$$\frac{Re_p}{C_{Dp}} = \frac{3}{4g}\, \frac{\rho_f^2}{\rho_p - \rho_f}\, \frac{V_t^3}{\mu_f}$$

where V_t is the terminal velocity of the particle.

Heywood sets

$$\left.\begin{aligned} C_{Dp}\ Re_p^2 &= P^3\ d_p^3 \\ \frac{Re_p}{C_{Dp}} &= \frac{V_t^3}{Q^3} \end{aligned}\right\} \qquad (7.6)$$

From experimental data, he then computes the values of the function $F\left(\log P d_p, \log \frac{V_t}{Q}\right) = 0$ which is valid for all circumstances of motion.

Let us consider equation (7.3). We shall assume that the viscous term is small with respect to the momentum term, whence:

$$\frac{dT}{dt} = g - A C_{Dp}\ T^2 \qquad \text{with } C_{Dp} = f(T)$$

introducing Re_p, we get:

$$\frac{dT}{dt} = g - k'' C_{Dp}\ Re_p^2 \qquad (7.7)$$

with $$k'' = \frac{3}{32} \frac{\mu_f^2}{r_p^3\ \rho_p\ \rho_f}$$

Then equation (7.7) allows us to use Heywood's method easily:

(a) At $t = 0$ $\frac{dZ}{dt} = 0$ and $T = U$ gives Re_p initial.

(b) From relations (7.6) we have: $\log (Re_p) = \log (Pd_p) + \log \left(\frac{V_t}{Q}\right)$.

The value of $\log (Re_p)$ initially is known from stage (a). By interpolating between the values of $\log (Pd_p)$ and $\log \left(\frac{V_t}{Q}\right)$ given by Heywood, it is possible to find a pair of values with a sum equal to $\log (Re_p)$.

(c) Knowing log (Pd_p), we can calculate the value of $C_{Dp} Re_p^2$ at t = 0 from relations (7.6).

(d) From equation (7.7) and given a time step Δt, it is possible to calculate the corresponding velocity step $\Delta T = (g - k'' C_{Dp} Re_p^2)\ \Delta t$, and the new value of T : $T_1 = T_o + \Delta T$. The procedure is then started again with T_1 as a new initial value.

7.2 Application to a bubble rising in a fluidised bed

7.2.1 Through-flow velocity

All theories of bubble motion in a fluidised bed suggest that the mean velocity of gas percolating through the bubble is given by the relation:

$$\bar{U} = U_b + k U_o \qquad (7.8)$$

(with respect to a stationary observer)

or in dimensionless form:

$$\frac{\bar{U}}{U_b} = 1 + \frac{k \varepsilon_o}{\alpha_b} \qquad (7.9)$$

with U_b as reference quantity.

$$\text{or,} \quad \frac{\bar{U}}{U_o} = k + \frac{\alpha_b}{\varepsilon_o} \qquad (7.10)$$

with U_o as reference quantity.

The values of k which can be found in the literature are listed in Table 7.1. This table shows there is some discrepancy between the theoretical results. Furthermore only one experimental result is reported.

In this work a numerical value of k was obtained for the two-dimensional case using the theoretical analysis outlined in the preceding sections. For this purpose a computer program was written to calculate the velocity of a falling particle starting at time t = 0 and $V_p = 0$ and placed in a stream of air of velocity $\bar{U} = U_b + k U_o$.

The calculation was carried out, proceeding step by step in time. At each step the particle Reynolds number was calculated and depending on its value the appropriate solution selected (laminar, intermediate or turbulent region).

The value of $\bar{U}$ was varied by varying the value of k and for each case the complete motion of the particle $V_p(t)$ was calculated.

7.2.2 Experimental

Films taken for the determination of the particle movement around a bubble described in Chapter 5 were used and the velocity of particles falling through the bubble was recorded. In these experiments it is difficult to find the exact moment at which the particle detaches from the bubble roof and therefore its position for time t = 0. However at the beginning of the movement, the curve $V_p(t)$ is linear. Time t = 0 was thus determined by extrapolating the experimental curve for particle velocity to $V_p = 0$ as shown in Figure 7.2.

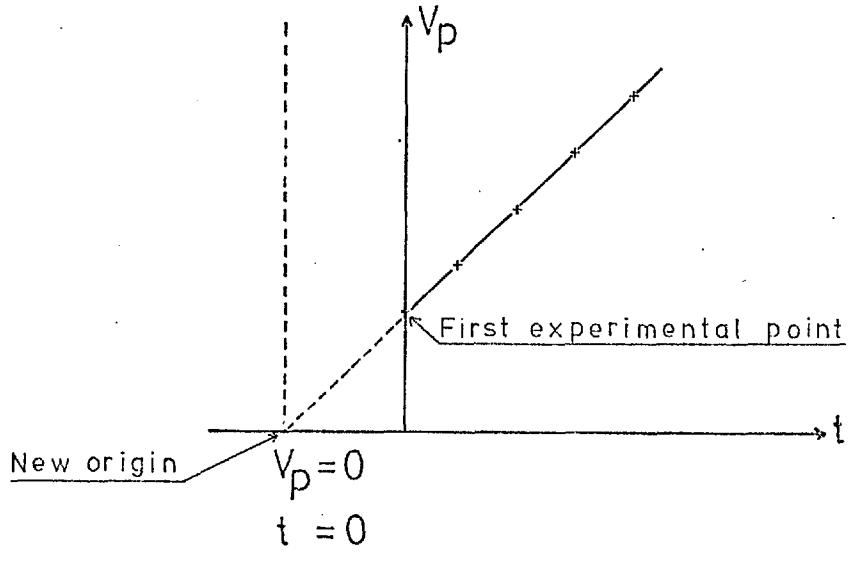


Figure 7.2

Depending on the position of the particle with respect to the bubble axis, the throughflow velocity will be different. A general curve $V_p(t)$ was determined by fitting all experimental data for a given bubble and thus the value of the through flow obtained from the general curve $V_p(t)$ is the average value.

The experimental determination of k was made for small values of the dimensionless time $\tau_p = \frac{U_b t}{d_p}$ when particles are near the apex of the bubble where the latter is closer to the assumed circular shape. For larger time the elongation of the bubble reduces the throughflow velocity and the particle moves faster. In the present experiments k was determined as the average for the first five values of τ_p. A set of typical results is presented in Table 7.2.

In this table the experimental value of the particle velocity

corresponds to the general curve $V_p(t)$. For each value of τ_p the value of k is determined by interpolating between theoretical values given in the upper part of the table. As mentioned previously it can be seen that the value of k experimental decreases when τ_p increases.

Experiments were carried out only for larger particles (Ballotini grades 7 and 8). With smaller particles bubbles were much more unstable and it was found impossible to follow individual particles falling through the bubble without the bubble splitting.

Experimental results are shown on Table 7.3.

7.3 Theoretical values of the through flow determined from the viscous theory for a two-dimensional bubble

Theoretical values of the throughflow can easily be determined from the values of the radial component of the gas velocity at the bubble surface.

$$Q = 2 \int_0^{\theta_r} \varepsilon_a u_r \, a \, d\theta \qquad (7.11)$$

where θ_r is the angle at which the flow of gas reverses and ε_a is the voidage at the bubble surface ($r = a$).

Thus the mean throughflow velocity is determined by:

$$\bar{U}' = \frac{\int_0^{\theta_r} \varepsilon_a u_r \, d\theta}{\sin \theta_r}$$

On the other hand:

$\bar{U}' = k U_o \; (= \bar{U} - U_b)$ with respect to axes moving with the bubble

thus:

$$k = \frac{\int_0^{\theta_r} \varepsilon_a u_r^+ \, d\theta}{\varepsilon_o \sin \theta_r}$$

where u_r^+ is the dimensionless radial component of the interstitial gas velocity with respect to u_o (i.e. $u_r^+ = \frac{u_r^*}{\alpha_b}$)

We shall follow Hargreaves and Pyle (108) in assuming a constant voidage ε_a at the bubble surface. Although a precise solution would require to take into account the voidage variations as defined in Chapter 2 (section 2.4.4), a good estimate can probably be obtained by assuming ε_a constant. Furthermore it has been seen in Chapter 4 that, by using Jackson's method, there is a large region of the bubble surface where no solution for the voidage is obtained, especially for low Reynolds numbers.

Thus:
$$k = \frac{\varepsilon_a}{\varepsilon_o} \quad \frac{\int_0^{\theta_r} u_r^+ \, d\theta}{\sin \theta_r} \qquad (7.12)$$

Variations of the radial component of the gas velocity u_r^+ as a function of the surface angle up to $\theta = 90^o$ are shown on Figure 7.3. On this figure the area comprised between the axes and a particular curve is thus proportional to the throughflow as shown by equation (7.11).

Figure 7.4 shows the variations of the angle θ_r and of the coefficient k (for the particular case $\varepsilon_a = \varepsilon_o$) as function of the Reynolds number. When the latter decreases, θ_r tends towards 90^o

and k towards Davidson's solution k = 2.

Finally values of the coefficient k calculated for various values of the ratio $\frac{\varepsilon_a}{\varepsilon_o}$ are shown on Table 7.4. These results can be usefully compared with those given by Hargreaves and Pyle (108). It can be seen that for intermediate Reynolds number the predicted values are lower than those calculated by Hargreaves and Pyle when $\frac{\varepsilon_a}{\varepsilon_o} > 1.1$.

Furthermore comparison of results in Tables 7.1 and 7.4 with the experimental value found in this work, k = 2.46, shows that Davidson's theory is again the best prediction.

7.4 Conclusion

The average value of the throughflow velocity is in fair agreement with Davidson's prediction of k = 2.0. Experimental results obtained in the experiments show that the throughflow velocity is upwards, its value being:

$$\bar{U} = U_b + 2.46\, U_o.$$

Furthermore, in all cases, particles were found to be in the transition regime where $0.5 < Re_p < 1000$.

It must be noted that the theory developed at the beginning of this chapter applies only to an isolated particle and can by no means be extended to the velocity of a falling "curtain" of particles (as it happens for small Ballotini grade 10) or to the "knife" formed during splitting. In the former cases one expects that the falling velocity of

a particle will strongly depend upon the particle concentration.

Finally it should be emphasized that this method of measurement is not very precise since:

(i) only particles close to the wall of the bed could be examined

(ii) in many cases, the bubble tends to elongate or split, which modifies the value of the through-flow velocity.

(iii) a particle examined is not perfectly isolated and might be influenced by neighbouring falling particles.

Authors	voidage at the bubble surface ε	two-dimensions k	three-dimensions k
1. Theories			
Davidson and Harrison (10)	constant $=\varepsilon_o$	2.0	3.0
Murray (12)	constant $=\varepsilon_o$	1.0	1.0
Sandford and Leung (109)	0.45 (1)	1.6	-
	0.48 (2)	1.9	2.0
Hargreaves and Pyle (108)	0.400	0.744	0.705
	0.425	0.933	0.880
	0.450	1.147	1.093
	0.475	1.422	1.340
	0.500	1.743	1.645
	0.525	2.120	2.000
	0.550	2.580	2.437
Pyle and Rose (110) (from equation 7.10)	-	-	4.0
Anwer (97) (from equation 7.10)	-	-	0.5
2. Direct measurements			
Judd (98)	-	5.1 (maximum value)	

(1) voidage measurements by Lockett and Harrison (7)

(2) calculated by Stewart (quoted by Sandford and Leung (109))

Table 7.1 Theoretical and experimental value of k in equation (7.8)

k \ time τ_p	0.01	0.02	0.03	0.04	0.05
0.5	0.229	0.455	0.678	0.898	1.116
1.0	0.224	0.445	0.663	0.878	1.031
1.5	0.219	0.434	0.647	0.856	1.063
2.0	0.213	0.423	0.629	0.833	1.033
2.5	0.207	0.410	0.610	0.808	1.001
3.0	0.200	0.397	0.591	0.781	0.968
3.5	0.193	0.383	0.569	0.752	0.932
4.0	0.186	0.368	0.547	0.723	0.895
4.5	0.178	0.353	0.524	0.692	0.856
Experimental value of particle velocity	0.208	0.417	0.625	0.834	1.042
k experimental	2.36	2.23	2.11	1.98	1.85

Table 7.2 Values of the dimensionless particle velocity $V^*_p = \frac{V_p}{U_b}$ as function of the dimensionless time $\tau_p = \frac{U_b t}{d_p}$

k averaged = 2.10

Ballotini grade 7 d_p (average) = 600 μm

Bubble velocity U_b = 40.8 cm/sec

Ballotini grade 7 d_p = 600 μm			Ballotini grade 8 d_p = 450 μm		
Bubble	U_b cm/sec	k averaged	Bubble	U_b cm/sec	k averaged
1	36.4	1.81	1	50.8	2.67
2	40.0	2.89	2	42.4	3.25
3	34.8	2.22	3	37.9	3.66
4	42.1	2.15	4	31.3	3.64
5	50.8	2.10	5	34.6	2.06
6	55.6	3.74	6	31.9	1.53
7	34.8	1.35	7	35.0	1.82
			8	38.7	2.18
k averaged k = 2.32			k averaged k = 2.60		
Average k for both sets of particles k = 2.46					

Table 7.3 Experimental values of k

ε_a / Re	$\varepsilon_a = \varepsilon_o = 0.4$ $\varepsilon_a/\varepsilon_o = 1$	$\varepsilon_a = 0.425$ $\varepsilon_a/\varepsilon_o = 1.0625$	$\varepsilon_a = 0.450$ $\varepsilon_a/\varepsilon_o = 1.125$	$\varepsilon_a = 0.475$ $\varepsilon_a/\varepsilon_o = 1.1875$	$\varepsilon_a = 0.500$ $\varepsilon_a/\varepsilon_o = 1.250$	$\varepsilon_a = 0.525$ $\varepsilon_a/\varepsilon_o = 1.3125$	$\varepsilon_a = 0.550$ $\varepsilon_a/\varepsilon_o = 1.375$
0.01	1.93	2.05	2.17	2.29	2.41	2.53	2.65
0.1	1.81	1.92	2.04	2.15	2.26	2.38	2.49
1.0	1.49	1.58	1.68	1.77	1.86	1.96	2.05
5.0	1.06	1.13	1.19	1.26	1.33	1.39	1.46
10.0	0.93	0.99	1.05	1.10	1.16	1.22	1.28
25.0	0.82	0.87	0.92	0.97	1.03	1.08	1.13
50.0	0.78	0.83	0.88	0.93	0.98	1.02	1.07
100.0	0.76	0.81	0.86	0.90	0.95	1.00	1.05
Jackson	0.73	0.78	0.82	0.87	0.91	0.96	1.00

Table 7.4. Theoretical values of k obtained from the viscous theory.

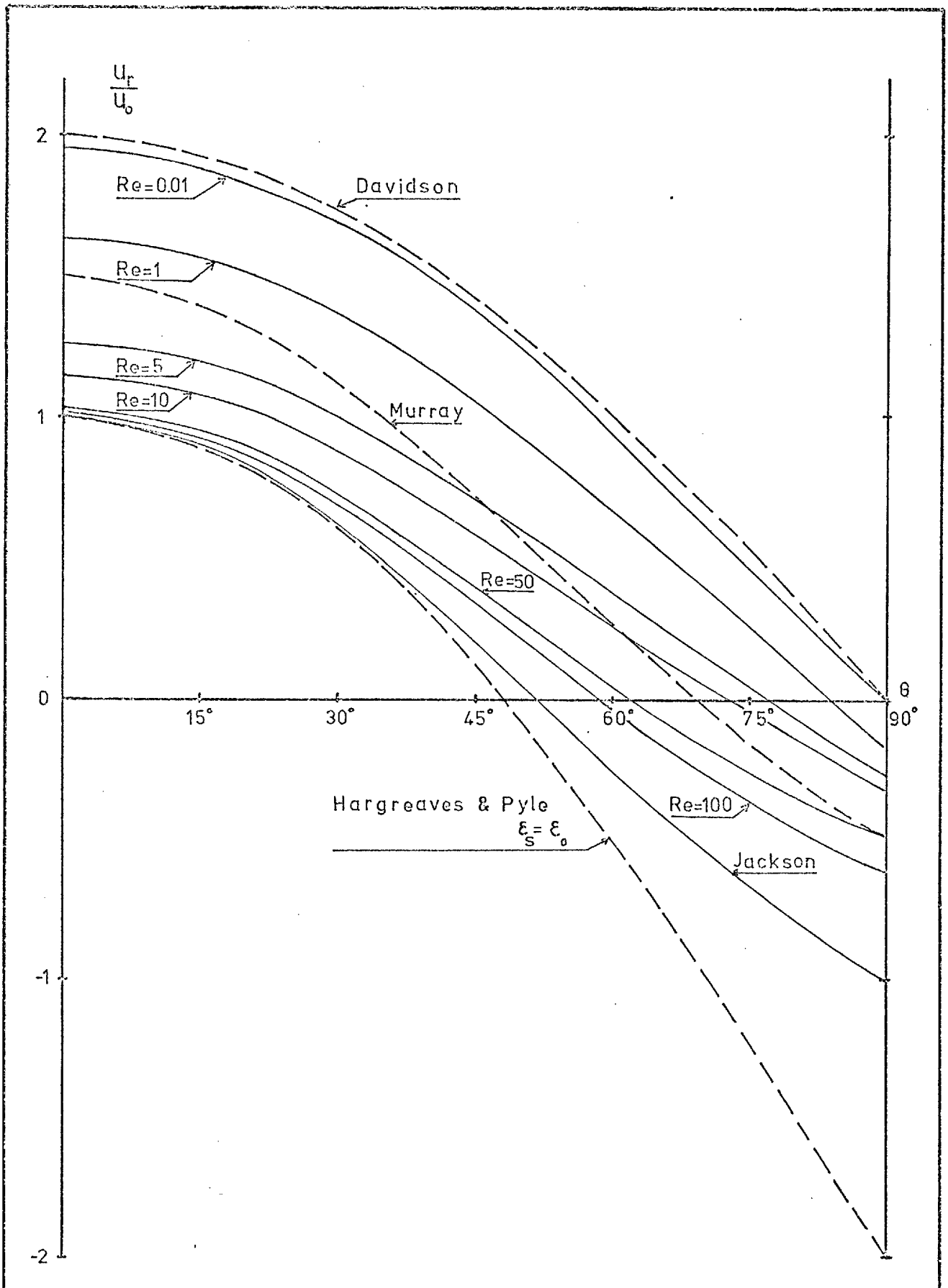


Figure 7.3 Radial velocity of gas at the bubble surface as a function of the surface angle.

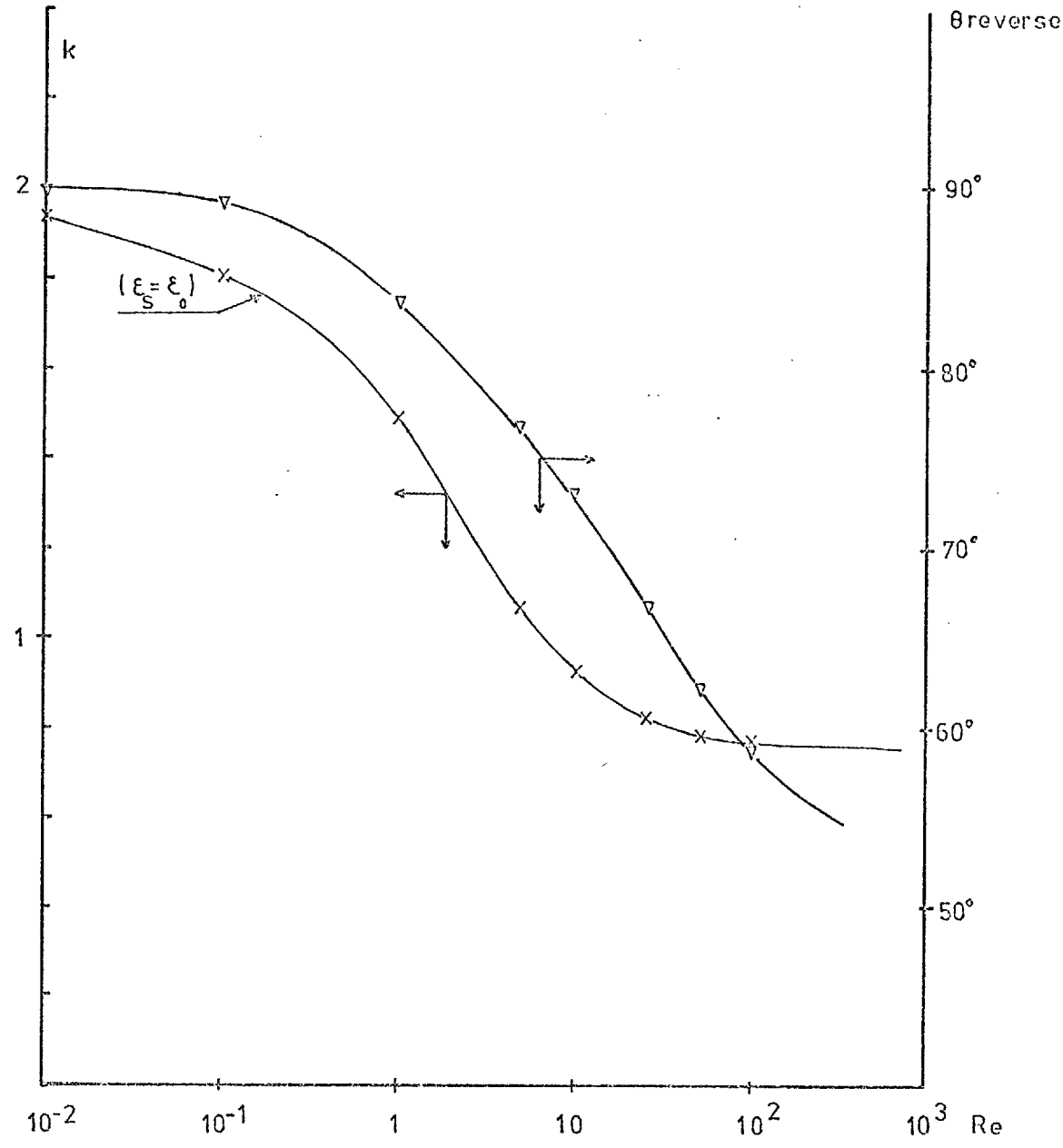


Figure 7.4 Variations of k and of the angle θ as a function of the Reynolds number.

CHAPTER 8

CONCLUSIONS

The theoretical and experimental work carried out in this thesis can be summarized as follows:

8.1 Theoretical results

1. A theoretical model for the motion of two dimensional bubbles in Newtonian liquids has been developed for bubble Reynolds numbers from 0.01 to 200. The time-independent Navier-Stokes equation for flow around a circular cylinder was solved with the boundary condition of zero tangential shear stress at the surface of the cylinder. The equation was put into finite-difference form and the transport equation for the vorticity was solved using Peaceman and Rachford alternating direction implicit method. This solution was then applied to the motion of bubbles in a two-dimensional fluidised bed, by assuming that the particulate phase behaves like a Newtonian liquid with finite viscosity.

2. From the above solution, variables of interest like the particle velocity, the particle drift and the drag coefficient were calculated.

In the case of particle drift, the looping predicted by the inviscid theory disappears as the Reynolds number decreases, the total drift becoming infinite for Stokes's flow. The predicted movement is upwards for particles situated near the bubble axis and downwards further away.

The drag coefficient for low Reynolds number ($Re < 1$) is well represented by the following relation $C_D = \frac{7.32}{Re}$

3. Voidage variations were included in the theoretical model following Jackson's method. The solution shows that variations in voidage fraction become smaller as the Reynolds number decreases. However it was also found that in this case there is a large region near the bubble where no solution for the voidage fraction can be calculated.

4. By assuming a Davies and Taylor approximation near the apex of the bubble, the bubble Froude number was calculated as a function of the Reynolds number. A maximum value of Fr ($Fr = 0.35$) was found at $Re = 5$. Below this value there is a sharp decrease in the value of Fr. At the other end of the curve, the value of Fr tends towards the Davies and Taylor result ($Fr = 0.25$).

5. Pressure variations were calculated along the axis of rise of the bubble and on the bubble surface. For the variations along the axis, the difference between the present theory and Jackson's solution is only significant when $Re < 10$. It is found that a solution obtained assuming Stokes's flow predicts a larger variation at the rear of the bubble than is predicted by Davidson's inviscid solution and is in good agreement with published data.

6. The solution for the gas flow is obtained from the solutions for the particulate flow, the pressure gradient and voidage variations. Cloud sizes predicted from this theory are larger than Davidson's prediction for low Reynolds numbers ($Re < 5$). Patterns for the gas streamlines have also been obtained.

8.2. Experimental results and comparison with theories

Experiments were carried out to test the validity of the above theory and of existing theories. Measurement of particle displacement and gas velocity variations were performed.

1. The first set of experiments shows the difference between a fully fluidised bed and a bed near incipient fluidisation conditions. In the latter case a Newtonian model is found to be unrealistic.

For a fully fluidised bed, complete looping of particles was observed for particles starting their motion near the axis of the bubble and within a distance of about $\frac{1}{4}$ of the bubble radius from it. This is similar to predictions obtained from the inviscid theory. For particles starting their motion further away there is a better agreement with the theory including viscous effect. Thus the behaviour of the particulate phase can be divided into two regions:

- a region very close to the bubble, with a width of about $\frac{1}{4}$ of the bubble radius, where convective terms are more important than viscous effects and which is thus well described by potential flow solution. We suggest that this could be attributed partly to an increase in voidage fraction of the particulate phase in this region.

- a region further away where viscous effects are important. In this region, although the present theory describes qualitatively the behaviour of the particles, the quantitative agreement is not very satisfactory. Therefore, presumably, the behaviour is not completely Newtonian.

2. The complete motion of the particles shows that the drift obtained experimentally is smaller than that predicted by the inviscid theory. This is in agreement with published data.

3. In the case of natural bubbles, the velocity field of the particulate flow was found to be slightly asymmetrical, the maximum value occurring at $\theta > 90^{o}$, in qualitative agreement with published data obtained from measurements of the heat transfer coefficient.

4. Gas velocity results show that there is a difference between the particles which were used in this work. In the case of small particles and $\alpha_b > 1$ Murray's theory or the present theory are good predictions of the gas velocity. In particular, cloud sizes are well represented by the above theories.

In the case of larger particles and with $\alpha_b < 1$ Davidson's theory is more satisfactory as measurements on the bubble axis and on the bubble sides show it.

5. Finally it has been possible to measure indirectly the value of the gas throughflow velocity by analyzing the motion of particles falling from the roof through the bubble. This value was found to be : $U = U_b + 2.46\, U_o$ thus showing a better agreement with Davidson's theory.

8.3 General conclusion

The theory attempting to describe the rheology of the particulate phase in term of a Newtonian behaviour developed in this work does not significantly improve on other theories of bubble motion. It is in fact worth asking whether a more complicated model should be introduced since this work tends to show that it is probably very difficult to derive a theory which would explain the behaviour of all variables. This question should be asked the more because factors like the true

shape of the bubble, the bubble wake, particles falling through the bubble, instability of the roof, all factors which presumably influence to some extent the behaviour of both phases in the vicinity of the bubble, have been completely neglected.

On the other hand, it is hoped that experiments carried out in this work will be useful in understanding what happens around a bubble rising in a fluidised bed.

Finally it should be emphasized that the theoretical model developed here for the bubble motion in a Newtonian fluid is not limited to bubbles in a fluidised bed.

REFERENCES

1.	P.N.Rowe, B.A.Partridge	Symposium on the Interaction between fluids and particles. (London. Inst. Chem. Eng.) p.135 (1962)
2.	K.S.Sutherland	Trans. Inst. Chem. Eng. vol.39 p.188 (1961)
3.	J.F.Davidson, D.Harrison (editors)	Fluidisation. Academic Press (1971)
4.	D.Kunii, O.Levenspiel	Fluidisation Engineering John Wiley. New York (1969)
5.	P.N.Rowe	Experimental properties of bubbles. Chapter 4 in Fluidisation edited by J.F.Davidson, D.Harrison. Academic Press (1971).
6.	H.Littman, G.A.J. Homolka	Chem. Eng. Sci. vol.28 p.2231 (1973)
7.	M.J.Lockett, D.Harrison	Proceedings of the International Symposium on Fluidisation of Eindhoven edited by A.A.H. Drinkenburg p.257 (1967). Netherlands University Press, Amsterdam
8.	O.E.Potter	Mixing - Chapter 7 in Fluidisation edited by J.F.Davidson, D. Harrison. Academic Press (1971)
9.	J.F.Davidson	Trans. Inst. Chem. Eng. vol.39 p.230 (1961)
10.	J.F.Davidson, D.Harrison	Fluidised Particles. Cambridge University Press (1963)
11.	R.Jackson	Trans. Inst. Chem. Eng. vol.41 p.22 (1963)
12.	J.D.Murray	J.Fluid. Mech. vol. 22 p.57 (1965)
13.	R.Jackson	Trans. Inst. Chem. Eng. vol.41. p.13 (1963)
14.	R.L.Pigford, T.Baron	Ind. Eng. Chem. Fund vol.4 p.81 (1965)

15. D. Geldart — Powder Technology vol. 7 p. 285 (1973)

16. J. A. H. de Jong, J. F. Nomden — Powder Technology vol. 9 p. 91 (1974)

17. J. A. Agbim, P. N. Rowe — Chem. Eng. Sci. vol. 26 p. 1293 (1971)

18. P. N. Rowe — Chem. Eng. Sci. vol. 24 p. 415 (1969)

19. J. D. Murray — J. Fluid. Mech. vol. 21 p. 465 (1965)

20. T. B. Anderson, R. Jackson — Ind. Eng. Chem. Fund vol. 7 p. 12 (1968)

21. O. Molerus — Proceedings of the International Symposium on Fluidisation of Eindhoven edited by A. A. H. Drinkenburg p. 134 (1967) Netherlands University Press, Amsterdam

22. E. Ruckenstein, M. Tzeculescu — Ibid, p. 180 (1967)

23. K. Rietema — Ibid, p. 201 (1967)

24. K. Rietema — Ibid, p. 154 (1967)

25. P. J. Buysman, G. A. L. Peersman — Ibid, p. 38 (1967)

26. K. Rietema — Chem. Eng. Sci. vol. 28 p. 1493 (1973)

27. J. Verloop, P. M. Heertjes — Powder Technology, vol. 7 p. 161 (1973)

28. K. Peters, A. Schmidt — Öst. Chem. Zeitung vol. 54 p. 253 (1953)

29. H. Trawinski — Chem. Ing. Tech. vol. 25 p. 201, p. 229 (1953)

30. T. C. Daniels — Rheologica Acta vol. 4 p. 27 (1967)

31. G. L. Matheson, W. A. Herbst, C. H. Hold — Ind. Eng. Chem. vol. 41 p. 1099 (1949)

32.	J. Furukawa, T. Ohmae	Ind. Eng. Chem. vol. 50 p. 821 (1958)
33.	H. Kramers	Chem. Eng. Sci. vol. 1 p. 35 (1952)
34.	W. W. Shuster, F. C. Haas	J. Chem. Eng. Data vol. 5 p. 525 (1960)
35.	P. Diekman, W. K. Forsythe	Ind. Eng. Chem. vol. 45 p. 1174 (1953)
36.	F. Fa-Key-Liu, C. Orr	J. Chem. Eng. Data vol. 5 p. 430 (1960)
37.	K. Schügerl, M. Merz, F. Fetting	Chem. Eng. Sci. vol. 15 p. 1 (1961)
38.	T. Hagyard, A. M. Sacerdote	Ind. Eng. Chem. Fund. vol. 5 p. 500 (1966)
39.	K. Schügerl	Rheological behaviour of fluidised systems. Chapter 6 in Fluidisation edited by J. F. Davidson, D. Harrison Academic Press (1971)
40.	N. I. Gelperin, V. G. Einstein	The analogy between fluidised beds and liquids. Chapter 11 in Fluidisation edited by J. F. Davidson, D. Harrison. Academic Press (1971)
41.	J. D. Murray	Rheologica Acta. vol. 6 p. 27 (1967)
42.	P. S. B. Stewart	Trans. Inst. Chem. Eng. vol. 46 p. 60 (1968)
43.	H. Reuter	Chem. Ing. Tech. vol. 35 p. 98 (1963)
44.	J. R. Grace	Can. J. of Chem. Eng. vol. 48 p. 30 (1970)
45.	P. N. Rowe, B. A. Partridge	Trans. Inst. Chem. Eng. vol. 43 p. 157 (1965)
46.	L. Neuzil, M. Turcajova	Coll. Czech. Chem. Comm. vol. 34 p. 3652 (1969)
47.	W. Siemes, L. Heller	Chem. Eng. Sci. vol. 17 p. 555 (1962)
48.	W. J. Rice et al.	Ind. Eng. Chem. Fund. vol. 8 p. 271 (1969)

49.	W. Brötz	Chem. Ing. Tech. vol. 24 p. 60 (1952)
50.	W.G. May	Chem. Eng. Prog. vol. 55 p. 49 (1959)
51.	M. Leva, M. Grummer	Chem. Eng. Prog. vol. 48 p. 307 (1952)
52.	J.J. van Deemter	Chem. Eng. Sci. vol. 13 p. 143 (1961
53.	E.R. Gilliland, E.A. Mason	Ind. Eng. Chem. vol. 41 p. 1191 (1949)
54.	J.J. van Deemter	Proceedings of the International Symposium on Fluidisation of Eindhoven edited by A. A. H. Drinken burg p. 334 (1967) Netherlands University Press. Amsterdam.
55.	R. C. Bailie	Ibid, p. 322 (1967)
56.	R. D. Toomey, H. F. Johnstone	Chem. Eng. Prog. Symp. Ser. No. 5 p. 51 (1953)
57.	L. Massimilla, J. W. Westwater	Am. Inst. Chem. J. vol. 6 p. 134 (1960)
58.	P. N. Rowe	Chem. Eng. Prog. Symp. Ser. No. 58 p. 42 (1962)
59.	P. N. Rowe, B. A. Partridge, A. G. Cheney, G. A. Henwood, E. Lyall	Trans. Inst. Chem. Eng. vol. 43 p. 271 (1965)
60.	G. Raso, G. Volpicelli, C. Maitz	Quaderni dell' ingegnere chem. ital. vol. 1 p. 157 (1965)
61.	I. N. Woolard, O. E. Potter	Am. Inst. Chem. Eng. J. vol. 14 p. 388 (1968)
62.	R. Singh, C. Fryer, O. E. Potter	Powder Technology vol. 6 p. 239 (1972)
63.	R. Toei, R. Matsuno, Y. Nagai	Mem. Fac. Eng. Kyoto Univ. vol. 28 p. 428 (1966)
64.	H. Reuter	Chem. Ing. Tech. vol. 35 p. 219 (1963)
65.	J. F. Davidson	Trans. Inst. Chem. Eng. vol. 39 p. 320 (1964)

66. C. Darwin — Proc. Camb. Phil. Soc. vol. 49 p. 342 (1953)

67. M. J. Lighthill — J. Fluid. Mech. vol. 1 p. 31 (1956)

68. J. C. Maxwell — Scientific papers edited by W. D. Niven Cambridge University Press. p. 208 vol. II (1890)

69. J. D. Gabor — Proceedings of the International Symposium on Fluidisation of Eindhoven edited by A. A. H. Drinkenburg p. 230 (1967) Netherlands University Press, Amsterdam

70. R. Collins — Chem. Eng. Sci. vol. 20 p. 747 (1965)

71. J. D. Gabor — Chem. Eng. Sci. vol. 26 p. 1247 (1971)

72. J. D. Gabor — Chem. Eng. J. vol. 4 p. 118 (1972)

73. G. Donsi, L. Massimilla, S. Crescitelli, G. Volpicelli — Powder Technology vol. 6 p. 217 (1972)

74. H. P. Meissner — Can. J. of Chem. Eng. vol. 48 p. 349 (1970)

75. J. Baeyens, D. Geldart — Preprints of the International Symposium on Fluidisation. Toulouse (1973) Cepadues Toulouse

76. T. Patureaux, F. Vergnes, P. le Goff — Ibid, (1973)

77. P. N. Rowe, B. A. Partridge, E. Lyall — Chem. Eng. Sci. vol. 19 p. 973 (1964)

78. P. F. Wace, S. J. Burnett — Trans. Inst. Chem. Eng. vol. 39 p. 168 (1961)

79. P. N. Rowe, B. A. Partridge — Chem. Eng. Sci. vol. 18 p. 511 (1963)

80. J. Anwer, D. L. Pyle — Preprints of the International Symposium on Fluidisation. Toulouse (1973) Cepadues Toulouse

81. R. Jackson — Fluid mechanical theory - Chapter 3 in Fluidisation edited by J.F. Davidson, D. Harrison. Academic Press (1971)

82. T.B. Anderson, R. Jackson — Ind. Eng. Chem. Fund. vol. 6 p. 527 (1967)

83. R.M. Davies, G.I. Taylor — Proc. Roy. Soc. vol. A200 p. 375 (1950)

84. G.D. Smith — Numerical solution of partial differential equations. Oxford University Press. London (1965)

85. J. Happel, H. Brenner — Low Reynolds number hydrodymanics Prentice Hall (1965)

86. R. Clift et al — International Conf. in Particle Technology IITRI (1973)

87. J.D. Murray — Technical Report No. 1. Grant APOO455-01. National Center for Air Pollution Control. U.S. Public Health Service (1966)

88. J.F. Richardson, W.M. Zaki — Trans. Inst. Chem. Eng. vol. 32 p. 35 (1954)

89. C.J. Apelt — Aero Res. Counc. Rep. and Mem. No. 3175 (1958)

90. J.S. Son, T.H. Hanratty — J. Fluid. Mech. vol. 35 p. 369 (1969)

91. D.W. Peaceman, H.H. Rachford — J. Soc. Ind. Appl. Math. vol. 3 p. 28 (1955)

92. D.B. Russell — Aero Res. Counc. Rep. and Mem. No. 3331 (1962)

93. B. Carnahan, H.A. Luther, J.O. Wilkes — Applied numerical methods. John Wiley New York (1969)

94. D.L. Fox — Numerical solutions of ordinary and partial differential equations. Addison-Wesley (1962)

95. A.D. Gosman et al. — Heat and mass transfer in recirculating flows. Academic Press (1969)

96.	F.O.Griffin, A.Meisen	Can. J. of Chem. Eng. vol. 51 p. 102 (1973)
97.	J.Anwer	Ph. D. Thesis University of London (1970)
98.	M.R.Judd	Ph. D. Thesis University of Cape Town (1965)
99.	L.S.Leung	Contribution to discussion. International Symposium on Fluidisation Toulouse (1973)
100.	E.Ower, R.C.Pankhurst	The measurement of air flow Oxford, Pergamon (1966)
101.	G.K.Batchelor	An introduction to fluid dynamics Cambridge University Press (1970)
102.	J.F.Harper	The motion of bubbles and drops through liquids. Advances in applied mechanics vol. 12 p. 59 et sq. Academic Press (1972)
104.	J.Tuot, R.Clift	Am. Inst. Chem. Eng. Symp. Ser. vol. 69 No. 128 p. 78 (1973)
105.	H.Lamb	Hydrodynamics - 6th ed. Cambridge University Press (1962)
106.	M.Motamedi-Lanjani	Ph. D. Thesis University of London (1971)
107.	H.Heywood	Symposium of the Interaction between fluids and particles (London Inst. Chem. Eng.) p. 1 (1962)
108.	J.H.Hargreaves, D.L.Pyle	Chem. Eng. Sci. vol. 27 p. 433 (1972)
109.	L.S.Leung, I.C.Sandford	Chem. Eng. Sci. vol. 24 p. 1391 (1969)
110.	D.L.Pyle, P.L.Rose	Chem. Eng. Sci. vol. 20 p. 25 (1965)
111.	DISA notice	Instruction manual 55 MIO system
112.	H.Littman, G.A.J.Hornolka	Chem. Eng. Prog. Symp. Series No. 105 vol. 66 p. 37 (1970)

APPENDICES

APPENDIX 1

IMPORTANT RELATIONS IN TWO-DIMENSIONAL FLOW

CYLINDRICAL COORDINATES

1. Components of the stress tensor

$$\tau_{rr} = -2\mu \frac{\partial v_r}{\partial r} + \left(\frac{2}{3}\mu - \lambda\right) \underline{\nabla} \cdot \underline{v}$$

$$\tau_{\theta\theta} = -2\mu \left(\frac{1}{r} \frac{\partial v_\theta}{\partial \theta} + \frac{v_r}{r}\right) + \left(\frac{2}{3}\mu - \lambda\right) \underline{\nabla} \cdot \underline{v}$$

$$\tau_{r\theta} = -\mu \left(r \frac{\partial}{\partial r} \left(\frac{v_\theta}{r}\right) + \frac{1}{r} \frac{\partial v_r}{\partial \theta}\right)$$

with $\underline{\nabla} \cdot \underline{v} = \frac{1}{r} \frac{\partial}{\partial r} (r v_r) + \frac{1}{r} \frac{\partial v_\theta}{\partial \theta}$

2. Viscous dissipation

$$\Phi_v = 2 \left\{ \left(\frac{\partial v_r}{\partial r}\right)^2 + \left(\frac{1}{r} \frac{\partial v_\theta}{\partial \theta} + \frac{v_r}{r}\right)^2 \right\} + \left\{ r \frac{\partial}{\partial r} \frac{v_\theta}{r} + \frac{1}{r} \frac{\partial v_r}{\partial \theta} \right\}^2 - \frac{2}{3} (\underline{\nabla} \cdot \underline{v})^2$$

with $\nabla^2 = \frac{\partial^2}{\partial r^2} + \frac{1}{r} \frac{\partial}{\partial r} + \frac{1}{r^2} \frac{\partial^2}{\partial \theta^2}$

3. Velocity components

If Ψ is the Stokes stream function:

$$v_r = -\frac{1}{r} \frac{\partial \Psi}{\partial \theta}$$

$$v_\theta = \frac{\partial \Psi}{\partial r}$$

4. Vorticity components

$$\sigma = \underline{\nabla} \times \underline{v}\big|_r = \frac{1}{r}\frac{\partial v_z}{\partial \theta} - \frac{\partial v_\theta}{\partial z} = 0 \quad \text{in two-dimensions}$$

$$\Phi = \underline{\nabla} \times \underline{v}\big|_\theta = \frac{\partial v_r}{\partial z} - \frac{\partial v_z}{\partial r} = 0 \quad \text{in two-dimensions}$$

$$\zeta = \underline{\nabla} \times \underline{v}\big|_z = \frac{1}{r}\frac{\partial}{\partial r}(rv_\theta) - \frac{1}{r}\frac{\partial v_r}{\partial \theta}$$

APPENDIX 2

APPLICATION OF HOT-WIRE ANEMOMETRY TO GAS VELOCITY MEASUREMENTS IN A FLUIDISED BED

In this appendix the basic principles of hot-wire anemometry are briefly described. It is not intended to give an extensive survey of all possible applications of this method of measurement, but rather to show how it can be used in this particular problem of fluidisation.

Some attention is also devoted to the calibration of the hot-wire probe since it needs to be performed with care.

A.2.1. Basic principle

The basic principle of hot-wire anemometry is to measure the loss of convective heat from an electrically heated wire. If this wire is situated in a flowing fluid, then the heat loss will be a measurement of the fluid velocity.

For small variations of temperature, the wire resistance varies according to a linear relation:

$$R(T) = R(T_o) \left\{ 1 + \alpha (T-T_o) \right\}$$

Furthermore the heat dissipation from the wire is related to the fluid velocity by King's law:

$$P = RI^2 = A + BU^n \qquad (A.2.1)$$

P : power

I : current intensity in the wire

U : fluid velocity

A, B : coefficients depending on physical properties of the fluid and wire.

It can be seen from relation (A. 2. 1) that the anemometer can be operated in two ways:

(i) I is maintained constant and the resistance R (i. e. the wire temperature according to the linear relation R(T)) varies with U. This is referred to as the constant-current operation.

(ii) Alternatively R (and therefore T) are maintained constant and the intensity variations will measure the power variations. This is referred to as the constant-temperature operation.

The last method is the most developed one. Operation in the constant current mode has great disadvantages since the wire temperature varies and modifies the local fluid properties (and thus constants A and B), which is not the case if the wire temperature is maintained constant. Furthermore it is noted (111) that the frequency response of the hot-wire in the constant current method cannot be easily compensated (i. e. compensation of cable impedance). Thus the only wide application of mode (i) is in measurements of temperature variations. In this work constant-temperature operation (ii) was employed.

The constant temperature anemometer is described in Figure A. 2. 1. It is basically a Wheatstone bridge in which one of the resistances is constituted by the hot-wire probe. The electric current heating the probe is supplied by a servo-amplifier.

When the bridge is unbalanced, due to a cooling effect, the servo-amplifier provides an increase in the output current which maintains R constant.

In order to operate the anemometer at its highest sensitivity, it is necessary for the cooling effect to be important for small variations of the velocity. The wire must therefore be heated well above the room temperature T_o. An overheating ratio is defined as:

$$a = \frac{R(T) - R(T_o)}{R(T_o)}$$

This should be taken as high as possible according to the maximum temperature that the sensor can stand. This also ensures that the instrument sensitivity will be almost independent of small temperature changes in the fluidising air. In the present case the recommended ratio $a = 0.8$ was used. This corresponds to a wire temperature of about $250^{o}C$.

A.2.2. Signal processing and sensor calibration

According to King's law (equation A.2.1) the output signal from the anemometer is not a linear function of the velocity but varies as:

$$E^2 = E_o^2 + kU_{eff}^n \qquad (A.2.2)$$

where E_o is the signal at zero flow velocity. U_{eff} is referred to as the effective velocity, or cooling velocity, and can be separated into three effects with different weighting factors:

$$U_{eff}^2 = U_{n1}^2 + h^2 U_{n2}^2 + k^2 U_t^2$$

where the following quantities are referred to as:

h : pitch factor

k : yaw factor

U_{n1}, U_{n2} : components of the velocity normal to the wire

U_t : tangential component along the wire.

The value of k depends mainly on the wire characteristics:

wire material, ratio $r = \frac{\text{wire length}}{\text{wire diameter}}$, and has to be determined

experimentally.

However for a tungsten wire, $k \sim o$ when the ratio $r \geqslant 600$ (111)

which is the case in this problem $(r = \frac{3000\ \mu m}{5\ \mu m} = 600)$.

In the system of axes shown on Figure A. 2. 2. we have:

$$U_x = U \cos\theta$$

$$U_z = U \sin\theta \cos\alpha$$

$$U_y = U \sin\theta \sin\alpha$$

In all velocity measurements reported in this work, the probe was kept horizontal and the velocity U was in the plane of the fluidised bed. Thus:

$$\alpha = \frac{\pi}{2}$$

and $U_{n1} = U_x = U \cos\theta$

$$U_{n2} = U_z = 0$$

$$U_t = U_y = U \sin\theta$$

In addition $k \sim o$ as noted previously. Therefore the effective velocity becomes:

$$U_{eff} = U \cos\theta$$

or

$$U_{eff} = u_x \qquad \text{(A. 2. 3)}$$

where u_x is the vertical component of the interstitial velocity.

Relation A. 2. 2 becomes:

$$E^2 - E_o^2 = k\, u_x^n$$

or in dimensionless form:

$$\frac{E - E_o^2}{E_o^2} = k' \left(\frac{u_x}{U_o} \right)^n \qquad \text{(A. 2. 4)}$$

where U_o is the superficial fluid velocity at minimum fluidisation.

The calibration of the probe has to be performed in an undisturbed flow. It is therefore not possible to carry out this calibration in a fluidised bed which is disturbed by the presence of bubbles when the air velocity is higher than the minimum fluidisation velocity.

The calibration was therefore done in an auxiliary packed bed connected to the same set of rotameters as the fluidised bed. The following procedure was then carried out:

(i) In the auxiliary bed, particles were supported by a porous distributor and therefore could be fluidised at a start. This ensured that the voidage was the same as that in the fluidised bed near incipient fluidisation.

(ii) The flow was then reversed and the calibration was performed recording the output voltage as function of the gas velocity.

A typical calibration curve is shown on Figure A. 2. 3. The coefficient n has been taken equal to $\frac{1}{2}$ and gives a good representation since the experimental relation is linear. When a bigger range of velocities is considered (say a range of 10 m/s or more), the

calibration curve $\frac{E^2 - E_o^2}{E_o^2}$ vs. $\sqrt{\frac{u}{U_o}}$ is no longer linear

and n is different from $\frac{1}{2}$. In this case a linearizer unit has to be included in the anemometry system. In regard to the calibration curve obtained it was thought unnecessary to include a linearizer in the system. We can also make the following remarks:

(i) The calibration was performed over a range of gas velocities wider than the range actually used in the gas velocity measurements. By doing so, more experimental points for the calibration curve could be recorded which gives a better accuracy.

(ii) As shown on Table A. 2. 1 the reproducibility of calibration results is good. These experimental values correspond to Figure A. 2. 3.

(iii) Velocity values obtained in the auxiliary bed were checked against these obtained in the actual apparatus operated under the minimum of fluidisation.

Some of these values are shown in Table A. 2. 2.

Although the agreement is not perfect it seems to fall within experimental error. However this table shows that the method of calibration is less precise for small Ballotini where gas velocity is very much lower.

(iv) The influence of increased voidage in the fluidised bed was neglected since all velocity measurements were made for bubbles injected in a bed maintained slightly under the minimum of fluidisation.

	E volts E_o = 10.47 volts (4 times actual voltage)			
u cm/sec	run 1	run 2	run 3	value retained
11.8	11.23	11.26	11.26	11.25
22.5	11.69	11.74	11.74	11.72
29.4	11.92	11.92	11.92	11.92
39.2	12.22	12.22	12.22	12.22
52.2	12.54	12.54	12.54	12.54
66.0	12.81	12.81	12.81	12.81
80.7	13.06	13.06	13.06	13.06
124.7	13.67	13.66	13.66	13.66
134.8	13.80	13.79	13.79	13.79
145.3	13.94	13.92	13.92	13.92
156.3	14.07	14.05	14.05	14.05
167.2	14.20	14.18	14.19	14.19
178.7	14.36	14.32	14.33	14.33
190.6	14.51	14.48	14.48	14.49

Table A. 2. 1 Output voltage as function of the superficial gas velocity.

Particles Ballotini	Velocity from calibration curve cm/sec	Velocity in fluidised bed cm/sec
7	39.0	42.5
8	40.0	42.5
10	10.0	12.5

Table A.2.2. Comparison of gas velocities obtained in the fluidised bed and in the auxiliary packed bed

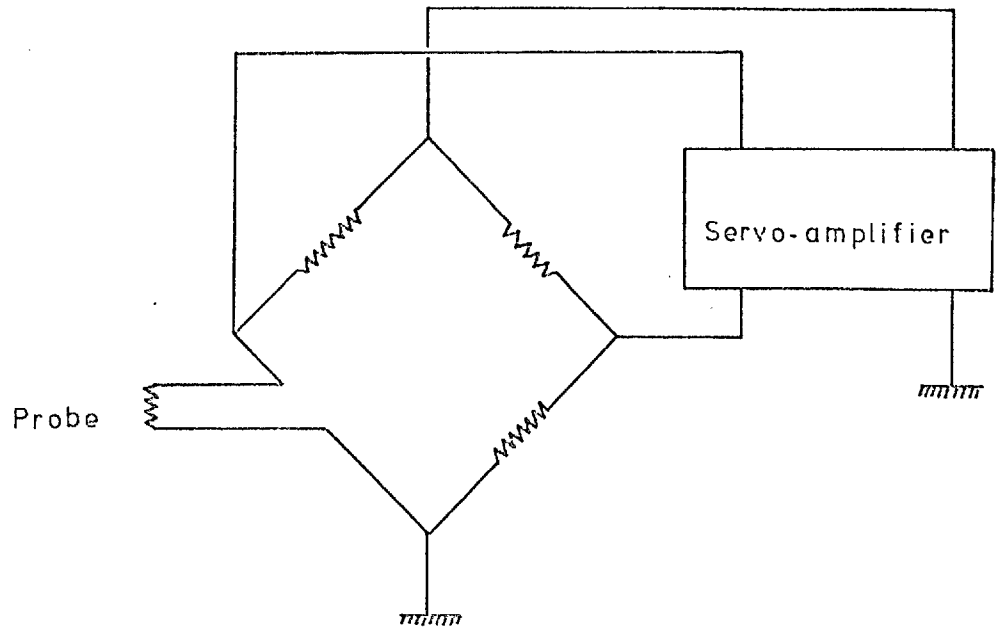


Figure A.2.1 Basic circuit of hot-wire anemometry

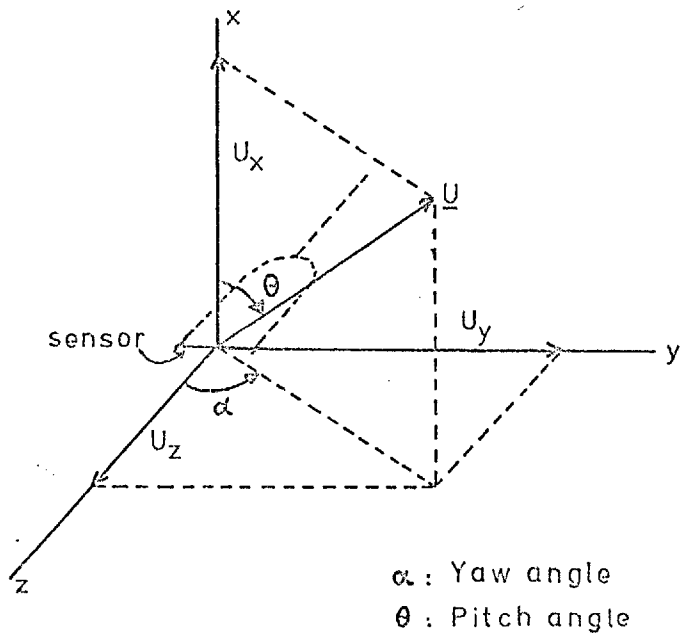


Figure A.2.2 General system of axes

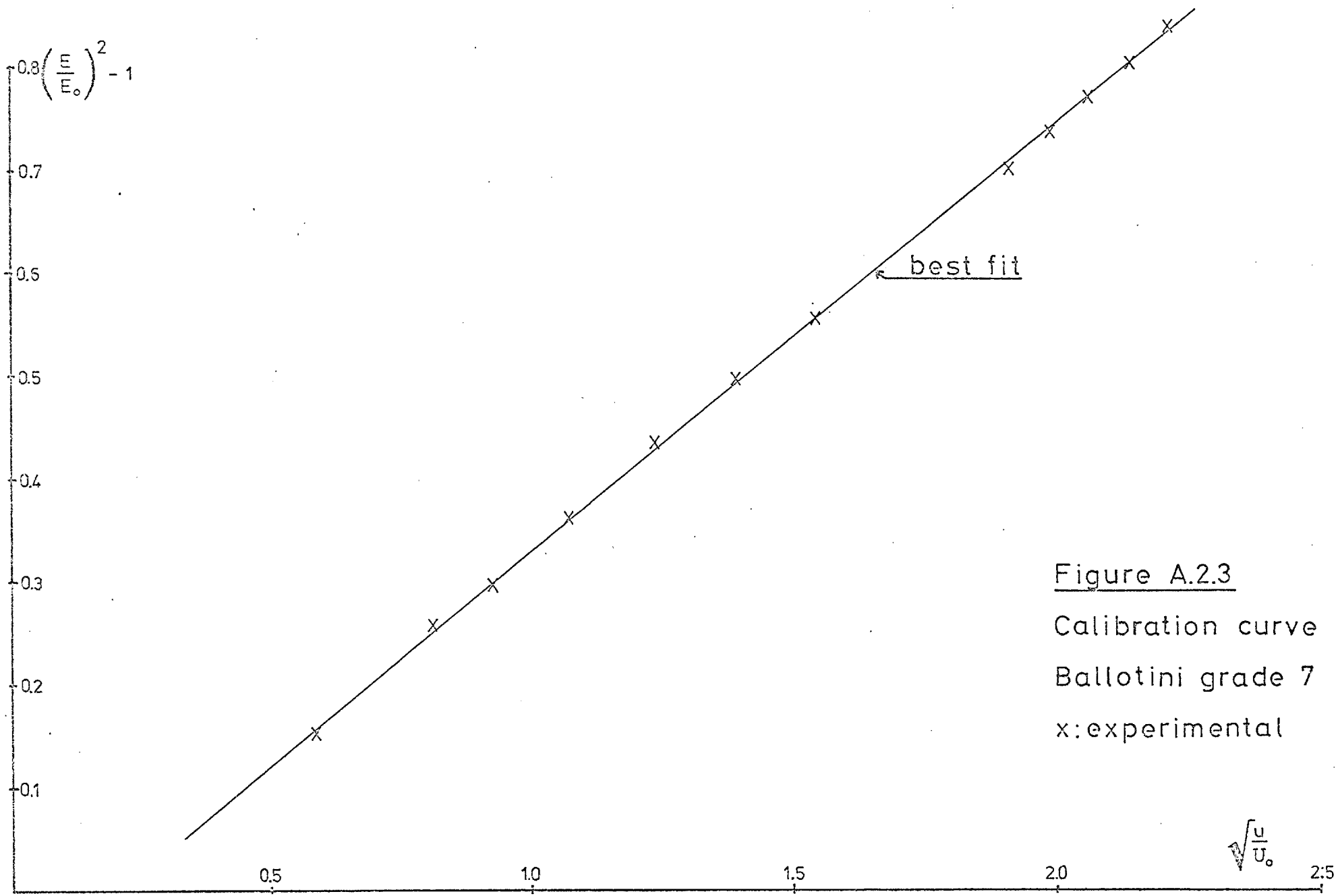


Figure A.2.3

Calibration curve

Ballotini grade 7

x: experimental

APPENDIX 3

The aim of this appendix is to recall the main results for the motion of a single isolated bubble in a two-dimensional fluidised bed, derived from Davidson's, Jackson's and Murray's theories (10, 11, 12). These results are used in Chapters 4 and 5 in comparison with the experimental data and with the present theory. We shall limit ourselves to a circular bubble; Collins's modification (70) to the bubble shape is not considered.

A.3.1. Particle motion

All three theories assume an inviscid and incompressible behaviour of the particulate phase which is therefore governed by the following equation:

$$\Psi = U_b \, r \sin\theta \left(1 - \frac{a^2}{r^2}\right) \qquad \text{(A.3.1)}$$

with axes defined in Figure A.3.1.

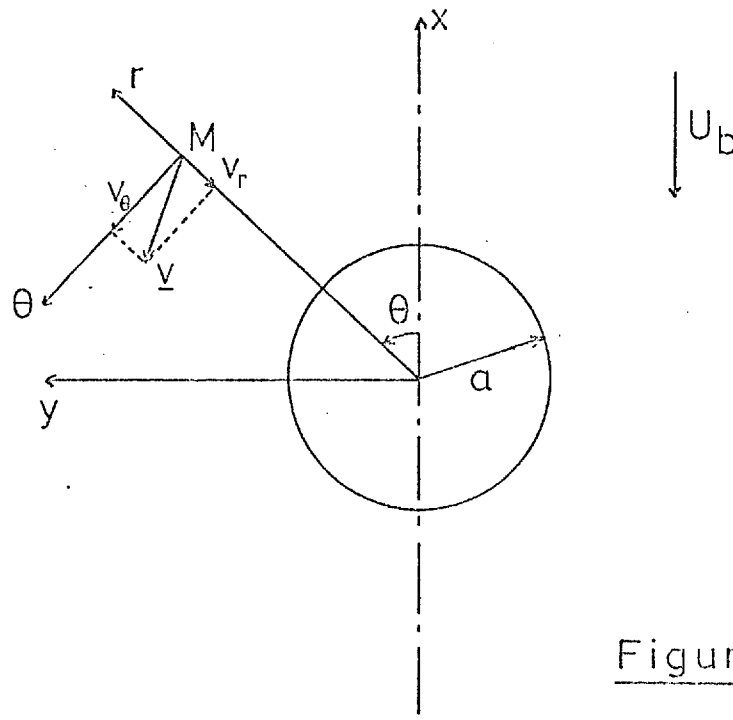


Figure A.3.1

The velocity components of the particles can easily be derived from the stream function as: (Appendix 1)

$$\left.\begin{aligned} v_r &= -U_b \cos\theta \left(1 - \frac{a^2}{r^2}\right) \\ v_\theta &= U_b \sin\theta \left(1 + \frac{a^2}{r^2}\right) \end{aligned}\right] \qquad \text{(A. 3. 2)}$$

If one observes the particulate phase in a system of axes fixed with respect to the fluidised bed, the rise of the bubble causes the drift of the particles. This displacement can be calculated numerically using the method described in Chapter 3 (section 3. 8).

Alternatively an analytical solution has been given by Darwin (66). When displaced by the bubble, a particle follows a curve called "elastica". Its parametric equations in w are the following:

$$\left.\begin{aligned} X(w) &= \frac{a}{k}\left\{\left(1 - \frac{1}{2}k^2\right) w - E(w)\right\} \\ Y(w) &= \frac{a}{k}\left\{k' + dnw\right\} \\ t(w) &= \frac{a}{k}\frac{1}{U_b}\, scw\left\{k' + dnw\right\} + X(w) \end{aligned}\right] \qquad \text{(A. 3. 3)}$$

where $k^2 = \dfrac{4a^2}{\Psi^2 + 4a^2}$ and $k^2 + k'^2 = 1$

and $E(w)$ is the elliptic integral of the second kind.

X, Y are the coordinates of the particle in axes fixed with respect to the fluidised bed, t is the time relative to the initial

position of the particle. When θ varies from 0 to π, w ranges from -K to +K where K is the complete elliptic integral of the first kind. The total drift of the particle is therefore given when $\theta = \pi$, and can be calculated from equations (A. 3. 3) using tables of elliptic functions. Some of the paths are shown in Figure 1.2 (Chapter 1).

A. 3. 2 Gas motion

The three theories mentioned above differ in the calculation of the gas flow patterns. Their main features are the following:

(i) Davidson assumes that the voidage for the particulate phase is constant and that the percolation of gas through the particles obeys Darcy's law. The pressure field is therefore Laplacian and the pressure inside the bubble is constant. As for the particulate flow, the gas flow field is equally Laplacian. Depending on the value of the ratio $\alpha_b = \frac{U_b}{u_o}$ the gas flow patterns will differ and typical patterns can be found in Davidson and Harrison (10) or in Jackson (11). When $\alpha_b > 1$, gas in a region close to the bubble is held and circulates within this region, thus forming a cloud.

(ii) In Jackson's theory, the voidage around the bubble is allowed to vary through the fluid-particle drag coefficient β which becomes a function of the voidage ε. The pressure field is therefore no longer Laplacian and the constancy of the pressure on the bubble surface is not satisfied. There is no analytical value for the gas flow stream function and it has to be calculated numerically from the values of the gas velocity.

(iii) As in Davidson's treatment, Murray assumes a constant voidage around the bubble. (Strictly speaking he assumes that

voidage variations are limited to a thin "boundary layer"). By linearizing the equation of motion for the particulate phase (section 1, Chapter 2), Murray finds a solution which satisfies an Oseen type approximation to the equations of continuity and motion for both phases. It results that, although the pressure field is Laplacian, the constancy of pressure on the bubble surface is not satisfied. The gas flow stream function satisfies Laplace's equation but the field is not symmetrical with respect to the equatorial plane of the bubble.

It follows from the features outlined above that the method of calculation will be different for each theory. This is shown in Table A.3.1. In this table only the final results are expressed. A detailed formulation of the problem of bubble motion according to the three theories mentioned above can be found in Jackson's survey (81).

Finally the equations used to compute various results and important variables are expressed in Table A.3.2. Those results are used in Chapters 5 and 6, to compare with the experimental data and with the present theory which is developed in Chapters 2 and 3.

1	Particulate phase Inviscid $\mu_p = 0$. Irrotational Constant voidage $\varepsilon = \varepsilon_0$ (except in Jackson's expression of the particle - fluid drag coefficient β) $\Longrightarrow \nabla^2 \psi = 0$			
	Davidson's solution	Jackson's solution		Murray's solution
2	Pressure distribution. * pressure field Laplacian $\nabla^2 P_f = 0$ * constancy of pressure on the bubble surface.	Pressure distribution. * pressure field non Laplacian. * pressure not constant on the bubble surface.		Pressure distribution * pressure field Laplacian $\nabla^2 P_f = 0$ * pressure not constant on the bubble surface.
3	Components of gas velocity from 1 and 2.	Voidage variations around the bubble.		Components of gas velocity from 1 and 2.
4	Gas flow stream function Laplacian $\nabla^2 \chi = 0$ $\Longrightarrow$ gas cloud when $\alpha_b > 1$	Components of gas velocity		Gas flow stream function Laplacian $\nabla^2 \chi = 0$ $\Longrightarrow$ gas cloud when $\alpha_b > 1$.
5	Velocity of rise of the bubble obtained by satisfying one component of the momentum equation at $\begin{cases} r = a \\ \theta = 0 \end{cases}$	Numerical values of gas flow stream function. $\Longrightarrow$ gas cloud when $\alpha_b > 1$		

Velocity of rise of the bubble obtained by satisfying the constancy of the bubble surface pressure over a region $\begin{cases} r = a \\ \theta \simeq 0 \end{cases}$

Table A.3.1

Theories of bubble motion

Theory	Pressure variations $\frac{p'^{*}_{f}}{\rho_f} + \frac{r}{a}\cos\theta$	Bubble rise velocity	Components of gas velocity u_r , u_θ	Gas flow stream function χ	Gas cloud dimension ($\chi = 0$)
Davidson	$\frac{a}{r}\cos\theta$	$U_b = 0.5(ga)^{\frac{1}{2}}$	$u_r = -U_b\cos\theta\left\{\frac{\alpha_b - 1}{\alpha_b} - \frac{\alpha_b + 1}{\alpha_b}\frac{a^2}{r^2}\right\}$ $u_\theta = U_b\sin\theta\left\{\frac{\alpha_b - 1}{\alpha_b} + \frac{\alpha_b + 1}{\alpha_b}\frac{a^2}{r^2}\right\}$	$\chi = U_b r\sin\theta\left\{\frac{\alpha_b - 1}{\alpha_b} - \frac{\alpha_b + 1}{\alpha_b}\frac{a^2}{r^2}\right\}$	$\frac{r_c}{a} = \left(\frac{\alpha_b + 1}{\alpha_b - 1}\right)^{\frac{1}{2}}$
Jackson	$\frac{a^2}{4r^2}\left[1 - 2\sin^2\theta - \frac{a^2}{2r^2}\right]$ with the Davies and Taylor result $U_b = 0.5(ga)^{\frac{1}{2}}$	$U_b = 0.5(ga)^{\frac{1}{2}}$	$u_r = -U_b\cos\theta\left\{1 - \frac{a^2}{r^2}\right\} + \frac{U_b\gamma}{\alpha_b}\left\{\cos\theta + \frac{a^3}{2r^3}(1 - 2\sin^2\theta) - \frac{a^5}{2r^5}\right\}$ $u_\theta = U_b\sin\theta\left\{\left(1 + \frac{a^2}{r^2}\right) - \frac{\gamma}{\alpha_b}\left(1 - \frac{a^3}{r^3}\cos\theta\right)\right\}$ with γ solution of: $\frac{\partial p_f}{\partial r}\frac{\partial \gamma}{\partial r} + \frac{1}{r}\frac{\partial p_f}{\partial \theta}\frac{\partial \gamma}{\partial \theta} + \gamma\nabla^2 p_f = 0$	No analytical expression	No analytical expression
Murray	$\frac{a^2}{4r^2}\cos 2\theta$	$U_b = 0.5(ga)^{\frac{1}{2}}$	$u_r = -U_b\cos\theta\left\{\frac{\alpha_b - 1}{\alpha_b} - \frac{a^2}{r^2}\right\} + \frac{U_b}{2\alpha_b}\frac{a^3}{r^3}\cos 2\theta$ $u_\theta = U_b\sin\theta\left\{\frac{\alpha_b - 1}{\alpha_b} + \frac{a^2}{r^2} + \frac{1}{\alpha_b}\frac{a^3}{r^3}\cos\theta\right\}$	$\chi = U_b r\sin\theta\left\{\frac{\alpha_b - 1}{\alpha_b} - \frac{a^2}{r^2} - \frac{1}{2\alpha_b}\frac{a^3}{r^3}\cos\theta\right\}$	Dimension given by the solution of: $(\alpha_b - 1)\frac{r_c^3}{a^3} - \alpha_b\frac{r_c}{a} - \frac{\cos\theta}{2} = 0$

Table A.3.2 Main results for the theories of bubble motion

APPENDIX 4

COMPUTER PROGRAMMES

A.4.1. Introduction

In this appendix, the computer programme used to calculate the particulate and the gas flows is presented.

For a reason of storage and computing time, the programme had to be divided in two parts:

(i) The first programme PRO1 calculates the solution for the particulate phase and for the following variables:

- pressure distribution
- drag coefficient
- path lines.

It also computes the streamfunction and vorticity contours. The converged results are written on a magnetic tape.

(ii) The second programme PRO2 calculates:

- the particle velocity field
- the drift profiles (lines $\tau' = cst$)
- the pressure gradient
- the values of Υ function and its contours
- the gas velocity field and the gas streamfunction.

The following values of the parameters were used:

number of points in r. direction : 51

number of points in θ. direction : 31

radius for the outer boundary $\rho_\infty = 7.14$ ($\xi_\infty = 0.625$)

increment in $\xi = 0.0125$

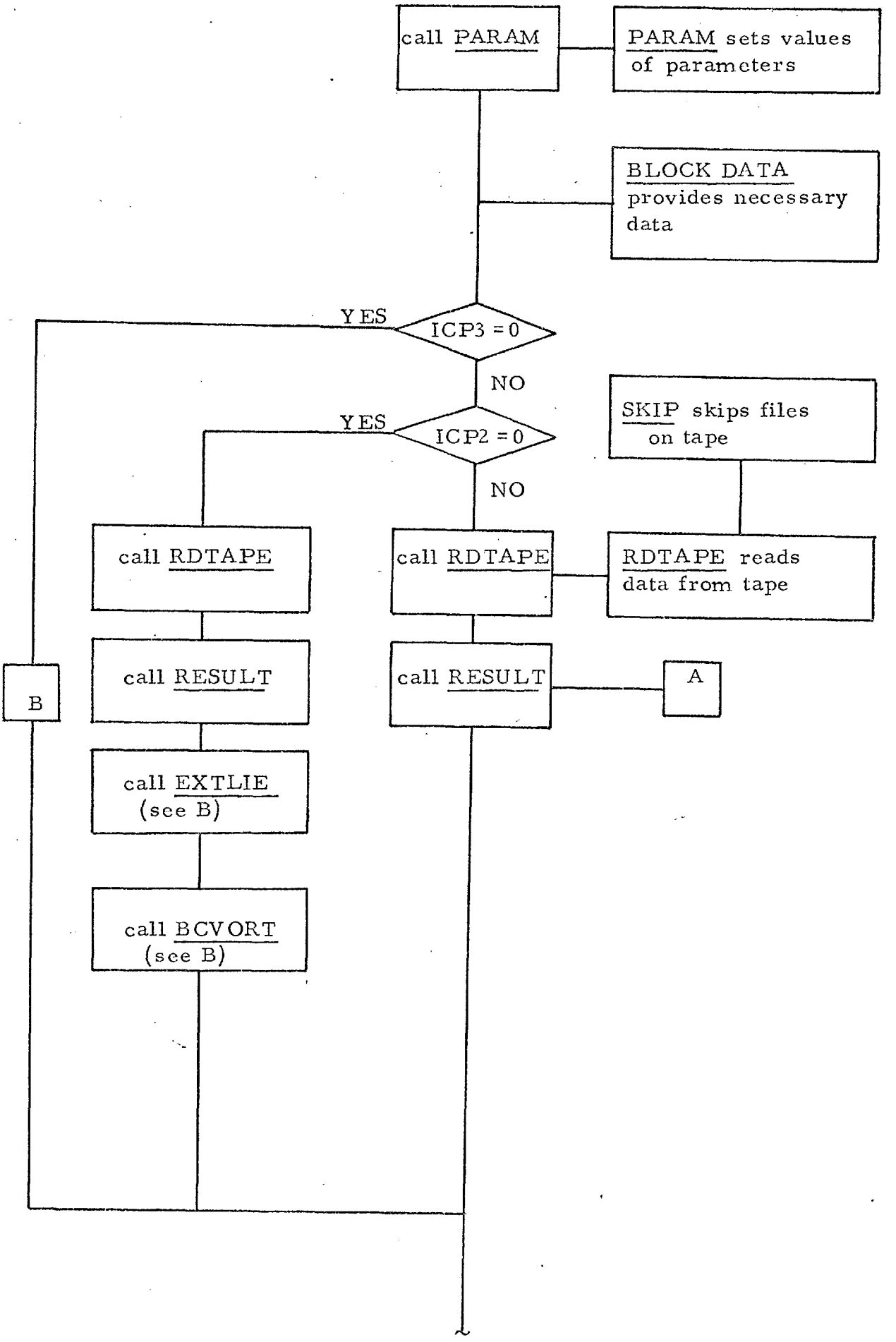
increment in $\eta = 1/30$ (corresponds to $\Delta\theta = 6^o$)

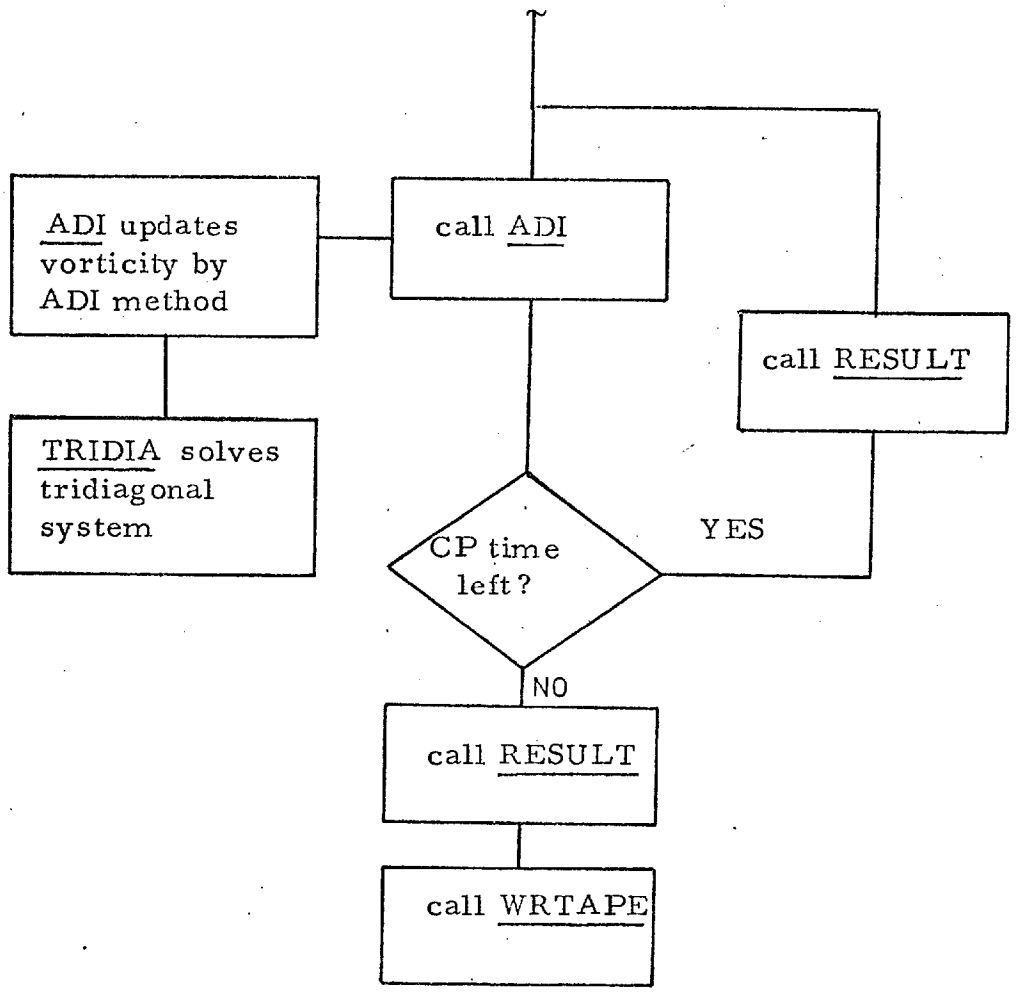
under-relaxation factor $\omega_v = 0.5$

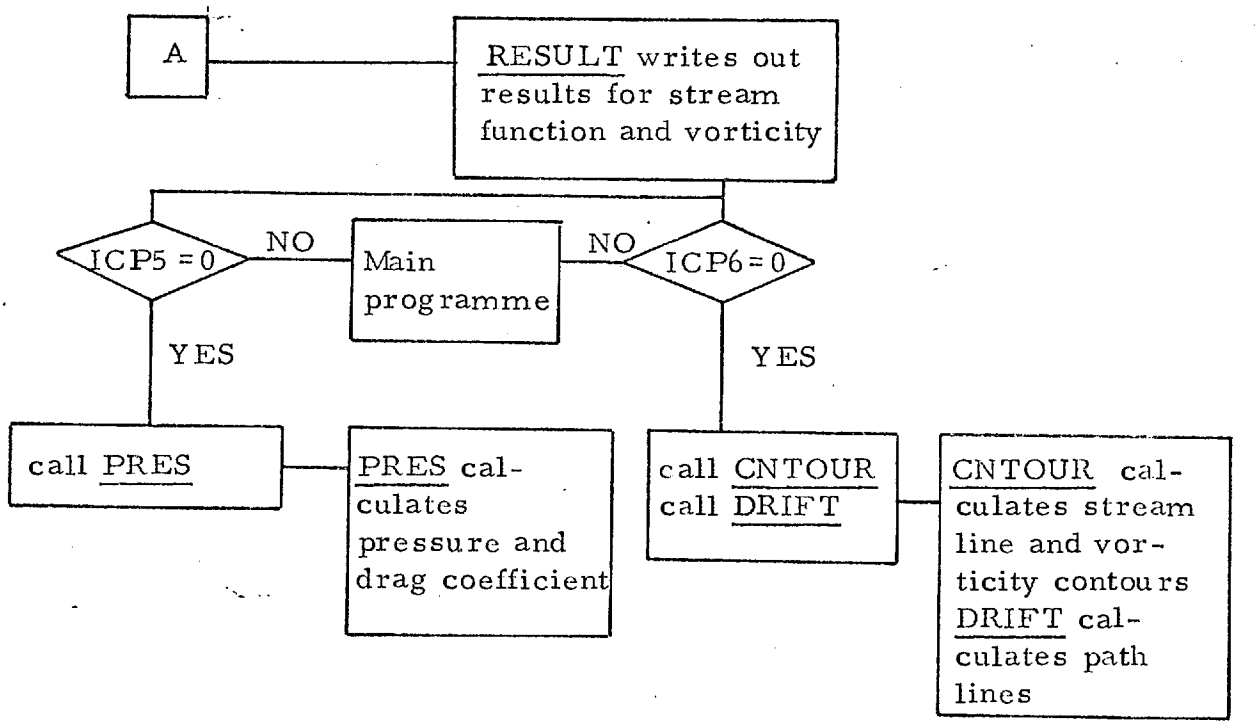
acceleration factor $\rho_a = 10,000.$

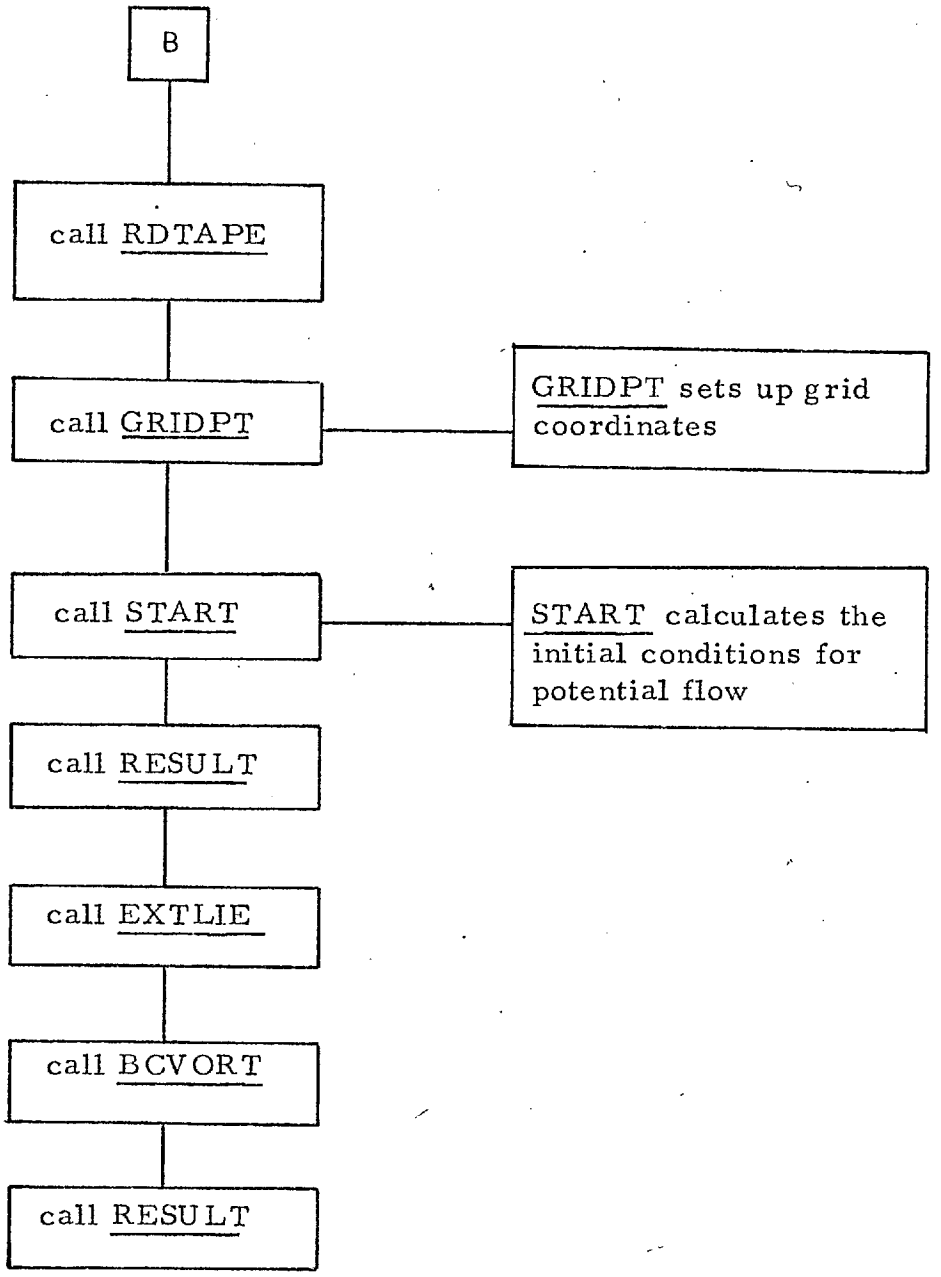
A.4.2. Flow diagrams

Flow diagram. Programme PRO1




ADI updates vorticity by ADI method
call ADI
call RESULT
TRIDIA solves tridiagonal system
CP time left?
YES
NO
call RESULT
call WRTAPE

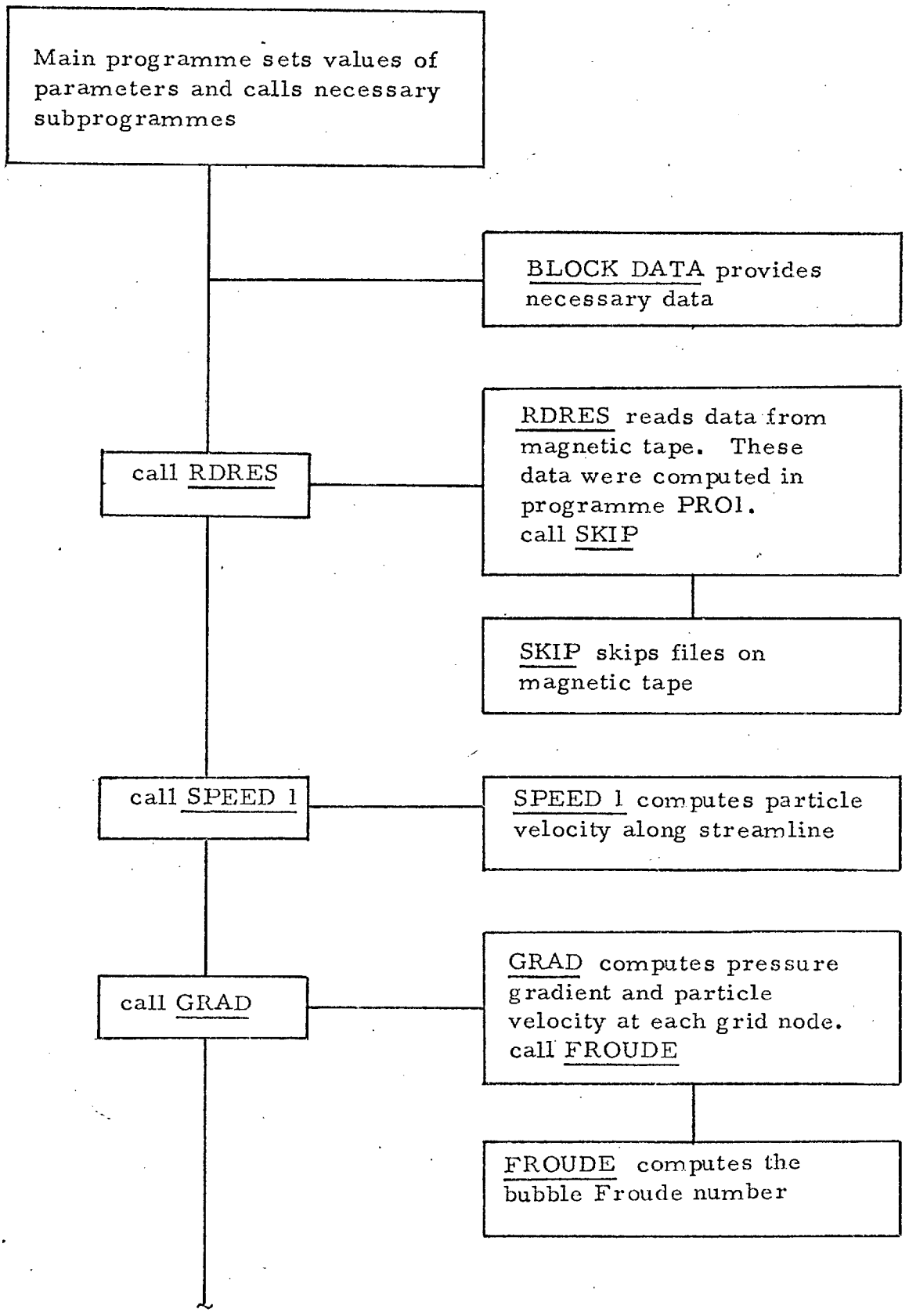

A
RESULT writes out results for stream function and vorticity
ICP5 = 0
NO
Main programme
NO
ICP6 = 0
YES
YES
call PRES
PRES calculates pressure and drag coefficient
call CNTOUR
call DRIFT
CNTOUR calculates stream line and vorticity contours
DRIFT calculates path lines

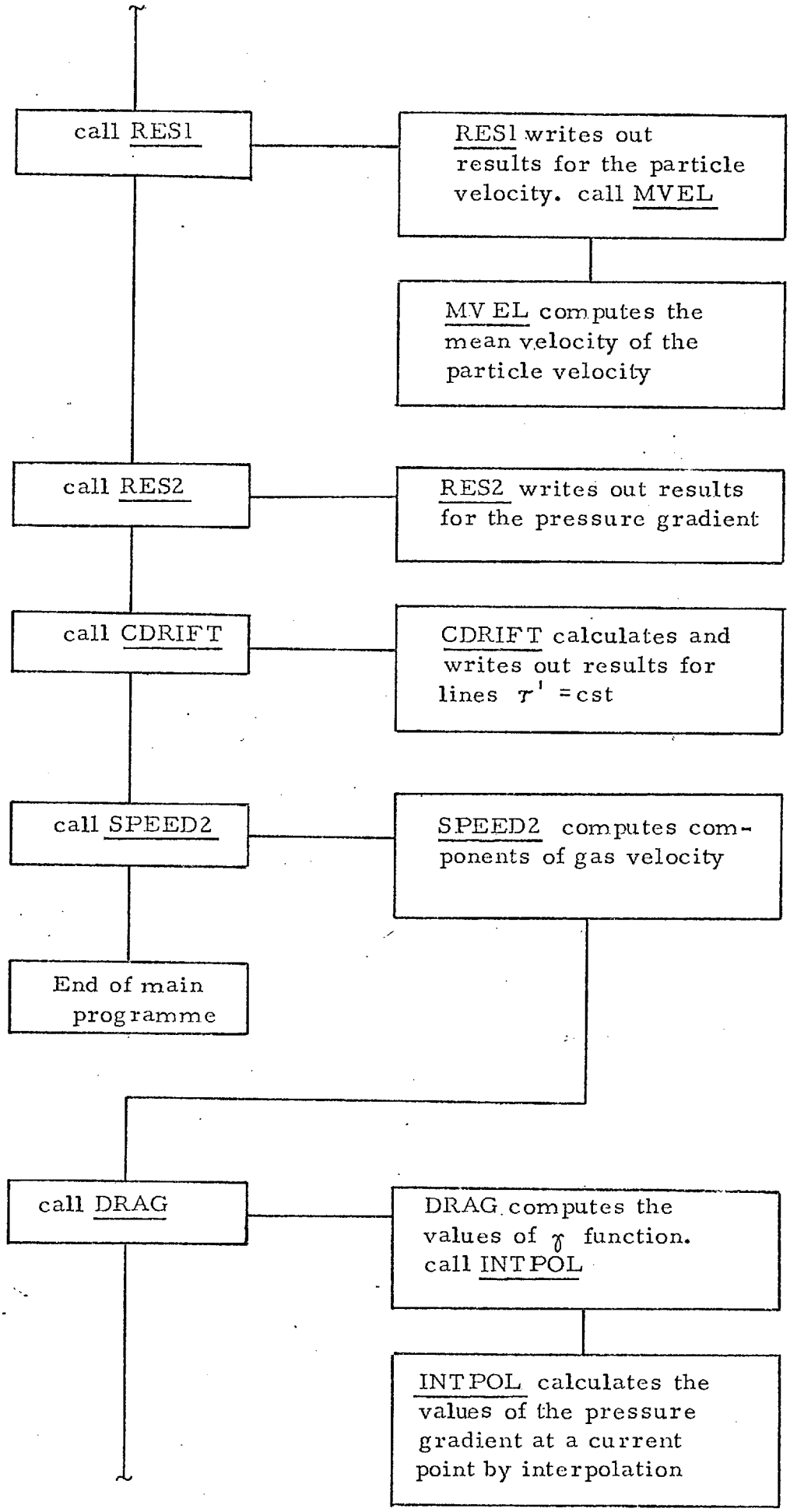


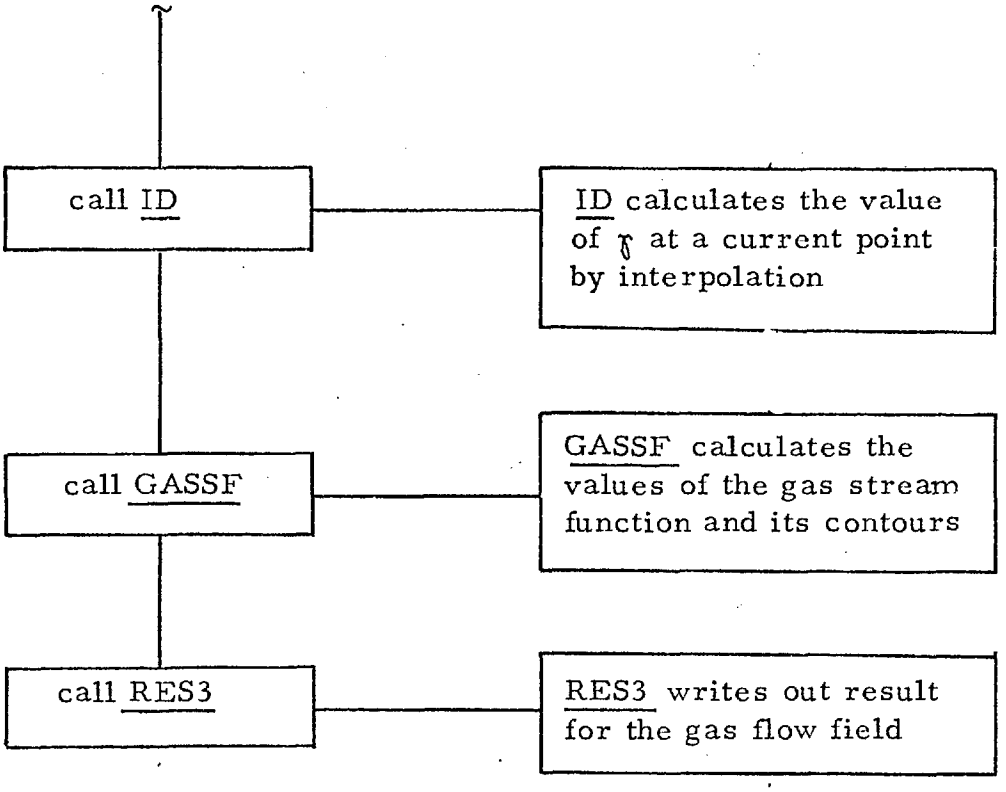
Flow diagram programme PRO1

Potential flow starting conditions

Flow diagram Programme PRO2




call RES1
RES1 writes out results for the particle velocity. call MVEL
MVEL computes the mean velocity of the particle velocity
call RES2
RES2 writes out results for the pressure gradient
call CDRIFT
CDRIFT calculates and writes out results for lines $\tau' = cst$
call SPEED2
SPEED2 computes components of gas velocity
End of main programme
call DRAG
DRAG computes the values of γ function. call INTPOL
INTPOL calculates the values of the pressure gradient at a current point by interpolation


call ID
ID calculates the value of ψ at a current point by interpolation
call GASSF
GASSF calculates the values of the gas stream function and its contours
call RES3
RES3 writes out result for the gas flow field

A.4.3 List of FORTRAN symbols

In this list only the main symbols appearing in COMMON statements are given. Other symbols are local variables used in sub-programs and are defined when necessary.

Program PRO1

FORTRAN symbol	Meaning
A	$A = \frac{1}{l^2} + \frac{1}{k^2}$
AL	l mesh size in transformed plane: η direction
AK	k mesh size in transformed plane: ξ direction
BO	coefficient in tridiagonal system $BO = \rho_a + \frac{4}{Re\, l^2}$
B1	coefficient in tridiagonal system $B1 = \rho_a - \frac{4}{Re\, k^2}$
CO	coefficient in tridiagonal system $CO = 4kl$
C1	coefficient in tridiagonal system $C1 = \frac{2}{Re\, l^2}$
C2	coefficient in tridiagonal system $C2 = \frac{2}{Re\, k^2}$
CDP	drag coefficient
CPSEC	central processor computing time on C.D.C. 6400
CR(I, K)	radial coordinates of positive streamfunction contours in the transformed plane (ξ, η).
CRT(I, K)	radial coordinates of positive stream function contours in the (ρ, θ) plane.
CRT1 (I, K)	radial coordinates of negative stream function
CRT2(I, K)	contours in the (ρ, θ) plane

FORTRAN symbol	Meaning
CRTV1(I, K)	radial coordinates ofvorticity contours in
CRTV2(I, K)	the (ρ , θ) plane
CSF(K)	positive values of contours for the stream function
CSFN(K)	negative values of contours for the stream function
CVORT(K)	values of contours for the vorticity
D	d_i coefficient in the tridiagonal system as defined by equations (3.21)
DP1(I, K)	ΔP_1^* pressure variations on the axis above the bubble
DP2(I)	ΔP_2^* pressure variations on the bubble surface
DP3(J)	ΔP_3^* pressure variations on the axis below the bubble
DSFR(I, K)	$\frac{\partial \Psi^*}{\partial \xi}$
DSFT(I, K)	$\frac{\partial \Psi^*}{\partial \eta}$
E(J)	$\pi e^{\pi\xi}$
EPS	ε : value of criterion for convergence: stream function
EPS1	ε_1 : value of criterion for convergence : vorticity
ETA(I)	η : variable in θ direction, transformed plane
FO	coefficient in tridiagonal system $F0 = \rho_a + \frac{4}{Re\, k^2}$
F1	coefficient in tridiagonal system $F1 = \rho_a - \frac{4}{Re\, l^2}$
ICP1	if ICP1 = 1, maximum number of iterations in the A.D.I. method is reached. Otherwise ICP1 =

FORTRAN symbol	Meaning
ICP2	If ICP2 = 0 all points have converged in the ADI method. Otherwise ICP2 = 1
ICP3	if ICP3 = 0 program starts from potential flow conditions. Otherwise ICP3 = 1
ICP4	if ICP4 = 1 an incorrect value of the acceleration factor ρ_a has been selected. Otherwise ICP4 = 0
ICP5	if ICP5 = 1 pressure variations are not calculated Otherwise ICP5 = 0
ICP6	if ICP6 = 0 stream function and vorticity contours, drift profiles are calculated. Otherwise ICP6 = 1
ICP7	if ICP7 = 1 partial results are written on tape if ICP7 = 0 converged results are written on tape
IFILE	file number on tape
ITAP	tape parameter from which results are read.
JTAP	tape parameter on which partial results are written
MINT	number of intervals in r direction = MPT-1
MK	MK = NINT or MK = MINT depending on the direction (η or ξ) updated in the A.D.I. method.
MNINT	NINT/2 + 1
MNISF	maximum number of iterations permissible in the S.O.R. method
MPT	number of points in r direction

FORTRAN symbol	Meaning
MUP	maximum number of unconverged points permissible. Normally MUP = 0
NC	number of positive contours for the streamfunction
NC1	number of negative contours for the streamfunction
NCVOR	number of contours for the vorticity
NDIP	number of iterations after which parameters like computing time, number of unconverged points are printed
NDTETA	increment in θ direction (degrees)
NDW	number of iterations after which partial results are printed
NI(K)	first value of the index in θ direction for contours calculation
NINT	number of intervals in θ direction = NPT - 1
NIP	iteration counter. When NIP = NDIP, parameters are printed out, after which NIP is set to 1 again
NISF	number of iterations for the streamfunction in the S.O.R. method
NITER	number of iterations for the A.D.I. method
NPT	number of points in θ direction
NS(K)	last value of the index in θ direction for contours calculation
NTAP	tape parameter on which converged results are written

FORTRAN symbol	Meaning
NTETA(I)	θ angle in degrees
NTETAI(K)	initial tangential coordinate for contours
NTETAS(K)	final tangential coordinate for contours
NUPST	number of unconverged points for the stream function in the S.O.R. method
NUPV	number of unconverged points for the vorticity in the A.D.I. method
NW	iteration counter. When NW = NDW partial results are printed out after which NW is set to 1 again.
OM	ω : over-relaxation factor
OMV	ω_v : under-relaxation factor
PI	π
PSI(I, J)	stream function for particulate flow Ψ^*
PSI1(I, J)	new estimate of Ψ^*
R(J)	ρ : radial coordinate
RE	Reynolds number for the bubble
RHO	ρ_a : acceleration factor
TD(I, K)	τ : dimensionless time on drift curve
TETA(I)	θ angle in radians
TIME	maximum time allowed for the calculation
V(J)	current vector in tridiagonal system as defined by relations (3.21)
VT(I)	V_θ^* : tangential velocity at the bubble surface

FORTRAN symbol	Meaning
X(J)	a_i : coefficient in tridiagonal system (relations 3.21)
XI(J)	ξ : variable in r direction : transformed plane
XD(I, K)	X^*: particle drift in x direction
Y(J)	b_i: coefficient in tridiagonal system (relations 3.21)
YD(I, K)	Y^*: particle drift in y direction
Z(J)	c_i : coefficient in tridiagonal system (relations 3.21)
ZETA(I, J)	ζ^*: vorticity
ZETA1(I, J)	new estimate of vorticity

Program PRO2

Only new symbols used in this program are explained. All other symbols which have been used in program PRO1 have been listed previously.

FORTRAN symbol	Meaning
ALPHAB(K)	α_b
ANG1	first increment in θ for determining the starting points of integration paths in calculation of γ function
ANG2	- ibid (second increment in θ)
ANG3	- ibid (third increment in θ)
CG(M)	values of $1/\gamma$ function contours
CRTG1(I, K)	radial coordinates of gas stream function contours
CRTG2(I, K)	
DELP	$\nabla^{*2} P_f^*$ value at any point (VR, VTETA) in the grid
DK	6k
DL	61
DPFR(I, J)	$\frac{\partial P_f^*}{\partial \rho}$ at grid nodes
DPFT (I, J)	$\frac{\partial P_f^*}{\partial \theta}$ at grid nodes
DPR(I, J)	$\frac{\partial P^*}{\partial \rho}$ at grid nodes
DPT(I, J)	$\frac{\partial P^*}{\partial \theta}$ at grid nodes
DTETA	increment in θ in calculation of γ function on an integration path

FORTRAN symbol	Meaning
FR	Froude number
GAMMA	$1/\Upsilon$
GCSF(K)	values of the gas streamfunction contours
MJ	number of values for τ' in calculation of lines $\tau' = \text{const}$
NALPHA	number of α_b numbers computed
NCG	number of contours for γ function
NCGS	number of contours for the gas streamfunction
NDL	increment of index in calculation of mean value of particle velocity
NL	maximum value of index in calculation of mean value of particle velocity
NPT1	NINT/2 + 1
NSP	number of paths of integration in the solution for Υ function
PHI(I, J)	values of gas streamfunction χ^* at grid nodes
PVM(I, K)	particle velocity with respect to axis moving with the bubble
PVS(I, K)	particle velocity with respect to stationary axis
PVX(I, K)	x. component of particle velocity w. r. t. moving axis
PVY(I, K)	y. component of particle velocity w. r. t. moving axis
RDC(I, K)	radial coordinate on lines $\tau' = \text{const}$
RG(M, K)	radial coordinate of Υ function controus
ST(I, K)	τ' = dimensionless time on drift curve with respect to an undisturbed plane at a distance XLIM above

FORTRAN symbol	Meaning
TAU(J)	τ : values of lines τ =const
TDC(I, K)	tangential coordinate on lines τ' = const
TL1	limit angle above which increment size is decreased in calculation of γ function
TG(M, K)	tangential coordinate of γ function contours
UR(I, J)	radial component of gas velocity
UT(I, J)	tangential component of gas velocity
UX(I, J)	x. component of gas velocity
UY(I, J)	y. component of gas velocity
V(I, J)	particle velocity at grid nodes
VDPR	$\frac{\partial P_f^*}{\partial \rho}$ at any point of coordinates (VR, VTETA)
VDPT	$\frac{\partial P_f^*}{\partial \theta}$ at any point of coordinates (VR, VTETA)
VR	radial coordinate of current point in gas velocity calculation
VR(I, J)	radial component of particle velocity at grid nodes
VT(I, J)	tangential component of particle velocity at grid nodes
VTETA	tangential coordinate of current point in gas velocity calculation
XDC(I, K)	x. coordinate on line τ' = const.
XLIM	x. coordinate of the undisturbed layer of particles in the drift profiles calculation
YDC(I, K)	y. coordinate on lines τ' = const.

A.4.4. Listings of programmes

Listing PRO1

```
      PROGRAM PRO1(INPUT,OUTPUT,TAPE5=INPUT,TAPE6=OUTPUT,TAPE1,TAPE2)
C*****
C*****THIS PROGRAM SIMULATES AN INCOMPRESSIBLE FLOW AROUND A CYLINDER
C*****WITH VIEW OF AN APPLICATION TO THE FLOW OF PARTICLES AROUND A
C*****RISING BUBBLE IN A TWO-DIMENSIONAL FLUIDISED BED.
C*****IT SOLVES THE TIME INDEPENDENT NAVIER-STOKES EQUATION USING
C*****PEACEMAN - RACHFORD ALTERNATING-DIRECTION-IMPLICIT METHOD.(ADI)
C*****THE SOLUTION FOR THE STREAM-FUNCTION EQUATION IS OBTAINED BY
C*****THE EXTRAPOLATED LIEBMANN METHOD (SOR).
C*****THE PRESSURE VARIATIONS ON THE AXIS OF RISE OF THE BUBBLE AND ON
C*****ITS SURFACE ARE COMPUTED AS WELL AS THE DRIFT OF PARTICLES CAUSED
C*****BY THE PASSAGE OF THE BUBBLE.
C*****
      COMMON/CONST/PI,EPS,EPS1,RE
      COMMON/MESH/AL,AK,MINT,NINT,MPT,NPT,MNINT,NDTETA
      COMMON/STRFUN/PSI(31,51),PSI1(31,51)
      COMMON/VORT/ZETA(31,51),ZETA1(31,51)
      COMMON/GRID/E(51),XI(51),R(51),ETA(31),TETA(31),NTETA(31)
      COMMON/CNTROL/ICP1,ICP2,ICP3,NUPV,NUPST,MUP,NISF,MNISF,NITER,
     1TIME,CPSEC,NW,NDW,NDIP
      COMMON/RELFAC/OM,OMV,RHO,A
      COMMON/TAPE/ITAP,JTAP,NTAP
      COMMON/FILE/ICP7,IFILE
      COMMON/CSTCOE/B0,B1,C0,C1,C2,F0,F1
      COMMON/APR/ICP5,DP1(51),DP2(31),DP3(51),VT(31),CDP
      COMMON/CTOUR/CSF(33),CR(31,33),DSFR(31,33),DSFT(31,33),
     1CRT(31,33),CSFN(10),NTETAI(33),NTETAS(33)
      COMMON/CTOUR1/CRTV1(31,25),CRTV2(31,25),CRT1(16,10),CRT2(16,10)
      COMMON/NCTOUR/ICP6,NC,NC1,NCVOR
      COMMON/VCTOUR/CVORT(25)
      COMMON/DRFT/XD(31,33),YD(31,33),TD(31,33)
C*****
C*****SET UP ALL PARAMETERS NEEDED IN THE CALCULATION
      CALL PARAM
C*****SET UP DATA REQUIRED FOR THE START OF THE COMPUTATION
      IF(ICP3.EQ.0) GO TO 1
      IF(ICP2.EQ.0) GO TO 2
C*****
C*****ICP3=1 AND ICP2=1 MEANS WE READ PREVIOUS ITERATION FROM THE TAPE
      CALL RDTAPE
      WRITE(6,100)
  100 FORMAT(1H1,5X,33HNEW ITERATION STARTED---DATA READ)
      ITER=1
      CALL RESULT
      NIP=0
      GO TO 200
C*****
C*****ICP3=1 AND ICP2=0 MEANS WE START COMPUTATION FOR A NEW RE NUMBER
    2 CALL RDTAPE
      WRITE(6,101)
  101 FORMAT(1H1,5X,35HNEW COMPUTATION STARTED---DATA READ)
      CALL RESULT
      DO 7000 J=1,MPT
      DO 7000 I=1,NPT
      PSI1(I,J)=PSI(I,J)
      ZETA1(I,J)=ZETA(I,J)
 7000 CONTINUE
      CALL EXTLIE
      CALL RCVORT
```

```
      NITER=1
      NW=1
      ITER=1
      NIP=0
      GO TO 200
C*****
C*****ICP3=0 AND ICP2=0 MEANS WE START FROM POTENTIAL FLOW CONDITIONS
    1 CALL GRIDPT
      CALL START
      WRITE(6,220)
  220 FORMAT(/5X,21HPOTENTIAL FLOW RESULT)
      ICP5=1
      CALL RESULT
      CALL EXTLIE
      IF(ICP1.EQ.1) GO TO 600
      CALL BCVORT
      WRITE(6,103)
  103 FORMAT(1H1,5X,41HFIRST COMPUTATION STARTED---DATA COMPUTED)
      DO 9000 I=1,NPT
      ZETA(I,1)=ZETA1(I,1)
 9000 CONTINUE
      DO 9001 J=1,MPT
      DO 9001 I=1,NPT
      PSI(I,J)=PSI1(I,J)
 9001 CONTINUE
      CALL RESULT
      ICP3=1
      ICP5=0
      NITER=1
      NW=1
      ITER=1
      NIP=0
C*****
  200 CONTINUE
C*****INITIAL CONDITIONS ARE ESTABLISHED---START ITERATIONS ON THE
C*****VORTICITY FIELD USING ADI METHOD
      CALL ADI
      IF(ICP1.EQ.0) GO TO 300
C*****ICP1=1 MEANS MAXIMUM NUMBER OF ITERATIONS IS REACHED FOR THE
C*****STREAM FUNCTION AND DIFFERENT PARAMETERS HAVE TO BE SET.
  600 WRITE(6,102)NITER
  102 FORMAT(5X,18HMAX. ITER. REACHED,5X,6HNITER=,I3)
      ICP5=1
      CALL RESULT
      STOP
C*****
  300 CONTINUE
C*****CHECK COMPUTING TIME.
      TSEC=CPSEC
      CALL SECOND(CPSEC)
      DSEC=CPSEC-TSEC
      TLEFT=TIME-CPSEC
      TITER=CPSEC/FLOAT(ITER)
      IF((TLEFT-TITER).LT.0.0) GOTO 500
      DO 5000 J=1,MPT
      DO 5000 I=1,NPT
      PSI(I,J)=PSI1(I,J)
      ZETA(I,J)=ZETA1(I,J)
 5000 CONTINUE
```

```
      NIP=NIP+1
      IF(NIP.NE.NDIP) GO TO 750
      CALL PRES
      WRITE(6,104) NITER,CPSEC,DSEC,NUPV,NUPST,CDP
  104 FORMAT(5X,6HNITER=,I4,2X,6HCPSEC=,F7.3,2X,5HDSEC=,F6.3,2X,
     15HNUPV=,I3,2X,6HNUPST=,I3,2X,4HCDP=,G12.5)
      NIP=0
  750 CONTINUE
      NW=NW+1
      IF(NW.EQ.NDW) GO TO 800
      GO TO 801
  800 NW=0
C*****WRITE OUT PARTIAL RESULTS
      WRITE(6,700)
  700 FORMAT(1H1)
      WRITE(6,802)NITER
  802 FORMAT(/20X,21HRESULTS FOR ITERATION,I4/)
      CALL RESULT
  801 CONTINUE
      ITER=ITER+1
      NITER=NITER+1
      GO TO 200
C*****
C*****TIME LIMIT IS REACHED---WRITE OUT FINAL RESULTS
  500 CONTINUE
      DO 6000 J=1,MPT
      DO 6000 I=1,NPT
      PSI(I,J)=PSI1(I,J)
      ZETA(I,J)=ZETA1(I,J)
 6000 CONTINUE
      NITER=NITER+1
C*****
C*****ICP7=0 MEANS WE WRITE THE CONVERGED RESULT ON A TAPE
      IF(ICP7.EQ.0)   ICP6=0
      CALL RESULT
      CALL WRTAPE
      WRITE(6,501)JTAP
  501 FORMAT(5X,21HDATA WRITTEN ON TAPE ,I1)
      STOP
      END
```

```
      SUBROUTINE PARAM
C*****
C*****THIS SUBROUTINE SETS UP ALL THE CONSTANTS AND PARAMETERS NEEDED
C*****IN THE COMPUTATION
C*****
      COMMON/CONST/PI,EPS,EPS1,RE
      COMMON/MESH/AL,AK,MINT,NINT,MPT,NPT,MNINT,NDTETA
      COMMON/CNTROL/ICP1,ICP2,ICP3,NUPV,NUPST,MUP,NISF,MNISF,NITER,
     1TIME,CPSEC,NW,NDW,NDIP
      COMMON/RELFAC/OM,OMV,RHO,A
      COMMON/TAPE/ITAP,JTAP,NTAP
      COMMON/FILE/ICP7,IFILE
      COMMON/CSTCOE/B0,B1,C0,C1,C2,F0,F1
      COMMON/APR/ICP5,DP1(51),DP2(31),DP3(51),VT(31),CDP
      COMMON/NCTOUR/ICP6,NC,NC1,NCVOR
C*****
C*****SET UP TAPE PARAMETERS
      ITAP=1
      JTAP=1
      NTAP=2
      IFILE=1
C*****
C*****SET UP CONTROL PARAMETERS
      RE=10.0
      ICP2=0
      ICP3=0
      ICP5=0
      ICP6=1
      ICP7=0
      TIME=1000.
      CPSEC=0.0
      MUP=0
      MNISF=200
      NDW=200
      NDIP=5
C*****
C*****SET UP ACCELERATION FACTOR
      RHO=10000.
C*****
C*****SET UP CONSTANTS
      PI=3.141592654
      EPS=1.0E-03
      EPS1=1.0E-03
C*****
C*****SET UP GRID PARAMETERS
      AL=1./30.
      AK=0.0125
      MINT=50
      NINT=30
      MPT=51
      NPT=31
      MNINT=NINT/2+1
      NDTETA=6
      A=1./AL**2+1./AK**2
C*****
C*****SET UP CONTOUR PARAMETERS
      NC=33
      NC1=10
      NCVOR=25
```

```
C*****
C*****COMPUTE RELAXATION FACTOR FROM RUSSEL AND FRANKEL FORMULAE AND
C*****TAKE AVERAGE
C*****RUSSEL FORMULA
      ANPT=FLOAT(NPT)
      AMPT=FLOAT(MPT)
      BA=1./ANPT**2+1./AMPT**2
      B=SQRT(BA)
      OMR=2./(1.+PI*B/1.414214)
C*****FRANKEL FORMULA
      T=COS(PI/ANPT)+COS(PI/AMPT)
      ALPHA=(2.-SQRT(4.-T**2))/T**2
      OMF=4.*ALPHA
      OM=(OMF+OMR)/2.
      OMV=0.5
C*****
C*****CALCULATE CONSTANT COEFFICIENTS FOR THE TRIDIAGONAL SYSTEMS
      B0=RHO+4.0/(RE*AL**2)
      B1=RHO-4.0/(RE*AK**2)
      C0=4.0*AK*AL
      C1=2.0/(RE*AL**2)
      C2=2.0/(RE*AK**2)
      F0=RHO+4.0/(RE*AK**2)
      F1=RHO-4.0/(RE*AL**2)
C*****
      RETURN
      END



      SUBROUTINE RDTAPE
C*****
C*****THIS SUBROUTINE READS DATA FROM PREVIOUS ITERATION OR FROM
C*****PREVIOUS SOLUTION
C*****
      COMMON/MESH/AL,AK,MINT,NINT,MPT,NPT,MNINT,NDTETA
      COMMON/STRFUN/PSI(31,51),PSI1(31,51)
      COMMON/VORT/ZETA(31,51),ZETA1(31,51)
      COMMON/GRID/E(51),XI(51),R(51),ETA(31),TETA(31),NTETA(31)
      COMMON/CNTROL/ICP1,ICP2,ICP3,NUPV,NUPST,MUP,NISF,MNISF,NITER,
     1TIME,CPSEC,NW,NDW,NDIP
      COMMON/TAPE/ITAP,JTAP,NTAP
      REWIND ITAP
      READ(ITAP)(E(J),XI(J),R(J),J=1,MPT)
      READ(ITAP)(ETA(I),TETA(I),NTETA(I),I=1,NPT)
      READ(ITAP)((PSI(I,J),I=1,NPT),J=1,MPT)
      READ(ITAP)((ZETA(I,J),I=1,NPT),J=1,MPT)
      READ(ITAP)NITER,NW
      RETURN
      END
```

```
      SUBROUTINE EXTLIF
C*****
C*****THIS SUBROUTINE CALCULATES THE SOLUTION FOR THE STREAM FUNCTION
C*****EQUATION USING EXTRAPOLATED LIEBMANN METHOD
C*****
      DIMENSION APSI(31,51),APSI1(31,51)
      COMMON/CONST/PI,EPS,EPS1,RE
      COMMON/MESH/AL,AK,MINT,NINT,MPT,NPT,MNINT,NDTETA
      COMMON/STRFUN/PSI(31,51),PSI1(31,51)
      COMMON/VORT/ZETA(31,51),ZETA1(31,51)
      COMMON/GRID/E(51),XI(51),R(51),ETA(31),TETA(31),NTETA(31)
      COMMON/CNTROL/ICP1,ICP2,ICP3,NUPV,NUPST,MUP,NISF,MNISF,NITER,
     1TIME,CPSEC,NW,NDW,NDIP
      COMMON/RELFAC/OM,OMV,RHO,A
      NISF=0
C*****
C*****COMPUTATION OF THE STREAM FUNCTION
      DO 2001 J=1,MPT
      DO 2001 I=1,NPT
      APSI(I,J)=PSI(I,J)
      APSI1(I,J)=PSI(I,J)
 2001 CONTINUE
 2005 CONTINUE
      DO 2000 J=2,MINT
      DO 2000 I=2,NINT
      APSI1(I,J)=(1.-OM)*APSI(I,J)+(OM/(2.*A))*((APSI1(I-1,J)+
     1APSI(I+1,J))/AL**2+(APSI1(I,J-1)+APSI(I,J+1))/AK**2
     2-ZETA1(I,J)*(E(J)**2))
 2000 CONTINUE
C*****
C*****TEST ON TWO CONSECUTIVE VALUES OF THE STREAM FUNCTION USING
C*****RELATIVE ERROR
      NUPST=0
      DO 2002 J=2,MINT
      DO 2002 I=2,NINT
      IF(ABS(APSI1(I,J)).EQ.0.0) GO TO 2002
      ERROR=ABS(APSI1(I,J)-APSI(I,J))/ABS(APSI1(I,J))
      IF(ERROR.LT.EPS)  GO TO 2002
      NUPST=NUPST+1
 2002 CONTINUE
C*****
C*****IF ALL ITERATIONS HAVE CONVERGED,RETURN,OTHERWISE CONTINUE CALCULATION
      IF(NUPST.EQ.MUP) GO TO 3000
      DO 2003  J=1,MPT
      DO 2003  I=1,NPT
      APSI(I,J)=APSI1(I,J)
 2003 CONTINUE
      NISF=NISF+1
      IF(NISF.GT.MNISF) ICP1=1
      IF(ICP1.EQ.1) GO TO 3000
      GO TO 2005
C*****
C*****ALL ITERATIONS HAVE CONVERGED
 3000 CONTINUE
      DO 2004 J=1,MPT
      DO 2004 I=1,NPT
      PSI1(I,J)=APSI1(I,J)
 2004 CONTINUE
      RETURN
      END
```

```
      SUBROUTINE GRIDPT
C*****
C*****THIS SUBROUTINE PROVIDES THE COORDINATE VALUES FOR EACH MESH
C*****POINT OF THE GRID
C*****
      COMMON/CONST/PI,EPS,EPS1,RE
      COMMON/MESH/AL,AK,MINT,NINT,MPT,NPT,MNINT,NDTETA
      COMMON/GRID/E(51),XI(51),R(51),ETA(31),TETA(31),NTETA(31)
C*****
C*****BUBBLE SURFACE
      ETA(1)=0.0
      TETA(1)=0.0
      NTETA(1)=0
      XI(1)=0.0
      R(1)=1.0
      E(1)=PI
C*****
C*****OUTER BOUNDARY
      ETA(31)=1.0
      TETA(31)=PI
      XI(51)=0.625
      R(51)=EXP(PI*XI(51))
      E(51)=PI*R(51)
C*****
C*****ANGULAR COORDINATES
      DO 1000 I=1,NINT
      ETA(I)=AL*FLOAT(I-1)
      TETA(I)=ETA(I)*PI
      NTETA(I+1)=NTETA(I)+NDTETA
 1000 CONTINUE
C*****
C*****RADIAL COORDINATES
      DO 2000 J=2,MINT
      XI(J)=AK*FLOAT(J-1)
      R(J)=EXP(PI*XI(J))
      E(J)=PI*R(J)
 2000 CONTINUE
      RETURN
      END
```

```
      SUBROUTINE BCVORT
C*****
C*****THIS SUBROUTINE COMPUTES THE VALUES OF THE VORTICITY AT THE
C*****BUBBLE SURFACE FROM THE VALUES OF THE STREAM FUNCTION NEAR THIS
C*****SURFACE
C*****
      COMMON/CONST/PI,EPS,EPS1,RE
      COMMON/MESH/AL,AK,MINT,NINT,MPT,NPT,MNINT,NDTETA
      COMMON/STRFUN/PSI(31,51),PSI1(31,51)
      COMMON/VORT/ZETA(31,51),ZETA1(31,51)
      COMMON/CNTROL/ICP1,ICP2,ICP3,NUPV,NUPST,MUP,NISF,MNISF,NITER,
     1TIME,CPSEC,NW,NDW,NDIP
      COMMON/RELFAC/OM,OMV,RHO,AA
C*****
C*****FOUR POINTS FORMULA IS USED
      D=((33.*AK)/PI+18.*(AK**2))*(PI**2)
      DO 1000 I=1,NINT
      ZETA1(I,1)=(108.*PSI1(I,2)-27.*PSI1(I,3)+4.*PSI1(I,4))/D
 1000 CONTINUE
      ZETA1(NPT,1)=0.0
C*****
C*****IF POTENTIAL FLOW STARTING CONDITION,RETURN,
C*****OTHERWISE UNDER-RELAXE SURFACE VORTICITY
      IF(ICP3.EQ.0) RETURN
      DO 1001 I=1,NINT
      ZETA1(I,1)=(1.-OMV)*ZETA(I,1)+OMV*ZETA1(I,1)
 1001 CONTINUE
      RETURN
      END

      SUBROUTINE START
C*****
C*****THIS SUBROUTINE COMPUTES THE VALUES OF THE STREAM FUNCTION AND
C*****OF THE  VORTICITY FOR THE BEGINNING OF THE CALCULATION
C*****(I.E. POTENTIAL FLOW CONDITION)
C*****
      COMMON/CONST/PI,EPS,EPS1,RE
      COMMON/MESH/AL,AK,MINT,NINT,MPT,NPT,MNINT,NDTETA
      COMMON/STRFUN/OPSI(31,51),OPSI1(31,51)
      COMMON/VORT/OZETA(31,51),OZETA1(31,51)
      COMMON/GRID/E(51),XI(51),R(51),ETA(31),TETA(31),NTETA(31)
C*****
C*****STREAM FUNCTION
      DO 1000 J=1,MPT
      DO 1000 I=1,NINT
      OPSI(I,J)=(EXP(PI*XI(J))-EXP(-PI*XI(J)))*SIN(TETA(I))
      OPSI1(I,J)=OPSI(I,J)
 1000 CONTINUE
      DO 3000 J=1,MPT
      OPSI(NPT,J)=0.0
      OPSI1(NPT,J)=0.0
 3000 CONTINUE
C****
C*****VORTICITY IS 0.0 EVERYWHERE
      DO 2000 J=1,MPT
      DO 2000 I=1,NPT
      OZETA(I,J)=0.0
      OZETA1(I,J)=0.0
 2000 CONTINUE
      RETURN
      END
```

```
      SUBROUTINE ADI
C*****
C*****THIS SUBROUTINE CALCULATES THE VORTICITY FIELD FOR A NEW ITERATION
C*****USING PEACEMAN AND RACHFORD ALTERNATING-DIRECTION IMPLICIT
C*****METHOD
C*****
      COMMON/CONST/PI,EPS,EPS1,RE
      COMMON/MESH/AL,AK,MINT,NINT,MPT,NPT,MNINT,NDTETA
      COMMON/STRFUN/PSI(31,51),PSI1(31,51)
      COMMON/VORT/ZETA(31,51),ZETA1(31,51)
      COMMON/GRID/EE(51),XI(51),R(51),ETA(31),TETA(31),NTETA(31)
      COMMON/CNTROL/ICP1,ICP2,ICP3,NUPV,NUPST,MUP,NISF,MNISF,NITER,
     1TIME,CPSEC,NW,NDW,NDIP
      COMMON/RELFAC/OM,OMV,RHO,AA
      COMMON/CSTCOE/B0,B1,C0,C1,C2,F0,F1
      COMMON/COEF/X(51),Z(51),D(51),Y
      COMMON/SOL/V(51)
      COMMON/LOOP/MK
      DIMENSION    A(31,51),C(31,51),E(31,51),G(31,51),A1(31,51),
     1E1(31,51),G1(31,51),ALPHA(31,51),BETA(31,51),ZETA2(31,51),
     2C11(31,51)
      EQUIVALENCE(ALPHA,BETA),(A,E1),(C,G1),(A1,E),(C11,G)
      ICP4=0
      MMINT=MINT-1
      NNINT=NINT-1
      VAL2=ABS(B0)
      VAL4=ABS(F0)
C*****
C*****VARIABLE COEFFICIENTS IN THE TRIDIAGONAL SYSTEM
C*****---FIRST DIRECTION
      DO 1000 J=2,MINT
      DO 1000 I=2,NINT
      A(I,J)=-((PSI(I,J+1)-PSI(I,J-1))/C0+C1)
      C(I,J)=(PSI(I,J+1)-PSI(I,J-1))/C0-C1
      A1(I,J)=-((PSI(I+1,J)-PSI(I-1,J))/C0-C2)
      C11(I,J)=(PSI(I+1,J)-PSI(I-1,J))/C0+C2
 1000 CONTINUE
C*****
C*****TEST ON THE VALUES OF THE COEFFICIENTS OF THE TRIDIAGONAL
C*****SYSTEM---FIRST DIRECTION
      DO 1001 I=2,NINT
      DO 1001 J=2,MINT
      IF(I.EQ.2.OR.I.EQ.NINT) GO TO 500
      VAL1=ABS(A(I,J))+ABS(C(I,J))
      GO TO 501
  500 IF(I.EQ.NINT) GO TO 502
      VAL1=ABS(C(2,J))
      GO TO 501
  502 VAL1=ABS(A(NINT,J))
  501 IF(VAL1.GE.VAL2) ICP4=1
 1001 CONTINUE
      IF(ICP4.EQ.1) GO TO 32
      GO TO 33
C*****
C*****IF TEST IS WRONG SET ANOTHER ACCELERATION FACTOR
   32 WRITE(6,570) NITER
  570 FORMAT(/5X,'ACC. FAC. WRONG',5X,'NITER=',I3)
      STOP
C*****
```

```
C*****WE START UPDATING THE VORTICITY FIELD AT THE FIRST HALF STEP
C*****---ROW BY ROW
   33  MK=NINT
       Y=B0
       DO 2000 J=2,MINT
       ALPHA(2,J)=A1(2,J)*ZETA(2,J-1)+B1*ZETA(2,J)+C11(2,J)*ZETA
      1(2,J+1)-A(2,J)*ZETA(1,J)
       ALPHA(NINT,J)=A1(NINT,J)*ZETA(NINT,J-1)+B1*ZETA(NINT,J)+C11
      1(NINT,J)*ZETA(NINT,J+1)-C(NINT,J)*ZETA(NPT,J)
       DO 100 I=3,NNINT
       ALPHA(I,J)=A1(I,J)*ZETA(I,J-1)+B1*ZETA(I,J)+C11(I,J)*ZETA(I,J+1)
  100  CONTINUE
       DO101 I=2,NINT
       X(I)=A(I,J)
       Z(I)=C(I,J)
       D(I)=ALPHA(I,J)
  101  CONTINUE
       CALL TRIDIA
       DO 2000 I=2,NINT
       ZETA2(I,J)=V(I)
 2000  CONTINUE
       DO 2001 J=1,MPT
       ZETA2(1,J)=0.0
       ZETA2(NPT,J)=0.0
 2001  CONTINUE
C*****
C*****THE VALUES OF THE VORTICITY AT THE WALL AT HALF STEP ARE
C*****TAKEN EQUAL TO THE PREVIOUS VALUES
       DO 2002 I=2,NINT
       ZETA2(I,1)=ZETA(I,1)
       ZETA2(I,MPT)=0.0
 2002  CONTINUE
C*****
C*****VARIABLE COEFFICIENTS IN THE TRIDIAGONAL SYSTEM
C*****---SECOND DIRECTION
       DO 1002 J=2,MINT
       DO 1002 I=2,NINT
       E(I,J)=-A1(I,J)
       G(I,J)=-C11(I,J)
       E1(I,J)=-A(I,J)
       G1(I,J)=-C(I,J)
 1002  CONTINUE
C*****
C*****TEST ON THE VALUES OF THE COEFFICIENTS OF THE TRIDIAGONAL
C*****SYSTEM---SECOND DIRECTION
       DO 1003 J=2,MINT
       DO 1003 I=2,NINT
       IF(J.EQ.2.OR.J.EQ.MINT) GO TO 600
       VAL3=ABS(E(I,J))+ABS(G(I,J))
       GO TO 601
  600  IF(J.EQ.MINT) GO TO 602
       VAL3=ABS(G(I,2))
       GO TO 601
  602  VAL3=ABS(E(I,MINT))
  601  IF(VAL3.GE.VAL4) ICP4=1
 1003  CONTINUE
       IF(ICP4.EQ.1) GO TO 32
C*****
C*****WE START UPDATING THE VORTICITY FIELD AT THE SECOND HALF STEP
```

```
C*****--- COLUMN BY COLUMN
      MK=MINT
      Y=F0
      DO 3000  I=2,NINT
      BETA(I,2)=E1(I,2)*ZETA2(I-1,2)+F1*ZETA2(I,2)+G1(I,2)*ZETA2(I+1,2)
     1-F(I,2)*ZETA2(I,1)
      BETA(I,MINT)=E1(I,MINT)*ZETA2(I-1,MINT)+F1*ZETA2(I,MINT)+
     1G1(I,MINT)*ZETA2(I+1,MINT)-G(I,MINT)*ZETA2(I,MPT)
      DO 200 J=3,MMINT
      BETA(I,J)=E1(I,J)*ZETA2(I-1,J)+F1*ZETA2(I,J)+G1(I,J)*ZETA2
     1(I+1,J)
  200 CONTINUE
      DO 201 J=2,MINT
      X(J)=E(I,J)
      Z(J)=G(I,J)
      D(J)=BETA(I,J)
  201 CONTINUE
      CALL TRIDIA
      DO 3000 J=2,MINT
      ZETA1(I,J)=V(J)
 3000 CONTINUE
      DO 3001 J=1,MPT
      ZETA1(I,J)=0.0
      ZETA1(NPT,J)=0.0
 3001 CONTINUE
C*****
C*****AGAIN VALUES OF THE VORTICITY AT THE WALL ARE TAKEN EQUAL TO THE
C*****PREVIOUS ONES---THE NEW VALUES WILL BE CALCULATED FURTHER FROM
C*****VALUES OF THE STREAM FUNCTION NEAR THE SURFACE
      DO 3002 I=2,NINT
      ZETA1(I,1)=ZETA(I,1)
      ZETA1(I,MPT)=0.0
 3002 CONTINUE
C*****
C*****THE VALUES OF THE STREAM FUNCTION AT THE NEW STEP ARE NOW COMPUTED
      ICP1=0
      CALL EXTL1E
      IF(ICP1.EQ.1) RETURN
C*****
C*****THE VALUES OF THE VORTICITY AT THE SURFACE ARE NOW COMPUTED
      CALL BCVORT
C*****
C***** TEST ON THE VALUES OF THE SURFACE VORTICITY
      ICP2=0
      NUPV=0
      DO 4000 I=2,NINT
      ERROR1=ABS(ZETA1(I,1)-ZETA(I,1))/ABS(ZETA1(I,1))
      IF(ERROR1.LT.EPS1) GO TO 4000
      NUPV=NUPV+1
 4000 CONTINUE
      IF((NUPV.GT.MUP).OR.(NUPST.GT.MUP)) ICP2=1
C*****
C*****IF ICP2=0 ALL THE POINTS OF THE GRID HAVE CONVERGED
      ICP2=1
      RETURN
      END
```

```
      SUBROUTINE TRIDIA
C*****
C*****THIS SUBROUTINE CALCULATES THE SOLUTION OF A SET OF LINEAR
C*****EQUATIONS WHEN THE MATRIX IS TRIDIAGONAL.
C*****
      DIMENSION BETA(51),GAMMA(51)
      COMMON/COEF/A(51),C(51),D(51),B
      COMMON/SOL/V(51)
      COMMON/LOOP/MK
C*****
C******COEFFICIENTS OF THE TRIDIAGONAL MATRIX.
      BETA(2)=B
      GAMMA(2)=D(2)/BETA(2)
      DO 100 K=3,MK
      BETA(K)=B-(A(K)*C(K-1))/BETA(K-1)
      GAMMA(K)=(D(K)-A(K)*GAMMA(K-1))/BETA(K)
  100 CONTINUE
C*****
C*****SOLUTION FOR THE VECTORS
      V(MK)=GAMMA(MK)
      NK=MK-2
      DO 200 K=1,NK
      KK=MK-K
      V(KK)=GAMMA(KK)-(C(KK)*V(KK+1))/BETA(KK)
  200 CONTINUE
      RETURN
      END
```

```
      SUBROUTINE RESULT
C*****
C*****THIS SUBROUTINE PRINTS OUT RESULTS FOR THE VORTICITY AND THE STREAM
C*****FUNCTION
C*****IT ALSO CALLS THE SUBROUTINE WHICH CALCULATES THE PRESSURE
C*****DISTRIBUTION AND THE DRAG COEFFICIENT
C*****
      COMMON/CONST/PI,EPS,EPS1,RE
      COMMON/MESH/AL,AK,MINT,NINT,MPT,NPT,MNINT,NDTETA
      COMMON/STRFUN/PSI(31,51),PSII(31,51)
      COMMON/VORT/ZETA(31,51),ZETA1(31,51)
      COMMON/GRID/E(51),XI(51),R(51),ETA(31),TETA(31),NTETA(31)
      COMMON/CNTROL/ICP1,ICP2,ICP3,NUPV,NUPST,MUP,NISF,MNISF,NITER,
     1TIME,CPSEC,NW,NDW,NDIP
      COMMON/RELFAC/OM,OMV,RHO,AA
      COMMON/APR/ICP5,DP1(51),DP2(31),DP3(51),VT(31),CDP
      COMMON/CTOUR/CSF(33),CR(31,33),DSFR(31,33),DSFT(31,33),
     1CRT(31,33),CSFN(10),NTETAI(33),NTETAS(33)
      COMMON/CTOUR1/CRTV1(31,25),CRTV2(31,25),CRT1(16,10),CRT2(16,10)
      COMMON/NCTOUR/ICP6,NC,NC1,NCVOR
      COMMON/VCTOUR/CVORT(25)
      COMMON/DRFT/XD(31,33),YD(31,33),TD(31,33)
C*****
C*****WRITE OUT STREAM FUNCTION VALUES
      WRITE(6,1)
      N1=8
      NR=MOD(MPT,N1)
      NN=MPT-NR
      DO 100 N=1,NN,N1
      N1=N+N1-1
      WRITE(6,2)(R(J),J=N,N1)
      WRITE(6,3)(NTETA(I),(PSI(I,J),J=N,N1),I=1,NPT)
      WRITE(6,5)
  100 CONTINUE
      NM=NN+1
      WRITE(6,4)(R(J),J=NM,MPT)
      WRITE(6,6)(NTETA(I),(PSI(I,J),J=NM,MPT),I=1,NPT)
      WRITE(6,5)
      WRITE(6,10)
C*****
C*****WRITE OUT VORTICITY VALUES
      DO 200 N=1,NN,N1
      N1=N+N1-1
      WRITE(6,2)(R(J),J=N,N1)
      WRITE(6,3)(NTETA(I),(ZETA(I,J),J=N,N1),I=1,NPT)
      WRITE(6,5)
  200 CONTINUE
      WRITE(6,4)(R(J),J=NM,MPT)
      WRITE(6,6)(NTETA(I),(ZETA(I,J),J=NM,MPT),I=1,NPT)
      WRITE(6,5)
      WRITE(6,11)OM,OMV,RHO
      WRITE(6,12)ICP1,ICP2,ICP3,NUPV,NUPST,NITER,TIME,CPSEC
    1 FORMAT(//50X,27HSTREAM FUNCTION COORDINATES/48X,31(1H*)/)
    2 FORMAT(8X,8(5X,2HR=,F6.2,2X))
    3 FORMAT(2X,I3,1H*,2X,8G15.5)
    4 FORMAT(8X,3(5X,2HR=,F6.2,2X))
    5 FORMAT(//56X,20(1H*)//)
    6 FORMAT(2X,I3,1H*,2X,3G15.5)
   10 FORMAT(1H1//50X,21HVORTICITY COORDINATES/48X,25(1H*)/)
```

```
   11 FORMAT(////13X,3HOM=,E11.4,5X,4HOMV=,E11.4,5X,4HRHO=,E12.5)
   12 FORMAT(//5X,5HICP1=,I1,3X,5HICP2=,I1,3X,5HICP3=,I1,3X,5HNUPV=,I3,
     13X,6HNUPST=,I3/3X,6HNITER=,I4,3X,5HTIME=,F4.0,3X,6HCPSEC=,F7.3)
C*****
C*****ICP5=0 MEANS WE CALCULATE THE PRESSURE DISTRIBUTION
      IF(ICP5.EQ.1) GO TO 500
      CALL PRES
      WRITE(6,55)
      WRITE(6,53)
      WRITE(6,50)(R(J),DP1(J),DP3(J),J=1,MPT)
      WRITE(6,54)
      WRITE(6,51)(NTETA(I),DP2(I),VT(I),I=1,NPT)
      WRITE(6,52)RE,CDP
   50 FORMAT(17X,F6.2,17X,G12.5,17X,G12.5)
   51 FORMAT(20X,I3,16X,G12.5,15X,G12.5)
   52 FORMAT(/20X,3HRE=,F5.1,5X,4HCDP=,G12.5)
   53 FORMAT(/20X,1HR,20X,8HDP ABOVE,20X,8HDP BELOW)
   54 FORMAT(/20X,4HTETA,20X,2HDP,20X,10HTANG. VEL.)
   55 FORMAT(//30X,34HPRESSURE DISTRIBUTION - DRAG COEF./28X,38(1H*))
C*****
C*****ICP6=0 MEANS WE NOW COMPUTE THE STREAM FUNCTION CONTOURS AND
C*****THE DRIFT PROFILE
  500 IF(ICP6.EQ.1) RETURN
      CALL CNTOUR
      CALL DRIFT
      RETURN
      END
```

```
      SUBROUTINE PRES
C*****
C*****THIS SUBROUTINE EVALUATES THE PRESSURE CHANGES ALONG THE AXIS OF
C*****THE MOVEMENT OF THE BUBBLE AND AROUND THE BUBBLE SURFACE.
C*****IT ALSO EVALUATES THE PRESSURE DRAG COEFFICIENT.
C*****
      DIMENSION VR(51),F(51),VAL(51),G(31),ANVAL(31),AVR(51),H(51),
     1AVAL(51),D(31,4),D2(31)
      COMMON/CONST/PI,EPS,EPS1,RE
      COMMON/MESH/AL,AK,MINT,NINT,MPT,NPT,MNINT,NDTETA
      COMMON/STRFUN/PSI(31,51),PSI1(31,51)
      COMMON/VORT/ZETA(31,51),ZETA1(31,51)
      COMMON/GRID/E(51),XI(51),R(51),ETA(31),TETA(31),NTETA(31)
      COMMON/APR/ICPS,DP1(51),DP2(31),DP3(51),VT(31),CDP
C*****
C*****APPROXIMATIONS TO DERIVATIVES
      DO 1000 J=1,MPT
      VR(J)=(18.*PSI(2,J)-9.*PSI(3,J)+2.*PSI(4,J))/(6.*AL)
      F(J)=(18.*ZETA(2,J)-9.*ZETA(3,J)+2.*ZETA(4,J))/(6.*AL)
      AVR(J)=(-18.*PSI(NPT-1,J)+9.*PSI(NPT-2,J)-2.*PSI(NPT-3,J))/(6.*AL)
      H(J)=(-18.*ZETA(NPT-1,J)+9.*ZETA(NPT-2,J)-2.*ZETA(NPT-3,J))/
     1(6.*AL)
 1000 CONTINUE
      DO 2000 I=1,NPT
      VT(I)=(18.*PSI(1,2)-9.*PSI(I,3)+2.*PSI(I,4))/(6.*AK*PI)
      G(I)=(-11.*ZETA(I,1)+18.*ZETA(I,2)-9.*ZETA(I,3)+2.*ZETA(I,4))/
     1(6.*AK)
 2000 CONTINUE
C*****
C*****PRESSURE ALONG THE AXIS ABOVE THE BUBBLE.
      VAL(1)=((F(MINT)+F(MPT))*AK)/2.
      DO 1001 J=2,MINT
      J1=MINT-J
      VAL(J)=VAL(J-1)+((F(J1+1)+F(J1+2))*AK)/2.
 1001 CONTINUE
      DO 1002 J=2,MINT
      DP1(J)=1.-(VR(J)/E(J))**2+(4./RE)*VAL(MPT-J)
 1002 CONTINUE
      DP1(MPT)=0.0
      DP1(1)=1.+(4./RE)*VAL(MINT)
      AK0=DP1(1)
C*****
C*****PRESURE AROUND THE BUBBLE SURFACE.
      ANVAL(1)=0.0
      DO 2001 I=2,NPT
      ANVAL(I)=ANVAL(I-1)+((G(I)+G(I-1))*AL)/2.
      DP2(I)=AK0-VT(I)**2+(4./RE)*ANVAL(I)
 2001 CONTINUE
      DP2(1)=AK0
      AK1=DP2(NPT)
C*****
C*****PRESSURE ALONG THE AXIS BELOW THE BUBBLE.
      AVAL(1)=((H(1)+H(2))*AK)/2.0
      DO 3001 J=2,MINT
      AVAL(J)=AVAL(J-1)+((H(J)+H(J+1))*AK)/2.0
      DP3(J)=AK1-(AVR(J)/E(J))**2-(4./RE)*AVAL(J-1)
 3001 CONTINUE
      DP3(1)=AK1
      DP3(MPT)=0.0
```

```
C*****
C*****PRESSURE DRAG COEFFICIENT
      DO 5000 I=2,NINT
      DO 5000 J=1,4
      D(I,J)=(PSI(I+1,J)-PSI(I-1,J))/(2.*AL)
 5000 CONTINUE
      DO 5001 J=1,4
      D(1,J)=(PSI(2,J)-PSI(1,J))/(2.*AL)
      D(NPT,J)=(PSI(NPT,J)-PSI(NPT-1,J))/(2.*AL)
 5001 CONTINUE
      DO 6000 I=1,NPT
      D2(I)=(-11.*D(I,1)+18.*D(I,2)-9.*D(I,3)+2.*D(I,4))/(6.*AK)
 6000 CONTINUE
      YVAL=((D2(1)+D2(2))*AL)/2.
      XVAL=((DP2(1)+DP2(2)*COS(PI*AL))*AL)/2.
      DO 7000 I=2,NINT
      YVAL=YVAL+((D2(I)+D2(I+1))*AL)/2.
      XVAL=XVAL+((DP2(I)*COS(TETA(I))+DP2(I+1)*COS(TETA(I+1)))*AL)/2.
 7000 CONTINUE
      CDP=PI*XVAL-(8.*YVAL)/(PI*RE)
      RETURN
      END
```

```
      SUBROUTINE CNTOUR
C*****
C*****THIS SUBROUTINE COMPUTES THE VALUES OF THE STREAM FUNCTION
C*****CONTOURS AND THE DERIVATIVES OF THE STREAM FUNCTION
C*****IT ALSO COMPUTES THE VORTICITY CONTOURS
C*****
      COMMON/CONST/PI,EPS,EPS1,RE
      COMMON/MESH/AL,AK,MINT,NINT,MPT,NPT,MNINT,NDTETA
      COMMON/STRFUN/PSI(31,51),PSI1(31,51)
      COMMON/VORT/ZETA(31,51),ZETA1(31,51)
      COMMON/GRID/E(51),XI(51),R(51),ETA(31),TETA(31),NTETA(31)
      COMMON/CTOUR/CSF(33),CR(31,33),DSFR(31,33),DSFT(31,33),
     1CRT(31,33),CSFN(10),NTETAI(33),NTETAS(33)
      COMMON/CTOUR1/CRTV1(31,25),CRTV2(31,25),CRT1(16,10),CRT2(16,10)
      COMMON/NCTOUR/ICP6,NC,NC1,NCVOR
      COMMON/VCTOUR/CVORT(25)
      COMMON/INTERG/NI(33),NS(33)
C*****
C*****STREAM FUNCTION CONTOURS
      DO 2000 K=1,NC
      ICP=1
      CRT(1,K)=0.000
      CRT(NPT,K)=0.000
      NI(K)=2
      NS(K)=NINT
      NTETAI(K)=6
      NTETAS(K)=174
      DO 1000 I=2,NINT
      DO 3000 J=1,MINT
      IF((CSF(K).GE.PSI(I,J)).AND.(CSF(K).LE.PSI(I,J+1))) GO TO 100
      IF(J.EQ.MINT) GO TO 200
 3000 CONTINUE
  200 IF(ICP.EQ.2) GO TO 201
      NTETAI(K)=NTETA(I+1)
      NI(K)=I+1
      CRT(I,K)=0.000
      GO TO 1000
  201 NTETAS(K)=NTETA(I-1)
      NS(K)=I-1
      CRT(I,K)=0.000
      DO 2011 L=I,NINT
      CRT(L,K)=0.000
 2011 CONTINUE
      GO TO 2000
  100 DSFR(I,K)=(PSI(I,J+1)-PSI(I,J))/AK
      CR(I,K)=XI(J)+(CSF(K)-PSI(I,J))/DSFR(I,K)
      CRT(I,K)=EXP(PI*CR(I,K))
      D1=(PSI(I+1,J+1)-PSI(I+1,J))/AK
      P1=PSI(I+1,J)+D1*(CR(I,K)-XI(J))
      D2=(PSI(I-1,J+1)-PSI(I-1,J))/AK
      P2=PSI(I-1,J)+D2*(CR(I,K)-XI(J))
      DSFT(I,K)=(P1-P2)/(2.*AL)
      ICP=2
 1000 CONTINUE
 2000 CONTINUE
C*****
C*****WRITE OUT STREAM FUNCTION CONTOURS
      WRITE(6,500)
  500 FORMAT(1H1)
```

```
      WRITE(6,501)
  501 FORMAT(50X,24HSTREAM FUNCTION CONTOURS/48X,28(1H*)/)
      K1=9
      KR=MOD(NC,K1)
      KN=NC-KR
      DO 10 K=1,KN,K1
      K1=K+K1-1
      WRITE(6,1)(CSF(KK),KK=K,K1)
      WRITE(6,2)(NTETA(I),(CRT(I,KK),KK=K,K1),I=1,NPT)
      WRITE(6,3)
   10 CONTINUE
      KM=KN+1
      WRITE(6,4)(CSF(KK),KK=KM,NC)
      WRITE(6,5)(NTETA(I),(CRT(I,KK),KK=KM,NC),I=1,NPT)
      WRITE(6,3)
    1 FORMAT(8X,9(7HCONTOUR,X,F4.2,X))
    2 FORMAT(2X,I3,1H*,2X,9G13.4)
    3 FORMAT(//56X,20(1H*)//)
    4 FORMAT(8X,6(7HCONTOUR,X,F4.2,X))
    5 FORMAT(2X,I3,1H*,2X,6G13.4)
      WRITE(6,7)
    7 FORMAT(//5X,3HCSF,5X,5HTETAI,5X,5HTETAS,5X,2HNI,5X,2HNS/
     15X,3(1H*),5X,5(1H*),5X,5(1H*),5X,2(1H*),5X,2(1H*))
      WRITE(6,6)(CSF(K),NTETAI(K),NTETAS(K),NI(K),NS(K),K=1,NC)
    6 FORMAT(5X,F4.2,5X,I3,7X,I3,5X,I2,6X,I2)
C*****
C*****CONTOURS FOR NEGATIVE VALUES OF THE STREAM FUNCTION
      DO 9005 K=1,NC1
      CRT1(MNINT,K)=0.000
      CRT2(MNINT,K)=0.000
      DO 9001 I=MNINT,NINT
      I1=1-NINT/2
      DO 9002 J=1,MINT
      IF((CSFN(K).LE.PSI(I,J)).AND.(CSFN(K).GE.PSI(I,J+1))) GO TO 9000
      IF(J.EQ.MINT) GO TO 9010
 9002 CONTINUE
 9000 CRP=XI(J)+AK*(CSFN(K)-PSI(I,J))/(PSI(I,J+1)-PSI(I,J))
      CRT1(I1,K)=EXP(PI*CRP)
      GO TO 9011
 9010 CRT1(I1,K)=0.000
 9011 CONTINUE
      DO 9003 J=1,MINT
      IF((CSFN(K).GE.PSI(I,J)).AND.(CSFN(K).LE.PSI(I,J+1))) GO TO 9004
      IF(J.EQ.MINT) GO TO 9020
 9003 CONTINUE
 9004 CRP=XI(J)+AK*(CSFN(K)-PSI(I,J))/(PSI(I,J+1)-PSI(I,J))
      CRT2(I1,K)=EXP(PI*CRP)
      GO TO 9001
 9020 CRT2(I1,K)=0.000
 9001 CONTINUE
 9005 CONTINUE
C*****
C*****WRITE OUT CONTOURS FOR NEGATIVE VALUES OF THE STREA FUNCTION
      WRITE(6,502)
  502 FORMAT(////50X,25HNEG.STREAM FUNC. CONTOURS/48X,30(1H*)/)
      K1N=5
      KRN=MOD(NC1,K1N)
      KNN=NC1-KRN
      DO 11 K=1,KNN,K1N
```

```
      K1N=K+KIN-1
      WRITE(6,20) (CSFN(KK),KK=K,K1N)
      DO 99 I=MNINT,NPT
      II=I-NINT/2
      WRITE(6,21) (NTETA(I),(CRT1(II,KK),KK=K,KIN))
      WRITE(6,22) (CRT2(II,KK),KK=K,K1N)
   99 CONTINUE
      WRITE(6,3)
   11 CONTINUE
   20 FORMAT(20X,5(5X,7HCONTOUR,F5.2))
   21 FORMAT(10X,I3,1H*,6X,5G17.4)
   22 FORMAT(20X,5G17.4)
C*****
C*****VORTICITY CONTOURS
      DO 2500 KK=1,NCVOR
      CRTV1(1,KK)=0.000
      CRTV1(NPT,KK)=0.000
      CRTV2(1,KK)=0.000
      CRTV2(NPT,KK)=0.000
      DO 1500 I=2,NINT
      DO 3500 J=1,MINT
      IF(ABS(ZETA(I,J)).LT.1.0E-03) GO TO 3501
      IF((CVORT(KK).GE.ZETA(I,J)).AND.(CVORT(KK).LE.ZETA(I,J+1)))
     1GO TO 151
 3501 IF(J.EQ.MINT) GO TO 1501
 3500 CONTINUE
  151 DVR=(ZETA(I,J+1)-ZETA(I,J))/AK
      CRV=XI(J)+(CVORT(KK)-ZETA(I,J))/DVR
      CRTV1(I,KK)=EXP(PI*CRV)
      GO TO 1511
 1501 CRTV1(I,KK)=0.000
 1511 CONTINUE
      DO 4500 J=1,MINT
      IF(ABS(ZETA(I,J)).LT.1.0E-03) GO TO 4501
      IF((CVORT(KK).LE.ZETA(I,J)).AND.(CVORT(KK).GE.ZETA(I,J+1)))
     1GO TO 150
 4501 IF(J.EQ.MINT) GO TO 1510
 4500 CONTINUE
  150 DVR=(ZETA(I,J+1)-ZETA(I,J))/AK
      CRV=XI(J)+(CVORT(KK)-ZETA(I,J1))/DVR
      CRTV2(I,KK)=EXP(PI*CRV)
      GO TO 1500
 1510 CRTV2(I,KK)=0.000
 1500 CONTINUE
 2500 CONTINUE
C*****
C*****WRITE OUT VORTICITY CONTOURS
      WRITE(6,550)
  550 FORMAT(////50X,18HVORTICITY CONTOURS/48X,22(1H*)/)
      KKR=MOD(NCVOR,KI)
      KKN=NCVOR-KKR
      DO 15 K=1,KKN,KI
      KK1=K+KI-1
      WRITE(6,1)(CVORT(KK),KK=K,KK1)
      DO 88 I=1,NPT
      WRITE(6,50)
      WRITE(6,2)(NTETA(I),(CRTV1(I,KK),KK=K,KK1))
      WRITE(6,32)(CRTV2(I,KK),KK=K,KK1)
   88 CONTINUE
```

```
      WRITE(6,3)
 15   CONTINUE
      KKM=KKN+1
      WRITE(6,5000)(CVORT(KK),KK=KKM,NCVOR)
      DO 89 I=1,NPT
      WRITE(6,50)
      WRITE(6,5500)(NTETA(I),(CRTV1(I,KK),KK=KKM,NCVOR))
      WRITE(6,5600)(CRTV2(I,KK),KK=KKM,NCVOR)
 89   CONTINUE
5000  FORMAT(8X,7(7HCONTOUR,X,F4.2,X))
 50   FORMAT(1X/)
 32   FORMAT(8X,9G13.4)
5600  FORMAT(8X,7G13.4)
5500  FORMAT(2X,I3,1H*,2X,7G13.4)
      WRITE(6,500)
      RETURN
      END
```

```
      BLOCK DATA
C*****
C*****THESE DATA ARE THE VALUES OF THE CONTOURS
C*****---STREAM FUNCTION
C*****---NEGATIVE STREAM FUNCTION
C*****---VORTICITY
      COMMON/CTOUR/CSF(33),CR(31,33),DSFR(31,33),DSFT(31,33),
     1CRT(31,33),CSFN(10),NTETA(33),NTETAS(33)
      COMMON/VCTOUR/CVORT(25)
      DATA(CSF(K),K=1,33)/0.00,0.05,0.10,0.15,0.20,0.25,0.30,0.35,0.40,
     10.45,0.50,0.60,0.70,0.80,0.90,1.00,1.10,1.20,1.30,1.40,1.50,1.60,
     21.70,1.80,1.90,2.00,2.20,2.40,2.60,2.80,3.00,3.50,4.00/
      DATA(CSFN(K),K=1,10)/-1.00,-0.50,-0.40,-0.30,-0.25,-0.20,
     1-0.15,-0.10,-0.05,0.00/
      DATA(CVORT(KK),KK=1,25)/-0.15,-0.10,-0.05,-0.01,0.00,
     10.01,0.02,0.04,0.06,0.08,0.1,0.2,0.3,0.4,
     20.5,0.6,0.7,0.8,0.9,1.0,1.1,1.2,1.3,1.4,1.5/
      END
```

```
      SUBROUTINE DRIFT
C*****
C*****THIS SUBROUTINE CALCULATES THE DRIFT OF A PARTICLE WHEN A BUBBLE
C*****RISES THROUGH THE FLUIDISED BED.
C*****XD=VERTICAL DISPLACEMENT
C*****YD=HORIZONTAL DISPLACEMENT
C*****TD=DIMENSIONLESS TIME---PARAMETER ON THE CURVE
C*****
      DIMENSION FONC1(31),SOM1(31),T(31)
      COMMON/CONST/PI,EPS,EPS1,RE
      COMMON/MESH/AL,AK,MINT,NINT,MPT,NPT,MNINT,NDTETA
      COMMON/GRID/E(51),XI(51),R(51),ETA(31),TETA(31),NTETA(31)
      COMMON/CTOUR/CSF(33),CR(31,33),DSFR(31,33),DSFT(31,33),
     1CRT(31,33),CSFN(10),NTETA1(33),NTETAS(33)
      COMMON/NCTOUR/ICP6,NC,NC1,NCVOR
      COMMON/INTERG/NI(33),NS(33)
      COMMON/DRFT/XD(31,33),YD(31,33),TD(31,33)
      WRITE(6,7000)
 7000 FORMAT(1HI,50X,14HPARTICLE DRIFT/48X,18(1H*)/)
      DO 1000 K=1,NC
      NNI=NI(K)
      NNS=NS(K)
      LI=NNI-1
      LS=NNS+1
C*****
C*****SET VALUES TO 0.0
      DO 5000 I=1,LI
      XD(I,K)=0.000
      YD(I,K)=0.000
      TD(I,K)=0.000
 5000 CONTINUE
      DO 5001 I=LS,NPT
      XD(I,K)=0.000
      YD(I,K)=0.000
      TD(I,K)=0.000
 5001 CONTINUE
C*****
C*****COMPUTATION OF THE DRIFT
      DO 2000 I=NNI,NNS
      FONC1(I)=(PI*CRT(I,K))*((PI*CRT(I,K))/DSFR(I,K)-SIN(TETA(I))
     1-COS(TETA(I))*(DSFT(I,K)/DSFR(I,K)))
 2000 CONTINUE
      NNS1=NNS-1
      DO 3000 I=NNI,NNS1
      SOM1(NNI)=0.0
      SOM1(I+1)=SOM1(I)+0.5*AL*(FONC1(I)+FONC1(I+1))
 3000 CONTINUE
      DO 4000 I=NNI,NNS
      T(I)=SOM1(I)-CRT(I,K)*COS(TETA(I))
      YD(I,K)=CRT(I,K)*SIN(TETA(I))
 4000 CONTINUE
      DO 9000 I=NNI,NNS
      XD(I,K)=SOM1(I)-SOM1(16)
      TD(I,K)=T(I)-T(16)
 9000 CONTINUE
C*****
C*****WRITE OUT VALUES OF THE DRIFT
      WRITE(6,7400)CSF(K)
 7400 FORMAT(5X,7HCONTOUR,F4.2/4X,13(1H-)/)
```

```
      WRITE(6,7100)
 7100 FORMAT(10X,4HTETA,15X,1HX,20X,1HY,20X,1HT)
      WRITE(6,7200)(NTETA(I),XD(I,K),YD(I,K),TD(I,K),I=NNI,NNS)
 7200 FORMAT(11X,I3,1H*,9X,G11.4,10X,G11.4,10X,G11.4)
      WRITE(6,7300)
 7300 FORMAT(/56X,20(1H*)/)
 1000 CONTINUE
      RETURN
      END
```

```
      SUBROUTINE WRTAPE
C*****
C*****THIS SUBROUTINE WRITES RESULTS ON MAGNETIC TAPES
C*****      ICP7=1 PARTIAL RESULTS ONLY ARE WRITTEN
C*****      ICP7=0 CONVERGED RESULTS ARE WRITTEN FOR A GIVEN RE NUMBER
C*****
      COMMON/CONST/PI,EPS,EPS1,RE
      COMMON/MESH/AL,AK,MINT,NINT,MPT,NPT,MNINT,NDTETA
      COMMON/STRFUN/PSI(31,51),PSI1(31,51)
      COMMON/VORT/ZETA(31,51),ZETA1(31,51)
      COMMON/GRID/E(51),XI(51),R(51),ETA(31),TETA(31),NTETA(31)
      COMMON/CNTROL/ICP1,ICP2,ICP3,NUPV,NUPST,MUP,NISF,MNISF,NITER,
     1TIME,CPSEC,NW,NDW,NDIP
      COMMON/TAPE/ITAP,JTAP,NTAP
      COMMON/FILE/ICP7,IFILE
      COMMON/CTOUR/CSF(33),CR(31,33),DSFR(31,33),DSFT(31,33),
     1CRT(31,33),CSFN(10),NTETAI(33),NTETAS(33)
      COMMON/CTOUR1/CRTV1(31,25),CRTV2(31,25),CRT1(16,10),CRT2(16,10)
      COMMON/NCTOUR/ICP6,NC,NC1,NCVOR
      COMMON/VCTOUR/CVORT(25)
      COMMON/DRFT/XD(31,33),YD(31,33),TD(31,33)
C*****
C*****PARTIAL RESULTS
      REWIND JTAP
      WRITE(JTAP)(E(J),XI(J),R(J),J=1,MPT)
      WRITE(JTAP)(ETA(I),TETA(I),NTETA(I),I=1,NPT)
      WRITE(JTAP)((PSI(I,J),I=1,NPT),J=1,MPT)
      WRITE(JTAP)((ZETA(I,J),I=1,NPT),J=1,MPT)
      WRITE(JTAP)NITER,NW
      END FILE JTAP
```

```
C*****
      IF(ICP7.EQ.1) RETURN
C*****
C*****CONVERGED RESULTS
      REWIND NTAP
      IF(IFILE.GT.1) CALL SKIP
      WRITE(NTAP) RE
      WRITE(NTAP)((PSI(I,J),I=1,NPT),J=1,MPT)
      WRITE(NTAP)((ZETA(I,J),I=1,NPT),J=1,MPT)
      WRITE(NTAP)(R(J),J=1,MPT)
      WRITE(NTAP)(TETA(I),I=1,NPT)
      WRITE(NTAP)((CRT(I,K),DSFR(I,K),DSFT(I,K),I=1,NPT),K=1,NC)
      WRITE(NTAP) ((CRT1(I,K),CRT2(I,K),I=1,MNINT),K=1,NC1)
      WRITE(NTAP)((CRTV1(I,K),CRTV2(I,K),I=1,NPT),K=1,NCVOR)
      WRITE(NTAP) (CSF(K),K=1,NC),(CSFN(K),K=1,NC1),(CVORT(K),K=1,NCVOR)
      WRITE(NTAP)((XD(I,K),YD(I,K),TD(I,K),I=1,NPT),K=1,NC)
      END FILE NTAP
      WRITE(6,1) NTAP
    1 FORMAT(/5X,'CONVERGED RESULTS WRITTEN ON TAPE',I2)
      RETURN
      END
```

```
      SUBROUTINE SKIP
C*****
C*****THIS SUBROUTINE SKIPS THE FILES ON MAGNETIC TAPE
C*****
      COMMON/TAPE/ITAP,JTAP,NTAP
      COMMON/FILE/ICP7,IFILE
      NFILE=1
    3 READ(NTAP) RESULT
      IF(EOF(NTAP)) 1,2
    1 NFILE=NFILE+1
      IF(NFILE.EQ.IFILE) RETURN
    2 GO TO 3
      END
```

Listing PRO2

```
      PROGRAM PRO2(INPUT,OUTPUT,TAPE5=INPUT,TAPE6=OUTPUT,TAPE3)
C*****
C*****THIS PROGRAM COMPUTES THE VELOCITY FIELD FOR THE PARTICULATE PHASE
C*****AND FOR THE GAS PHASE.
C*****IT PROVIDES THE VALUES OF THE DRAG COEFFICIENT AROUND THE BUBBLE.
C*****IT ALSO COMPUTES THE GAS STREAM FUNCTION.
C*****
      COMMON/PARAM/PI,RE,MINT,NINT,MPT,NPT,NPT1,NDTETA,NC,FR
      COMMON/CONST/NALPHA,XLIM,MJ,NL,NDL,NCGS,NCG,NSP
      COMMON/SIZE/AL,AK,DL,DK
      COMMON/FIELD/PSI(31,51),ZETA(31,51)
      COMMON/GRID/R(51),TETA(31),NTETA(31)
      COMMON/DRFT/XD(31,33),YD(31,33),TD(31,33)
      COMMON/DER/DSFR(31,33),DSFT(31,33),CRT(31,33)
      COMMON/CNTOUR/CSF(33)
      COMMON/VAL/ALPHAB(10),GCSF(23)
      COMMON/DC/RG(12,50),TG(12,50),CG(12)
      COMMON/DGCOEF/TL1,ANG1,ANG2,ANG3,DTETA
C*****
C*****SET THE VALUES OF THE PARAMETERS
      DATA(ALPHAB(K),K=1,10)/0.25,0.50,0.75,1.00,1.25,1.50,1.75,2.00,
     12.50,5.00/
      DATA(GCSF(K),K=1,23)/-3.00,-2.00,-1.75,-1.50,-1.25,-1.00,-0.75,
     1-0.50,-0.25,-0.10,-0.05,0.00,0.05,0.10,0.25,0.50,0.75,1.00,1.25,
     21.50,1.75,2.00,3.00/
      DATA(CG(L),L=1,12)/1.00,0.95,0.90,0.85,0.80,0.70,0.60,0.50,0.40,
     10.30,0.20,0.10/
C*****
C*****TAPE PARAMETERS
      NTAP=3
      IFILE=1
C*****GRID PARAMETERS
      MINT=50
      NINT=30
      MPT=51
      NPT=31
      NPT1=16
      NDTETA=6
      AL=1./30.
      AK=0.0125
      DL=6.*AL
      DK=6.*AK
      NTETA(1)=0
      DO 1 I=1,NINT
      NTETA(I+1)=NTETA(I)+NDTETA
    1 CONTINUE
C*****CONTOUR PARAMETERS
      NC=33
      NCGS=23
      NCG=12
      NSP=50
      XLIM=3.
C*****EXECUTION PARAMETERS
      PI=3.1415926536
      NL=15
      NDL=2
      MJ=14
      NALPHA=10
C*****
```

```
C*****PARAMETERS USED IN SUBROUTINE DRAG
      TL1=PI/8.
      ANG1=PI/60.
      ANG2=PI/900.
      ANG3=PI/180.
      DTETA=PI/9000.
C*****
C*****READ DATA FROM MAGNETIC TAPE
      CALL RDRES(IFILE,NTAP)
C*****
C*****CALCULATION OF THE PARTICLE VELOCITY
      CALL SPEED1
C*****
C*****CALCULATION OF THE PRESSURE GRADIENT
      CALL GRAD
C*****
C*****RESULTS FOR THE PARTICLE VELOCITY
      CALL RES1
C*****
C*****
C*****LINES TAU =CST
      CALL CDRIFT
C*****RESULTS FOR THE PRESSURE GRADIENT
      CALL RES2
C*****
C*****CALCULATION OF THE GAS FIELD
      CALL SPEED2
C*****
      STOP
      END
```

```
      SUBROUTINE RDRES(IFILE,NTAP)
C*****
C*****THIS SUBROUTINE READS FROM A MAGNETIC TAPE THE CONVERGED SOLUTION
C*****FOR THE PARTICULATE FLOW
C*****
      COMMON/PARAM/PI,RE,MINT,NINT,MPT,NPT,NPT1,NDTETA,NC,FR
      COMMON/FIELD/PSI(31,51),ZETA(31,51)
      COMMON/GRID/R(51),TETA(31),NTETA(31)
      COMMON/DRFT/XD(31,33),YD(31,33),TD(31,33)
      COMMON/DER/DSFR(31,33),DSFT(31,33),CRT(31,33)
      COMMON/CNTOUR/CSF(33)
      REWIND NTAP
      IF(IFILE.GT.1) CALL SKIP(IFILE,NTAP)
      READ(NTAP)RE
      READ(NTAP)((PSI(I,J),I=1,NPT),J=1,MPT)
      READ(NTAP)((ZETA(I,J),I=1,NPT),J=1,MPT)
      READ(NTAP)(R(J),J=1,MPT)
      READ(NTAP)(TETA(I),I=1,NPT)
      READ(NTAP)((CRT(I,K),DSFR(I,K),DSFT(I,K),I=1,NPT),K=1,NC)
      READ(NTAP) DUMMY
      READ(NTAP) DUMMY
      READ(NTAP) (CSF(K),K=1,NC),(DUMMY,K=1,10),(DUMMY,K=1,25)
      READ(NTAP)((XD(I,K),YD(I,K),TD(I,K),I=1,NPT),K=1,NC)
C*****
      WRITE(6,1)
    1 FORMAT(1X//5X,'DATA READ FROM MAGNETIC TAPE'//)
      RETURN
      END
```

```
      SUBROUTINE SKIP(IFILE,NTAP)
C*****
C*****THIS SUBROUTINE SKIPS THE FILES ON MAGNETIC TAPE
C*****
      NFILE=1
    3 READ(NTAP) RESULT
      IF(EOF(NTAP)) 1,2
    1 NFILE=NFILE+1
      IF(NFILE.EQ.IFILE) RETURN
    2 GO TO 3
      END
```

```
      SUBROUTINE SPEED1
C*****
C*****THIS SUBROUTINE COMPUTES THE VELOCITY OF A PARTICLE BOTH
C*****      ---WITH RESPECT TO STATIONARY AXIS
C*****      ---WITH RESPECT TO AXIS MOVING WITH THE BUBBLE AT VELOCITY UB
C*****
      COMMON/PARAM/PI,RE,MINT,NINT,MPT,NPT,NPT1,NDTETA,NC,FR
      COMMON/DRFT/XD(31,33),YD(31,33),TD(31,33)
      COMMON/DER/DSFR(31,33),DSFT(31,33),CRT(31,33)
      COMMON/LIMIT/NI(33),NS(33)
      COMMON/PVEL/PVS(31,33),PVM(31,33),PVX(31,33),PVY(31,33)
      COMMON/GRID/R(51),TETA(31),NTETA(31)
      REAL L1,L2
C*****
C*****SET VALUES TO 0.
      DO 8000 K=1,NC
      DO 8000 I=1,NPT
      PVX(I,K)=0.0
      PVY(I,K)=0.0
      PVS(I,K)=0.
      PVM(I,K)=0.
 8000 CONTINUE
C*****
C*****-------STATIONARY AXIS-------
      DO 1000 K=1,NC
      NI(K)=2
      NS(K)=NINT
      ICP=1
      DO 2000 I=1,NPT
      IF(ICP.EQ.2) GO TO 100
      IF(ABS(XD(I,K)).GT.0.0) GO TO 100
      NI(K)=I+1
      GO TO 2000
  100 ICP=2
      IF(ABS(XD(I,K)).GT.0.0) GO TO 2000
      NS(K)=I-1
       IF(NTETA(I).EQ.90) GO TO 2000
      GO TO 1000
 2000 CONTINUE
 1000 CONTINUE
      DO 3000 K=1,NC
      MI=NI(K)
      MS=NS(K)
      MNI=MI+1
      MNS=MS-1
      DO 4000 I=MNI,MNS
      AL1=(XD(I,K)-XD(I-1,K))**2+(YD(I,K)-YD(I-1,K))**2
      AL2=(XD(I,K)-XD(I+1,K))**2+(YD(I,K)-YD(I+1,K))**2
      L1=SQRT(AL1)
      L2=SQRT(AL2)
      AT1=ABS(TD(I,K)-TD(I-1,K))
      AT2=ABS(TD(I,K)-TD(I+1,K))
      VEL1=L1/AT1
      VEL2=L2/AT2
      PVS(I,K)=(VEL1+VEL2)*0.5
 4000 CONTINUE
      AL2=(XD(MI,K)-XD(MI+1,K))**2+(YD(MI,K)-YD(MI+1,K))**2
      AT2=ABS(TD(MI,K)-TD(MI+1,K))
      L2=SQRT(AL2)
```

```
      AL1=(XD(MS,K)-XD(MS-1,K))**2+(YD(MS,K)-YD(MS-1,K))**2
      AT1=ABS(TD(MS,K)-TD(MS-1,K))
      L1=SQRT(AL1)
      PVS(MI,K)=L2/AT2
      PVS(MS,K)=L1/AT1
C*****
C*****-------MOVING AXIS-------
      DO 6000 I=MI,MS
      PVRM=-DSFT(I,K)/(PI*CRT(I,K))
      PVTM=DSFR(I,K)/(PI*CRT(I,K))
      PV=PVRM**2+PVTM**2
      PVM(I,K)=SQRT(PV)
      PVX(I,K)=PVRM*COS(TETA(I))-PVTM*SIN(TETA(I))
      PVY(I,K)=PVRM*SIN(TETA(I))+PVTM*COS(TETA(I))
 6000 CONTINUE
 3000 CONTINUE
      RETURN
      END
```

```
      SUBROUTINE FROUDE
C*****
C*****THIS SUBROUTINE COMPUTES THE FROUDE NUMBER FROM THE VALUES OF
C*****DERIVATIVES OF VORTICITY AND VELOCITY NEAR THE APEX OF THE BUBBLE.
C*****
      COMMON/PARAM/PI,RE,MINT,NINT,MPT,NPT,NPT1,NDTETA,NC,FR
      COMMON/SIZE/AL,AK,DL,DK
      COMMON/FIELD/PSI(31,51),ZETA(31,51)
      COMMON/VELOC/VT(31,51),VR(31,51),V(31,51)
      DIMENSION DZT(4)
C*****
C*****SECOND DERIVATIVE OF VORTICITY AT R=1,TETA=0.
      DO 1000 J=1,4
      DZT(J)=(18.*ZETA(2,J)-9.*ZETA(3,J)+2.*ZETA(4,J))/DL
 1000 CONTINUE
      ADZ=(-11.*DZT(1)+18.*DZT(2)-9.*DZT(3)+2.*DZT(4))/DK
      DZ=ADZ/(PI**2)
C*****VELOCITY DERIVATIVE
      ADVTT=(18.*VT(2,1)-9.*VT(3,1)+2.*VT(4,1))/DL
      DVTT=ADVTT/PI
C*****FROUDE NUMBER
      A=DVTT**2-(2.*DZ)/RE
      FR=1./A
      WRITE(6,1) FR
    1 FORMAT(//5X,3HFR=,G12.5,////)
      RETURN
      END
```

```
      SUBROUTINE GRAD
C*****
C*****THIS SUBROUTINE COMPUTES THE VALUES OF THE PRESSURE GRADIENT
C*****AT EACH NODE OF THE GRID
C*****
      COMMON/PARAM/PI,RE,MINT,NINT,MPT,NPT,NPT1,NDTETA,NC,FR
      COMMON/FIELD/PSI(31,51),ZETA(31,51)
      COMMON/GRID/R(51),TETA(31),NTETA(31)
      COMMON/SIZE/AL,AK,DL,DK
      COMMON/VELOC/VT(31,51),VR(31,51),V(31,51)
      COMMON/GRADP/DPR(31,51),DPT(31,51)
      COMMON/GRADPF/DPFR(31,51),DPFT(31,51)
C*****
C*****PARTICLE VELOCITY AT EACH NODE OF THE GRID
      DO 1000 I=1,NPT
      DO 2000 J=2,MINT
      DR=R(J+1)-R(J-1)
      VT(I,J)=(PSI(I,J+1)-PSI(I,J-1))/DR
 2000 CONTINUE
      VT(I,1)=(18.*PSI(I,2)-9.*PSI(I,3)+2.*PSI(I,4))/(DK*PI)
      VT(I,MPT)=(11.*PSI(I,MPT)-18.*PSI(I,MPT-1)+9.*PSI(I,MPT-2)
     1-2.*PSI(I,MPT-3))/(DK*PI*R(MPT))
 1000 CONTINUE
      DO 3000 J=1,MPT
      DO 4000 I=2,NINT
      DT=TETA(I+1)-TETA(I-1)
      VR(I,J)=-(1./R(J))*((PSI(I+1,J)-PSI(I-1,J))/DT)
 4000 CONTINUE
      VR(1,J)=-(1./(PI*R(J)))*((18.*PSI(2,J)-9.*PSI(3,J)+2.*PSI(4,J))/
     1DL)
      VR(NPT,J)=-(1./(PI*R(J)))*((-18.*PSI(NPT-1,J)+9.*PSI(NPT-2,J)-
     12.*PSI(NPT-3,J))/DL)
 3000 CONTINUE
      DO 9000 I=1,NPT
      DO 9000 J=1,MPT
      V2=VT(I,J)**2+VR(I,J)**2
      V(I,J)=SQRT(V2)
 9000 CONTINUE
C*****
C*****COMPUTATION OF FROUDE NUMBER
      CALL FROUDE
C*****
C*****DERIVATIVES OF THE VELOCITY AND VORTICITY
      DO 5000 I=1,NPT
      DO 6000 J=1,MPT
      IF(J.NE.1.AND.J.NE.MPT) GO TO 100
      IF(J.EQ.MPT) GO TO 901
      DVRR=(-11.*VR(I,1)+18.*VR(I,2)-9.*VR(I,3)+2.*VR(I,4))/(PI*DK)
      DVTR=(-11.*VT(I,1)+18.*VT(I,2)-9.*VT(I,3)+2.*VT(I,4))/(PI*DK)
      DZR=(-11.*ZETA(I,1)+18.*ZETA(I,2)-9.*ZETA(I,3)+2.*ZETA(I,4))/
     1(PI*DK)
      GO TO 400
  901 DVRR=(11.*VR(I,MPT)-18.*VR(I,MPT-1)+9.*VR(I,MPT-2)-2.*VR(I,MPT-3))
     1/(PI*DK*R(MPT))
      DVTR=(11.*VT(I,MPT)-18.*VT(I,MPT-1)+9.*VT(I,MPT-2)-2.*VT(I,MPT-3))
     1/(PI*DK*R(MPT))
      DZR=(11.*ZETA(I,MPT)-18.*ZETA(I,MPT-1)+9.*ZETA(I,MPT-2)-2.*ZETA
     1(I,MPT-3))/(PI*DK*R(MPT))
      GO TO 400
```

```
  100 DR=R(J+1)-R(J-1)
      DVRR=(VR(I,J+1)-VR(I,J-1))/DR
      DVTR=(VT(I,J+1)-VT(I,J-1))/DR
      DZR=(ZETA(I,J+1)-ZETA(I,J-1))/DR
  400 IF(I.NE.1.AND.I.NE.NPT) GO TO 200
      IF(I.EQ.NPT) GO TO 902
      DVRT=(-11.*VR(1,J)+18.*VR(2,J)-9.*VR(3,J)+2.*VR(4,J))/(PI*DL)
      DVTT=(-11.*VT(1,J)+18.*VT(2,J)-9.*VT(3,J)+2.*VT(4,J))/(PI*DL)
      DZT=(-11.*ZETA(1,J)+18.*ZETA(2,J)-9.*ZETA(3,J)+2.*ZETA(4,J))/
     1(PI*DL)
      GO TO 300
  902 DVRT=(11.*VR(NPT,J)-18.*VR(NPT-1,J)+9.*VR(NPT-2,J)-2.*VR(NPT-3,J))
     1/(PI*DL)
      DVTT=(11.*VT(NPT,J)-18.*VT(NPT-1,J)+9.*VT(NPT-2,J)-2.*VT(NPT-3,J))
     1/(PI*DL)
      DZT=(11.*ZETA(NPT,J)-18.*ZETA(NPT-1,J)+9.*ZETA(NPT-2,J)-2.*ZETA
     1(NPT-3,J))/(PI*DL)
      GO TO 300
  200 DT=TETA(I+1)-TETA(I-1)
      DVRT=(VR(I+1,J)-VR(I-1,J))/DT
      DVTT=(VT(I+1,J)-VT(I-1,J))/DT
      DZT=(ZETA(I+1,J)-ZETA(I-1,J))/DT
C*****
C*****PRESSURE GRADIENT
  300 FAC1=VR(I,J)*DVRR+(VT(I,J)*DVRT)/R(J)-(VT(I,J)**2)/R(J)
      FAC2=-(2.*DZT)/(RE*R(J))
      DPR(I,J)=2.*(FAC2-FAC1)
      DPR(I,MPT)=0.0
      FAC3=VR(I,J)*DVTR+(VT(I,J)*DVTT)/R(J)+(VT(I,J)*VR(I,J))/R(J)
      FAC4=(2.*DZR)/RE
      DPT(I,J)=(2.*R(J))*(FAC4-FAC3)
      DPT(I,MPT)=0.0
      DPFR(I,J)=DPR(I,J)-(2.*COS(TETA(I)))/FR
      DPFT(I,J)=DPT(I,J)+(2.*SIN(TETA(I))*R(J))/FR
      DPFT(NPT,J)=0.
 6000 CONTINUE
 5000 CONTINUE
      RETURN
      END
```

```
      SUBROUTINE RES1
C*****
C*****THIS SUBROUTINE PRINTS OUT THE RESULTS FOR THE PARTICLE VELOCITY
C*****RESULTS PRINTED ARE THE FOLLOWING
C*****     1-VELOCITY WITH RESPECT TO STATIONARY AXIS
C*****     2-VELOCITY ALONG PARTICLE STREAMLINES W.R.T. MOVING AXIS AT UB
C*****     3-VELOCITY AT EACH NODE OF THE GRID W.R.T. MOVING AXIS AT UB
C*****
      COMMON/PARAM/PI,RE,MINT,NINT,MPT,NPT,NPT1,NDTETA,NC,FR
      COMMON/GRID/R(51),TETA(31),NTETA(31)
      COMMON/PVEL/PVS(31,33),PVM(31,33),PVX(31,33),PVY(31,33)
      COMMON/VELOC/VT(31,51),VR(31,51),V(31,51)
      COMMON/CNTOUR/CSF(33)
C*****
      WRITE(6,1) RE
    1 FORMAT(50X,19(1H*)/50X,'*PARTICULATE  FLOW*'/50X,'*      RE=',
     1F6.2,'     *'/50X,19(1H*)////)
C*****
C*****VELOCITY WITH RESPECT TO STATIONARY AXIS
      N1=8
      NR=MOD(NC,N1)
      NN=NC-NR
      NM=NN+1
      WRITE(6,2)
    2 FORMAT(50X,'STATIONARY AXIS'/49X,17(1H*)/)
      DO 100 N=1,NN,N1
      N1=N+N1-1
      WRITE(6,3)(CSF(K),K=N,N1)
      WRITE(6,4)(NTETA(I),(PVS(I,K),K=N,N1),I=1,NPT)
      WRITE(6,5)
  100 CONTINUE
      WRITE(6,6)(CSF(K),K=NM,NC)
      WRITE(6,7)(NTETA(I),(PVS(I,K),K=NM,NC),I=1,NPT)
      WRITE(6,5)
C*****
C*****CALCULATION OF THE MEAN VELOCITY
      CALL MVEL
C*****
C*****VELOCITY ALONG STREAMLINES--X VELOCITY----Y VELOCITY
      WRITE(6,8)
    8 FORMAT(//50X,'VELOCITY ALONG STREAMLINES'/49X,28(1H*)/)
      DO 200 N=1,NN,N1
      N1=N+N1-1
      WRITE(6,3)(CSF(K),K=N,N1)
      WRITE(6,4)(NTETA(I),(PVM(I,K),K=N,N1),I=1,NPT)
      WRITE(6,12)
      WRITE(6,4)(NTETA(I),(PVX(I,K),K=N,N1),I=1,NPT)
      WRITE(6,12)
      WRITE(6,4)(NTETA(I),(PVY(I,K),K=N,N1),I=1,NPT)
      WRITE(6,5)
  200 CONTINUE
      WRITE(6,6)(CSF(K),K=NM,NC)
      WRITE(6,7)(NTETA(I),(PVM(I,K),K=NM,NC),I=1,NPT)
      WRITE(6,12)
      WRITE(6,7)(NTETA(I),(PVX(I,K),K=NM,NC),I=1,NPT)
      WRITE(6,12)
      WRITE(6,7)(NTETA(I),(PVY(I,K),K=NM,NC),I=1,NPT)
      WRITE(6,5)
    3 FORMAT(8X,8(3X,'CONTOUR=',F4.2))
```

```
    4 FORMAT(2X,I3,1H*,2X,8G15.5)
    5 FORMAT(/56X,20(1H*)/)
    6 FORMAT(8X,3X,'CONTOUR=',F4.2)
    7 FORMAT(2X,I3,1H*,2X,G15.5)
C*****
C*****VELOCITY AT GRID NODES
      NR=MOD(MPT,NI)
      NN=MPT-NR
      NM=NN+1
      WRITE(6,9)
    9 FORMAT(//50X,'VELOCITY AT GRID NODES'/49X,24(1H*)/)
      DO 300 N=1,NN,NI
      N1=N+NI-1
      WRITE(6,10)(R(J),J=N,N1)
      WRITE(6,11)(NTETA(I),(V(I,J),J=N,N1),I=1,NPT)
      WRITE(6,12)
      WRITE(6,11)(NTETA(I),(VR(I,J),J=N,N1),I=1,NPT)
      WRITE(6,12)
      WRITE(6,11)(NTETA(I),(VT(I,J),J=N,N1),I=1,NPT)
      WRITE(6,5)
  300 CONTINUE
      WRITE(6,13)(R(J),J=NM,MPT)
      WRITE(6,14)(NTETA(I),(V(I,J),J=NM,MPT),I=1,NPT)
      WRITE(6,12)
      WRITE(6,14)(NTETA(I),(VR(I,J),J=NM,MPT),I=1,NPT)
      WRITE(6,12)
      WRITE(6,14)(NTETA(I),(VT(I,J),J=NM,MPT),I=1,NPT)
      WRITE(6,5)
   10 FORMAT(8X,8(5X,2HR=,F6.2,2X))
   11 FORMAT(2X,I3,1H*,2X,8G15.5)
   12 FORMAT(/61X,10(1H+)/)
   13 FORMAT(8X,3(5X,2HR=,F6.2,2X))
   14 FORMAT(2X,I3,1H*,2X,3G15.5)
      RETURN
      END
```

```
      SUBROUTINE MVEL
C*****
C*****THIS SUBROUTINE COMPUTES THE MEAN VELOCITY FOR THE PARTICLE FLOW
C*****WITH RESPECT TO STATIONARY AXIS.
C*****
      COMMON/PARAM/PI,RE,MINT,NINT,MPT,NPT,NPT1,NDTETA,NC,FR
      COMMON/CONST/NALPHA,XLIM,MJ,NL,NDL,NCGS,NCG,NSP
      COMMON/GRID/R(51),TETA(31),NTETA(31)
      COMMON/CNTOUR/CSF(33)
      COMMON/DRFT/XD(31,33),YD(31,33),TD(31,33)
      COMMON/LIMIT/NI(33),NS(33)
      MNPT=NINT/2+1
      MNPT1=NINT/2
      WRITE(6,1)
    1 FORMAT(//50X,'MEAN VELOCITY'/49X,15(1H*)/)
      DO 8000 J=1,NL,NDL
      NNI=NI(J)
      NNS=NS(J)
      WRITE(6,400) YD(MNPT,J)
  400 FORMAT(//10X,'MAX. DISTANCE=',F5.2/10X,'LENGTH          TIME        VEL
     1OCITY')
      DO 8000 JJ=NNI,MNPT1
      DIST=0.
      ACVEL=0.
      NJ=NPT-JJ
      DO 7000 I=JJ,NJ
      AL=SQRT((XD(I+1,J)-XD(I,J))**2+(YD(I+1,J)-YD(I,J))**2)
      DIST=DIST+AL
      ACVEL=ACVEL+AL/(TD(I+1,J)-TD(I,J))
 7000 CONTINUE
      DELT=TD(NPT+1-JJ,J)-TD(JJ,J)
      N=NJ+1-JJ
      VEL=ACVEL/FLOAT(N)
      WRITE(6,500)DIST,DELT,VEL
  500 FORMAT(10X,F8.3,5X,F5.2,5X,F6.3)
 8000 CONTINUE
      WRITE(6,600)
  600 FORMAT(/56X,20(1H*)//)
      RETURN
      END
```

```
      SUBROUTINE RES2
C*****
C*****THIS SUBROUTINE PRINTS OUT THE RESULTS FOR THE PRESSURE GRADIENT.
C*****      P IS THE TOTAL PRESSURE INCLUDING THE HYDROSTATIC PRESSURE
C*****      PF IS THE PRESSURE OF THE FLUID
C*****
      COMMON/PARAM/PI,RE,MINT,NINT,MPT,NPT,NPT1,NDTETA,NC,FR
      COMMON/GRID/R(51),TETA(31),NTETA(31)
      COMMON/GRADP/DPR(31,51),DPT(31,51)
      COMMON/GRADPF/DPFR(31,51),DPFT(31,51)
C*****
      NI=8
      NR=MOD(MPT,NI)
      NN=MPT-NR
      NM=NN+1
      WRITE(6,1)
      DO 100 N=1,NN,NI
      N1=N+NI-1
      WRITE(6,2) (R(J),J=N,N1)
      WRITE(6,3)(NTETA(I),(DPR(I,J),J=N,N1),I=1,NPT)
      WRITE(6,8)
      WRITE(6,3)(NTETA(I),(DPT(I,J),J=N,N1),I=1,NPT)
      WRITE(6,4)
  100 CONTINUE
      WRITE(6,5)(R(J),J=NM,MPT)
      WRITE(6,6)(NTETA(I),(DPR(I,J),J=NM,MPT),I=1,NPT)
      WRITE(6,8)
      WRITE(6,6)(NTETA(I),(DPT(I,J),J=NM,MPT),I=1,NPT)
      WRITE(6,4)
      WRITE(6,7)
      DO 200 N=1,NN,NI
      N1=N+NI-1
      WRITE(6,2) (R(J),J=N,N1)
      WRITE(6,3)(NTETA(I),(DPFR(I,J),J=N,N1),I=1,NPT)
      WRITE(6,8)
      WRITE(6,3)(NTETA(I),(DPFT(I,J),J=N,N1),I=1,NPT)
      WRITE(6,4)
  200 CONTINUE
      WRITE(6,5)(R(J),J=NM,MPT)
      WRITE(6,6) (NTETA(I),(DPFR(I,J),J=NM,MPT),I=1,NPT)
      WRITE(6,8)
      WRITE(6,6) (NTETA(I),(DPFT(I,J),J=NM,MPT),I=1,NPT)
      WRITE(6,4)
    1 FORMAT(//50X,'TOTAL PRESSURE GRADIENT'/49X,25(1H*)/)
    2 FORMAT(8X,8(5X,2HR=,F6.2,2X))
    3 FORMAT(2X,I3,1H*,2X,8G15.5)
    4 FORMAT(/56X,20(1H*)/)
    5 FORMAT(8X,3(5X,2HR=,F6.2,2X))
    6 FORMAT(2X,I3,1H*,2X,3G15.5)
    7 FORMAT(//50X,'GAS PRESSURE GRADIENT'/49X,23(1H*)/)
    8 FORMAT(/56X,20(1H+)/)
      RETURN
      END
```

```
      SUBROUTINE CDRIFT
C*****
C*****THIS SUBROUTINE COMPUTES THE LINES TAU=CST FROM THE DRIFT CONTOURS
C*****
      COMMON/PARAM/PI,RE,MINT,NINT,MPT,NPT,NPT1,NDTETA,NC,FR
      COMMON/CONST/NALPHA,XLIM,MJ,NL,NDL,NCGS,NCG,NSP
      COMMON/GRID/R(51),TETA(31),NTETA(31)
      COMMON/DRFT/XD(31,33),YD(31,33),TD(31,33)
      COMMON/DER/DSFR(31,33),DSFT(31,33),CRT(31,33)
      COMMON/CNTOUR/CSF(33)
      COMMON/LIMIT/NI(33),NS(33)
      DIMENSION TAU(14),ST(31,33),RDC(31,33),TDC(31,33),XDC(31,33),
     1YDC(31,33)
      DIMENSION PT(3)
      DATA(TAU(J),J=1,14)/0.5,1.0,1.5,2.0,2.5,3.0,3.5,4.0,4.5,5.0,5.5,
     16.0,7.0,8.0/
      KI=2
      ITEST=1
      NPI=0
      WRITE(6,100)
  100 FORMAT(//50X,'DRIFT CONTOURS   LINES TAU=CST'/49X,32(1H*)/)
C*****
C*****VALUES FOR TLIM
      WRITE(6,101)
  101 FORMAT(10X,'1- DRIFT CONTOURS'/9X,19(1H-)/)
      DO 1000 K=2,NC
      NNI=NI(K)
      NNS=NS(K)
      DO 9998 I=NNI,NNS
      XCRT=CRT(I,K)*COS(TETA(I))
      IF(XCRT.LT.XLIM) GO TO 880
      XCRT1=CRT(I+1,K)*COS(TETA(I+1))
      IF(XCRT.GE.XLIM.AND.XCRT1.LE.XLIM) GO TO 881
 9998 CONTINUE
      WRITE(6,150)
  150 FORMAT(5X,'ERROR,NO VALUE FOR XLIM FOUND')
      STOP
  880 KI=KI+1
      GO TO 1000
  881 SLOPE3=(TETA(I+1)-TETA(I))/(XCRT1-XCRT)
      TTL=TETA(I)+SLOPE3*(XLIM-XCRT)
      RLIM=XLIM/COS(TTL)
      SLOPE4=(TD(I+1,K)-TD(I,K))/(CRT(I+1,K)-CRT(I,K))
      TLIM=TD(I,K)+SLOPE4*(RLIM-CRT(I,K))
      DO 9997 I=NNI,NNS
      ST(I,K)=TD(I,K)-TLIM
 9997 CONTINUE
C*****
C*****EXTRAPOLATION FOR SMALL VALUES OF CSF USING A PARABOLIC FITTING
      IF(KI.EQ.2) GO TO 882
      NPI=NPI+1
      IF(NPI.LE.3) GO TO 883
      GO TO 882
  883 PT(NPI)=TLIM
      IF(NPI.EQ.3) GO TO 885
      GO TO 882
  885 DS12=CSF(KI+1)**2-CSF(KI)**2
      DS13=CSF(KI+2)**2-CSF(KI)**2
      D12=CSF(KI+1)-CSF(KI)
```

```
      D13=CSF(KI+2)-CSF(KI)
      DT12=PT(2)-PT(1)
      DT13=PT(3)-PT(1)
      A=(DT12*D13-DT13*D12)/(DS12*D13-DS13*D12)
      B=(DT12*DS13-DT13*DS12)/(D12*DS13-D13*DS12)
      C=PT(1)-A*CSF(KI)**2-B*CSF(KI)
      ITEST=0
      KKI=KI-1
      DO 9995 M=2,KKI
      NII=NI(M)
      NSS=NS(M)
      ATLIM=A*CSF(M)**2+B*CSF(M)+C
      DO 9995 I=NII,NSS
      ST(I,M)=TD(I,M)-ATLIM
 9995 CONTINUE
  882 CONTINUE
      WRITE(6,210) CSF(K)
  210 FORMAT(///10X,7HCONTOUR,F4.2/10X,4HTETA,10X,1HX,15X,1HY,15X,1HT,
     115X,2HST,15X,3HCRT)
      WRITE(6,310)(NTETA(I),XD(I,K),YD(I,K),TD(I,K),ST(I,K),CRT(I,K),
     1I=NNI,NNS)
      WRITE(6,311)TLIM
  310 FORMAT(10X,I3,5G17.5)
  311 FORMAT(5X,'TLIM=',G13.5)
 1000 CONTINUE
      IF(ITEST.EQ.1) GO TO 1001
      DO 1002 K=2,KKI
      NNI=NI(K)
      NNS=NS(K)
      TLIM=TD(5,K)-ST(5,K)
      WRITE(6,210) CSF(K)
      WRITE(6,310)(NTETA(I),XD(I,K),YD(I,K),TD(I,K),ST(I,K),CRT(I,K),
     1I=NNI,NNS)
      WRITE(6,311)TLIM
 1002 CONTINUE
 1001 CONTINUE
C*****
C*****CALCULATION OF THE LINES TAU=CST
      WRITE(6,102)
  102 FORMAT(1X///10X,'2-LINES TAU=CST'/9X,18(1H-)/)
      DO 2001 K=2,NC
      NNI=NI(K)
      NNS=NS(K)
      DO 2001 J=1,MJ
      NNS1=NNS-1
      DO 2002 I=NNI,NNS1
      IF(TAU(J).GE.ST(I,K).AND.TAU(J).LE.ST(I+1,K)) GO TO 7700
      IF(TAU(J).GT.ST(NNS,K)) GO TO 7701
      IF(TAU(J).LT.ST(NNI,K)) GO TO 7701
 2002 CONTINUE
      WRITE(6,50)
   50 FORMAT(5X,'ERROR,NO VALUE FOR TAU')
      STOP
 7701 RDC(J,K)=0.0
      TDC(J,K)=0.0
      XDC(J,K)=0.0
      YDC(J,K)=0.0
      GO TO 2001
 7700 SLOPE1=(CRT(I+1,K)-CRT(I,K))/(ST(I+1,K)-ST(I,K))
```

```
      RDC(J,K)=CRT(I,K)+SLOPE1*(TAU(J)-ST(I,K))
      SLOPE2=(TETA(I+1)-TETA(I))/(CRT(I+1,K)-CRT(I,K))
      ATDC=TETA(I)+SLOPE2*(RDC(J,K)-CRT(I,K))
      XDC(J,K)=RDC(J,K)*COS(ATDC)
      YDC(J,K)=RDC(J,K)*SIN(ATDC)
      TDC(J,K)=(ATDC/PI)*180.
 2001 CONTINUE
      DO 2000 J=1,MJ
      XINF=XLIM-TAU(J)
      WRITE(6,8) TAU(J),XINF
      WRITE(6,7)
      WRITE(6,6)(CSF(K),RDC(J,K),TDC(J,K),XDC(J,K),YDC(J,K),K=2,NC)
    6 FORMAT(5X,F4.2,4G17.5)
    7 FORMAT(6X,'CSF',9X,'RDC',14X,'TDC',14X,'XDC',14X,'YDC')
    8 FORMAT(//10X,'CONTOUR TAU=',F4.2,5X,'X LIMIT AT INF.=',F5.1)
 2000 CONTINUE
      RETURN
      END
```

```
      SUBROUTINE SPEED2
C*****
C*****THIS SUBROUTINE COMPUTES THE GAS VELOCITY AT EACH NODE OF THE GRID
C*****FROM THE VALUES OF
C*****     -THE PARTICLE VELOCITY
C*****     -THE GAS PRESSURE GRADIENT
C*****     -THE VALUES OF THE DRAG COEFFICIENT AROUD THE BUBBLE
C*****
      COMMON/PARAM/PI,RE,MINT,NINT,MPT,NPT,NPT1,NDTETA,NC,FR
      COMMON/CONST/NALPHA,XLIM,MJ,NL,NDL,NCGS,NCG,NSP
      COMMON/VELOC/VT(31,51),VR(31,51),V(31,51)
      COMMON/GRID/R(51),TETA(31),NTETA(31)
      COMMON/GRADP/DPR(31,51),DPT(31,51)
      COMMON/GRADPF/DPFR(31,51),DPFT(31,51)
      COMMON/GSTFR/PHI(16,51),CRTG1(16,23),CRTG2(16,23)
      COMMON/VAL/ALPHAB(10),GCSF(23)
      COMMON/GVEL/UX(16,51),UY(16,51),UR(16,51),UT(16,51)
C*****
      WRITE(6,100)
  100 FORMAT(//////////55X,10(1H*)/55X,'*GAS FLOW*'/55X,10(1H*)///)
C*****
C*****CALCULATION OF GAMMA FUNCTION AROUND THE BUBBLE
      CALL DRAG
C*****
      DO 1000 K=1,NALPHA
      VALPHA=ALPHAB(K)
      DO 2000 I=1,NPT1
      DO 2000 J=1,MPT
      IF(R(J).GE.2.0) GO TO 2
      AR=R(J)
      ATETA=TETA(I)
      CALL ID(AR,ATETA,GAMMA)
      GO TO 3
    2 GAMMA=1.0
    3 COEF=(0.5*GAMMA*FR)/VALPHA
      UR(I,J)=VR(I,J)-COEF*DPFR(I,J)
      UT(I,J)=VT(I,J)-(COEF*DPFT(I,J))/R(J)
      UX(I,J)=UR(I,J)*COS(TETA(I))-UT(I,J)*SIN(TETA(I))
      UY(I,J)=UR(I,J)*SIN(TETA(I))+UT(I,J)*COS(TETA(I))
 2000 CONTINUE
      CALL GASSF(VALPHA)
      CALL RES3(VALPHA)
 1000 CONTINUE
      RETURN
      END
```

```
      SUBROUTINE DRAG
C*****
C*****THIS SUBROUTINE CALCULATES THE VARIATIONS OF GAMMA FUNCTION
C*****(ACCORDING TO JACKSON'S ANALYSIS)
C*****
      COMMON/PARAM/PI,RF,MINT,NINT,MPT,NPT,NPT1,NDTETA,NC,FR
      COMMON/CONST/NALPHA,XLIM,MJ,NL,NDL,NCGS,NCG,NSP
      COMMON/GRID/R(51),TETA(31),NTETA(31)
      COMMON/DC/RG(12,50),TG(12,50),CG(12)
      COMMON/DGCOEF/TL1,ANG1,ANG2,ANG3,DTETA
C*****
      REAL INVG1,INVG2,IANGLE
      NSP1=NSP-1
      ICP=1
      ANGLE=0.
      IANGLE=ANG1
      WRITE(6,600)
  600 FORMAT(///50X,'VARIATIONS OF THE DRAG COEFFICIENT'/49X,36(1H*)//
     110X,'VALUES OF THE STARTING POINTS'/10X,29(1H-)/10X,'   TETA
     1  R          X          Y        GAMMA      RMIN       RFIN    ')
C*****
C*****SET VALUES TO ZERO
      DO 2000 M=1,NCG
      DO 2000 K=1,NSP
      RG(M,K)=0.0
      TG(M,K)=0.0
 2000 CONTINUE
C*****
C*****ITERATIONS FOR DIFFERENT STARTING POINTS
      DO 4000 K=2,NSP
  551 ANGLE=ANGLE+IANGLE
      IP=0
      M=1
      IF(ANGLE.GE.TL1) IANGLE=ANG3
      T1=ANGLE
      IF(T1.GT.(PI/2.)) GO TO 4000
      INVG1=1.
      R1=2./COS(T1)
      Y=R1*SIN(T1)
      X=R1*COS(T1)
      G1=1./INVG1
      AT1=T1*180./PI
      RMIN=R1
      SR1=R1
      SG1=G1
      SX=X
      SY=Y
C*****
C*****ITERATIONS ALONG AN INTEGRATION PATH
      DO 3000 J=2,10000
      T2=T1+DTETA
      CALL INTPOL(R1,T1,DPR,DPT,DELP)
      R2=R1*(1.+(DPR/DPT)*(T2-T1))
      INVG2=INVG1*(1.-(DELP/DPT)*R2*(T2-T1))
      IF(R2.GE.1.0.AND.R2.LE.R(MPT)) GO TO 100
      GO TO 4002
  100 CALL INTPOL(R2,T2,DPR,DPT,DELP)
      INVG2=INVG1*(1.-(DELP/DPT)*R2*(T2-T1))
      IF(R2.LT.RMIN) RMIN=R2
```

```
      G2=1./INVG2
      G1=1./INVG1
      X=R2*COS(T2)
      Y=R2*SIN(T2)
      AT2=T2*180./PI
   53 IF(M.LE.4) DELG=0.025
      IF(M.GT.4) DELG=0.050
      IF(ABS(G2-CG(M)).LT.DELG) GO TO 51
      RFIN=R2
      IF(T2.GT.(PI/2.)) GO TO 4002
      IF(M.EQ.NCG) GO TO 4002
      M=M+1
      GO TO 53
   51 IF(R2.GT.2.00) GO TO 71
      RG(M+1,K)=R2
      TG(M+1,K)=AT2
      GO TO 72
   71 RG(M+1,K)=0.0
      TG(M+1,K)=0.0
   72 IF(G2.GT.G1) GO TO 4003
      R1=R2
      T1=T2
      INVG1=INVG2
 3000 CONTINUE
      WRITE(6,501)
  501 FORMAT(5X,'END OF ITERATION REACHED SUB. DRAG')
      STOP
 4003 IP=1
C*****
 4002 RFIN=R1
      IF(ICP.EQ.2) GO TO 4001
      IF(RFIN.LE.RMIN) GO TO 4001
      WRITE(6,500) AT1,SR1,SX,SY,SG1,RMIN,RFIN
      WRITE(6,700)
  700 FORMAT(10X,'NEW VALUE OF IANGLE PRECE DING POINT')
      ANGLE=ANGLE-IANGLE
      IANGLE=ANG2
      ICP=2
      GO TO 551
 4001 WRITE(6,500) AT1,SR1,SX,SY,SG1,RMIN,RFIN
  500 FORMAT(12X,F5.1,3X,6G10.4)
      RG(1,K)=2.00
      TG(1,K)=AT1
 4000 CONTINUE
C*****
      DO 7000 M=1,NCG
      DO 7000 K=2,NSP1
      IF(TG(M,K-1).GT.TG(M,K).AND.IG(M,K).LE.TG(M,K+1).AND.TG(M,K).
     1EQ.0.0) GO TO 85
      GO TO 7000
   85 TG(M,K-1)=0.0
      RG(M,K-1)=0.0
 7000 CONTINUE
      DO 8000 M=1,NCG
      TG(M,1)=0.0
      RG(M,1)=RG(M,2)
 8000 CONTINUE
      DO 9000 M=2,NCG
      DO 9001 K=1,NSP1
```

```
      IF(TG(M,K).NE.0.0.AND.TG(M,K+1).EQ.0.0) GO TO 90
      GO TO 9001
   90 IF(TG(M,K).GE.90.0) GO TO 9000
      GO TO 91
 9001 CONTINUE
  256 WRITE(6,255) K,M,DENOM
  255 FORMAT(5X,'IRREGULAR BEHAVIOUR',5X,'K=',I2,5X,'M=',I2,5X,'DENOM=',
     1G11.4)
      GO TO 9000
   91 DENOM=TG(M,K-1)-TG(M,K)
      IF(ABS(DENOM).GT.1.0E-03) GO TO 92
      GO TO 256
   92 IF(IP.EQ.1.OR.TG(M,K).LT.80.0) GO TO 9000
      SLOPE=(RG(M,K-1)-RG(M,K))/DENOM
      RG(M,K+1)=RG(M,K)+SLOPE*(90.0-TG(M,K))
      TG(M,K+1)=90.0
 9000 CONTINUE
C*****
C*****VALUES OF GAMMA FUNCTION CONTOURS
      WRITE(6,800)
  800 FORMAT(////10X,'GAMMA FUNCTION CONTOURS'/10X,23(1H-))
      WRITE(6,66)
      WRITE(6,62) (CG(M),M=1,NCG)
      DO 8500 K=1,NSP
      WRITE(6,60) (K,(RG(M,K),M=1,NCG))
      WRITE(6,61) (TG(M,K),M=1,NCG)
 8500 CONTINUE
      WRITE(6,65)
   60 FORMAT(5X,I2,3X,12F7.3)
   61 FORMAT(10X,12F7.1/)
   62 FORMAT(10X,12F7.2/10X,12(3X,4(1H-)))
   65 FORMAT(//50X,20(1H+)//)
   66 FORMAT(//10X,'R--CONTOURS      T--CONTOURS'/)
      RETURN
      END
```

```
      SUBROUTINE INTPOL(VR,VTETA,VDPR,VDPT,VDELP)
C*****
C*****THIS SUBROUTINE COMPUTES THE VALUES OF GRADPF AT ANY POINT AS WELL
C*****AS THE VALUES OF THE SECOND DERIVATIVES OF THE PRESSURE FIELD.
C*****INTERPOLATION IS MADE FOLLOWING
C*****      -LINES TETA=CST
C*****      -LINES R=CST
C*****
      COMMON/PARAM/PI,RE,MINT,NINT,MPT,NPT,NPT1,NDTETA,NC,FR
      COMMON/GRID/R(51),TETA(31),NTETA(31)
      COMMON/GRADPF/DPFR(31,51),DPFT(31,51)
      DIMENSION PDR(4),PDT(4),DR(4),DT(4)
C*****
      DO 1000 J=1,MINT
      IF(VR.GE.R(J).AND.VR.LE.R(J+1)) GO TO 100
 1000 CONTINUE
      WRITE(6,150)
 150  FORMAT(5X,'ERROR IN INTPOL')
      STOP
  100 DO 2000 I=1,NINT
      IF(VTETA.GE.TETA(I).AND.VTETA.LE.TETA(I+1)) GOTO 200
 2000 CONTINUE
      WRITE(6,150)
      STOP
 200  PDR(1)=DPFR(I,J)
      PDR(2)=DPFR(I,J+1)
      PDR(3)=DPFR(I+1,J)
      PDR(4)=DPFR(I+1,J+1)
      PDT(1)=DPFT(I,J)
      PDT(2)=DPFT(I,J+1)
      PDT(3)=DPFT(I+1,J)
      PDT(4)=DPFT(I+1,J+1)
C*****
C*****INTERPOLATION ALONG R=CST
      KK=0
      DO 3000 K=1,4,2
      KK=KK+1
      SLOPE=(PDR(K+1)-PDR(K))/(R(J+1)-R(J))
      DR(KK)=PDR(K)+SLOPE*(VR-R(J))
      SLOPE=(PDT(K+1)-PDT(K))/(R(J+1)-R(J))
      DT(KK)=PDT(K)+SLOPE*(VR-R(J))
 3000 CONTINUE
      SLOPE=(DR(2)-DR(1))/(TETA(I+1)-TETA(I))
      VR1=DR(1)+SLOPE*(VTETA-TETA(I))
      SLOPE=(DT(2)-DT(1))/(TETA(I+1)-TETA(I))
      VT1=DT(1)+SLOPE*(VTETA-TETA(I))
C*****
C*****INTERPOLATION ALONG TETA=CST
      DO 4000 K=1,2
      KK=KK+1
      SLOPE=(PDR(K+2)-PDR(K))/(TETA(I+1)-TETA(I))
      DR(KK)=PDR(K)+SLOPE*(VTETA-TETA(I))
      SLOPE=(PDT(K+2)-PDT(K))/(TETA(I+1)-TETA(I))
      DT(KK)=PDT(K)+SLOPE*(VTETA-TETA(I))
 4000 CONTINUE
      SLOPE=(DR(4)-DR(3))/(R(J+1)-R(J))
      VR2=DR(3)+SLOPE*(VR-R(J))
      SLOPE=(DT(4)-DT(3))/(R(J+1)-R(J))
      VT2=DT(3)+SLOPE*(VR-R(J))
```

```
C*****
C*****THE VALUES OF GRADPF AT A POINT (VR,VTETA) ARE TAKEN AS THE AVERAGE
C*****OF THE VALUES OBTAINED BY THE INTERPOLATION ALONG R=CST AND ALONG
C*****TETA=CST
      VDPR=0.5*(VR1+VR2)
      VDPT=0.5*(VT1+VT2)
C*****
C*****CALCULATION OF SECOND DERIVATIVES AND LAPLACIAN
      RLIM=0.5*(R(J+1)+R(J))
      TLIM=0.5*(TETA(I+1)+TETA(I))
      IF(VR.LE.RLIM.AND.VTETA.LE.TLIM)  IJ=1
      IF(VR.GT.RLIM.AND.VTETA.LE.TLIM)  IJ=2
      IF(VR.LE.RLIM.AND.VTETA.GT.TLIM)  IJ=3
      IF(VR.GT.RLIM.AND.VTETA.GT.TLIM)  IJ=4
      GO TO (50,60,70,80),IJ
   50 VD2PR=(VDPR-DR(3))/(VR-R(J))
      VD2PT=(VDPT-DT(1))/(VTETA-TETA(I))
      GO TO 90
   60 VD2PR=(VDPR-DR(4))/(VR-R(J+1))
      VD2PT=(VDPT-DT(1))/(VTETA-TETA(I))
      GO TO 90
   70 VD2PR=(VDPR-DR(3))/(VR-R(J))
      VD2PT=(VDPT-DT(2))/(VTETA-TETA(I+1))
      GO TO 90
   80 VD2PR=(VDPR-DR(4))/(VR-R(J+1))
      VD2PT=(VDPT-DT(2))/(VTETA-TETA(I+1))
   90 VDELP=VD2PR+VDPR/VR+VD2PT/VR**2
C*****
      RETURN
      END
```

```
      SUBROUTINE ID(VR,VTETA,GAMMA)
C*****
C*****THIS SUBROUTINE CALCULATES THE VALUE OF GAMMA FOR A GIVEN POINT
C*****(VR,VTETA) BY INTERPOLATING BETWEEN THE VALUES RG(I,J) AND TG(I,J)
C*****FOUND BY DRAG.
C*****
      COMMON/PARAM/PI,RE,MINT,NINT,MPT,NPT,NPT1,NDTETA,NC,FR
      COMMON/CONST/NALPHA,XLIM,MJ,NL,NDL,NCGS,NCG,NSP
      COMMON/DC/RG(12,50),TG(12,50),CG(12)
      NNCG=NCG-1
      NNSP=NSP-1
      DO 1000 M=1,NNCG
      DO 2000 K=1,NNSP
      IF(RG(M,K).EQ.0.0) GO TO 2000
      IF(VTETA.GE.TG(M,K).AND.VTETA.LE.TG(M,K+1)) GO TO 1001
 2000 CONTINUE
      IF(M.EQ.1) GO TO 1000
      WRITE(6,100)
  100 FORMAT(5X,'ERROR IN VTETA INTERPOLATION*** SUB. ID')
      STOP
 1001 SLOPE1=(RG(M,K+1)-RG(M,K))/(TG(M,K+1)-TG(M,K))
      YM1=RG(M,K)+SLOPE1*(VTETA-TG(M,K))
      IF(M.EQ.2.AND.VR.GT.YM1) GO TO 3100
      MM=M+1
      DO 2100 K=1,NNSP
      IF(TG(MM,K).EQ.0.0) GO TO 2100
      IF(VTETA.GE.TG(MM,K).AND.VTETA.LE.TG(MM,K+1)) GO TO 1100
 2100 CONTINUE
      GAMMA=CG(M)
      RETURN
 1100 SLOPE2=(RG(MM,K+1)-RG(MM,K))/(TG(MM,K+1)-TG(MM,K))
      YM2=RG(MM,K)+SLOPE2*(VTETA-TG(MM,K))
      IF(VR.LE.YM1.AND.VR.GE.YM2) GO TO 3000
      IF(CG(M).EQ.CG(NCG)) GO TO 3200
      IF(VR.LT.YM2.AND.RG(MM+1,K).EQ.0.0) GO TO 200
      GO TO 1000
  200 GAMMA=CG(MM)
      RETURN
 1000 CONTINUE
 3000 GAMMA=CG(MM)
      RETURN
 3100 GAMMA=CG(M)
      RETURN
 3200 GAMMA=CG(NCG)
      RETURN
      END
```

```
      SUBROUTINE GASSF(VALPHA)
C*****
C*****THIS SUBROUTINE COMPUTES THE STREAM FUNCTION FOR THE GAS FLOW AT
C*****EACH NODE OF THE GRID FROM THE VALUES OF THE GAS VELOCITY.
C*****CONTOURS OF THE GAS STREAM FUNCTION ARE FOUND BY LINEAR INTERPOLATION
C*****
      COMMON/PARAM/PI,RE,MINT,NINT,MPT,NPT,NPT1,NDTETA,NC,FR
      COMMON/CONST/NALPHA,XLIM,MJ,NL,NDL,NCGS,NCG,NSP
      COMMON/GRID/R(51),TETA(31),NTETA(31)
      COMMON/GSTFR/PHI(16,51),CRTG1(16,23),CRTG2(16,23)
      COMMON/VAL/ALPHAB(10),GCSF(23)
      COMMON/GVEL/UX(16,51),UY(16,51),UR(16,51),UT(16,51)
C*****
C*****VALUES OF THE GAS STREAM FUNCTION AT THE OUTER BOUNDARY
      DO 1000 I=1,NPT1
      PHI(I,MPT)=((VALPHA-1.)/VALPHA)*R(MPT)*SIN(TETA(I))
 1000 CONTINUE
C*****
C*****VALUES OF THE GAS STREAM FUNCTION AT THE GRID NODES
      DO 2000 J=1,MINT
      JJ=MPT-J
      DO 2000 I=1,NPT1
      PHI(I,JJ)=PHI(I,JJ+1)-0.5*(R(JJ+1)+R(JJ))*(UT(I,JJ+1)-UT(I,JJ))
     1-UT(I,JJ)*(R(JJ+1)-R(JJ))+R(JJ)*(UT(I,JJ+1)-UT(I,JJ))
 2000 CONTINUE
C*****
      DO 7000 I=1,NPT1
      DO 7000 K=1,NCGS
      CRTG1(I,K)=0.0
      CRTG2(I,K)=0.0
 7000 CONTINUE
      DO 6000 K=1,NCGS
      DO 6000 I=2,NPT1
      DO 4000 J=1,MINT
      IF(GCSF(K).GE.PHI(I,J).AND.GCSF(K).LE.PHI(I,J+1)) GO TO 100
 4000 CONTINUE
      GO TO 500
  100 DSFG=(PHI(I,J+1)-PHI(I,J))/(R(J+1)-R(J))
      CRTG1(I,K)=R(J)+(GCSF(K)-PHI(I,J))/DSFG
  500 DO 4100 J=1,MINT
      IF(GCSF(K).LE.PHI(I,J).AND.GCSF(K).GE.PHI(I,J+1)) GO TO 200
 4100 CONTINUE
      GO TO 6000
  200 DSFG=(PHI(I,J+1)-PHI(I,J))/(R(J+1)-R(J))
      CRTG2(I,K)=R(J)+(GCSF(K)-PHI(I,J))/DSFG
 6000 CONTINUE
      RETURN
      END
```

```
      SUBROUTINE RES3(VALPHA)
C*****
C*****THIS SUBROUTINE WRITES OUT THE RESULTS FOR THE GAS VELOCITY AS WELL AS
C*****THE GAS STREAM FUNCTION CONTOURS.
C*****
      COMMON/PARAM/PI,RF,MINT,NINT,MPT,NPT,NPT1,NDTETA,NC,FR
      COMMON/CONST/NALPHA,XLIM,MJ,NL,NDL,NCGS,NCG,NSP
      COMMON/GRID/R(51),TETA(31),NTETA(31)
      COMMON/GSTFR/PHI(16,51),CRTG1(16,23),CRTG2(16,23)
      COMMON/VAL/ALPHAB(10),GCSF(23)
      COMMON/GVEL/UX(16,51),UY(16,51),UR(16,51),UT(16,51)
C*****
C*****RESULTS FOR THE GAS VELOCITY
      WRITE(6,1) VALPHA
    1 FORMAT(//50X,'RESULT FOR ALPHAB=',F5.2/49X,25(1H-)//)
      WRITE(6,2)
    2 FORMAT(10X,'GAS VELOCITY'/10X,12(1H-)/)
      NI=8
      NR=MOD(MPT,NI)
      NN=MPT-NR
      NM=NN+1
      DO 1000 N=1,NN,NI
      N1=N+NI-1
      WRITE(6,10) (R(J),J=N,N1)
      WRITE(6,11) (NTETA(I),(UR(I,J),J=N,N1),I=1,NPT1)
      WRITE(6,12)
      WRITE(6,11) (NTETA(I),(UT(I,J),J=N,N1),I=1,NPT1)
      WRITE(6,13)
 1000 CONTINUE
      WRITE(6,14) (R(J),J=NM,MPT)
      WRITE(6,15) (NTETA(I),(UR(I,J),J=NM,MPT),I=1,NPT1)
      WRITE(6,12)
      WRITE(6,15) (NTETA(I),(UT(I,J),J=NM,MPT),I=1,NPT1)
      WRITE(6,13)
C*****
C*****STREAM FUNCTION VALUES
      WRITE(6,3)
    3 FORMAT(//10X,'GAS STREAM FUNCTION'/10X,19(1H-)/)
      DO 2000 N=1,NN,NI
      N1=N+NI-1
      WRITE(6,10) (R(J),J=N,N1)
      WRITE(6,11) (NTETA(I),(PHI(I,J),J=N,N1),I=1,NPT1)
      WRITE(6,13)
 2000 CONTINUE
      WRITE(6,14) (R(J),J=NM,MPT)
      WRITE(6,15) (NTETA(I),(PHI(I,J),J=NM,MPT),I=1,NPT1)
      WRITE(6,13)
C*****
C*****GAS STREAM FUNCTION CONTOURS
      WRITE(6,5)
    5 FORMAT(//10X,'GAS STREAM FUNCTION CONTOURS'/10X,28(1H-)/)
      NR=MOD(NCGS,NI)
      NN=NCGS-NR
      NM=NN+1
      DO 3000 N=1,NN,NI
      N1=N+NI-1
      WRITE(6,16) (GCSF(K),K=N,N1)
      DO 500 I=1,NPT1
      WRITE(6,11) (NTETA(I),(CRTG1(I,K),K=N,N1))
```

```
      WRITE(6,17) (CRTG2(I,K),K=N,N1)
  500 CONTINUE
      WRITE(6,13)
 3000 CONTINUE
      WRITE(6,18) (GCSF(K),K=NM,NCGS)
      DO 501 I=1,NPT1
      WRITE(6,19) (NTETA(I),(CRTG1(I,K),K=NM,NCGS))
      WRITE(6,20) (CRTG2(I,K),K=NM,NCGS)
  501 CONTINUE
      WRITE(6,13)
   10 FORMAT(8X,8(5X,2HR=,F6.2,2X))
   11 FORMAT(2X,I3,1H*,2X,8G15.5)
   12 FORMAT(/56X,20(1H+)/)
   13 FORMAT(/56X,20(1H*)/)
   14 FORMAT(8X,3(5X,2HR=,F6.2,2X))
   15 FORMAT(2X,I3,1H*,2X,3G15.5)
   16 FORMAT(8X,8(2X,'CONTOUR=',F5.2))
   17 FORMAT(8X,8G15.5/)
   18 FORMAT(8X,7(2X,'CONTOUR=',F5.2))
   19 FORMAT(2X,I3,1H*,2X,7G15.5)
   20 FORMAT(8X,7G15.5/)
      RETURN
      END
```

APPENDIX 5

CALCULATION OF THE FROUDE NUMBER IN THE CASE OF STOKES'S FLOW FOR THE THREE-DIMENSIONAL CASE

For potential flow solution, the Davies and Taylor approximation ensures that the pressure variations at the apex of a bubble are small.

This condition can be written as:

$$\left.\frac{\partial^2 P_f}{\partial \theta^2} = 0 \right| \begin{matrix} \theta = 0 \\ r = a \end{matrix} \qquad \text{(Chapter 2)}$$

Let us try to apply the Davies and Taylor approximation in the case of a very viscous flow around the bubble.

We shall only be concerned with the three-dimensional case where it is possible to find an analytical solution for the streamfunction.

The streamfunction is given by:

$$\Psi = \frac{U_b}{2} \left\{ 1 - \frac{3}{2}\frac{a}{r} + \frac{1}{2}\frac{a^3}{r^3} \right\} r^2 \sin^2\theta$$

In the case of a viscous flow the momentum term is negligible in comparison with the viscous effect term and the tangential component of the equation reduces to: (axisymmetrical flow)

$$-\frac{1}{r}\frac{\partial P_f}{\partial \theta} + \rho_p(1-\varepsilon_o)g\sin\theta + \mu_p \nabla^2 v_\theta + \frac{2}{r^2}\frac{\partial v_r}{\partial \theta} - \frac{v_\theta}{r^2\sin^2\theta} = 0$$

with $\nabla^2 = \frac{1}{r^2}\frac{\partial}{\partial r}\left(r^2\frac{\partial}{\partial r}\right) + \frac{1}{r^2\sin\theta}\frac{\partial}{\partial \theta}\left(\sin\theta\frac{\partial}{\partial \theta}\right)$

In addition $v_r = -\frac{1}{r^2\sin\theta}\frac{\partial \Psi}{\partial \theta}$

$$v_\theta = \frac{1}{r\sin\theta}\frac{\partial \Psi}{\partial r}$$

Replacing the values of v_r and v_θ in the θ-component of the momentum equation, we get:

$$-\frac{1}{r}\frac{\partial P_f}{\partial \theta} + \rho_p(1-\varepsilon_o)g\sin\theta + \mu_p U_b \sin\theta - \frac{3}{2}\frac{a}{r^3} = 0$$

The Davies and Taylor approximation then becomes:

$$\frac{\partial^2 P_f}{\partial \theta^2} = 0 \Bigg|_{\substack{\theta=0 \\ r=a}} \Rightarrow \frac{3}{2}\mu_p\frac{U_b}{a^2} = \rho_p(1-\varepsilon_o)g$$

and the bubble velocity:

$$U_b = \frac{2}{3}\frac{\rho_p(1-\varepsilon_o)}{\mu_p}ga^2 \qquad \text{(A.5.1)}$$

which means that, by assuming a Davies and Taylor approximation for a viscous flow past a spherical bubble, the velocity of the bubble is found to be proportional to the square of the bubble radius. In the case of potential flow the approximation leads to:

$$U_b = \frac{2}{3} \; g^{\frac{1}{2}} a^{\frac{1}{2}}$$

Putting equation (A. 5. 1) in dimensionless form, we finally get:

$$Fr = \frac{1}{3} \; Re$$